Dissertation

submitted to the

Combined Faculty of Mathematics, Engineering and Natural Sciences
of Heidelberg University, Germany

for the degree of

Doctor of Natural Sciences

put forward by

Marc Oliver Boucsein

born in Hannover, Germany

Oral examination:

23.07.2024

An end-to-end pipeline to study and model proton radiation-induced effects of the central nervous system as a function of dose and linear energy transfer at the single-cell level in 3D

Referees:
Prof. Dr. Dr. Jürgen Debus
Prof. Dr. Michael Hausmann

Abstract

Proton therapy is a promising form of brain radiotherapy due to its characteristic Bragg peak profile sparing normal tissue. However, late side effects have been observed and the underlying mechanisms are not fully understood. An end-to-end pipeline was first proposed to investigate late brain tissue-specific radiation-induced effects associated with the central nervous system (CNS) as a function of dose and linear energy transfer (LET) at the single-cell level in 3D for a well-established preclinical experiment mimicking patient treatment. This pipeline includes Monte Carlo-based dose and LET calculation, target delivery verification, image processing tasks including preprocessing, local-affine multi-step registrations, a topology-preserving segmentation, and analysis modules using 2-point density correlation functions, the Riemann elastic metric, and the CNS network size to measure compactness, shape and size heterogeneity. As a proof of principle, the pipeline was applied to investigate the observed radiation-induced astrogliosis segmented with a Dice coefficient of 0.86, achieving a maximum dose and LET uncertainty of 2.5 Gy and 2 keV/mum. In conclusion, the analysis reveals that the process of astrogliosis can be considered as a functional acting unit showing a radiation-induced late effect as a function of the brain tissue type, dose and LET indicating a variable relative biological effectiveness.

Zusammenfassung

Die Protonentherapie ist aufgrund ihres charakteristischen Bragg-Peak-Profils, das normales Gewebe besonders schont, eine vielversprechende Form der Hirnbestrahlung. Es wurden jedoch späte Nebenwirkungen beobachtet, und die zugrunde liegenden Mechanismen sind nicht vollständig geklärt. Wir haben erstmalig eine End-to-End-Pipeline entwickelt, um späte hirngewebsspezifische strahleninduzierte Effekte im Zusammenhang mit dem Zentralnervensystem (ZNS) als Funktion der Dosis und des linearen Energietransfers (LET) auf Einzelzellebene in 3D für ein etabliertes präklinisches Experiment, das die Patientenbehandlung nachahmt, zu untersuchen. Die Pipeline umfasst Monte-Carlo-basierte Dosis- und LET-Berechnungen, Zielverifizierung, Bildverarbeitungsaufgaben einschließlich Bildvorverarbeitung, lokal-affine mehrstufige Registrierungen, topologieerhaltende Segmentierung und Analysemodule unter Verwendung von 2-Punkt-Dichtekorrelationsfunktionen, der Riemannschen Elastizitätsmetrik und der ZNS-Netzwerkgröße zur Messung von Kompaktheit, Form und Größenheterogenität. Als proof of principle wurde die Pipeline verwendet, um die beobachtete strahleninduzierte Astrogliose zu untersuchen, segmentiert mit einem Dice-Koeffizienten von 0.86, mit einer maximalen Dosis und LET-Unsicherheit von 2.5 Gy und 2 keV/mum. Zusammenfassend zeigt die Analyse, dass der Prozess der Astrogliose als eine funktionelle Einheit verstanden werden kann, die einen strahleninduzierten Späteffekt als Funktion des Hirngewebetyps, der Dosis und der LET aufweist, was auf eine variable relative biologische Wirksamkeit hinweist.

Contents

I Introduction

1 Introduction 3

II Fundamentals

2 Interaction of protons with matter 9
2.1 Doses and LET 9
2.2 Simulation via Monte-Carlo 12
2.3 Biological interaction and relative biological effect 16

3 Cells of Central nervous system 17

4 Imaging and Image processing 19
4.1 Microscopic imaging 19
4.2 Magnetic resonance imaging 20
4.3 Registration 22
4.4 Segmentation 24

III Material & Methods

5 Preclinical Experiment Setup 33
5.1 CBCT and X-ray imaging 34
5.2 Treatment 34
5.3 MRI follow-up 36
5.4 Histology 36
5.5 Data reading and visualization 38

6 Monte-Carlo beam transport simulations 39
6.1 Monte-Carlo simulation of dose and LET 39

7 Preprocessing 47
7.1 Preprocessing of the CBCT and X-ray images for 3D position reconstruction 47
7.2 Preprocessing of the histological images 50

8 Quantification of dose delivery accuracy in 3D 53
8.1 Step A1: Repositioning Accuracy 55
8.2 Step A2: Uncertainties of A-priori dose 55
8.3 Step B1: 3D Position Reconstruction 56
8.4 Step B2: Evaluation of Position Uncertainty 57
8.5 Step B3: Uncertainty of A-posteriori dose 57
8.6 Software Implementation 57

9 Registration 59
9.1 B-Spline interpolation 59
9.2 CBCT-Atlas registration 63
9.3 Histology-Atlas registration 67

10 Segmentation 77
10.1 Segmentation of reactive astrocytes 77

11 Analysis 83
11.1 Analysis of number density of reactive astrocytes 83
11.2 Analysis of reactive astrocytes using correlation functions 83
11.3 Analysis of the morphology of reactive astrocytes 84

IV Results

12 Monte-Carlo beam transport simulations 89
12.1 Monte-Carlo simulation of dose and LET 89

13 Preprocessing 93
13.1 Preprocessing of the CBCT and X-ray images for 3D position reconstruction 93
13.2 Preprocessing of the histological images 96

14 Quantification of dose delivery accuracy in 3D 99
14.1 Step A1: Repositioning Accuracy 99
14.2 Step A2: Uncertainties of A-priori dose 100

14.3 Step B1: 3D Position Reconstruction 102
14.4 Step B2: Evaluation of Position Uncertainty 102
14.5 Step B3: Uncertainty of A-posteriori dose 104

15 Registration 107
15.1 CBCT-Atlas registration 107
15.2 Histology-Atlas registration 109

16 Segmentation 115
16.1 Segmentation of reactive astrocytes 115

17 Analysis 119
17.1 Analysis of number density of reactive astrocytes 119
17.2 Analysis of reactive astrocytes using correlation functions 123
17.3 Analysis of the morphology of reactive astrocytes 128

V & Discussion & Conclusion

18 Disccusion and Conclusion 139
18.1 Discussion: Monte-Carlo Simulation 139
18.2 Discussion: Dose delivery quantification 139
18.3 Discussion: Registration 141
18.4 Discussion: Segmentation 143
18.5 Discussion: Analysis 145
18.6 Conclusion 149

VI Appendix

19 List of Acronyms 153

20 Publications 155
20.1 Peer-Reviewed articles 155
20.2 Oral presentation at conferences 155

Bibliography 157

List of Figures 185

List of Tables 188

Part I

Introduction

Introduction 3

Introduction

1

Radiotherapy is one of the most common forms of therapy to treat cancer using the ionization power of particles. The last few years have been exciting times for hadron therapy, with more and more treatment facilities being built [146] and new types of particles being used [140, 241]. The most used particle for hadron therapy are protons [146]. An advantage over conventional photon therapy is the characteristic Bragg peak of protons, which allows efficient sparing of normal tissue with maximal dose delivery in the target tumor region [151]. However, particles such as protons generally have a higher ionization density than photons caused by a higher linear energy transfer (LET). To compare and relate physically the treatment modalities achieving the same clinical/biological endpoint, the concept of Relative biological effectiveness (RBE) has been established for the clinical application. In general, some recent in vitro and in vivo studies indicate that the RBE is dependent on treatment parameters such as dose and LET [235]. In addition, it was found that the RBE is also related to medical/biological parameters such as tissue type, biological endpoint or volume effect, describing the increased tissue complication with increased irradiated volume [56, 170, 243].

In general, there exist three options to investigate the RBE:

Clinical assessment, in vivo in animals or in vitro.

In vitro experiments allows the modeling of RBE under controlled experimental conditions. However, the translational predictions are very limited because cells are considered outside of a living organism without the possibility to study cell interactions related to the tissue. Fundamental in vivo effects such as volume effects can not be considered. Most in vitro RBE experiments use the clonogenic survival as a measure for biological effectiveness [235]. This measure is capable of modeling tumor response. However, its predictive value for the response of normal tissue cells is limited [235]. In addition, the conventional approach of using cloning assays to model RBE dependent on cell survival introduces substantial uncertainty due to delayed abortive cells, which complicates the binary classification between dead and live cells [109].

Another option is to perform clinical assessments directly. Clinical assessments are very difficult to perform because of the lack of cellular resolution and the fact that often only physiological endpoints can be considered. Furthermore, influencing factors caused by the human lifestyle of the study participants as well as environmental influences in general are difficult to control [235]. In addition, it is challenging to standardize the relevant treatment parameters such as irradiated volume, location of the tumour, individual radiosensitivity, comorbidities or patient positioning [235]. All in all, this can only reveal an integral response that has clinical implications as a locally resolved response.

In contrast to in vitro or clinical studies, in vivo preclinical studies overcome the limitations of not being able to adequately control confounding factors and have the potential to be clinically translatable. This is due to the fact that clinically relevant physical and medical parameters can be used for in vivo preclinical studies that mimic the clinical treatment [235]. Unfortunately, there are only limited in vivo data for the radiation-induced responses to date [136, 236] due to the manifold issues of in vivo experiments [235].

In general for the clinical routine a constant RBE value of 1.1 for protons independent of dose and LET has been historically established and used until today as a result of the uncertainty of experimental in vitro and in vivo data [169, 171]. However, some serious radiation-induced late effects of brain proton radiotherapy have been clinically observed in patients, such as radiation necrosis of the central nervous system (CNS), which may be associated with a variable RBE [8, 29]. This reveals increased clinical evidence of a variable RBE. Such brain lesions may be caused by the breakdown of the blood-brain barrier, which affects the CNS [5, 10, 38]. As a result, the assumption of a constant RBE is becoming less and less acceptable. However, the underlying mechanisms are not fully understood and most in vivo experiments focus only on early tissue responses [168, 200, 237]. Saager, et. al [200] proposed a reliable preclinical model based on the spinal cord of rats, considering the radiation-induced myelopathy as clinical/biological endpoint. Nonetheless, a preclinical model to study RBE at the single cell level in 3D in the context of the CNS, especially for the brain, has not been established to date.

As a first step to address these issues, a preclinical in vivo experiment based on the irradiation of mice was established to investigate the late effects of brain proton radiotherapy at the single cell level in 3D as a function of normal brain tissue, dose and linear energy transfer (LET) [222]. The preclinical in vivo experiment incorporates a wealth of information in multimodal images. These include X-ray images for accurate proton irradiation, Cone-beam computed tomography (CBCT) images for treatment planning and Monte Carlo simulation, Magnetic resonance imaging (MRI) to monitor the health of the mice, and histological images of cells to visualize biological effects at the single cell level in 3D. The goal of this preclinical experiment is to mimic the clinical proton radiation therapy with physically and clinically equivalent treatment parameters, to investigate late side radiation effects on normal brain tissue at the single cell level in 3D indicating variable RBE.

Fur this purpose, an end-to-end pipeline has been developed for the correlation and analysis of the radiation response as measured by cell-level histology with physical treatment parameters such as dose and LET.

Generally, such a pipeline must meet a number of requirements in terms of target accuracy (dose delivery and registration), segmentation and analysis. In general, targeting accuracy for small animal irradiation is recommended to be on the order of 0.1mm [254], especially for proton irradiation due to the characteristic Bragg peak. Furthermore, segmentation should preserve the morphology of cells to reveal, for example, radiation-induced responses of astrocyte processes that allow synapse-astrocyte communication via neurotransmitters [44]. In addition, the segmentation and analysis should be designed in a way that it is simultaneously sufficiently sensitive and specific. The analysis should also be able to resolve brain region-specific, dose-dependent, and LET-dependent responses indicative of RBE effects. Moreover, the analysis should be able to resolve further large-scale biological phenomena, such as cell tiling, to investigate systematic underlying processes at the cellular level. In summary, the aim of this work is to establish a pipeline that can meet these requirements to better understand the cellular mechanisms that could trigger radiation necrosis and the radiation-induced response as a function of the physical treatment parameters (dose and LET) at the single cell level in 3D in vivo.

The proposed pipeline in this thesis consists of five modules in total that meet the requirements:

- Monte Carlo Simulation of 3D dose and LET distribution
- Treatment planning and dose delivery verification
- Registration of the image modalities
- Detecting of radiation-induced response by segmentation
- Analysis of the radiation-induced response

As a first step to demonstrate the feasibility of studying late radiation-induced effects at the single-cell level, the pipeline was applied to our preclinical in vivo experiment to study the radiation-induced response of astrocytes (astrogliosis) as a function of brain region, dose, and LET, indicating the variability of RBE.

The thesis reflects the pipeline structure.

The foundations of our pipeline are explained in Chapter 2-4.

Chapter 5 describes the experimental setup and the workflow of the preclinical experiment for the investigation of late side effects induced by radiation.

Chapters 6 and 12 show how the Monte Carlo (MC) simulation of the 3D dose and LET distributions was performed and the statistical uncertainty of the dose and LET simulations.

Chapters 7 and 13 describe the preprocessing steps for dose delivery verification, registration, and segmentation.

In Chapters 8 and 14, a dose delivery quantification approach is proposed that determines and minimizes the dose placement uncertainties, the a-priori dose, caused by positional uncertainties during treatment. With this approach, the a-priori dose can be adjusted to obtain an MC-computed a-posteriori dose minimizing the effect of positional uncertainties on dose delivery.

In Chapters 9 and 15, the multi-step registration approach is illustrated using a 4′,6-Diamidin-2-phenylindol-Magnetic resonance imaging template (DAPI-MRI template) to correlate histology images with the dose and LET distribution, and the residual registration errors are quantified. This registration approach is based on a Graphics processing unit accelerated (GPU-accelerated) 3D B-spline interpolator, self-developed Napari packages, and a GPU-enabled registration toolkit performing local-affine transformations.

In Chapters 10 and 16, to segment reactive astrocytes as a result of proton irradiation, a U-Net model was proposed that was trained with a topology preserving loss. The performance has been benchmarked against other machine learning approaches such as Random Forest as well as traditional methods such as Thresholding. In addition, the effect of preprocessing and the choice of an appropriate loss was investigated.

In Chapters 11 and 17, the analysis modules for the investigation of the radiation-induced response in terms of astrogliosis are presented. Four analysis modules were conducted in three brain regions (the hippocampus, the midbrain, and the thalamus): The analysis of the number density of astrocytes in predefined cubes, the analysis of the compactness of astrogliosis using 2-point density correlation functions, the analysis of the heterogeneity of astrocytic shape using the Riemann elastic metric, and the size of processes of reactive astrocytes as a function of dose and LET.

Part II

Fundamentals

Interaction of protons with matter 9
Cells of Central nervous system 17
Imaging and Image processing 19

Interaction of protons with matter

2

2.1 Doses and LET

2.1.1 Definition

This section is based on [111, 162, 172, 205, 261]. The physical dose describes the energy E deposited into a mass element dm. The physical dose deposited results from two main types of interactions: Coulomb interactions and the nuclear reactions. For the first time, Bohr [22] described the interaction of charged particles with matter by means of the calculating of momentum of a stationary unbound electron and the impact parameter b, the distance of the closest path in the absence of the Coulomb interaction. According to the definition of the impact parameter three regimes can be defined for the intersection of protons with matter with respect to the atomic radius a.

"Soft" collision a $\ll$ b :
Coulomb interactions with the entire atomic electrons resulting in a small energy transfer.

"Hard" collision a $\approx$ b :
Coulomb interactions with single electrons result in large energy losses and determine the range in matter.

"Nuclear" collision a $\gg$ b :
Coulomb interactions with the entire atomic nucleus determine the lateral penumbral sharpness. Generation of Bremsstrahlung, but it is negligible for the therapeutic energy window in the radiology (a few MeV - 300 MeV). There are also nuclear reactions with the nucleus, but these are less frequent.

All these described interactions result in the characteristic depth dose profile consisting of a low dose build-up region at the entrance of the matter followed by the so-called Bragg peak (the maximum energy deposition region) compared to photons. This is a key advantage of protons over photons that is exploited in proton therapy to protect normal tissue behind the tumor. The main contribution to the physical dose for a proton beam comes from the Coulomb interactions [15]:

Proton beam energy	Contribution by Coulomb interactions
100 MeV	95 %
150 MeV	90 %
250 MeV	80 %

Tab. 2.1: The contributions to the absorbed dose from Coulomb interactions for different proton energies.

To include quantum mechanical effects, the impact parameter b was replaced by the momentum transfer, which takes on the task of distinguishing between different collision types such as "soft" and "hard" collisions. The first quantum mechanical description was done by Hans Bethe using a perturbation theory in the the charge z of the particle up to the second order and extending the formula to the relativistic case. Bloch extended this to the fourth order. Further corrections such as the density and shell correction were added to the formula. The density correction by Fermi is a consequence of the fact that the electric field of the projectiles is prone to polarize the atoms of the target. This leads to a shielding effect of the electric field far from the particle path and a smaller contribution to the energy loss without this consideration. Nonetheless, this effect is not significant for energies larger than 10^3 MeV, which are outside of the therapeutic window of proton irradiation, The shell effect is only important when the velocity of the particles is of the same order of magnitude as the velocity of the orbital electrons of the atoms of the target, where the assumption that the orbital electrons are stationary is no longer valid. Like the previously described effect, this is also negligible. Thus, for our therapeutic energy range of proton irradiation the Bethe-Block formula up to the second order looks like

$$-\left(\frac{\mathrm{d}E}{\mathrm{d}x}\right) = 4\pi N_{\mathrm{A}} r_{\mathrm{e}}^2 m_{\mathrm{e}} c^2 \rho z_{\mathrm{eff}}^2 \frac{Z}{A}\frac{1}{\beta^2}\left[\frac{1}{2}\ln\left(\frac{2m_{\mathrm{e}}c^2\beta^2\gamma^2 T_{\max}}{I^2}\right) - \beta^2\right] \tag{2.1}$$

N_{A}: Avogadro constant
$r_e = e^2/(4\pi\epsilon_0 m_e c^2)$: Classical electron radius
e: Elementary charge
ϵ_0: Vacuum permittivity
m_e: Rest mass of electron
c: Speed of light
ρ: Density of the target
Z: Atomic number of the target
A: Atomic mass of the target
I: Mean excitation energy
$\beta = v/c$: Speed of the projectile given by v
$\gamma = 1/\sqrt{1-\beta^2}$: Lorentz factor

with the maximum energy transfer per collision given by

$$T_{\max} = \frac{2m_e c^2\beta^2\gamma^2}{1 + 2\gamma m_e/M + m_e^2/M^2} \tag{2.2}$$

dependent on the rest mass of the projectile M,
and with the effective charge z_{eff} [13],

$$z_{\text{eff}} = z\left(1 - \exp\left(-125\beta z^{-\frac{2}{3}}\right)\right), \tag{2.3}$$

with the atomic number z of the projectile. This describes the collection of electrons by low-energy incident particles, especially heavy ions. Note that the Bethe-Bloch formula describes the mean loss of energy in matter. This means that to obtain the mean range of the particles, the energy loss described by the Bethe-Bloch formula must be integrated to over the energy according to

$$R = \int_E^0 \frac{\mathrm{d}E}{\mathrm{d}E/\mathrm{d}x} \tag{2.4}$$

In radiotherapy the definition of the linear energy transfer, LET, is common. The LET is defined by the mean energy loss dE of the considered particle through matter along a distance dl. The so-called unrestricted LET including all secondary electrons corresponds to the electronic stopping power, which can be described by the Bethe-Bloch formula 2.1. In general, there is no one type of particle with a specific energy level. Thus, it is necessary to weight the LET by the underlying energy and particle type. There are two weighting techniques. In our work, the dose-averaged LET is used, LET_d, defined as

$$LET_d = \frac{\sum_{p=\text{particle type}} \int LET_p(E) D_p(E)\, \mathrm{d}E}{\sum_{p=\text{particle type}} \int D_p(E)\, \mathrm{d}E} \tag{2.5}$$

$LET_p(E)$ corresponds the LET with an energy E of all particles of type p. $D_p(E)$ denotes the dose of all particles of type p with an energy E.

2.1.2 Detection

This section is based on [205]. There are a variety of dosimetric approaches to dose measurement based on ionization of gases or semiconductors, scintillation in certain materials, radiochromic films, luminescence, or chemical processes. Ionization chambers, semiconductor detectors, scintillation detectors, and radiochromic films are the most common dose measurement methods.

Ionization chambers in the simplest form correspond to a plate or cylindrical capacitor filled with a gas. A so-called multi-layer ionization chamber consists of a large number of parallel plate ionization chambers arranged in a row, which operate simultaneously to read out the dose [69]. When, for example, a proton hits the chamber, electron-ion pairs are produced, resulting in a ionization current. This current is proportional to the energy of the incoming radiation.

The operation of semiconductor detectors is similar to that of ionization chambers. Incoming radiation produces electrons and electron holes in the semiconductor, where the number of generated electrons is proportional to the energy of the incoming radiation.

On the other hand, the scintillation detectors use the luminescence in organic materials, fluids, inorganic substances or noble gas. This effect is due to the excitation of the atoms, which results in a spontaneous emission of photons with an energy similar to the incoming radiation. Nowadays, CCD sensors are employed to analyze these photons.

Another option is radiochromic film. Radiochromic films are based on the darkening of the film caused by the chemical reaction of the incoming radiation. The coloration (darkening) of the film can be read out with a transmission scanner and correlated to the dose D applying the following calibration [149],

$$D(I) = \frac{a + c \cdot 10^{\log(I)-\log(I_0)} - 1}{10^{\log(I)-\log(I_0)} - b} \tag{2.6}$$

The parameters a, b, c denote the fitting parameters. I_0 corresponds to the intensity of the light of a non-irradiated film. I corresponds to the intensity of the light of an irradiated film.

2.2 Simulation via Monte-Carlo

This section is based on [20, 33, 185, 205, 208, 265]. Since the Bethe-Bloch equation (2.1) is just a rough approximation of the mean energy loss by interactions of particles with matter, Monte Carlo simulations are required to model the interactions via the Boltzmann transport equation and to compute the resulting dose and LET. Monte Carlo simulations involve generating a large number of particles and tracking their behavior statistically. The more particles simulated, the more accurate the results become. In general, Monte Carlo simulation in radiotherapy consists of three key elements:

The Geometric modeling including the treatment machine, the beam line, and the irradiated anatomy,

Particle tracking modeling of interactions using cross-sectional data for different materials and particle types,

Scoring of the physical quantities in the target anatomy.

Accurate geometric modeling is needed to accurately simulate the particle trajectory. Thus, geometric modeling involves the representation of the irradiated anatomy using voxelized images. For this purpose, CT imaging based on X-ray images is commonly used. X-ray imaging is based on the physical principles of X-ray generation and the interaction of X-ray photons with tissue. X-ray photons are generated by an X-ray tube consisting of a cathode and an anode in a vacuum. The cathode emits a focused stream of electrons that are accelerated toward the anode. When the high-speed electrons hit the anode, they undergo a sudden deceleration. This rapid deceleration causes the electrons to release energy in the form of X-rays. The X-ray spectrum consists of a continuous spectrum (Bremsstrahlung) and characteristic X-rays, which are produced when electrons eject inner-shell electrons from the anode material.

The interaction of X-ray photons with tissues can be described by the attenuation of the X-ray photon beam obeying the Beer-Lambert law. For a non-monoenergetic X-ray photon beam for inhomogeneous matter along the photon beam line L, the

Beer-Lambert law looks like

$$I = \int w(E)\, \exp\left(-\int_L \mu(E,s)\mathrm{d}s\right) \mathrm{d}E, \tag{2.7}$$

where I denotes the intensity of the outgoing X-ray photons and μ describes the attenuation coefficient depending on the energy E and the position in the material s. $w(E)$ corresponds to the incoming energy spectrum of the X-ray photons. The main relevant contributions to the attenuation of X-ray photons for the X-ray imaging (<150 keV) are given by the photoelectric effect, the Compton effect and the Rayleigh effect.

The photoelectric effect is a phenomenon in which photons ionize atoms and eject electrons. The energy of the photon is transferred to the electron. For the photoelectric effect to occur, the energy of the photon must be greater than or equal to the binding energy of the electron in the material to break free the electrons. The attenuation is inversely proportional to E^3 and proportional to the atomic number Z given by Z^4. Thus, the photoelectric effect is the most dominant effect at low energies and for materials with higher atomic numbers leading to high attenuation. On the other hand, the Compton effect describes the scattering of photons by electrons for higher energy of photons as it is the case with the photoelectric effect.

The Rayleigh effect describes the scattering of a X-ray photon at an atom or a molecule without any energy being transferred to it, except for possible changes in the rotational energy. This effect has only a small impact on X-ray imaging.

The final 2D X-ray image is a negative projection of the scanned anatomy, with denser areas that have absorbed more X-ray photons appearing lighter (white or gray) and lighter areas that have absorbed less X-ray photons appearing darker.

To obtain 3D information and images, X-rays are taken from multiple angles to create cross-sectional images and reconstructed in computed tomography (CT). For example, consider 1D parallel beam X-ray projections generated from a 2D parallel beam geometry. The attenuation coefficient in the 2D Euclidean space $\mu(x,y)$ can be reconstructed by a set of line integrals $p(\vartheta,\chi)$ with $\vartheta \in [0,2\pi), \chi \in \mathbb{R}$ given by

$$p(\vartheta,\chi) = \int \mu(x,y)\; \delta(x\mathrm{cos}(\vartheta) + y\mathrm{sin}(\vartheta) - \chi)\; \mathrm{d}x\mathrm{d}y \tag{2.8}$$

Applying now the filtered backprojection, which used the Fourier transformation $P(\vartheta,u)$ of $p(\vartheta,\chi)$ given by $\mathcal{F}$

$$P(\vartheta,u) = \int \mu(x,y)\; \exp(-2\pi\mathrm{i}u(x\mathrm{cos}(\vartheta) + y\mathrm{sin}(\vartheta)))\; \mathrm{d}x\mathrm{d}y \tag{2.9}$$

The attenuation coefficient in the 2D Euclidean space $\mu(x,y)$ can now be computed as follows

$$\mu(x,y) = \int P(\vartheta,u)\; \exp(2\pi\mathrm{i}u(x\mathrm{cos}(\vartheta) + y\mathrm{sin}(\vartheta)))|u|\; \mathrm{d}\vartheta\mathrm{d}u \tag{2.10}$$

This expression is equal to the inverse Fourier transform given by

$$\mu(x,y) = \int \mathcal{F}^{-1}[u \cdot P(\vartheta,u)](\vartheta, x\mathrm{cos}(\vartheta) + y\mathrm{sin}(\vartheta)))\; \mathrm{d}\vartheta \tag{2.11}$$

$$= \int \mathcal{F}^{-1}[u \cdot P(\vartheta,u)](\vartheta,\chi)\; \mathrm{d}\vartheta \tag{2.12}$$

Now in our case assume that there exists a Fourier transform $\mathcal{F}[f](u)$ of a function f, which is equal to $|u|$. This function is known as the filter kernel. In general, the attenuation coefficient expression in 2.10 can then be expressed using the convolution theorem as

$$\mu(x, y) = \int \mathcal{F}^{-1}[\mathcal{F}[f](u) \cdot P(\vartheta, u)](\vartheta, \chi) \, \mathrm{d}\vartheta \tag{2.13}$$

$$= \int \mathcal{F}^{-1}[\mathcal{F}[f](\chi) \cdot p(\vartheta, \chi)](\vartheta, \chi) \, \mathrm{d}\vartheta \tag{2.14}$$

This means that, for example, the reconstruction of 2D X-ray images can be conducted by applying a convolution of a filter kernel and each projection $p(\vartheta, \chi)$. However, image acquisition using a parallel beam X-ray setup is not as fast.

For this reason, a fan-beam geometry approach is commonly used for 2D X-ray imaging, which records a projection by illuminating the entire detector. Therefore, 2D X-ray imaging fan-beam geometry was developed, recording one projection by illuminating the whole detector. For this reconstruction task, there exists also an analytic procedure [33]. To acquire 3D images cone-beam computed tomography (CBCT) geometry is commonly used. This means that a rectangular grid of detector pixels are irradiated similar to the fan-beam geometry in 2D, but now in 3D. The X-ray illumination is performed along a circular trajectory acquiring projections. This means that only the 2D slice associated with the trajectory of the X-ray source can be accurately reconstructed [245]. Nonetheless, there are some filtered-backprojection-type reconstruction alternatives [64].

A further essential step is the conversion of the Hounsfield scale HU used in CT to the material density required to model the particle interaction by Monte Carlo simulation.

The Hounsfield scale HU is defined as

$$HU = 1000 \frac{\mu_{\text{Tissue}} - \mu_{\text{Water}}}{\mu_{\text{Water}}} \tag{2.15}$$

By definition, air has a Hounsfield value of -1000 because μ_{air} is equal to zero, and water has a Hounsfield value of zero.

To convert the Hounsfield scale to the required materials a so-called Hounsfield look-up table (HLUT) is generally used in radiotherapy.

A common approach is the so-called Schneider approach [206]. This approach is based on CT-specific correction factors, which are used to assign tissues of similar Hounsfield values to the corresponding material density value. If CT-specific correction factors are not available, the so-called Mata approach can be used, where a CT-specific HLUT is generated to assign material classes of a given density [181].

To mimic the behavior of particles Monte Carlo simulations are based on the generation of pseudo-random numbers provided by an initial state, a seed value, to sample step lengths, energy losses and interaction type according to a specified distribution. True randomness is not possible without any external sources, because given the same initial conditions (e.g., the state of the system and the algorithm), a computer will produce the same output every time. True randomness, on the other hand, implies

that outcomes are unpredictable and cannot be determined from any known set of initial conditions. As a result, given the same seed, you'll get the same sequence of numbers. However, pseudo-random numbers obey the same statistical properties that resemble true randomness, making them suitable for MC simulation.
A variety of sampling methods exist for sampling from complex distributions such as energy loss. All of these methods are based on the sampling from a uniform distribution on the interval [0,1]. The most commonly used method of sampling is the Inverse-Transform method. Consider the transformation $\eta = P(x)$ for the cumulative distribution $P(x)$ of the probability distribution function $p(x)$, where η corresponds to a uniformly distributed pseudo-random number and x corresponds to a pseudo-random number according to a probability distribution function $p(x)$ that models, for example, the step size. Then the inverse transformation is given by $x = P^{-1}(\eta)$. This means that any pseudo number obeying a complex distribution can easily be sampled by the uniform distribution on the interval [0,1]. For instance, the probability distribution function of the step length l can be determined by

$$p(l) = \lambda_m^{-1} \exp(-l/\lambda_m) \tag{2.16}$$

with the mean path length $\lambda_m = 1/\rho\sigma$. σ denotes the total cross section and ρ corresponds to the atomic density of the material. According to the Inverse-Transform sampling method as described above the step length l is obtained by

$$l = -\lambda_m \ln(1 - \eta) \tag{2.17}$$

If no inverse transformation exists, it is necessary to use other approaches such as the rejection sampling [36]. In general, the MC simulation procedure for a primary particle involves the following steps:

- Kick off a particle in the phase space.
- Model material by its density and their transition.
- Compute σ for the current energy of the particle at material boundary.
- Calculate λ_m.
- Sample step length l.
- Decide the type i of interaction following the distribution $P_i = \sigma_i/\sigma$ given by the differential cross section σ_i of the interaction type.
- Sample and update other quantities such as the energy loss or directional changes from given probability distribution functions for the specified interaction type.
- If secondaries are produced by the decided interaction type, they can be considered by the steps described above.
- Score the dose and the LET at the end of the track in the target volume.
- Start the procedure from the beginning except when the particle is below a predefined energy threshold or is outside the considered phase space.

In radiotherapy, Monte Carlo simulations are generally considered the gold standard for dose and LET calculations due to their accuracy and ability to handle complex treatment scenarios. However, they are relatively slow until now, so dose and LET computations for treatment optimization are done in clinical routine by approximations such as the pencil-beam kernel method and the point-kernel method.

2.3 Biological interaction and relative biological effect

This section is based on [205, 261] When radiation hits biological matter, as in proton therapy, interaction processes emerge, which lead to a series of radiation damages, both intentional in the tumor and unintentional in normal tissue. The success of radiation therapy is limited by the unwanted reactions of normal tissues. The goal is to maximize the tumor complication probability (TCP) while minimizing the normal tissue complication probability (NTCP). In general, the regenerative ability of tumor cells is less than that of normal tissue. This effect is exploited by fractionated radiotherapy. Due to the characteristic Bragg peak, proton radiotherapy offers a decisive advantage in the protection of normal tissue.

Among other things, the ionization density is crucial for the radiation effect, which induces secondary biochemical processes. This means that high LET particles, which possess a high ionization density, cause more biological radiation damage. The Deoxyribonucleic acid (DNA) in the cell nucleus is generally very sensitive to radiation. The most critical damages are the double-strand breaks (DSB) in the DNA, which results into gen mutations, chromosomal aberrations, genomic instability, and cell death such as necrosis. Necrosis is referred to as accidental cell death. The cell size increases, organelles of the cells break up and the cell content flows out into the extracellular space. This in turn causes inflammation. Compared to single-strand breaks, which can be repaired error-free with an accuracy of 99 %, DSBs are very difficult to repair.

To compare high-LET (proton) radiotherapy with low-LET (photon) radiotherapy in terms of higher ionization potential and damage, Relative Biological Effectiveness (RBE) was introduced. The definition is based on the absorbed dose of a reference radiation D_{ref} and the dose D_{Y} of the investigated radiation, resulting in the same amount of biological injury, as follows

$$RBE = \left.\frac{D_{\text{ref}}}{D_{\text{Y}}}\right|_{\text{Biological isoeffect}} \tag{2.18}$$

As mentioned above, the RBE depends on the LET, but also on the dose (decreasing RBE with increasing dose [271, 276]), as well as on the biological endpoint [168] such as the onset of necrosis or also the time. The relationship between RBE and LET is still a part of the current state of research. However, some trends are observed in vitro that the RBE is nearly independent for low LET radiation less than 10 keV/μm, reaches a maximum at 100 keV/μm, and then decreases [37, 46, 127, 207].

3

Cells of Central nervous system

The central nervous system (CNS) is a complex and vital component of a body responsible for coordinating and regulating numerous physiological processes. It consists of the brain and the spinal cord. The CNS plays a pivotal role in regulating and coordinating nearly all bodily functions. Its tasks encompass sensory processing, motor control, cognitive functions, emotional regulation, and the maintenance of homeostasis. In the CNS there are two types of cells: Neurons and glial cells, which depict the whole of all nerve cells in the CNS [204].

Neurons are the fundamental building blocks of the nervous system and play a central role in transmitting information throughout the body. This allows us to perceive our environment, control our movements, and carry out a wide range of other physiological functions [204]. Glial cells in the CNS can be divided into oligodrocytes, microglia and astrocytes [204].

Oligodendrocytes are central to myelination and the maintenance of neuronal function in the CNS. Their role in myelinating axons and maintaining the integrity of the myelin sheath is crucial for efficient nerve signal transmission [130, 141]. In neuroinflammatory conditions, these cells can be both affected by inflammation and contribute to the inflammatory response. Understanding their role in neuroinflammation is critical to developing treatments that can preserve or restore myelin and improve outcomes in neuroinflammatory diseases such as multiple sclerosis [158].

Microglia are the resident immune cells of the CNS and play crucial roles in maintaining brain health, responding to injury and infection, and regulating the immune response in the brain. They are derived from myeloid progenitor cells, which originate in the yolk sac during early embryonic development. They migrate to the CNS and become resident immune cells [70]. When microglia detect signs of injury or infection, they can become activated and release pro-inflammatory cytokines/chemokines [104]. This response helps recruit other immune cells to the site of injury or infection [193]. They can exist in different states of activation, ranging from a resting, surveillance state to pro-inflammatory (M1-like) and anti-inflammatory (M2-like) states. The balance between these states is critical for proper immune function in the CNS [40]. Microglia are key players in neuroinflammatory processes. While their activation is essential for defense against pathogens and for promoting tissue repair, chronic or excessive activation of microglia can contribute to neurodegenerative diseases and neuroinflammatory conditions. Their ability to sense and respond to changes in the brain environment makes them key players in both health and disease.

Astrocytes are a type of glial cell in the CNS that play various critical roles in maintaining the health and function of neurons and other brain cells. Reactive astrocytes are a specific state or response of astrocytes to injury, disease, or other pathological conditions in the CNS [178, 263].

Astrocytes are involved in regulating the levels of neurotransmitters (chemical messengers) in the synaptic cleft between neurons [116]. They can also modulate synaptic transmission by releasing signaling molecules that influence synaptic plasticity, which refers to changes in the strength and efficiency of neuronal connections [42, 44, 126, 166, 221]. This modulation can have both positive and negative implications for neural circuit and the functional recovery [202]. They also aid in the removal of excess neurotransmitters and the recycling of neurotransmitter precursors by neurons [42]. Furthermore, they are responsible for regulating energy metabolism in the brain. In addition, they help deliver nutrients, such as glucose, to neurons and play a crucial role in maintaining the brain's energy balance [39, 221]. Moreover, astrocytes contribute to the formation and maintenance of the blood-brain barrier, regulating the exchange of substances between blood and brain tissue [116, 178, 263]. Beyond that functions, they help maintain the balance of ions in the extracellular space, which is crucial for proper neuronal function [42, 105].

Reactive astrocytes, as mentioned above, respond to various forms of brain injury or disease. Astrogliosis refers to an increase in the number of cells [94] expressing glial fibrillary acidic protein (GFAP) [57] that can have beneficial and detrimental effects on the CNS [219]. They may provoke morphological changes [94]. In general, GFAP is thus use as a standard marker for astrocytes [123]. Unfortunately, the role of GFAP is not yet fully understood and is the subject of ongoing research. It is presumed that GFAP maintain the cell shape and support the mobility of astrocytes [26].

One of the primary effects of astrogliosis is the formation of glial scars [277]. When the CNS is injured or damaged, reactive astrocytes migrate to the site of injury and proliferate, creating a physical barrier [215]. This glial scar can be both protective and inhibitory [101]. They can deposit extracellular matrix molecules, such as chondroitin sulfate proteoglycans, which can impede neural regeneration/axon growth [273]. It helps contain the damage and prevent it from spreading to healthy tissue and can also support neural regeneration/ axon growth [6, 84, 219]. Furthermore, astrogliosis can release pro-inflammatory molecules, including cytokines and chemokines, contributing to neuroinflammation in the CNS [43, 219]. As a part of the immune response this helps to recruit immune cells to the site of injury and remove (cellular) debris [116]. However, excessive or prolonged inflammation can also be detrimental to the surrounding neurons and tissue [133]. Moreover, astrogliosis can provide various forms of neuroprotection. They can release neurotrophic factors [99, 116] that help support and protect nearby neurons. In summary, astrogliosis is a complex and dynamic response of astrocytes to CNS injury or disease. It has both beneficial and detrimental effects on the CNS, but their tasks and effects are not fully understood [221].

4

Imaging and Image processing

4.1 Microscopic imaging

This section is mainly based on [25, 58, 115, 124, 176, 184, 197]. Several microscopic techniques, such as light (optical) microscopy, electron microscopy, and scanning probe microscopy, can be used to image histological samples. The advantage of electron microscopy and scanning probe microscopy over light microscopy is that higher resolution can be achieved. However, the disadvantage for biological slides is that the electron microscopy and scanning probe microscopy may impair the biological slides [98, 262]. Thus, the most commonly used microscopic technique is light microscopy to investigate histology. In general, there are many light microscopy techniques such as wide-field microscopy or confocal microscopy. All of these techniques used for scientific purposes are variants of compound microscopy techniques nowadays.

A compound microscope that uses two or more lenses to magnify the image of a sample as opposed to a simple microscope, which uses only one lens [262]. The objective lens is the primary lens responsible for magnifying the sample. It is located near the sample and produces an enlarged real image. Objective lenses come in various magnification powers, typically 4x, 10x, 40x, and 100x. The secondary lens, the ocular lens (eyepiece), is the lens closest to the observer's eye. It further magnifies the real image produced by the objective lens. Common eyepiece magnifications are 10x or 15x.

The bright-field microscopy is one of the most common and straightforward microscopy wide-field technique. It relies on transmitted light to illuminate biological samples, resulting in images that show dark features of varying intensity on a bright background, depending on the absorption strength of the sample density. A bright-field microscope typically uses a built-in light source, such as a halogen or LED lamp, that is positioned below the stage where the sample is placed. This light source provides uniform illumination.

Confocal microscopy is an advanced imaging technique used to obtain high-resolution histological images. It offers improved optical sectioning (the ability to generate low-noise images of the focal planes) reducing background noise compared to conventional microscopy. Confocal microscopes typically use laser light sources for their illumination. These lasers emit specific wavelengths of light to excite fluorophores in the sample. However, the confocal microscopy technique does not only work with fluorescent light, but also with scattered or reflected light. Two pinholes are the crucial elements in confocal microscopy in contrast to the wide- field microscopy. The first pinhole focuses the light just on a small part of the biological sample Another pinhole aperture is placed in front of the detector. It allows only the fluorescence emitted from the focal plane to pass through, while rejecting out-of-focus light.

During the microscopy process the sample is moved to scan. This enables a 2D or even 3D imaging. The speed of movement determines the quality of the acquired images. Compared to wide-field microscopy, where many focal planes, both in-focus as well as some out-of-focus, are merged, the improved optical sectioning is a key feature of confocal microscopy. In general, confocal microscopy achieves a higher contrast and resolution of images of samples and can better microscopically examine thick samples compared to wide-field microscopy, but requires more light intensity.

When the effect of fluorescence is used to image a biological sample instead of using external visible light sources, the microscopic imaging technique is called fluorescence microscopy technique. The fluorescence effect corresponds to the absorption of photons by the electrons of a sample at one wavelength and the excitation of the electrons to a higher energy level with the subsequent spontaneous emission of photons with longer wavelength caused by the electron transition back to the ground state. The spontaneous emission of photons with longer wavelength is the result of the energy loss due to vibrational relaxation [11, 115].

In addition, there are super-resolution microscopy techniques to overcome the diffraction limit of light discovered by Ernst Abbe. It states that the minimum resolution d is approximately limited by half the wavelength of light λ traveling through a medium of refractive index n and the aperture angle θ as follows

$$d = \frac{\lambda}{2n\sin(\theta)} \tag{4.1}$$

For instance, Stimulated Emission Depletion (STED) in fluorescence microscopy uses an additional laser to de-excite the sample in specific regions by stimulated emission after excitation [83, 268]. This means that the resolution is increased because the non-depleted area is much smaller than the illuminated excited primal area [55]. With super-resolution microscopy techniques such as STED, the lateral resolution can be improved from about 200 nm down to few nanometers.

In summary, light (optical) microscopy using the effect of fluorescence allows the investigation of biological processes and mechanisms on the nanometer scale.

4.2 Magnetic resonance imaging

This section is based on [205] and [30]. Magnetic resonance imaging (MRI) is based on the principles of nuclear magnetic resonance (NMR), a phenomenon that occurs when nuclei with an odd mass number and/or odd number of protons and neutrons are excited by radiofrequency (RF) pulses in the presence of a magnetic field. Because the resulting MR signal depends on tissue-specific parameters, MRI is a non-invasive imaging technique that can provide detailed structural and functional information about the living specimen. The most commonly imaged nuclei in clinical MRI are hydrogen nuclei (protons), which are highly abundant in living specimens due to their high water content. When placed in a strong external magnetic field (B_0), the nuclear spins align either parallel or antiparallel to the magnetic field. These different orientations of the spins correspond to slightly different energy states, which are proportional to the magnetic field.

To create an MRI image, a brief RF pulse at a specific frequency is applied perpendicular to the main magnetic field (B_0). This pulse excites the nuclear spins from their equilibrium positions (aligned with B_0) to the transverse plane, which corresponds to a flip angle of 90°. After the RF pulse is turned off, the flipped nuclear spins begin to precess around the axis of the main magnetic field (B_0) with the Larmor frequency. The Larmor frequency is proportional to the strength of the magnetic field and the gyromagnetic ratio of the nucleus (e.g., 42.58 MHz for protons at 1 T). The repetition time (T_R) corresponds to the time between 90° pulses and the echo time (T_E) corresponds to the time between the 90° RF pulse and the MR signal.

As the excited spins precess, they return to their equilibrium state. One type of MR sequence that is used for imaging is the spin-echo sequence. There are two relaxation mechanisms involved in this:

Spin-lattice relaxation is defined by the spin–lattice relaxation time T_1. It describes the recovery of the nuclear spins along the direction of B_0. T_1 is affected by tissue properties and can vary between different types of tissue. The process of spin-lattice relaxation results in the recovery of the longitudinal magnetization.

Spin-Spin relaxation is defined by spin–spin relaxation time T_2. It describes the loss of phase coherence among the spins in the transverse plane. T_2 is affected by the interactions among neighboring nuclei (e.g., proton-proton interactions) and the tissue environment. T_2 decay results in the loss of transverse magnetization. An additional dephasing effect described by T_2^* relaxation occurs due to inhomogeneities in the static magnetic field. To overcome this effect, a 180° RF pulse is applied after the 90° RF pulse.

The resulting spin-echo signal S is given by

$$S = M_0 \left(1 + e^{-T_R/T_1} - 2e^{-(T_R - T_E/2)/T_1}\right) e^{-T_E/T_2}, \tag{4.2}$$

where M_0 corresponds to the strength of magnetization in the direction of B_0.

When no 180° RF pulse is applied then the inhomogneity in the static magnitc field B_0 leads to a dephasing decribed by T_2^*

In summary, the relaxation processes described above generate an RF signal that is detected by receiver coils in the MRI scanner. This signal contains information about the relaxation times of the tissue (T_1 and T_2) and the spatial distribution of the spin density of the nuclei. MRI requires spatial encoding, which can be realized by means of additional magnetic gradient fields (gradient coils). By varying the current in these gradient coils, different regions of the sample are assigned unique frequencies, allowing spatial information to be reconstructed. The acquired signals are processed to reconstruct a two- or three-dimensional image based on the spatial encoding information using a Fast Fourier Transform. The resulting MR images can provide detailed anatomical and physiological information. In general, MRI can generate images with various image contrasts by manipulating the timing and type of RF pulses. Different MR sequences can be used to obtain T_1-weighted, T_2-weighted and proton density-weighted image contrasts. The image contrast of MRI is superior to CT images for soft tissue types, allowing for better classification. In summary,

T_1-weighted MR sequences (short T_E and T_R times) result in an image, where fatty tissue appears bright. On the other hand, T_2-weighted MR sequences (long T_E and T_R times) result in an image, where watery structures appear bright.

4.3 Registration

This section is based on [72, 224]. Image registration is a complex process that involves aligning corresponding regions of interest of images. In general, image registration is a classical optimization problem. The goal is to align images to a target image by determining the transformation aligning the images. Typical transformations can be divided into two categories: Deformable and non-deformable. The most common deformable transformations are deformation transformations parameterized by splines such as cubic multidimensional B-splines [108] or Thin-plate splines [24]. In general, non-deformable transformations can be categorized into translation, rigid (translation + rotation), similarity (translation + rotation + scaling) or affine (translation + rotation + scaling + shearing) transformations.

The optimization process is controlled by the selection of the similarity measure (a loss function), which weights the features or landmarks of the images based on the intensity or structure. The most common similarity measures are the Normalized Correlation Coefficient (NCC) for mono-modal image registration and the Mutual Information (MI) for multi-modal image registration. The similarity measure is usually evaluated at grid positions called voxels for 3D images and pixels for 2D images.

There are several approaches to optimizing this. In general, the most common approach is the Gradient descent method. It is given by

$$\mu^{(i+1)} = \mu^{(i)} - \alpha g_i, \tag{4.3}$$

where $\mu^{(i+1)}$ represents the updated parameters at time step $i+1$ and $\mu^{(i)}$ are the current parameters. α denotes the learning rate. g_i represents the gradient of the loss at the time step i.

A modification of the Gradient descent is given by the Adaptive Movement Estimation (Adam) optimization [106], which is a Stochastic Gradient descent method (SGD). A Stochastic Gradient descent method selects a random subset compared to the Gradient descent method. The Adam optimization process is given by

$$\mu^{(i+1)} = \mu^{(i)} - \frac{\alpha}{\sqrt{\hat{v}_\mu} + \epsilon} \hat{m}_\mu, \tag{4.4}$$

where $\hat{m}_\mu$ and $\hat{v}_\mu$ are defined as

$$\hat{m}_\mu = \frac{m_\mu^{(i+1)}}{1 - \beta_1^i} \tag{4.5}$$

$$\hat{v}_\mu = \frac{v_\mu^{(i+1)}}{1 - \beta_2^i} \tag{4.6}$$

with

$$m_\mu^{(i)} = \beta_1 m_\mu^{(i-1)} + (1 - \beta_1) g_i \tag{4.7}$$

$$v_\mu^{(i)} = \beta_2 v_\mu^{(i-1)} + (1 - \beta_2) g_i^2. \tag{4.8}$$

The term $\hat{m}_\mu$ corresponds to the bias-corrected first moment estimate. The term $\hat{v}_\mu$ corresponds to the bias-corrected second moment estimate. $m_\mu^{(i)}$ corresponds to the first moment estimate at time step i $v_\mu^{(i)}$ is the second moment estimate at time step i. β_1 is the exponential decay rate for the first moment estimate. β_2 denotes the exponential decay rate for the second moment estimate. ϵ is a small constant to prevent division by zero.
Another modification of the Stochastic Gradient descent method is given by the addition of a momentum [161], which stores the parameter update Δmu of the previous step. The optimization process is given by

$$\mu^{(i+1)} = \mu^{(i)} - \alpha g_i + \gamma \Delta \mu, \tag{4.9}$$

where γ corresponds to a scalar value in the interval $[0, 1]$ to weight the contribution of the earlier stages.
To evaluate the moving images during optimization and to obtain the final image at the end, interpolation techniques can be applied to approximate the intensities of off-grid positions of an image created by the transformation. The most common interpolators are Neighest Neighbour interpolator, Linear interpolator and higher order interpolators such as B-Spline interpolators.
Moreover, some deep learning approach has been applied to speed up image registration tasks such as 3D deformable registration [9, 66], which use neural network to extract features of moving images and target image to compare. The next section describes the foundations of deep learning used to solve segmentation tasks.

4.4 Segmentation

The following part of this section is based on [2, 21, 75]. Segmentation is an essential task in image processing, involving the identification of distinct regions or objects and the assignment of each image pixel to a label corresponding to an object. In general, the segmentation task can be divided into two categories: **Semantic Segmentation** and **Instance Segmentation**. Semantic segmentation and instance segmentation are two distinct methods differing in their objectives and outputs. In semantic segmentation, pixels that belong to the same class or category are grouped together. For instance, in an image of multiple houses, semantic segmentation would classify each pixel as belonging to a category house with one label. The output of the semantic segmentation is a region-level semantic map that assigns only one label to each class. Instance segmentation, on the other hand, aims to identify and differentiate each object instance in an image, and additionally assigns an identifier to each instance of an object, even if they belong to the same semantic class. For instance, in an image of multiple houses instance segmentation would label each house separately distinguishing them as individual instances. The output of instance segmentation is an object-level map. There are several segmentation techniques available, especially for instance segmentation, each with its own characteristics and suitability for different applications [27, 75, 77, 129, 210, 213]. The following part will briefly describes some of the segmentation methods used in this thesis and provides a comparison among them.

1. Thresholding [210]:

Thresholding is a simple technique that is widely used for segmentation purposes. It involves selecting a threshold value based on a selected feature distribution of the image and classifying the image pixels based on their selected feature values. All intensities of image pixels above the threshold will be allocated to one class and those below the threshold will be allocated to another class. It is fast and effective when there is a clear intensity separation between objects. The most common thresholding method is the Otsu's method, which is based on the minimization of the weighted sum of class variances [167].

2. Random forest [19, 27, 226]:

Random Forest is a typically fast machine learning approach compared to other deep learning approaches that uses an ensemble of separate hundreds of decision trees that make predictions independently to improve generalization and reduce overfitting to classify and segment pixels in an image. In a decision tree, each internal node is the result of a defined decision rule that is based on a particular feature of the input data. The tree branches out from each internal node to represent different possible outcomes of that feature. The final predicted class is represented by the leaf nodes of the tree. The process of building a decision tree involves selecting the best feature according to some criteria at each internal node. This categorizes the data to achieve the desired result. This continues until a stopping criterion is satisfied. For example, the predefined maximum depth is achieved. Each decision tree in the forest is trained independently on random subsets of the data. By aggregating the predictions of all trees, the final segmentation result is determined. Random Forests use techniques such as random feature selection and bootstrapping to mitigate overfitting, making segmentation results more generalizable. However, feature engineering is still important, such as removing irrelevant features and designing informative features based on prior knowledge to achieve good segmentation performance. In addition, Random Forest-based segmentation performs pixel-by-pixel classification, meaning that it assigns a class label to each pixel individually based on its selected features. Each pixel's classification is based solely on its own feature values, without considering the spatial relationships with neighboring pixels. This limits their ability to capture complex semantic patterns and context in image segmentation tasks. Nevertheless, a Random Forest provides interpretability by measuring and ranking the importance of features for a better understanding of relevant features.

3. Deep learning [2, 77, 93, 125, 152, 213]:

Compared to Random Forest, Deep Learning models have the advantage of automatically learning relevant features from the input data eliminating the need for explicit feature engineering. Deep learning architectures are designed to learn hierarchical representations of features through multiple layers of non-linear transformations. No manual feature engineering is required, as the network learns to infer meaningful, task-specific features directly from the data. They provide an end-to-end approach to feature learning and classification simultaneously. This approach allows optimizing the feature extraction process specifically for the given task, resulting in potentially more informative and task-specific features. During the learning process, they implicitly perform feature selection by assigning higher importance to more relevant features. The model learns to focus on the features that contribute most to the prediction task, effectively selecting the most beneficial features for the given problem. However, it's important to note that feature engineering can still be beneficial in certain cases when using Deep Learning models. It can be used to preprocess and augment the data, perform dimensionality reduction, or extract specific domain-specific features that are not easily learned by the model. Feature engineering in deep learning focuses on data preprocessing and augmentation rather than handcrafting features as in traditional machine learning methods. In addition, Deep Learning models are able to capture complex patterns and contextual information. Contextual understanding is achieved by using convolution and pooling operations, for example, to incorporate contextual information from neighboring pixels in contrast to Random Forest. Nonetheless, they possess a lack of interpretability compared to traditional methods like random forest due to their more complex model architecture. Furthermore, they are computationally time-consuming due its complex architectures and costly due to Graphics Processing Unit (GPU) hardware resource-demanding. Nevertheless, in recent years, deep learning approaches have provided state-of-the-art performance for many segmentation tasks. In the following, the workflow for applying deep learning models are demonstrated and how a model is generally built.

Each Deep Learning model is built by so-called neurons, which are inspired by our biological neurons. In a model of interconnected neurons, the task of a neuron is to process and transmit information. Each neuron receives input from other neurons or external sources, applies a mathematical transformation to the input, and produces an output associated with a weight. Weights determine how each input affects the neuron's output. They are adjusted during the training process to optimize the model's performance. The weighted sum of the inputs is passed through a so-called activation function, which establishes non-linearity into the neuron's output. A popular activation function is ReLU (Rectified Linear Unit), defined as

$$ReLU(x) = \begin{cases} x & \text{if} \, x > 0 \\ 0 & \text{if} \, x \leq 0 \end{cases} \quad \text{with} \quad ReLU'(x) = \begin{cases} 1 & \text{if} \, x > 0 \\ 0 & \text{if} \, x \leq 0 \end{cases} \tag{4.10}$$

In addition, before passing through the activation function, a bias term can be added to the weighted sum. The bias causes the neuron to translate the activation function, affecting overall behavior of each neuron. It enables breaking the symmetry among neurons and capturing prior knowledge, resulting in different outputs, and learning individual features for neurons with the same weights, e.g. to properly handle class imbalance. The output is then passed to other neurons in the model, forming a chain of information flow.

In summary, an artificial neuron can be described mathematically by

$$\text{outputs} = f(\sum_{\text{inputs}} \text{inputs} \cdot w + b), \tag{4.11}$$

where the weights w and the bias b are generally optimizable.

Neurons of the same mathematical operation are organized in layers, forming the basis of the Deep Learning approach. Often, the layers are categorized into three classes:

Input layer: The input layer defines the shape and format of the input data, such as the dimensions and channels of an image.

Hidden layers: Hidden layers are intermediate layers between the input and output layers. They usually consist of multiple neurons. The neurons of the hidden layer obtain the results of the previous layer and apply mathematical transformations such as described in 4.11. The number of hidden layers and their neurons are hyperparameters that can be adjusted based on the complexity of the task. Common layers are so-called convolutional layers (CNN), where the spatial dimension of the data is reduced by simultaneously increasing the channel dimension. The channels corresponds to the feature map containing the learned features. The output of a jth convolutional layer $a^j_{i,c}$ of the ith neuron corresponding to the channel c, can be described by

$$a^j_{i,c} = f(\sum_{k=-K,...,K} \sum_{l=1,...,N^{j-1}_{\text{channel}}} a^{j-1}_{i+k,l} \cdot w^j_{k,l,c} + b^j_c), \tag{4.12}$$

where j denotes the index of the current layer. The index k corresponds the index of a kernel with kernel size $K \times K$. The index $c \in \{1, ..., N^j_{\text{channel}}\}$ and l denote the channel of the current layer as well as the previous layer. N^j_{channel} are the number of channels of the jth convolutional layer. The weight $w^j_{k,l,c}$ acts as $N^{j-1}_{\text{channel}} \cdot N^j_{\text{channel}}$

convolutional kernels. b^j describes the corresponding bias of the jth layer.

Output layer: The output layer generates the final outcome. Depending on the type of task, such as binary classification or multi-class classification, the number of neurons is selected differently. For instance, these layers are often fully connected layers, where every neuron is connected to every neuron in the previous layer. The reason for this is that the number of weights and the biases that need to be optimized are related to the square of the number of the previous layer. Thus, they are used only after some layers, where the input was downsampled. The output a_i^j can be related to the input of the previous layers a_k^{j-1} as follows

$$a_i^j = f(\sum_k a_k^{j-1} \cdot w_{k,i}^j + b_i^j), \tag{4.13}$$

where $w_{k,i}^j$ and b_i^j denote the weights and biases. f denotes the activation function. The index i corresponds to the ith neuron. The index j denotes the jth fully-connected layer. The index k describes the number of all neurons of the previous layer. In general, this layer type can be used to perform segmentation [129], classifications [216] or to predict transformation parameters for registering images [90].

To learn features from different resolutions of the data, there are also downsampling and upsampling layers. In general, downsampling and upsampling layers have no parameters to optimize. For downsampling, max pooling is common. Max pooling operates on a local region of the input, typically defined by a small window. This window slides over the spatial dimensions of the data, moving in predefined steps. At each position, it extracts a subset of features. For each subset, the max pooling layer takes the maximum value from that subset. It is an effective way to obtain the most important feature of this region. To upsample the spatial resolution, interpolation techniques are applied. where image pixels/voxels themselves contain less information.

In recent years, so-called encoder-decoder network architectures, such as the U-Net architecture, have become a widely used architecture for various image segmentation tasks [196]. They consist of multiple convolutional and pooling layers. The encoder part is responsible for capturing high-level features from the input data. These layers increase the number of channels (feature maps) while decreasing the spatial dimensions. This part condenses the input image into a compact representation. The decoder part reconstructs the spatial information and upsamples the feature maps to produce an output that matches the spatial dimensions of the input. It consists of several convolutional and upsampling layers. These layers incrementally increase spatial dimensions to input size while reducing feature maps. The skip connections connect the encoder and decoder at multiple levels, allowing the decoder to make use of information from the encoder at different scales. This means that the output of each encoder block is concatenated to the corresponding decoder block. These skip connections are a key feature of U-Net to preserve spatial details, for example.

The workflow for establishing a Deep Learning approach for training tasks such as segmentation typically involves the following steps:

1. Data preparation
This includes dividing your dataset into training, validation, and test sets, and performing any necessary data preprocessing steps such as normalization, resizing, or data augmentation. Data augmentation describes a procedure in which a series of transformations are applied to improve the diversity of the training dataset. These transformations create variations of the original data, but retain the same underlying information. This is used to reduce overfitting by adding a form of implicit regularization and making the result more generalizable. By applying random spatial transformations such as deformations, rotations, and scaling, the model is forced to learn features that are invariant to these transformations. However, it should be used with caution to avoid introducing unrealistic or misleading augmentations. Typically, supervised learning groups training data into input-target pairs (the input and the desired output). This is the most common type of training.

2. Model Selection and Architecture Design
Choose an appropriate neural network architecture for your task, such as convolutional neural networks (CNNs) for image-related tasks. Specify the number of layers, the types of layers (convolutional, pooling, fully connected, etc.), and the activation function for each layer. In terms of the spatial and channel dimensions of the model, define the input shape of your input data.

3. Choice of loss function
Define an appropriate loss function that measures the discrepancy between the predicted outputs of the model and the desired output in the training data. It guides the optimization process and provides a quantitative measure of model performance. A common loss function for segmentation tasks is the cross-entropy loss CE [47],

$$CE = -\sum_{c}^{C} t_c \ln(p_c), \tag{4.14}$$

where t_c corresponds to the target segmentation and C characterize the number of classes. p_c denotes the predicted probability map for each class of the model, generated by a softmax-activation of the output layer given by

$$f(w)_i = \frac{e^{w_i}}{\sum_{j=1}^{C} e^{w_j}} \tag{4.15}$$

with the weight w_i for each class. Another common loss function/ evaluation measure for segmentation tasks is the dice coefficient loss DSC [50, 238] given by

$$DSC = \frac{2|A \cap B|}{|A| + |B|} \tag{4.16}$$

with the predicted segmentation A and the target segmentation B.$|.|$ characterizes the cardinality. For registration tasks, the mean absolute error and the mean squared error are usually used.

3. Choice of optimization method
Select an optimization method, such as Adam or Stochastic Gradient Descent (SGD), and set its parameters, including the learning rate. The common methods of optimization and the way in which optimization is performed in general have been described comprehensively in the previous section. For Deep Learning models, optimization algorithms such as SGD or Adam are used to update the weights and biases of the model based on the gradients computed during backpropagation [195] using the chain rule to minimize the chosen loss function.

4. Model training
Initialize the model with random weights or pre-trained weights from a similar task or architecture. Feed training data to the model in batches (multiple samples), provided that the training data is cut into equal-sized subsections (called patches) to avoid exceeding existing CPU/GPU memory limits. Compute the forward pass and calculate the loss between the predicted output and the input target. Backpropagate the gradients through the entire network and update the model weights and biases using the selected optimizer. Iterate this process for multiple epochs, adjusting the model parameters to minimize the loss, and evaluate the model's performance on the validation set.
An epoch is defined as a number of iterations or a run over the entire training dataset. The described training approach, where gradients of multiple samples are accumulated in so-called batches (mini-batch gradient descent), stabilizes and improves the optimization process.

Part III

Material & Methods

Preclinical Experiment Setup 33

Monte-Carlo beam transport simulations 39

Preprocessing 47

Quantification of dose delivery accuracy in 3D 53

Registration 59

Segmentation 77

Analysis 83

Preclinical Experiment Setup

5

In this thesis, an analysis pipeline for an established preclinical experiment based on the proton brain irradiation of mice [222] was developed to study late radiation-induced effects as function of dose and LET at the single-cell level in 3D. The established preclinical experiment comprises 21 mice (11 C57BL/6JRj and 10 C3H/HeNRj mice), where the right brain hemisphere was irradiated with a pristine proton Bragg peak. The mice were killed either when serious side effects, occurred followed by magnetic resonance imaging (MRI), or after six months, and the brain was excised and stained. An overview of the established peclinical model is displayed in Figure 5.1,

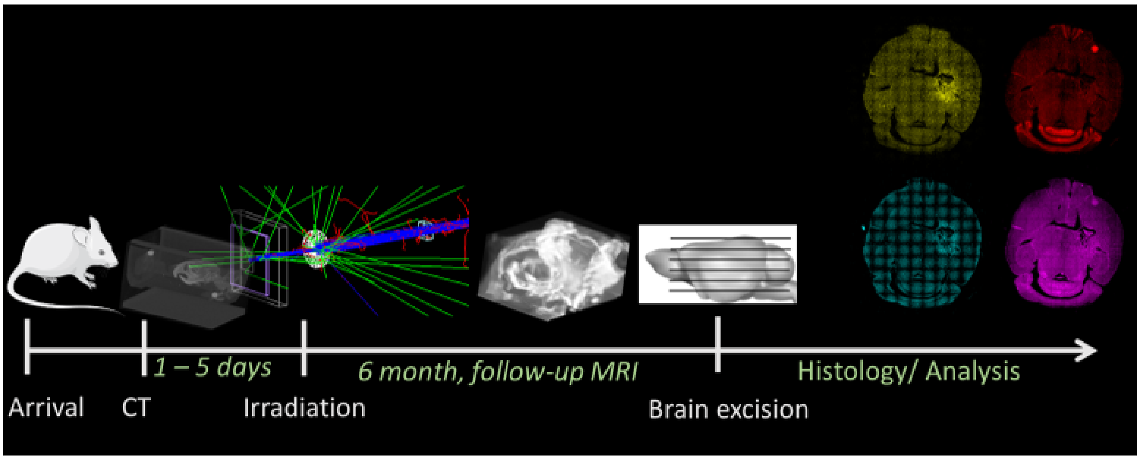

Fig. 5.1: Overview of the workflow for the preclinical experiment to investigate radiation-induced response after the proton irradiation of normal brain tissue.

In the following, the two mouse strains will be abbreviated as “B6“ and “C3H“. Two strains were selected to include biological diversity in order to be able to observe differences in terms of radiosensitivity [267].

In this thesis, the pipeline was applied to six irradiated and two non-irradiated mice that were already stained and microscopically imaged. The following sections describe key parts of the preclinical experiment for the pipeline.

5.1 CBCT and X-ray imaging

The mice were delivered two weeks before irradiation. One week prior to dose delivery, cone beam computed tomography (CBCT) imaging and X-ray imaging were conducted [242], as displayed in Figure 5.2.

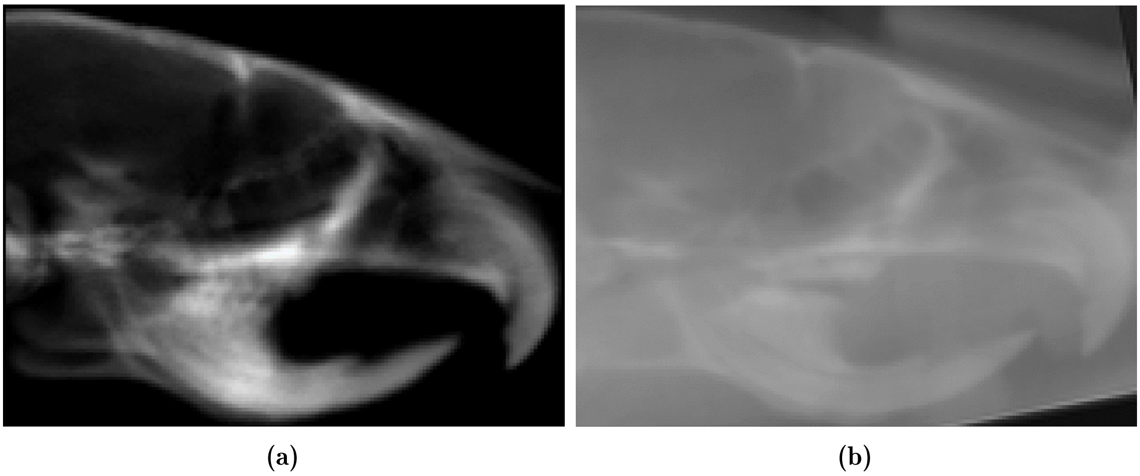
(a)

(b)

Fig. 5.2: An exemplary CBCT slice (subfigure 5.2a) and an exemplary X-ray image (subfigure 5.2b) of a mouse.

The CBCT imaging parameters were 60 kV, 5 mA, and the image voxel spacing was 100 μm x 100 μm x 100 μm. The X-ray imaging parameters were 60 kV, 5 mA, and an image pixel spacing of 100 μm x 100 μm. The CBCT was taken with a custom designed bed unit in [155]. The proton brain irradiation was run on a different day. The detailed logs are presented in [230, 231].

5.2 Treatment

For the treatment, the target area/point, specifically the right hippocampal region, was identified based on the Allen Mouse Brain Atlas and the recorded CBCT image [**Allen mouse atlas**]. In addition, an X-ray image was recorded shortly before the treatment for 2D repositioning of the mouse according to the target region at the experimental beamline. The mice were irradiated with doses ranging from 0 to 85 Gy with a pristine proton Bragg peak with a spot width of 4 mm (1-sigma) in the air at the isocenter. Three dose points were considered at 40 Gy, 60 Gy, and 80 Gy for C3H and 45 Gy, 65 Gy, and 85 Gy for B6. The beam position spread was 4.75 mm in the x-direction and 5.75 mm in the y-direction. The beam angular spread was 3.5 mrad in the x-direction and 5.5 mrad in the y-direction.

After the proton beam exits, the beamline consists of three collimators with decreasing collimator size down to 4 mm. A PC (Polycarbonate) block was placed between the second and third collimator to act as a range shifter to stop the proton beam in the right hemisphere of the brain. The spot energy was 92.4 MeV when leaving the nozzle and was reduced to about 27 MeV by the PC slab before entering the mouse. An exemplary schematic experimental setup for the proton irradiation is shown in Figure 5.3.

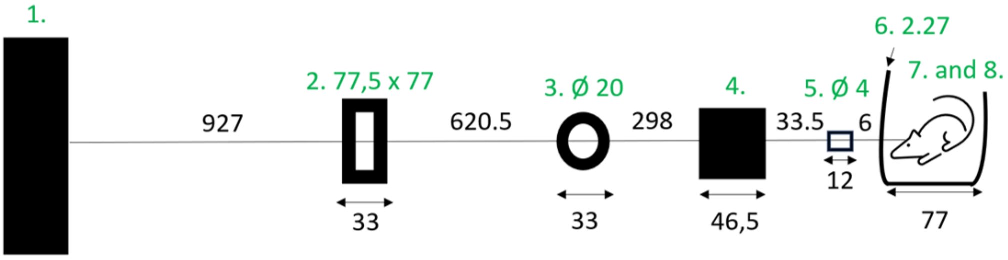

(a)

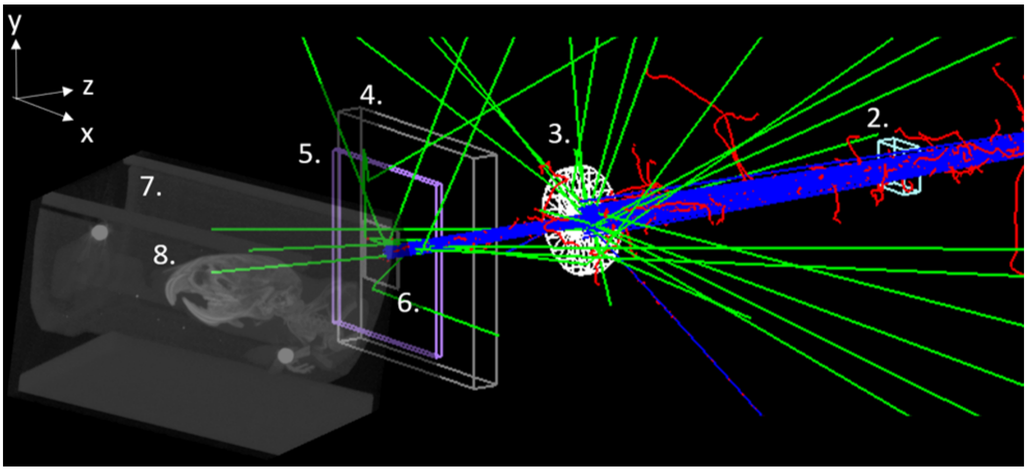

(b)

Fig. 5.3: Experimental preclinical beamline. 1. Beam exit, 2. First cylindrical brass collimator with 77,5 times 77 mm^2 size, 3. Second cylindrical brass collimator with 20mm diameter, 4. PC range-shifter with a thickness of 46.5mm, 5. Square brass collimator with 4mm diameter, 6. PMMA transport box with a wall thickness of 2.27mm, 7. Bedding unit and 8. The irradiated mouse. The subfigure 5.3a shows the schematic experimental setup in millimeters. The subfigure 5.3b visualizes an exemplary run of 100 particles of the setup in TOPAS. Protons are displayed in blue. Electrons are displayed in red. Gamma rays are displayed in green.

5.3 MRI follow-up

Magnetic resonance imaging (T_1-weighted and T_2-weighted) with a 1 T small animal MR scanner (nanoScan® PET/MRI, Mediso Medical Imaging Systems, Budapest, Hungary) was applied to physiologically monitor the evolution of radiation-induced injuries in mice as shown in Figure 5.4. The repetition time T_R was 15 ms 1000 ms for T_1 and 1000 ms for T_2. The echo time T_E was 3.1 ms for T_1 and 97.7 ms for T_2.

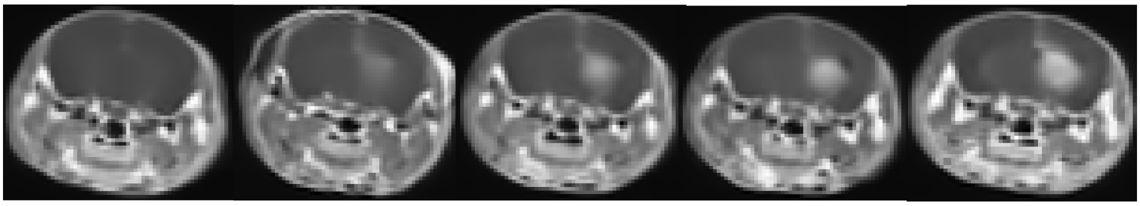

Fig. 5.4: An exemplary MRI follow-up (T1-weighted) of a mouse irradiated with 65 Gy showing contrast enhancing brain lesions at the timepoints (from left to right): Immediately before the proton irradiation, 3 weeks, 7 weeks, 11 weeks and 20 weeks after the proton irradiation.

5.4 Histology

Brain tissue was fixed in 4% formalin and prepared for paraffin embedding using a Benchtop Tissue Processor. The embedded samples were sectioned into 3 μm thick slices transversely across the brain at a distance of 100 μm from each other. Hematoxylin & eosin or immunofluorescence staining was then performed on these sections. Following dewaxing, rehydration, and heat-induced antigen retrieval, Antibody staining, such as rat anti-GFAP (Glial fibrillary acidic protein) was conducted. The sections were blocked prior to incubation with a primary antibody (rat anti-GFAP) and a secondary antibody (anti-rat AlexaFluor488). The staining was followed by DAPI counterstaining revealing all cell nuclei.

The study used an Axio Scan.Z1 digital slide scanner with a Plan-Apochromat 10x/0.45 M27 objective and an effective numerical aperture of 0.45 to acquire image tiles. Image tiles were automatically stitched and *.czi image pyramids were automatically created with a 16-bit image depth and the highest resolution corresponding to 0.65 μm x 0.65 μm. In this thesis, the reactive astrocytes stained by GFAP are considered and the DAPI counterstaining are used for registration. An exemplary stained section is shown in Figure 5.5.

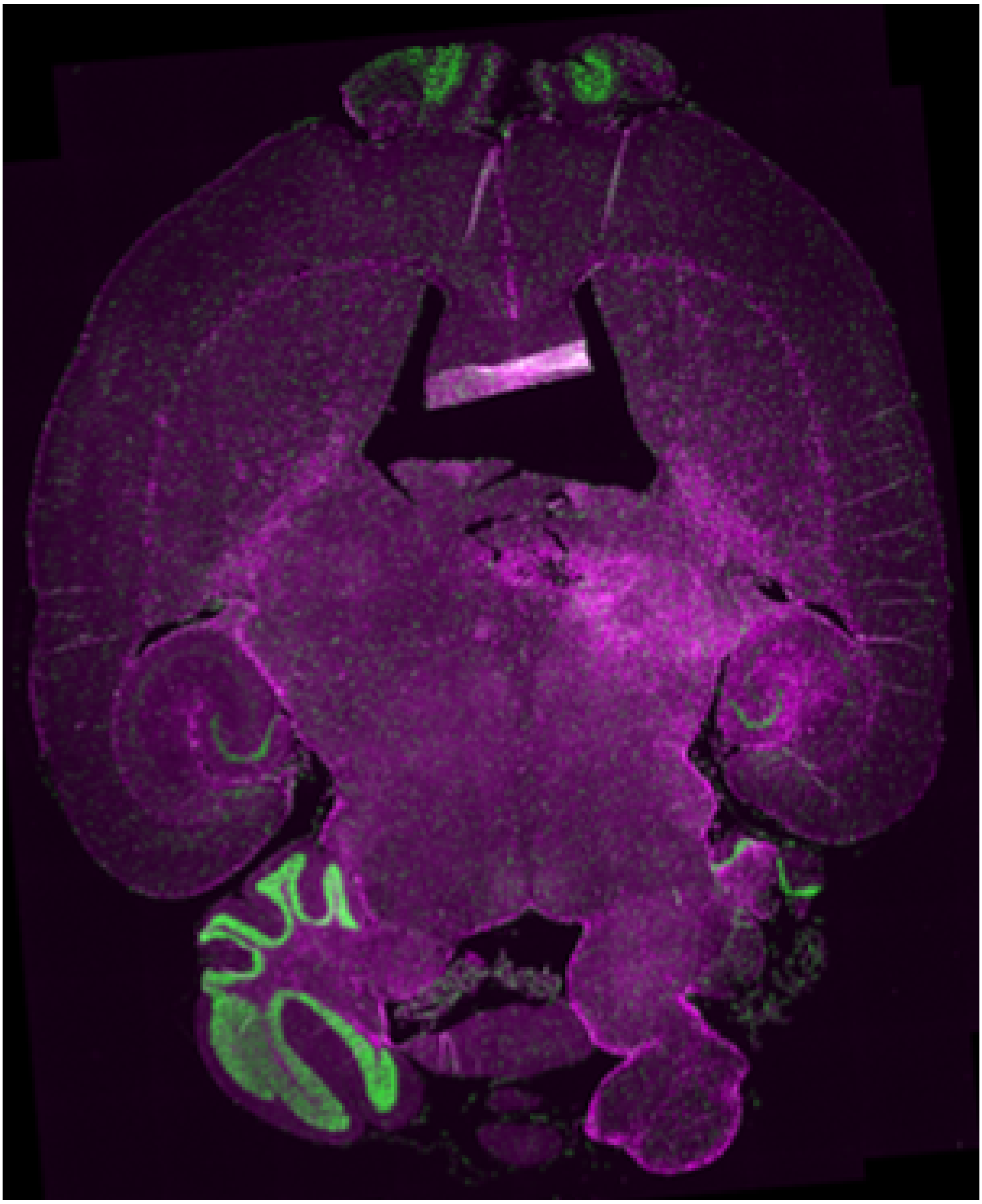

Fig. 5.5: An exemplary GFAP-stained histological slice (magenta) overlayed on the corresponding DAPI-stained slice (green) of a C3H mouse irradiated with 60 Gy.

5.5 Data reading and visualization

The work is based on multiple output data formats due to the proprietary devices used for fluorescence microscopy (*.czi data format) or imaging for treatment and health status monitoring of mice (*.dcm data format). In order to be able to process and view the images together, the file formats for all intermediate and output images of our experiment in the pipeline were standardized to the "Neuroimaging Informatics Technology Initiative" format, NIfTI (*.nii data format), which contains all necessary initial metadata such as resolution, size or exposure time.

For reading and writing (Digital Imaging and Communications in Medicine) DICOM and NIfTI files, a medical image reader/writer "napari-medical-image-formats" has been developed for the Napari software [156]. The implementation is based on Pydicom [143] and ITK [95, 96, 147, 274]. The plugin allows users to load medical image data directly into the Napari viewer for easy visualization, metadata management and analysis in a user-friendly way within the Napari ecosystem.

To read and process the CZI files effectively, a reader was adapted from the CZI file package in Python [48] to read the files or region of interest (roi) and process each tile/roi independently via multithreading. The tiles may or may not overlap each other. The meta-information is defined by a user-defined dictionary or extracted from the original CZI files themselves. Any necessary stitching of tiles/rois is also performed according to the meta-information provided by the user-defined dictionary or by the original CZI files.

Monte-Carlo beam transport simulations

6.1 Monte-Carlo simulation of dose and LET

Monte Carlo simulations were performed using TOPAS MC 3.5 software [180] to obtain the dose and LET for each point of the brain defined by the corresponding CBCT image. For this purpose, essential elements of the experimental beamline were implemented with experimental verification of the simulated beam parameters using EBT3 films [31, 67] as shown in 5.3. The simulation was conducted with a total of 10^{10} particles that were split into 100 independent runs with 10^{8} particles in each run. To achieve a fast computation time, a phase-space file was generated after the third collimator.
The adapted simulation file is described in Algorithm 1.

Algorithm 1 TOPAS MC file: Setup geometry and Phasespace

```
$s : Ge/World/Material$ = "Air"
$d : Ge/World/HLX = 1.0\,\mathrm{m}$
$d : Ge/World/HLY = 1.0\,\mathrm{m}$
$d : Ge/World/HLZ = 2.0\,\mathrm{m}$
$b : Ge/World/Invisible$ = "True"
$s : Ge/PMMA/Type$ = "TsBox"
$s : Ge/PMMA/Parent$ = "World"
$s : Ge/PMMA/Material$ = "Lucite"

**Generate PMMA transport box**
$d : Ge/PMMA/HLX = 5\,\mathrm{cm}$
$d : Ge/PMMA/HLY = 5\,\mathrm{cm}$
$d : Ge/PMMA/HLZ = 1.135\,\mathrm{mm}$
$d : Ge/PMMA/TransZ = -1.6935\,\mathrm{cm}$

**Load the Phasespace file in the Monte Carlos TOPAS World**
$s : So/Phasespace/Type$ = "PhaseSpace"
$s : So/Phasespace/PhaseSpaceFileName$ = "Phasespace_file"
$s : So/Phasespace/Component$ = "World"
$b : So/Phasespace/PhaseSpaceIncludeEmptyHistories$ = "False"

**Conversion of Hounsfield Units in materials [Schneider]**
$includeFile$ = Felicia_SPR.txt
$s : Ge/Patient/ImagingtoMaterialConverter$ = "Schneider"

**Mouse = Patient**
$s : Ge/Patient/Type$ = "TsDicomPatient"
$s : Ge/Patient/Parent$ = "World"
$s : Ge/Patient/DicomDirectory$ = "Path_to_SPR_data"
$sv : Ge/Patient/DicomModalityTags$ = 1 "CT"

**Positioning of the mouse**
$d : Ge/Patient/TransX = 0\,\mathrm{m}$
$d : Ge/Patient/TransY$ = Y_Shift_Target_in_Topas {algorithm 3}
$d : Ge/Patient/TransZ$ = Z_Shift_Target_in_Topas {algorithm 3}
$d : Ge/Patient/RotY = 270\,\mathrm{deg}$
$d : Ge/Patient/RotX = 0.0\,\mathrm{deg}$
$d : Ge/Patient/RotZ = 0\,\mathrm{deg}$
$iv : Gr/Patient/ShowSpecificSlicesZ = 1\,1$

**Scoring (see Algorithm 2)**
```

Algorithm 2 TOPAS MC file: Scoring

```
Scoring
$s : Sc/Dose/Quantity$ = "DoseToMedium"
$s : Sc/Dose/Component$ = "Patient"
$s : Sc/Dose/OutputFile$ = "Dose"
$b : Sc/Dose/OutputToConsole$ = "False"
$s : Sc/Dose/IfOutputFileAlreadyExists$ = "Overwrite"
$s : Sc/Dose/OutputType$ = "DICOM"
$b : Sc/Dose/OutputAfterRun$ = "True"

$s : Sc/LET/Quantity$ = "LET"
$s : Sc/LET/Component$ = "Patient"
$s : Sc/LET/OutputFile$ = "LET"
$s : Sc/LET/IfOutputFileAlreadyExists$ = "Overwrite"
$b : Sc/LET/OutputToConsole$ = "False"
$s : Sc/LET/OutputType$ = "DICOM"
$b : Sc/LET/OutputAfterRun$ = "True"

Number of runs
$i : Tf/NumberOfSequentialTimes = 100$
$i : Ts/NumberOfThreads = 0$
```

A Hounsfield look-up table was used to convert the CBCT numbers in each voxel to stopping power ratios (SPR), and then the MATA-approach [181] was used to synthesize material-assigned volumes based on the SPR values. Dose and dose-weighted LET[1] were calculated for each voxel of a subset of the CBCT image around a selected hippocampal target point.

The step-by-step upper LET cut-off was set to 1000 keV/µm in the simulations. In addition, to avoid too high values for the LET in air, the dose deposition of secondary electrons in regions with densities less than 0.1 g/cm^3 (1/10 of the water density) was ignored. The conversion of the target point of the CBCT to the TOPAS coordinate system as well as the positioning of the mice on a subset of the CBCT in the simulation was performed fully automatically by a Python translation script as shown in Algorithm 3. The implementation used the NumPy package [80] and the Pydicom package [143].

---

[1] In the following parts of this thesis, LET refers to dose-weighted LET.

Algorithm 3 Conversion: CBCT coordinate system to TOPAS coordinate system

```
Input: full_dicom_path_folders, CBCTVolume_Size_X_All,
    CBCTVolume_Size_Y_All, Origin_Y_All, Origin_Z_All,
    Shift_Y_All, Shift_Z_All,
    {CBCTVolume_Size_X_All, CBCTVolume_Size_Y_All, Origin_Y_All,
    Origin_Z_All, are calculated according to Algorithm 4,
    Shift_Y_All, Shift_Z_All are calculated according to Algorithm 5}
Output: X_Shift_Target_in_Topas, Y_Shift_Target_in_Topas,
    Z_Shift_Target_in_Topas
length_folder ← len(full_dicom_path_folders)
CBCTVolume_Size_Z_All ← list()
$l \leftarrow 0$
while $l <$ length_folder do
    Count_files ← len(glob.glob(full_dicom_path_folders[$l$], $"*.dcm"$))
    {glob built in python module to find all the pathnames matching a specified
    pattern}
    CBCTVolume_Size_Z_All.append(Count_files)
    $l \leftarrow l + 1$
end while
X_Shift_Target_in_Topas ← −(CBCTVolume_Size_Z_All/20
  + Origin_Z_All) + Shift_Z_All
Y_Shift_Target_in_Topas ← −(−CBCTVolume_Size_Y_All/20
  + Origin_Y_All) + Shift_Y_All)
Z_Shift_Target_in_Topas ← CBCTVolume_Size_X_All)/20
return X_Shift_Target_in_Topas, Y_Shift_Target_in_Topas,
    Z_Shift_Target_in_Topas
```

Algorithm 4 Determination of the origin system

```
Input: path_list {List of the DICOM-files for every mouse corresponding to the left
    image corner}
Output: CBCTVolume_Size_X_All, CBCTVolume_Size_Y_All,
    Origin_Y_All, Origin_Z_All
Origin_Y_All ← list()
Origin_Z_All ← list()
CBCTVolume_Size_X_All ← list()
CBCTVolume_Size_Y_All ← list()
for path in sorted(path_list) do
    dataset ← dcmread(path)
    Origin_Y ← float(dataset.ImagePositionPatient[1])
    Origin_Z ← float(dataset.ImagePositionPatient[2])
    CBCTVolume_Size_X ← dataset.Columns
    CBCT_Volume_Size_Y ← dataset.Rows
    Origin_Y_All.append(Origin_Y)
    Origin_Z_All.append(Origin_Z)
    CBCTVolume_Size_X_All.append(CBCTVolume_Size_X)
    CBCTVolume_Size_Y_All.append(CBCTVolume_Size_Y)
end for
return CBCTVolume_Size_X_All, CBCTVolume_Size_Y_All,
    Origin_Y_All, Origin_Z_All
```

Algorithm 5 Function reading the RT and RT_Struct_Class to obtain the Earpin=(0,0,0)=Isocenter in CBCT and the selected Target coordinates, as well as compute the translation vector from earpin to target

```
Input: path_list_RT {List of RT structure files}
Output: Shift_Y_All, Shift_Z_All
Shift_Y_All ← list()
Shift_Z_All ← list()
for path in sorted(path_list_RT) do
    metadata ← dcmread(path)
    DICOM_RT_Metadata ← dict()
    $i \leftarrow 0$
    while $i <$ length(metadata.ROIContourSequence) do
        Coordinates, name ← RT_Struct _Class(metadata, i){Algorithm 6}
        DICOM_RT_Metadata[name] ← Coordinates
        $i \leftarrow i + 1$
    end while
    Earpin ← DICOM_RT_Metadata.get('Earpin')
    Target ← DICOM_RT_Metadata.get('Target')
    Shift_Y ← Target.coordinates[1] − Earpin.coordinates[1]
    Shift_Z ← Target.coordinates[2] − Earpin.coordinates[2]
    Shift_Y_All.append(Shift_Y)
    Shift_Z_All.append(Shift_Z)
end for
return Shift_Y_All, Shift_Z_All
```

Algorithm 6 RT_Struct_Class holds relevant data from DICOM RT Structure file

```
Input: metadata, index
Output: coordinates, name
name = metadata.RTROIObservationsSequence[index].ROIObservationLabel
ROI_Contour_Sequence ← metadata.ROIContourSequence[index]
coordinates ← ROI_Contour_Sequence .ContourSequence[0].ContourData
    {Store coordinates}
Observation_Sequence ← metadata.RTROIObservationsSequence[index]
Observation_Number ← Observation_Sequence.ReferencedROINumber
Contour_Sequence ← metadata.ROIContourSequence[index]
Contour_Number ← Contour_Sequence.ReferencedROINumber
if Contour_Sequence ≠ Contour_Number {Check if index leads to same ROI
    when different DICOM fields are accessed} then
    coordinates ← list()
end if
return coordinates, name
```

Each voxel of the CBCT image was finally assigned a dose and a LET value. The dose was rescaled to relative units with respect to the applied maximum dose.
In addition, the amount of the secondaries like neutrons, alpha particles, and heavier particles on the LET was investigated. For this purpose, a custom scorer was written in C++ to measure their effect. The implementation of the custom step-by-step LET scorer is shown in Algorithm 7.

Algorithm 7 Step-by-step LET Scorer in TOPAS

```
Input: astep
Output: LET
fMaxScoredLET $\leftarrow$ 1000 MeV/mm/(g/cm$^3$) {1000 keV/$\mu$m in water}
density $\leftarrow$ aStep $\rightarrow$ GetPreStepPoint() $\rightarrow$ GetMaterial() $\rightarrow$ GetDensity()
fNeglectSecondariesBelowDensity $\leftarrow$ 0.1 g/cm$^3$
stepLength $\leftarrow$ aStep $\rightarrow$ GetStepLength()
if stepLength $\leq 0$ then
    return false
end if
LET $\leftarrow 0$
for particle do
    eDep $\leftarrow$ aStep $\rightarrow$ GetTotalEnergyDeposit()
    density $\leftarrow$ aStep $\rightarrow$ GetPreStepPoint() $\rightarrow$ GetMaterial() $\rightarrow$ GetDensity()
    dEdx $\leftarrow 0$
    dEdx $\leftarrow$ eDep/stepLength
    weight $\leftarrow 1.0$
    weight = weight $\cdot$ (eDep/MeV)
    if fMaxScoredLET $\leq 0$ or dEdx/density $<$ fMaxScoredLET then
        if particle = Secondary and density $>$ fNeglectSecondariesBelowDensity then
            LET $\leftarrow$ AccumulateHit(aStep, weight $\cdot$ dEdx/density)
        end if
        if particle = Primary then
            LET $\leftarrow$ AccumulateHit(aStep, weight $\cdot$ dEdx/density)
        end if
    end if
end for
return LET
```

7

Preprocessing

7.1 Preprocessing of the CBCT and X-ray images for 3D position reconstruction

Prior to 3D position reconstruction (as described in the next chapter), some essential steps are required, such as removing the mouse bed, earpins, and mouse head. This is done using a morphological binarization procedure and the CBCT image is then cropped to the relevant part. The procedure is described in Algorithm 8. The preprocessing steps were implemented by the python packages NumPy [80] and scikit-image [259].

Algorithm 8 Preprocessing of CBCT images

```
Input: CBCT (image)
Output: Preprocessed CBCT (image)
CBCT ← intensity_range_normalization(CBCT, range=(0,1))
CBCT_mask ← CBCT[$CBCT \leq 0.05$] = 0
CBCT_map ← label(CBCT_mask, connectivity=1-connected sense)
CBCT_object_areas ← regionprops.area(CBCT_map)
CBCT_map ← remove_small_holes(CBCT_map
CBCT_object_max_area ← max(CBCT_map)
CBCT_map ← remove_small_objects(CBCT_map,
    area_threshold = CBCT_object_max_area − 1)
CBCT ← CBCT[CBCT_map = 0] = 0
CBCT ← crop_non_zero_mask(CBCT, CBCT_map)
return CBCT
```

In addition, the X-ray was cropped and oriented to the CBCT image by our self-developed Napari tools **napari-nd-cropper** and **napari-elementary-numpy-operations**. The implementations are based on pyQt5 [188].

napari-nd-cropper allows users to easily define regions of interest within their multidimensional image data and interactively crop them to focus on the relevant parts. This tool allows the user to crop a region of interest of a predefined size based on a double-click, an interaction box, or the view. The graphical user interface (GUI) is displayed in Figure 7.1.

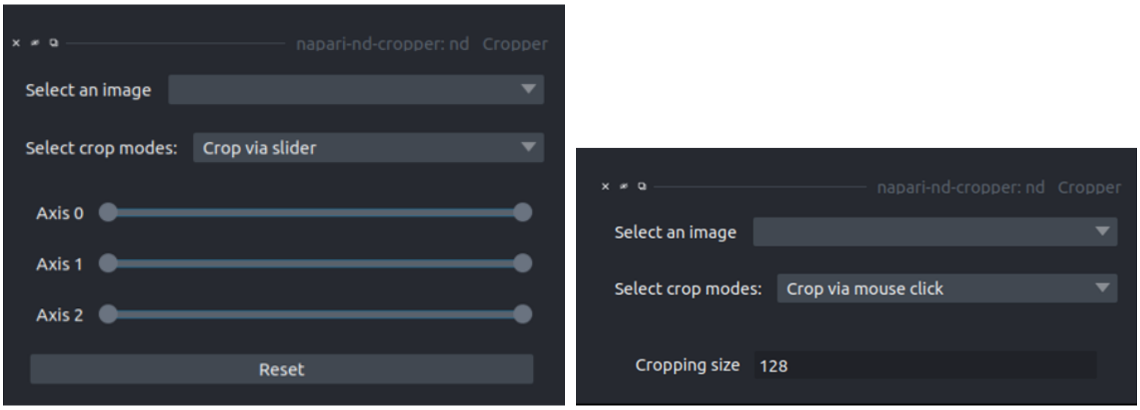

Select crop modes: Crop via slider

Select crop modes: Crop via mouse click

Cropping size 128

(a)

(b)

Fig. 7.1: The Graphical User Interface of the Napari plugin **napari-nd-cropper**. The subfigure 7.1a displays the cropping mode with sliders. The subfigure 7.1b displays the cropping mode via mouse clicks with predefined cropping size.

napari-elementary-numpy-operations simplifies and accelerates the image processing workflow within Napari ecosystem by providing essential NumPy operations such as flipping, swapping axes, or 90°-rotation directly in the Napari viewer. Users can interactively experiment with various operations and quickly assess the impact on the image data without the need for additional coding. NumPy is a popular Python library for numerical computations, and this plugin leverages its functionality to allow users to manipulate the image data in various ways and instantly visualize the outcomes. The graphical user interface is displayed in Figure 7.2.

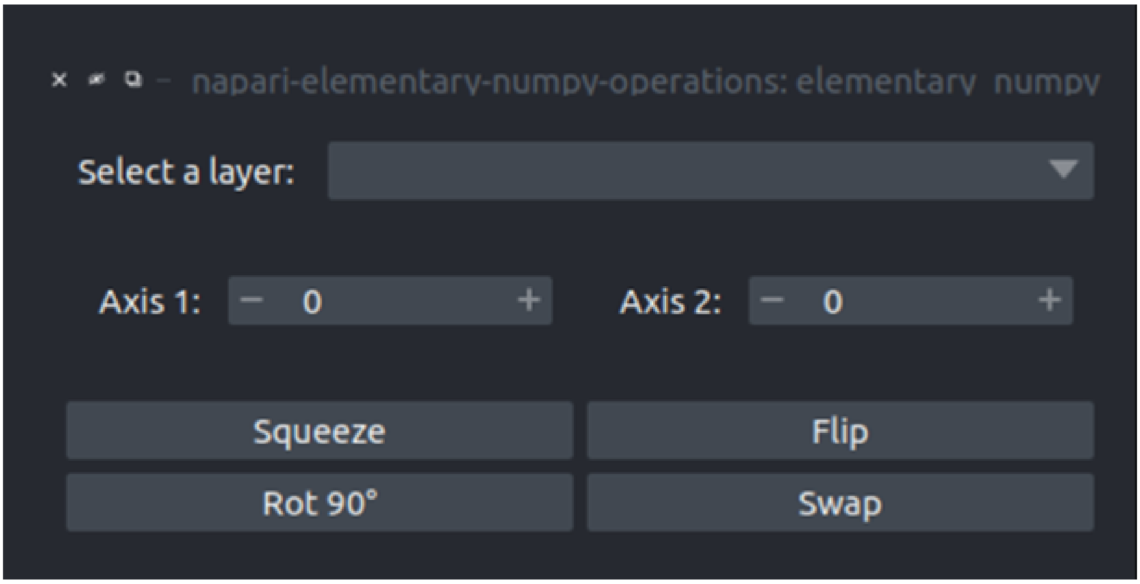

Axis 1: 0

Axis 2: 0

Fig. 7.2: The Graphical User Interface of the Napari plugin **napari-elementary-numpy-operations**.

Additonally, the intensity values of the CBCT and X-ray images were normalized to a range between 0 and 1. In a further step, the X-ray images were convolved with a 3x3 averaging kernel for denoising. The X-ray image was also adjusted to match the cumulative histogram of the CBCT image using the match_histograms implementation of scikit-image. This process is summarized in the Algorithm 9. The preprocessing steps were implemented by the python packages NumPy, SciPy [256] and scikit-image.

Algorithm 9 Preprocessing of X-ray images

```
Input: X-ray image (X-ray), CBCT image (CBCT)
Output: Preprocessed X-ray image
X-ray ← pad(X-ray, $\text{new\_shape} = (\text{CBCT.shape}(1), \text{CBCT.shape}(2))$)
X-ray ← resample(X-ray, X-ray_resolution, CBCT_resolution)
X-ray ← intensity_range_normalization(X-ray, range=(0,1))
X-ray ← convolve(X-ray, $\text{kernel} = \text{ones}((3,3))/9$, $\text{mode} = '\textit{same}'$)
Cov(X-ray, CBCT) ← covariance(X-ray, CBCT)
Offset(X-ray, CBCT) ← CBCT.mean() $-$ Cov(X-ray, CBCT) $\cdot$ X-ray.mean()
X-ray ← Cov(X-ray, CBCT) $\cdot$ X-ray $+$ Offset(X-ray, CBCT)
X-ray ← match_histogram(X-ray, mean_projection(CBCT))
return X-ray
```

7.2 Preprocessing of the histological images

After the histological data acquisition an effect called vignetting still exists in each tile in general [97]. Vignetting refers to a phenomenon in which the illumination intensity or fluorescence signal gradually decreases toward the edges of the field of view. It appears as a gradual darkening from the center to the periphery of the image. It can be caused by a variety of factors, including the optical characteristics of the microscope, lens aberrations, detector sensitivity, and uneven illumination across the microscope field of view due to factors such as uneven light source intensity, improper alignment of the illumination system, or sample properties e.g. variations in slice thickness. In our case, this results in a grid pattern of the final stitched image as shown in Figure 7.3.

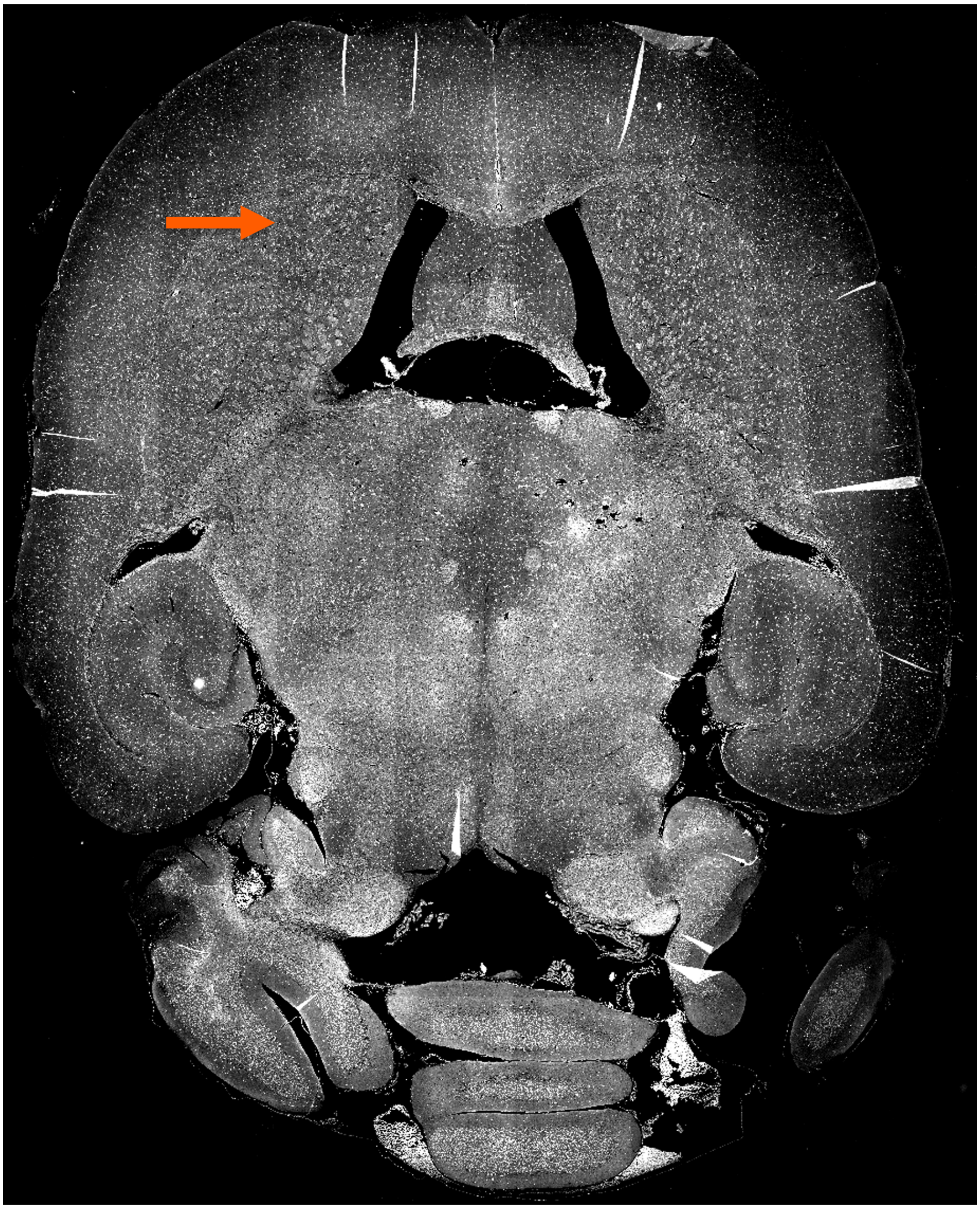

Fig. 7.3: An example of vignetting grid pattern in our fluorescence microscopy image data. The orange arrow indicates the darker areas producing the grid pattern.

Removing the effects of vignetting is essential for accurate and reliable image registration of the histological images because the grid pattern distracts the algorithms by providing additional local minima that are difficult for the optimizers to escape. Furthermore, it can affect the performance of the segmentation of astrocytes, as it will be investigated in Section 10.1.

To approximate and eliminate the vignetting effect, all tiles are averaged into one image using the following formula

$$t_{\mathrm{mean}}(x,y) = \frac{1}{N}\sum_{i=1}^{N} t_i(x,y), \tag{7.1}$$

where $t_i(x,y)$ represents the individual tiles located at (x,y) and N denotes the total number of tiles covering an entire histological image. A Gaussian blur was then applied to remove the high spatial frequency information while preserving the low spatial frequency information that makes up the vignetting profile, and used as a normalization according to

$$t_{\mathrm{corrected}}(x,y) = t_i(x,y)/\mathrm{Gfilter}(t_{\mathrm{mean}}(x,y)) \tag{7.2}$$

with the Gaussian filter function Gfilter corresponding to the 3x3 Gaussian kernel g with a standard deviation of 1, of the following form:

$$g(x,y) = \frac{1}{\sum_{x,y} e^{-\frac{x^2+y^2}{2}}} e^{-\frac{x^2+y^2}{2}} \tag{7.3}$$

The scikit-image implementation was used for the Gaussian blur.

Quantification of dose delivery accuracy in 3D

8

Our goal in this work is to study late radiation-induced effects as a function of dose and LET at the single-cell level in 3D, which requires dose delivery accuracy on the order of 0.1 mm [254] in 3D and not only in 2D, especially for protons with steep LET around the Bragg peak. Positioning uncertainties relative to the beam result in dose delivery errors. Since our research question requires accurate knowledge of the dose at any given point in the irradiated volume, but not accurate deposition of a specific dose to a specific location, residual errors of image guidance can be accounted for by calculating the a-posteriori dose.

A total of 42 C3H/He and ten C57/BL6 mice were used to evaluate our approach. The protocols and the detailed experimental procedures of our project and the previous project were described in [230, 231]. CBCT and X-ray data of mice from two projects were investigated (Landesdirektion Sachsen, DD24.1-5131/449/32; DD24.1-5131/394/50 [230, 231]). Nevertheless, the Monte Carlo beam transport simulations used for evaluation are still the same as those described in Chapter 6.

To investigate the dose delivery accuracy and the a-posteriori dose corresponding to the real dose, a multi-step process (Figure 8.1) was proposed.

In step A1, the repositioning accuracy of mice using 3D CBCT imaging are quantified. In step A2, the effects of positional uncertainties on dose delivery are determined via Monte Carlo simulations and the degrees of freedom in positioning the mouse skull are ranked according to the magnitude of dose change from a-priori dose. In step B1, a 2D-3D image matching algorithm is presented to determine the setup error of the mouse skull from a single 2D projection image with high accuracy. With this algorithm, the actual animal positions during delivery can be determined and fed into the Monte Carlo dose calculation to obtain the a-posteriori dose. Next, in step B2, the accuracy of the matching algorithm is quantified, yielding distributions of the residual uncertainties about the mouse position during irradiation. Finally, the associated dose uncertainties for the a-posteriori dose are quantified in step B3.

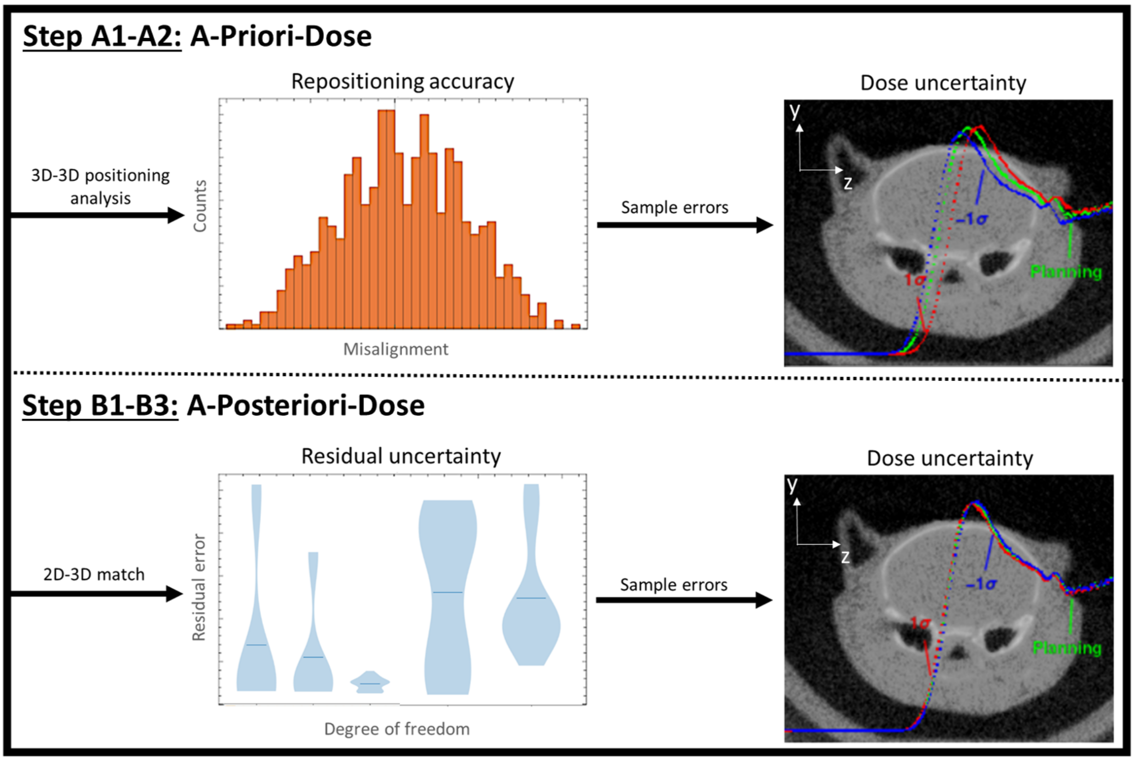

Fig. 8.1: Overview of the presented steps for a-priori dose and a-posteriori dose calculation consisting of quantification of the repositioning/residual uncertainty and the resulting dose localization uncertainty.

8.1 Step A1: Repositioning Accuracy

The statistical distribution of setup errors in all six degrees of freedom was extracted from the CBCT images acquired for all animals for dose computation. Here, it was assumed that due to the genetic similarity of inbred mouse strains, all animals of the same strain, age, and sex were anatomically similar enough to be treated as the same individual, so that the set of 52 CBCTs could be treated as different setup realizations of the same animal of the same strain. To acquire the error distributions, all possible pairs of CBCT images were registered rigidly against each other, yielding $(10 \cdot 9/2 + 42 \cdot 41/2) = 906$ registrations for ten C57/BL6 mice and 42 C3H/He mice, respectively. Statistical distributions of relative misalignments in all six degrees of freedom of a target region were extracted from the registration operations. The ten C57/BL6 mice and 42 C3H/He mice were registered separately using the self-developed optimization algorithm toolkit described in the next chapter with mutual information loss with a number of bins equal to 64 and the same optimizer settings as described in Section 9.2. However, the setup errors are analyzed together because the relative misalignments can be considered independent of the specific mouse strain. To estimate the distribution of setup errors from the distribution of relative misalignments between all pairs of mice, the following rationale was used:

It is assumed that the setup errors in all degrees of freedom are drawn from a normal distribution $N_a(\mu_a, \sigma_a^2)$ with mean μ_a and unknown variance σ_a^2. Since the absolute misalignments of two mice are independent but come from the same distribution $N_a(\mu_a, \sigma_a^2)$, it could be assumed that the distribution $N_r(\mu_r, \sigma_r^2)$ of the relative misalignments between two mice emerges from the difference of two $N_a(\mu_a, \sigma_a^2)$. Therefore, the standard deviation σ_a^2 could be estimated as

$$\sigma_a = \frac{\sigma_r}{\sqrt{2}} \tag{8.1}$$

The necessary preprocessing of the CBCT images was described in Section 7.1.

8.2 Step A2: Uncertainties of A-priori dose

For five randomly chosen planning CBCTs, dose distributions were calculated with Monte Carlo according to Chapter 6 for misalignments corresponding to the quantiles of the $1\sigma_a$ standard error for the statistical distributions of the setup uncertainties in all six degrees of freedom.

For this purpose, the CBCT image was individually translated or rotated for each experimental setup error in the positive and negative directions by the quantiles of the $1\sigma_a$ standard error for the statistical distributions of the misalignments. The dose was calculated and then transformed back to the reference coordinate system in which the a-priori dose was calculated. This results in three dose curves corresponding to $1\sigma_a$, $-1\sigma_a$ and the unbiased dose curve, respectively.

The dosimetric impact of each setup error was quantified by the shift of the distal gradient of the Bragg peak, computed at 50% of the maximum dose.

8.3 Step B1: 3D Position Reconstruction

To determine the actual irradiation position of the mouse for the computation of the a-posteriori dose, a 2D-3D image matching algorithm was developed that matches the kV-lateral X-ray image to a DRR (digitally reconstructed radiograph) generated from the CBCT by means of mean projection. The matching algorithm requires DRR at various angles, which is calculated on the fly. This not only facilitated the registration of the 2D images, but also helped determine the rotation angles of the mouse, as the projected anatomical structure best matched the X-ray image for optimal rotation angles. Thereby, the orientation of the mouse during the acquisition of DRRs could be reconstructed.

The image matching algorithm was implemented in PyTorch [173] and is GPU-capable. The Gradient Normalized Cross Correlation similarity [119] was chosen as the loss function, which was minimized using an Adam optimizer provided by PyTorch. The Gradient Normalized Cross Correlation similarity is given by

$$GNCC(I,J) = 1 - 0.5 \cdot NCC(G_x(I)(G_x(J)) - 0.5 \cdot NCC(G_y(I)(G_y(J)) \tag{8.2}$$

with the definition of the Normalized Cross Correlation $NCC(G_x(I)(G_x(J))$

$$NCC(G_x(I)(G_x(J)) = \frac{\sum_{x,y}\left(G_x(I) - \overline{G}_x(I)\right)\left(G_x(J) - \overline{G}_x(J)\right)}{\sqrt{\sum_{x,y}\left(G_x(I) - \overline{G}_x(I)\right)^2 \sum_{x,y}\left(G_x(J) - \overline{G}_x(J)\right)^2}} \tag{8.3}$$

and the normalized cross correlation $NCC(G_y(I)(G_y(J))$

$$NCC(G_y(I)(G_y(J)) = \frac{\sum_{x,y}\left(G_y(I) - \overline{G}_y(I)\right)\left(G_y(J) - \overline{G}_y(J)\right)}{\sqrt{\sum_{x,y}\left(G_y(I) - \overline{G}_y(I)\right)^2 \sum_{x,y}\left(G_y(J) - \overline{G}_y(J)\right)^2}} \tag{8.4}$$

G_x and G_y describe the Sobel-operator in the direction x and y, respectively, convolved with a provided image. The Sobel-operator G_x and G_y are given by 3x3 kernels of the following forms

$$G_x = \begin{pmatrix} 1 & 0 & -1 \\ 2 & 0 & -2 \\ 1 & 0 & -1 \end{pmatrix} \tag{8.5}$$

$$G_y = \begin{pmatrix} 1 & 2 & 1 \\ 0 & 0 & 0 \\ -1 & -2 & -1 \end{pmatrix} \tag{8.6}$$

I represents the generated DDR and J denotes the target X-ray image.

During the optimization process, the standard deviation was monitored of the Grad-NCC similarity metric to stop at a final convergence, which was set to 10^{-6}. The initial learning rate was set to 0.01 and was decreased to 0.001 if the standard deviation of the last ten iterations was below 0.001. The decay factor for the first momentum was set to 0.9. The decay factor for the infinity norm was set to 0.999. The necessary preprocessing of the X-ray images was described in Section 7.1.

8.4 Step B2: Evaluation of Position Uncertainty

To quantify the accuracy of the matching algorithm, a simulation study with 200 registrations was performed. For this purpose, pairs of CBCTs and simultaneously acquired lateral DRRs of mice are randomly generated. The CBCTs were subjected to random translation and rotation parameters according to the misalignment distributions derived in step B1. The matching algorithm was then tasked with recovering the original position of the CBCT. Deviations in all degrees of freedom μ_e were recorded in an absolute way.

8.5 Step B3: Uncertainty of A-posteriori dose

Dose distributions were calculated with Monte Carlo according to Chapter 6 corresponding to the quantiles of the 1σ standard error after 3D position reconstruction by 2D-3D image matching following the procedure described in Step A2. The uncertainties of the position of the distal dose gradient were determined accordingly.

8.6 Software Implementation

The tools described above have been implemented in the following environments:

1. Preprocessing
2. Monte Carlo simulation
3. 3D position reconstruction by 2D-3D image matching

These environments were combined into a graphical user interface called the “Treatment Planning System (TPS)”, which was built on top of the Napari framework. The implementation is based on pyQt5 provided by the magicgui package [157]. The graphical user interface is shown in Figure 8.2.

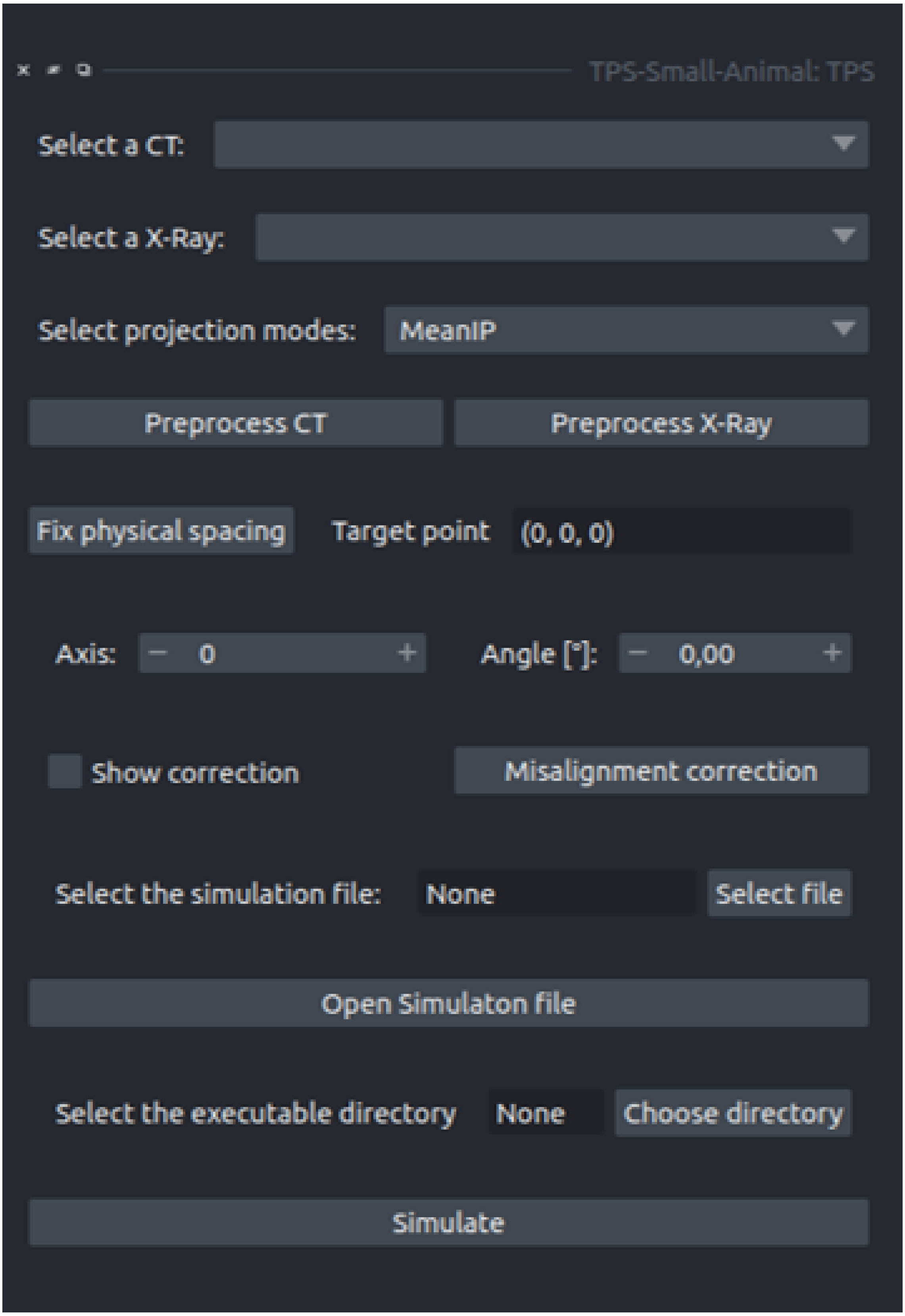

Select projection modes: MeanIP

Target point (0, 0, 0)

Axis: − 0 +

Angle [°]: − 0,00 +

Select the simulation file: None

Select the executable directory None

Fig. 8.2: The Graphical User Interface of the Napari plugin **Treatment Planning System (TPS)**.

Registration

9

9.1 B-Spline interpolation

All registrations used in this thesis are based on cubic B-spline interpolation. B-Splines are a type of piecewise polynomial function commonly used for interpolation. The degree of the B-spline determines the smoothness of the interpolation. The resulting interpolated values $p(x)$ of an image based on cubic B-splines can be expressed as [248–250]

$$p(x) = \sum_{i=1} c[i']\beta^3(x - i') \text{ for } i' \in \mathbb{Z}. \tag{9.1}$$

The cubic B-Spline bases are given by

$$\beta^3(x) = \begin{cases} \frac{1}{6}(4 - 3|x|^2 \cdot (2 - |x|)), & \text{if } |x| < 1 \\ \frac{1}{6}(2 - |x|)^3, & \text{if } 1 \leq |x| < 2 \\ 0, & \text{if } 2 \leq |x| \end{cases}. \tag{9.2}$$

This can be easily obtained by the following recursive formula

$$\beta^n(x) = (\beta^{n-1} * \beta^0)(x) \tag{9.3}$$

with β^0 defined a box function in the range [-0.5,0.5]

$$\beta^0(x) = \frac{1}{2}\left(\text{sgn}(x + \frac{1}{2}) - \text{sgn}(x - \frac{1}{2})\right). \tag{9.4}$$

The coefficients $c[i]$ describe the weights that contribute to the original samples f located on the uniform grid.

To avoid smoothing of the interpolated samples due to the fact that the samples inevitably do not cover the original sample points when using the raw version for B-spline interpolation 9.1, the concept of prefiltering [28] is used. For this purpose, 9.1 is rewritten as a discrete convolution,

$$f(i) = (c * b_3)[i] \tag{9.5}$$

with

$$b_3[i] = \beta^3(x)\Big|_{x=i}. \tag{9.6}$$

According to the convolution theorem, the convolution can be expressed as the product of its Fourier transform $C(z)$ and $B_3(z)$,

$$F(z) = (C \cdot B_3)(z) \qquad \text{with} \qquad z = e^{iw} \tag{9.7}$$

This can be converted to

$$C(z) = (F \cdot B_3^{-1})(z) \tag{9.8}$$

with

$$B_3^{-1} = \frac{\lambda}{z_p z^{-1} - 1} \frac{z_p}{1 - z_p z}. \tag{9.9}$$

The pole z_p is given by $\sqrt{3} - 2$ and the parameter λ is equal to 6.
To obtain the expression c, B_3^{-1} can be considered as a composition of two filters, a causal filter c^+ and an anti-causal filter c^- [28, 198]. The filters can be written as recursive filters according to

$$c^-[i] = z_p(c^-[i+1] - c^+[i]) \tag{9.10}$$
$$c^+[i] = \lambda f[i] + z_p c^+[i-1] \tag{9.11}$$

For the constant boundary conditions

$$c[i] = \begin{cases} 0 & \forall\, i < 0 \\ c[N-1] & \forall i \geq N \end{cases}, \tag{9.12}$$

the boundary coefficients $c^+[0]$ and $c^-[N-1]$ are given by

$$c^-[N-1] = \frac{z_p}{z_p - 1} c^+[N-1] \tag{9.13}$$
$$c^+[0] = \lambda \left(f[0] + \sum_{i}^{M-1} z_p^{i+1} f[i] \right) \tag{9.14}$$

The B-spline coefficients c are then given by

$$c[i] = c^-[i] \tag{9.15}$$

Our implementation of the prefiltering follows the implementation in [198]. Cubic B-spline prefiltering and interpolation are described in Algorithms 10 and 11.

Algorithm 10 Prefiltering for Cubic B-Spline

```
Input: $inp$: Input tensor
Output: Filtered tensor of $inp$
dim ← $inp.dim()$
for $d$ in range(dim) do
    $pole \leftarrow \sqrt{3} - 2$
    $lambda \leftarrow 6.0$
    $inp \leftarrow inp \cdot lambda$
    $inp \leftarrow$ movedim($inp, dim, 0$)
    $n \leftarrow$ shape of $inp[0]$
    $inp[0] \leftarrow$ bound.const.causal($inp, pole, dim = 0$, keepdim=False) {This function use 9.14}
    for $i \leftarrow 1$ to $n - 1$ do
        $inp[i] \leftarrow inp[i] + inp[i-1] \cdot pole$
    end for
    $inp[-1] \leftarrow$ bound.const.anticausal($inp, pole, dim = 0$, keepdim=False) {This function use 9.13}
    for $i \leftarrow n - 2$ to 0  (step -1) do
        $inp[i] \leftarrow (inp[i+1] - inp[i]) \cdot pole$
    end for
    $inp \leftarrow$ movedim($inp, 0, dim$)
end for
return $inp$
```

Algorithm 11 Cubic Image B-spline Interpolation with Deformation Field

```
Input: Input image $I$, deformation field $Df$, output image size $W \times H \times D$
Output: Interpolated image $I_{\text{interp}}$
Initialize $I_{\text{interp}}$ as an empty image of size $W \times H \times D$
$I \leftarrow$ Prefilter($I$) {Prefiltering according to Algorithm 10}
for $x = 0$ to $W - 1$ do
    for $y = 0$ to $H - 1$ do
        for $z = 0$ to $D - 1$ do
            $d_x \leftarrow Df[x, y, z, 0]$ {Deformation in x-direction}
            $d_y \leftarrow Df[x, y, z, 1]$ {Deformation in y-direction}
            $d_z \leftarrow Df[x, y, z, 2]$ {Deformation in z-direction}
            $x_{\text{orig}} \leftarrow x + d_x$ {Original x-coordinate in input image}
            $y_{\text{orig}} \leftarrow y + d_y$ {Original y-coordinate in input image}
            $z_{\text{orig}} \leftarrow z + d_z$ {Original z -coordinate in input image}
            $x_{\text{floor}} \leftarrow \lfloor x_{\text{orig}} \rfloor$ {Floor of x-coordinate}
            $y_{\text{floor}} \leftarrow \lfloor y_{\text{orig}} \rfloor$ {Floor of y-coordinate}
            $z_{\text{floor}} \leftarrow \lfloor z_{\text{orig}} \rfloor$ {Floor of z-coordinate}
            $u \leftarrow x_{\text{orig}} - x_{\text{floor}}$ {Fractional part of x-coordinate}
            $v \leftarrow y_{\text{orig}} - y_{\text{floor}}$ {Fractional part of y-coordinate}
            $w \leftarrow z_{\text{orig}} - z_{\text{floor}}$ {Fractional part of z-coordinate}
            $p_{\text{interp}} \leftarrow 0$ {Interpolated pixel value}
            for $i = 0$ to 3 {Iterate over i-nodes for x} do
                for $j = 0$ to 3{Iterate over j-nodes for y} do
                    for $k = 0$ to 3 {Iterate over k-nodes for z} do
                        $x_{\text{curr}} \leftarrow x_{\text{floor}} + i$ {Current x-coordinate}
                        $y_{\text{curr}} \leftarrow y_{\text{floor}} + j$ {Current y-coordinate}
                        $z_{\text{curr}} \leftarrow z_{\text{floor}} + k$ {Current z-coordinate}
                        if $x_{\text{curr}}$, $y_{\text{curr}}$ and $z_{\text{curr}}$ are within image bounds then
                            $weight \leftarrow$ CubicBSpline($u - i$) $\cdot$ CubicBSpline($v - j$) $\cdot$ CubicBSpline($w - k$) {Cubic B-spline bases as defined in 9.2}
                            $p_{\text{curr}} \leftarrow I[x_{\text{curr}}, y_{\text{curr}}, z_{\text{curr}}]$ {Pixel value at current coordinate}
                            $p_{\text{interp}} \leftarrow p_{\text{interp}} + weight \cdot p_{\text{curr}}$ {Weighted sum}
                        end if
                    end for
                end for
            end for
            $I_{\text{interp}}[x, y, z] \leftarrow p_{\text{interp}}$ {Set interpolated pixel value}
        end for
    end for
end for
return $I_{\text{interp}}$
```

9.2 CBCT-Atlas registration

The CBCT-Atlas registration process consists of two steps. In the first step, a mouse MRI template published by [53, 189, 191, 227, 246] was affinely registered to a mouse DAPI template, which was registered to the Allen Nissl Atlas [229, 260]. An average registration error of 0.1 mm has been reported [229]. Finally, a MRI-Nissl-DAPI atlas is obtained. Prior to this, the reference mouse DAPI template was resliced according to the horizontal histological slices and resampled to an in-plane resolution of 10 μm x 10 μm and resolution between the horizontal slices of 30 μm.

In a second step, the CBCT images were rigidly registered to the MRI-Nissl-DAPI atlas. For the registrations, an optimization algorithm toolkit based on PyTorch was developed, which allows for GPU execution as well as backpropagation gradient computation. The implementations allow optimization of each transformation parameter individually or by self-selected groups, and provide access to all relevant optimization parameters via a JavaScript Object Notation (JSON) data format [183] as shown in Figure 9.1.

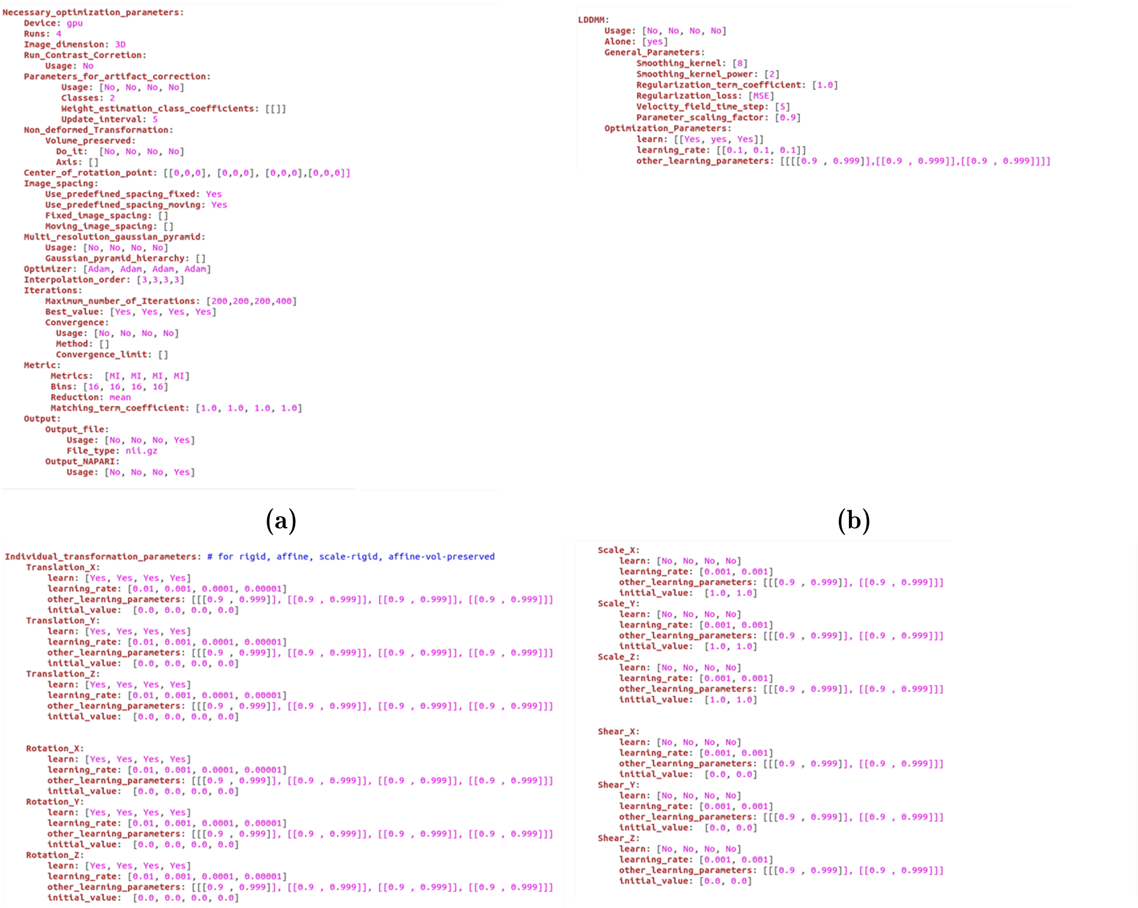

```
Necessary_optimization_parameters:
    Device: gpu
    Runs: 4
    Image_dimension: 3D
    Run_Contrast_Corretion:
        Usage: No
    Parameters_for_artifact_correction:
           Usage: [No, No, No, No]
           Classes: 2
           Weight_estimation_class_coefficients: [[]]
           Update_interval: 5
    Non_deformed_Transformation:
        Volume_preserved:
          Do_it:  [No, No, No, No]
          Axis: []
    Center_of_rotation_point: [[0,0,0], [0,0,0], [0,0,0],[0,0,0]]
    Image_spacing:
        Use_predefined_spacing_fixed: Yes
        Use_predefined_spacing_moving: Yes
        Fixed_image_spacing: []
        Moving_image_spacing: []
    Multi_resolution_gaussian_pyramid:
        Usage: [No, No, No, No]
        Gaussian_pyramid_hierarchy: []
    Optimizer: [Adam, Adam, Adam, Adam]
    Interpolation_order: [3,3,3,3]
    Iterations:
        Maximum_number_of_Iterations: [200,200,200,400]
        Best_value: [Yes, Yes, Yes, Yes]
        Convergence:
          Usage: [No, No, No, No]
          Method: []
          Convergence_limit: []
    Metric:
         Metrics:  [MI, MI, MI, MI]
         Bins: [16, 16, 16, 16]
         Reduction: mean
         Matching_term_coefficient: [1.0, 1.0, 1.0, 1.0]
    Output:
        Output_file:
            Usage: [No, No, No, Yes]
            File_type: nii.gz
        Output_NAPARI:
            Usage: [No, No, No, Yes]
```

(a)

```
LDDMM:
     Usage: [No, No, No, No]
     Alone: [yes]
     General_Parameters:
           Smoothing_kernel: [8]
           Smoothing_kernel_power: [2]
           Regularization_term_coefficient: [1.0]
           Regularization_loss: [MSE]
           Velocity_field_time_step: [5]
           Parameter_scaling_factor: [0.9]
     Optimization_Parameters:
           learn: [[Yes, yes, Yes]]
           learning_rate: [[0.1, 0.1, 0.1]]
           other_learning_parameters: [[[[0.9 , 0.999]],[[0.9 , 0.999]],[[0.9 , 0.999]]]]
```

(b)

```
Individual_transformation_parameters: # for rigid, affine, scale-rigid, affine-vol-preserved
    Translation_X:
        learn: [Yes, Yes, Yes, Yes]
        learning_rate: [0.01, 0.001, 0.0001, 0.00001]
        other_learning_parameters: [[[0.9 , 0.999]], [[0.9 , 0.999]], [[0.9 , 0.999]], [[0.9 , 0.999]]]
        initial_value:  [0.0, 0.0, 0.0, 0.0]
    Translation_Y:
        learn: [Yes, Yes, Yes, Yes]
        learning_rate: [0.01, 0.001, 0.0001, 0.00001]
        other_learning_parameters: [[[0.9 , 0.999]], [[0.9 , 0.999]], [[0.9 , 0.999]], [[0.9 , 0.999]]]
        initial_value:  [0.0, 0.0, 0.0, 0.0]
    Translation_Z:
        learn: [Yes, Yes, Yes, Yes]
        learning_rate: [0.01, 0.001, 0.0001, 0.00001]
        other_learning_parameters: [[[0.9 , 0.999]], [[0.9 , 0.999]], [[0.9 , 0.999]], [[0.9 , 0.999]]]
        initial_value:  [0.0, 0.0, 0.0, 0.0]


    Rotation_X:
        learn: [Yes, Yes, Yes, Yes]
        learning_rate: [0.01, 0.001, 0.0001, 0.00001]
        other_learning_parameters: [[[0.9 , 0.999]], [[0.9 , 0.999]], [[0.9 , 0.999]], [[0.9 , 0.999]]]
        initial_value:  [0.0, 0.0, 0.0, 0.0]
    Rotation_Y:
        learn: [Yes, Yes, Yes, Yes]
        learning_rate: [0.01, 0.001, 0.0001, 0.00001]
        other_learning_parameters: [[[0.9 , 0.999]], [[0.9 , 0.999]], [[0.9 , 0.999]], [[0.9 , 0.999]]]
        initial_value:  [0.0, 0.0, 0.0, 0.0]
    Rotation_Z:
        learn: [Yes, Yes, Yes, Yes]
        learning_rate: [0.01, 0.001, 0.0001, 0.00001]
        other_learning_parameters: [[[0.9 , 0.999]], [[0.9 , 0.999]], [[0.9 , 0.999]], [[0.9 , 0.999]]]
        initial_value:  [0.0, 0.0, 0.0, 0.0]
```

```
    Scale_X:
        learn: [No, No, No, No]
        learning_rate: [0.001, 0.001]
        other_learning_parameters: [[[0.9 , 0.999]], [[0.9 , 0.999]]]
        initial_value:  [1.0, 1.0]
    Scale_Y:
        learn: [No, No, No, No]
        learning_rate: [0.001, 0.001]
        other_learning_parameters: [[[0.9 , 0.999]], [[0.9 , 0.999]]]
        initial_value:  [1.0, 1.0]
    Scale_Z:
        learn: [No, No, No, No]
        learning_rate: [0.001, 0.001]
        other_learning_parameters: [[[0.9 , 0.999]], [[0.9 , 0.999]]]
        initial_value:  [1.0, 1.0]


    Shear_X:
        learn: [No, No, No, No]
        learning_rate: [0.001, 0.001]
        other_learning_parameters: [[[0.9 , 0.999]], [[0.9 , 0.999]]]
        initial_value:  [0.0, 0.0]
    Shear_Y:
        learn: [No, No, No, No]
        learning_rate: [0.001, 0.001]
        other_learning_parameters: [[[0.9 , 0.999]], [[0.9 , 0.999]]]
        initial_value:  [0.0, 0.0]
    Shear_Z:
        learn: [No, No, No, No]
        learning_rate: [0.001, 0.001]
        other_learning_parameters: [[[0.9 , 0.999]], [[0.9 , 0.999]]]
        initial_value: [0.0, 0.0]
```

(c)

(d)

Fig. 9.1: An exemplary JSON Data format input file for the CBCT-Atlas registration. The subfigure 9.1a displays the general settings. The subfigure 9.1b displays the specific settings for a deformable registration. The subfigure 9.1c displays the specific settings for a rigid registration. The subfigure 9.1d displays the additional settings for an affine registration.

All resampling and interpolation steps are performed according to Section 9.1. For the loss function, the mutual information loss [110] was chosen, defined as follows

$$L_{\mathrm{MI}}(I_{\mathrm{target}}, I_{\mathrm{moving}}) = -\sum_{i=1}^{N_{\mathrm{bins}}} \sum_{j=1}^{N_{\mathrm{bins}}} p(i,j) \log \left(\frac{p(i,j)}{p(i) \cdot p(j)} \right) \tag{9.16}$$

I_{target} and I_{moving} denote the target and moving images, respectively. N_{bins} describes the number of bins used for histogram-based calculations. In our case, N_{bins} was set to 16 for the registration of the CBCT image to the DAPI template and 64 for the registration of the MRI template to the DAPI template. $p_{\text{target}}(i, j)$ is the joint histogram probability corresponding to the intensity values i and j in the target and the moving image. $p(i)$ and $p(j)$ represent the marginal histogram probabilities corresponding to the intensity values i and j in the fixed and moving images, respectively. The mutual information loss function quantifies the statistical dependence between the intensity values of corresponding fixed and moving images. The negative sign in the formula indicates that minimizing this loss function is equivalent to maximizing mutual information during the registration process. Note that no prior information about the intensity values of the images is required. The Adam algorithm provided by PyTorch was used for optimization. The initial learning rate was set to 0.01 and was decreased step by step by a factor of 0.1 every 200 iterations until it reached 10^{-5}. The maximum number of iterations was set to 1000. The decay factor for the first momentum was set to 0.9. The decay factor for the infinity norm was set to 0.999.

The evaluation was performed by placing landmarks in the CBCT and MRI template as shown in Figure 9.2. Four landmarks were placed to the brains per slice in total.

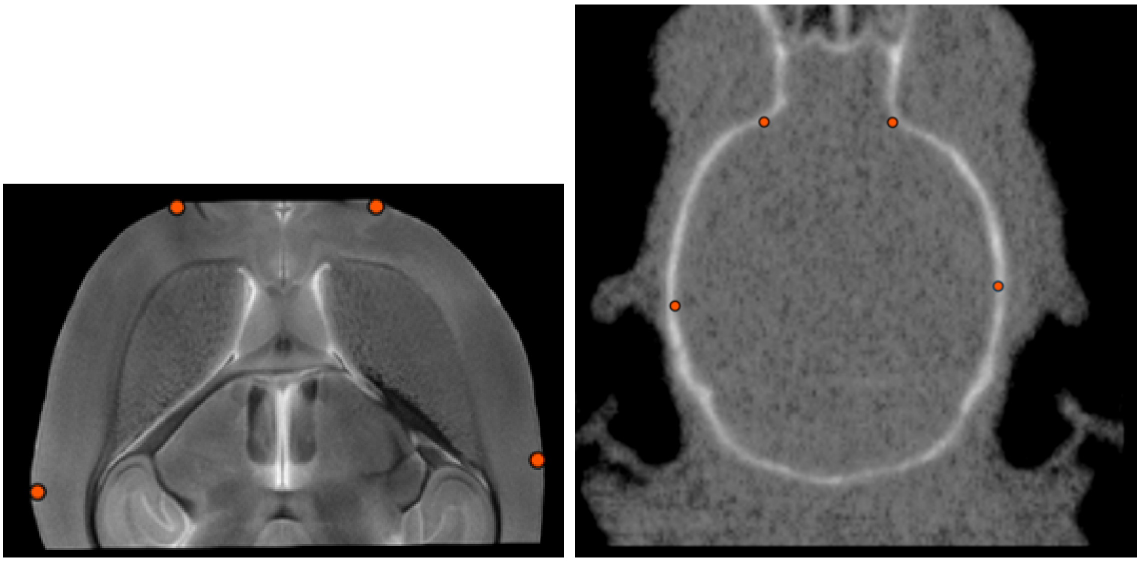

(a)

(b)

Fig. 9.2: An exemplary 2D view of the MRI template (subfigure 9.2a) and a CBCT image (subfigure 9.2b) with the set of seeded landmarks denoted by orange points.

Figure 9.3 shows the landmarks placed to evaluate the registration of the MRI template and the DAPI-Nissl combined template for a slice.

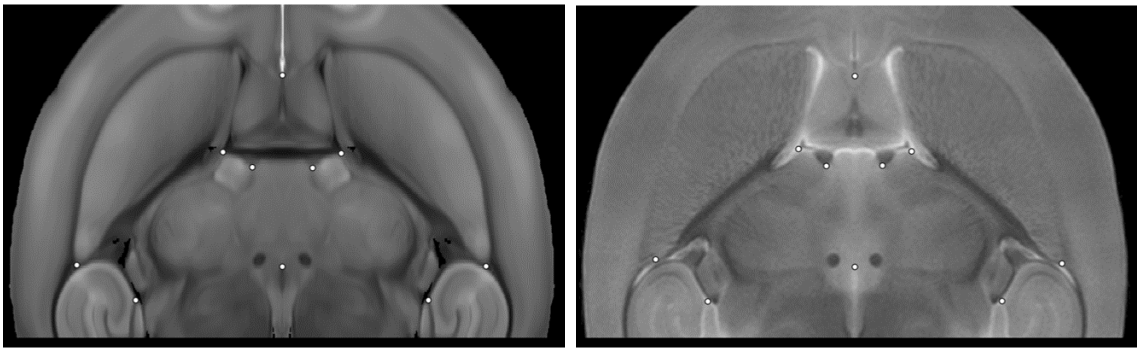

(a) **(b)**

Fig. 9.3: An exemplary 2D view of the DAPI-Nissl combined template (subfigure 9.3a) and the MRI template (subfigure 9.3b) with the set of seeded landmarks denoted by white points.

The residual registration error was then measured by the average of the Euclidean distance between corresponding landmarks of the target and the moving image as follows

$$d_{\mathrm{MRRE}} = \frac{1}{S \cdot N} \sum_{s=1}^{S} \sum_{s=1}^{S} ||L_{\mathrm{s,\ i,\ target}} - L_{\mathrm{s,\ i,\ registered}}||, \tag{9.17}$$

where N corresponds to the number of landmarks per slice, which was set to 4 for the registration of CBCT image to the DAPI template and 10 for the MRI template registration to the Nissl-DAPI combined template. S denotes the maximal number of considered slices, which was 30 in our case. $L_{\mathrm{s,\ i,\ target}}$ and $L_{\mathrm{s,\ i,\ registered}}$ represent the position of the ith landmark in the slice s of the target image and the registered (transformed) image, respectively. $||...||$ denotes the euclidean norm.

9.3 Histology-Atlas registration

Registering the histology to the MRI-Nissl-DAPI template is a complicated 3D-2D registration problem due to the many local minima where you can get stuck. For registration, the DAPI counterstain to the GFAP stain was used, which is in the same coordinate system, and the DAPI template from the MRI-Nissl-DAPI template generated in the previous section. As a result, a multi-step approach was established to address this The additional experimental information about the location of the slices in the mouse brain with an accuracy of about 300μm was used. The registration approach consists of a composition of the following transformations

$$T = T_{\text{3D-2D}} \circ T_{\text{Slice-Cutting-Angle}} \circ T_{\text{In-plane}} \circ T_{\text{In-plane-Translation}}. \tag{9.18}$$

The evaluation was conducted by setting landmarks in the histological slices and the MRI-Nissl-DAPI template as exemplarily displayed in Figure 9.4.

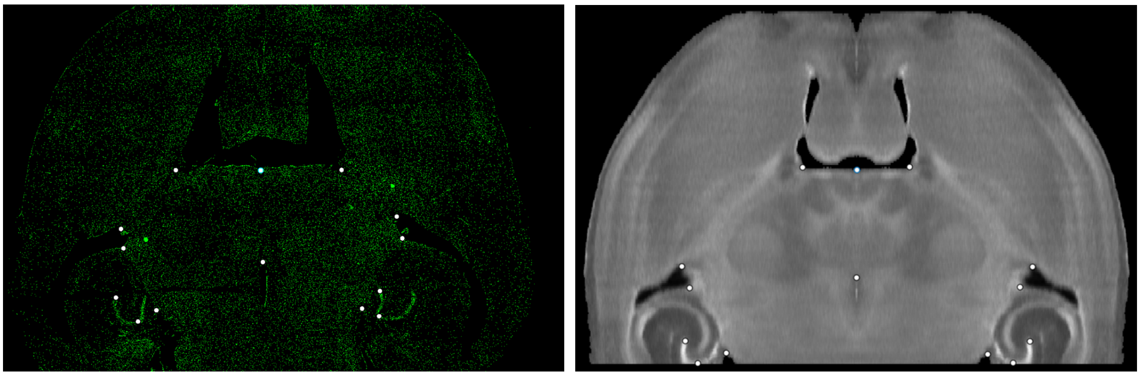

(a) (b)

Fig. 9.4: An exemplary 2D view of a DAPI-stained slice (subfigure 9.4a) and the MRI-Nissl-DAPI template (subfigure 9.4b) with the set of seeded landmarks denoted by white points.

Fourteen landmarks were placed on each slice s. The registration error is then determined again according to Equation 9.17 in the previous section. As a first step for the registration, each histological slice was downsampled to the in-plane resolution of 10 μm x 10 μm of the MRI-Nissl-DAPI template according to Section 9.2. In addition, the following steps were applied to the histological images after vignetting removal (see Section 7.2) as described in Algorithm 12 to adjust the histological images so that their cumulative histogram matches that of the DAPI template. The preprocessing steps were again implemented using the Python packages NumPy , SciPy and scikit-image.

Algorithm 12 Adjust cumulative histological histogram to match that of the DAPI-Template

```
Input: histological image, DAPI-Template
Output: Matched histological image
histology ← pad(histology,
   new_shape = (DAPI-Template.shape(1), DAPI-Template.shape(2)))
histology ← intensity_range_normalization(histology, range=(0,1))
Cov(histology, DAPI-Template) ← covariance(histology, DAPI-Template)
Offset(histology, DAPI-Template) ← DAPI-Template.mean()
   − Cov(histology, DAPI-Template) · histology.mean()
histology ← Cov(histology, DAPI-Template) · histology
   + Offset(histology, DAPI-Template)
histology ← match_histogram(histology, silce_of(DAPI-Template))
return histology
```

9.3.1 $T_{\text{In-plane-Translation}}$-Transformation

First, an in-plane transformation $T_{\text{In-plane-Translation}}$ is performed to roughly align the histological images and the DAPI template. This transformation is based on the calculation of the centroids c of the histological slices and the DAPI template, determined by their raw moments as follows

$$\vec{c}_{\text{Template}} = \begin{pmatrix} M_{100}/M_{000} \\ M_{010}/M_{000} \\ M_{001}/M_{000} \end{pmatrix} \quad \textit{and} \quad \vec{c}_{\text{Histology}} = \begin{pmatrix} M_{10}/M_{00} \\ M_{01}/M_{00} \end{pmatrix} \tag{9.19}$$

with

$$M_{ijk,\text{Template}} = \sum_i \sum_j \sum_k x_i y_j z_k f(x,y,z) \quad \textit{and} \quad M_{ij,\text{Histology}} = \sum_i \sum_j x_i y_j f(x,y), \tag{9.20}$$

where $f(x,y,z)$ and $f(x,y)$ correspond to intensity values of the images at the position (x,y,z) and (x,y), respectively. Note that due to the experimental cutting process, a rough approximation of the slice position is known. The accuracy is given by 300 μm. Thus, the resulting in-plane transformation $T_{\text{In-plane-Translation}}$ based on the shift of the centroids of the plane of the MRI-Nissl-DAPI template and the histological slice is given by

$$T_{\text{In-plane-Translation}} = \left[\begin{array}{ccc:c} 1 & 0 & 0 & -c_{1,\text{shift}} \\ 0 & 1 & 0 & -c_{2,\text{shift}} \\ 0 & 0 & 1 & 0 \\ 0 & 0 & 0 & 1 \end{array}\right] \tag{9.21}$$

with

$$c_{1,\text{shift}} = c_{1,\text{Template}} - c_{1,\text{Histology}} \tag{9.22}$$

$$c_{2,\text{shift}} = c_{2,\text{Template}} - c_{2,\text{Histology}}. \tag{9.23}$$

9.3.2 $T_{\text{In-plane}}$-Transformation

The transformation $T_{\text{In-plane}}$ corresponds to a 2D in-plane registration. The histological slices are now affinely registered to the slices of the DAPI template, which was sectioned according to the experimentally known location. The registration was again conducted by our developed registration toolkit. The searched transformation $T_{\text{In-plane}}$ can be decomposed by the RQ-decomposition theorem (decomposition of a real matrix into an orthogonal matrix R and an upper triangular matrix S) as follows

$$T_{\text{In-plane}} = S_{\text{In-plane}} \cdot R_{\text{In-plane}} + t_{\text{Translation}} \tag{9.24}$$

with

$$S_{\text{In-plane}} = \left[\begin{array}{ccc:c} s_{1,plane} & g_{plane} & 0 & 0 \\ 0 & s_{2,plane} & 0 & 0 \\ 0 & 0 & 1 & 0 \\ 0 & 0 & 0 & 1 \end{array}\right] \tag{9.25}$$

$$R_{\text{In-plane}} = \left[\begin{array}{ccc:c} \cos(\phi_{plane}) & -\sin(\phi_{plane}) & 0 & 0 \\ \sin(\phi_{plane}) & \cos(\phi_{plane}) & 0 & 0 \\ 0 & 0 & 1 & 0 \\ 0 & 0 & 0 & 1 \end{array}\right] \tag{9.26}$$

$$t_{\text{Translation}} = \left[\begin{array}{ccc:c} 1 & 0 & 0 & t_{1,plane} \\ 0 & 1 & 0 & t_{2,plane} \\ 0 & 0 & 1 & 0 \\ 0 & 0 & 0 & 1 \end{array}\right] \tag{9.27}$$

The decomposition is unique if the diagonal entries of the upper triangular matrix are positive, because assume there are two decompositions with $t_{\text{Translation}} = 0$.

$$T = S_1 \cdot R_1 = S_2 \cdot R_2 \tag{9.28}$$

Then it holds for $T^T \cdot T$

$$TT^T = S_1 R_1 R_1^T S_1^T = S_1 S_1^T = S_2 R_2 R_2^T S_2^T = S_2 S_2^T \iff \left(S_2^{-1} S_1\right)^T = S_1^{-1} S_2 \tag{9.29}$$

Note that the upper T denotes the transpose of the matrix. The left side of 9.29 corresponds to a lower triangular matrix and the right side corresponds to an upper triangular matrix, since the inverse of an upper triangular matrix is still an upper triangular matrix. To satisfy the equation 9.29 both sides must be diagonal and the diagonal entries must be equal and greater than 0. Hence, $S_1 = S_2$ and consequently $R_1 = R_2$. In other words, the decomposition is unique if the transformation matrix T is invertible and the diagonal entries of S are greater than 0, which is ensured in our case.

Therefore, this registration has six optimization parameters:
$(\phi_{plane}, s_{1,plane}, s_{1,plane}, g_{plane}, t_{1,plane}, t_{2,plane})$.

The parameter ϕ_{plane} corresponds to the in-plane rotation and three parameters $s_{1,plane}, s_{1,plane}, g_{plane}$ correspond to the shearing and scaling. The parameters $t_{1,plane}$, $t_{2,plane}$ denote the in-plane translation parameters. All of the parameters were optimized as a group.

For the loss function, the mutual information defined in 9.16 was chosen, again. N_{bins} was set to 32. Again, the Adam optimizer was used with an initial learning rate setting of 0.01 and a decay step-by-step by a factor of 0.1 every 200 iterations up to 10^{-5}. The maximum iteration was 1000. The decay factor for the first momentum was set to 0.9. The decay factor for the infinity norm was set to 0.999.

9.3.3 $T_{\text{Slice-Cutting-Angle}}$-Transformation

The third transformation $T_{\text{Slice-Cutting-Angle}}$ has the goal to localize the slice position in the DAPI template with a higher accuracy than 300μm and determine the two cutting angles α and β. Finally, the DAPI template should be registered to each histological slice according to the cutting angles and the correct slice location. Therefore, the transformation $T_{\text{Slice-Cutting-Angle}}$ is given by a composition of two rotations describing the cutting angles α and β evaluated at a variable slice localization z_{Slice} around the known experimental slice location in the DAPI template as follows

$$T_{\text{Slice-Cutting-Angle}} = (R_\alpha \cdot R_\beta)\Big|_{z=z_{Slice}} \tag{9.30}$$

with

$$R_\alpha = \left[\begin{array}{ccc:c} \cos(\alpha) & 0 & \sin(\alpha) & 0 \\ 0 & 1 & 0 & 0 \\ -\sin(\alpha) & 0 & \cos(\alpha) & 0 \\ 0 & 0 & 0 & 1 \end{array}\right] \tag{9.31}$$

$$R_\beta = \left[\begin{array}{ccc:c} 1 & 0 & 0 & 0 \\ 0 & \cos(\beta) & -\sin(\beta) & 0 \\ 0 & \sin(\beta) & \cos(\beta) & 0 \\ 0 & 0 & 0 & 1 \end{array}\right] \tag{9.32}$$

In total, there are three three optimization parameters for this registration at the end:
$(\alpha, \beta, z_{Slice})$.

The optimization was performed via manual registration using our developed tool **Partial-Aligner** for the open-source visualization software Napari that enables manual affine registration of 2D, and 3D multimodal images via Comboboxes and Sliders for each affine transformation parameter. In addition, the **Partial-Aligner** allows users to select and align regions of interest between two or more images. So it can also be used to restore image artifacts. The implementation was done by means of pyQt5 provided by the magicgui package. All in all, the plugin provides an intuitive graphical user interface that allows users to interactively align images and rois. The graphical user interface is displayed in Figure 9.5.

Image
Label None
Rotation angle x 0,00
Rotation angle y 0,00
Rotation angle z 0,00
Translation x 0,00
Translation y 0,00
Translation z 0,00
Scale x 1,00
Scale y 1,00
Scale z 1,00
Shear x 0,00
Shear y 0,00
Shear z 0,00
☐ Absolute values

(a)

Image
Label None
Rotation angle x 0,00
Rotation angle y 0,00
Rotation angle z 0,00
Translation x 0,000
Translation y 0,000
Translation z 0,00
Scale x 1,00
Scale y 1,00
Scale z 1,00
Shear x 0,00
Shear y 0,00
Shear z 0,00
☑ Absolute values

(b)

Image
Label None
Rotation angle z 0,00
Translation x 0,00
Translation y 0,00
Scale x 1,00
Scale y 1,00
Shear x 0,00
☐ Absolute values

(c)

Image
Label None
Rotation angle z 0,00
Translation x 0,000
Translation y 0,000
Scale x 1,00
Scale y 1,00
Shear x 0,00
☑ Absolute values

(d)

Fig. 9.5: The Graphical User Interface of the Napari plugin **Partial-Aligner**. The subfigure 9.5a displays the interface for 3D images with the slider option. The subfigure 9.5b displays the interface for 3D images with the combo box option. The subfigure 9.5c displays the interface for 2D images with the slider option. The subfigure 9.5d displays the interface for 2D images with the combo box option.

Furthermore, an interaction box was coupled to the individual affine transformation parameters of the **Partial-Aligner**, to control these via mouse interaction, as shown in Figure 9.6.

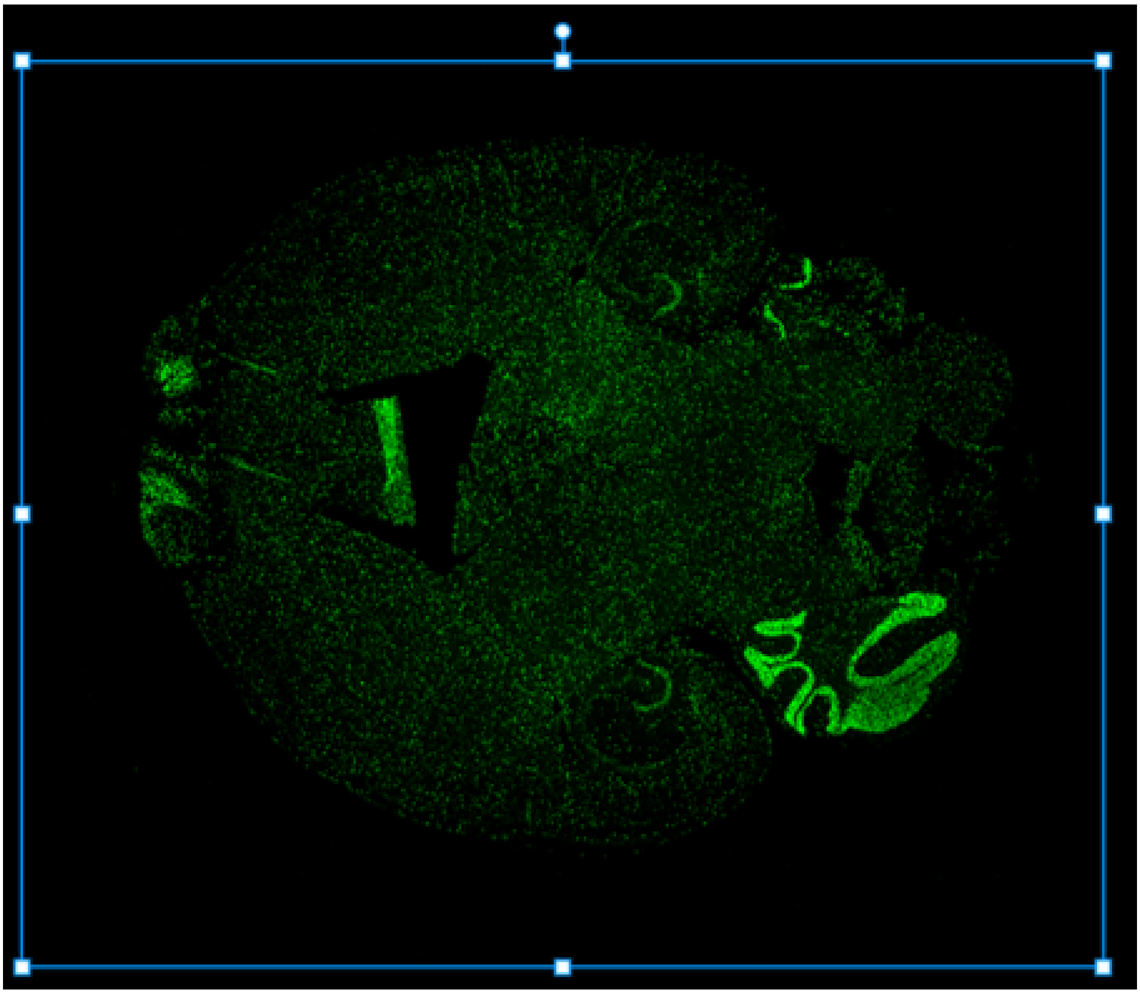

Fig. 9.6: The established interaction box to Napari (blue), which is controlled by the mouse. The image in green corresponds to a DAPI-stainend histological slice.

9.3.4 $T_{\text{3D-2D}}$-Transformation

The last searched transformation $T_{\text{3D-2D}}$ corresponds to a 3D-2D affine registration. Now, all parameters of an affine transformation were optimized jointly. The transformation $T_{\text{3D-2D}}$ of the DAPI template is again defined by the QR decomposition as follows

$$T_{\text{3D-2D}} = S_{\text{3D-2D}} \cdot R_{\phi_1} \cdot R_{\phi_2} \cdot R_{\phi_3} + t_{\text{3D-2D}}\Big|_{z=z_{Slice}} \tag{9.33}$$

with

$$S_{\text{3D-2D}} = \left[\begin{array}{ccc:c} s_1 & g_1 & g_3 & 0 \\ 0 & s_2 & g_2 & 0 \\ 0 & 0 & s_3 & 0 \\ 0 & 0 & 0 & 1 \end{array}\right] \tag{9.34}$$

$$R_{\phi_1} = \left[\begin{array}{ccc:c} \cos(\phi_1) & -\sin(\phi_1) & 0 & 0 \\ \sin(\phi_1) & \cos(\phi_1) & 0 & 0 \\ 0 & 0 & 1 & 0 \\ 0 & 0 & 0 & 1 \end{array}\right] \tag{9.35}$$

$$R_{\phi_2} = \left[\begin{array}{ccc:c} \cos(\phi_2) & 0 & \sin(\phi_2) & 0 \\ 0 & 1 & 0 & 0 \\ -\sin(\phi_2) & 0 & \cos(\phi_2) & 0 \\ 0 & 0 & 0 & 1 \end{array}\right] \tag{9.36}$$

$$R_{\phi_3} = \left[\begin{array}{ccc:c} 1 & 0 & 0 & 0 \\ 0 & \cos(\phi_3) & -\sin(\phi_3) & 0 \\ 0 & \sin\phi_3) & \cos(\phi_3) & 0 \\ 0 & 0 & 0 & 1 \end{array}\right] \tag{9.37}$$

$$t_{\text{3D-2D}} = \left[\begin{array}{ccc:c} 1 & 0 & 0 & t_1 \\ 0 & 1 & 0 & t_2 \\ 0 & 0 & 1 & t_3 \\ 0 & 0 & 0 & 1 \end{array}\right] \tag{9.38}$$

evaluated at z_{Slice}. In total, there are 12 transformation parameters to optimize: $(s_1, s_2, s_3, g_1, g_2, g_3, \phi_1, \phi_2, \phi_3, t_1, t_2, t_3)$
The optimization was conducted by using our developed Napari plugin **napari-3D-Slicer**. This interface provides access to a JSON data format where all relevant optimization parameters such as learning rate, slice location, loss function, etc. can be adjusted in the same way as described in Section 9.2 and displayed in Figure 9.1. An exemplary JSON Data format input file is shown in Figure 9.7.

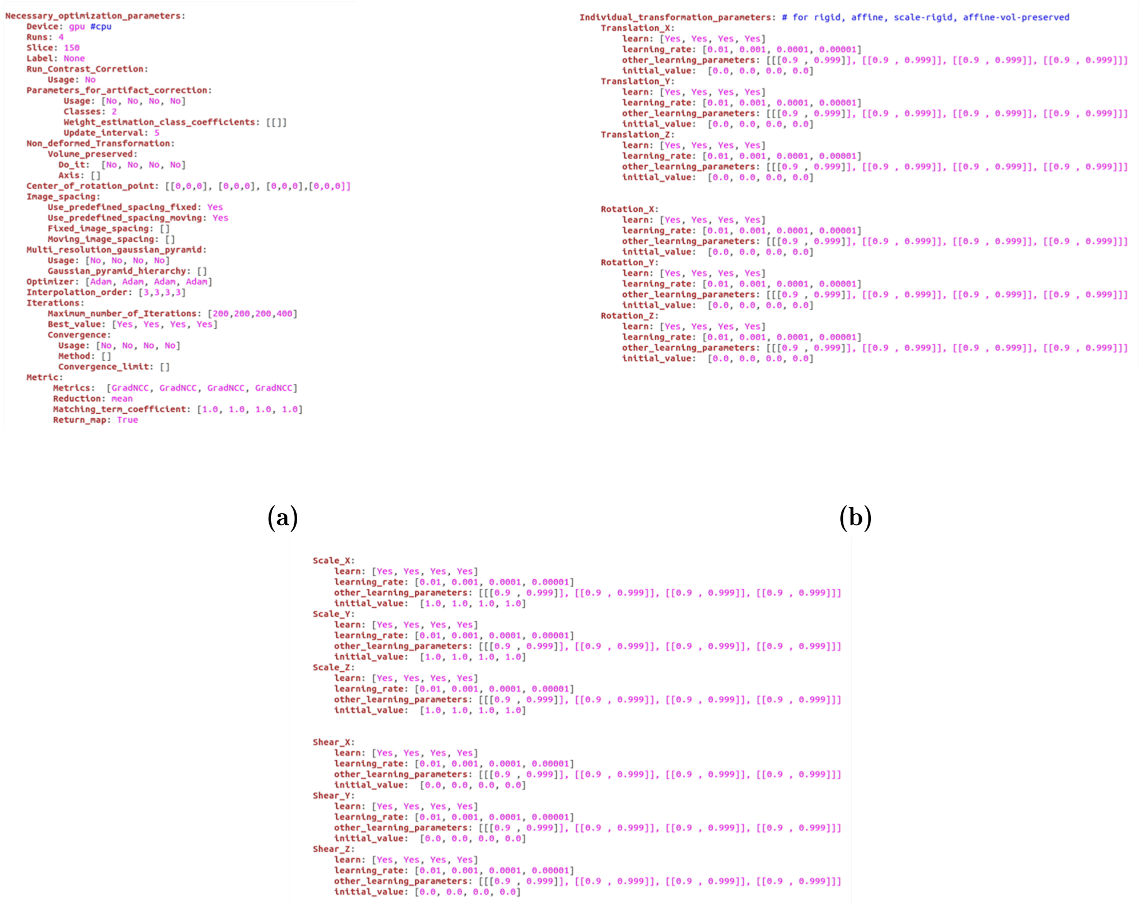

```
Necessary_optimization_parameters:
    Device: gpu #cpu
    Runs: 4
    Slice: 150
    Label: None
    Run_Contrast_Corretion:
        Usage: No
    Parameters_for_artifact_correction:
           Usage: [No, No, No, No]
           Classes: 2
           Weight_estimation_class_coefficients: [[]]
           Update_interval: 5
    Non_deformed_Transformation:
        Volume_preserved:
          Do_it:  [No, No, No, No]
          Axis: []
    Center_of_rotation_point: [[0,0,0], [0,0,0], [0,0,0],[0,0,0]]
    Image_spacing:
        Use_predefined_spacing_fixed: Yes
        Use_predefined_spacing_moving: Yes
        Fixed_image_spacing: []
        Moving_image_spacing: []
    Multi_resolution_gaussian_pyramid:
        Usage: [No, No, No, No]
        Gaussian_pyramid_hierarchy: []
    Optimizer: [Adam, Adam, Adam, Adam]
    Interpolation_order: [3,3,3,3]
    Iterations:
        Maximum_number_of_Iterations: [200,200,200,400]
        Best_value: [Yes, Yes, Yes, Yes]
        Convergence:
          Usage: [No, No, No, No]
          Method: []
          Convergence_limit: []
    Metric:
         Metrics:  [GradNCC, GradNCC, GradNCC, GradNCC]
         Reduction: mean
         Matching_term_coefficient: [1.0, 1.0, 1.0, 1.0]
         Return_map: True
```

(a)

```
Individual_transformation_parameters: # for rigid, affine, scale-rigid, affine-vol-preserved
    Translation_X:
        learn: [Yes, Yes, Yes, Yes]
        learning_rate: [0.01, 0.001, 0.0001, 0.00001]
        other_learning_parameters: [[[0.9 , 0.999]], [[0.9 , 0.999]], [[0.9 , 0.999]], [[0.9 , 0.999]]]
        initial_value:  [0.0, 0.0, 0.0, 0.0]
    Translation_Y:
        learn: [Yes, Yes, Yes, Yes]
        learning_rate: [0.01, 0.001, 0.0001, 0.00001]
        other_learning_parameters: [[[0.9 , 0.999]], [[0.9 , 0.999]], [[0.9 , 0.999]], [[0.9 , 0.999]]]
        initial_value:  [0.0, 0.0, 0.0, 0.0]
    Translation_Z:
        learn: [Yes, Yes, Yes, Yes]
        learning_rate: [0.01, 0.001, 0.0001, 0.00001]
        other_learning_parameters: [[[0.9 , 0.999]], [[0.9 , 0.999]], [[0.9 , 0.999]], [[0.9 , 0.999]]]
        initial_value:  [0.0, 0.0, 0.0, 0.0]


    Rotation_X:
        learn: [Yes, Yes, Yes, Yes]
        learning_rate: [0.01, 0.001, 0.0001, 0.00001]
        other_learning_parameters: [[[0.9 , 0.999]], [[0.9 , 0.999]], [[0.9 , 0.999]], [[0.9 , 0.999]]]
        initial_value:  [0.0, 0.0, 0.0, 0.0]
    Rotation_Y:
        learn: [Yes, Yes, Yes, Yes]
        learning_rate: [0.01, 0.001, 0.0001, 0.00001]
        other_learning_parameters: [[[0.9 , 0.999]], [[0.9 , 0.999]], [[0.9 , 0.999]], [[0.9 , 0.999]]]
        initial_value:  [0.0, 0.0, 0.0, 0.0]
    Rotation_Z:
        learn: [Yes, Yes, Yes, Yes]
        learning_rate: [0.01, 0.001, 0.0001, 0.00001]
        other_learning_parameters: [[[0.9 , 0.999]], [[0.9 , 0.999]], [[0.9 , 0.999]], [[0.9 , 0.999]]]
        initial_value:  [0.0, 0.0, 0.0, 0.0]
```

(b)

```
    Scale_X:
        learn: [Yes, Yes, Yes, Yes]
        learning_rate: [0.01, 0.001, 0.0001, 0.00001]
        other_learning_parameters: [[[0.9 , 0.999]], [[0.9 , 0.999]], [[0.9 , 0.999]], [[0.9 , 0.999]]]
        initial_value:  [1.0, 1.0, 1.0, 1.0]
    Scale_Y:
        learn: [Yes, Yes, Yes, Yes]
        learning_rate: [0.01, 0.001, 0.0001, 0.00001]
        other_learning_parameters: [[[0.9 , 0.999]], [[0.9 , 0.999]], [[0.9 , 0.999]], [[0.9 , 0.999]]]
        initial_value:  [1.0, 1.0, 1.0, 1.0]
    Scale_Z:
        learn: [Yes, Yes, Yes, Yes]
        learning_rate: [0.01, 0.001, 0.0001, 0.00001]
        other_learning_parameters: [[[0.9 , 0.999]], [[0.9 , 0.999]], [[0.9 , 0.999]], [[0.9 , 0.999]]]
        initial_value:  [1.0, 1.0, 1.0, 1.0]


    Shear_X:
        learn: [Yes, Yes, Yes, Yes]
        learning_rate: [0.01, 0.001, 0.0001, 0.00001]
        other_learning_parameters: [[[0.9 , 0.999]], [[0.9 , 0.999]], [[0.9 , 0.999]], [[0.9 , 0.999]]]
        initial_value:  [0.0, 0.0, 0.0, 0.0]
    Shear_Y:
        learn: [Yes, Yes, Yes, Yes]
        learning_rate: [0.01, 0.001, 0.0001, 0.00001]
        other_learning_parameters: [[[0.9 , 0.999]], [[0.9 , 0.999]], [[0.9 , 0.999]], [[0.9 , 0.999]]]
        initial_value:  [0.0, 0.0, 0.0, 0.0]
    Shear_Z:
        learn: [Yes, Yes, Yes, Yes]
        learning_rate: [0.01, 0.001, 0.0001, 0.00001]
        other_learning_parameters: [[[0.9 , 0.999]], [[0.9 , 0.999]], [[0.9 , 0.999]], [[0.9 , 0.999]]]
        initial_value: [0.0, 0.0, 0.0, 0.0]
```

(c)

Fig. 9.7: An exemplary JSON Data format input file for the Histology-Atlas 3D-2D registration. The subfigure 9.7a displays the general settings. The subfigure 9.7b displays the specific settings for a rigid registration. The subfigure 9.7c displays the additional settings for an affine registration.

The graphical user interface is displayed in Figure 9.8.

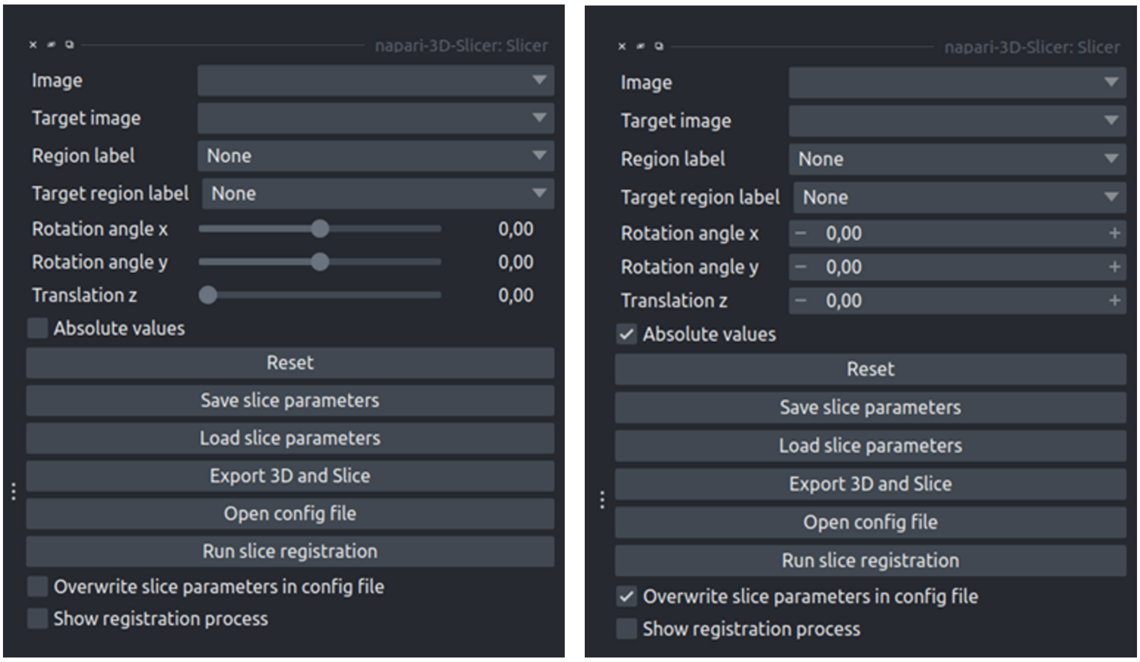

napari-3D-Slicer: Slicer

Image

Target image

Region label None

Target region label None

Rotation angle x 0,00

Rotation angle y 0,00

Translation z 0,00

☐ Absolute values

☐ Overwrite slice parameters in config file

☐ Show registration process

(a)

napari-3D-Slicer: Slicer

Image

Target image

Region label None

Target region label None

Rotation angle x − 0,00 +

Rotation angle y − 0,00 +

Translation z − 0,00 +

☑ Absolute values

☑ Overwrite slice parameters in config file

☐ Show registration process

(b)

Fig. 9.8: The Graphical User Interface of the Napari plugin **napari-3D-Slicer**. The subfigure 9.8a displays the interface with the slider option. The subfigure 9.8b displays the interface with the combo box option.

The implementation used PyTorch, which allows for GPU execution and backpropagation gradient computation for optimization. The Python package magigui based on pyQt5 was used for the graphical user interface. The Gradient Normalized Cross Correlation similarity defined in 8.2 was chosen for the loss function. The Adam optimizer was applied with an initial learning rate of 0.01. It gradually decreased by a factor of 0.1 every 200 iterations until it reached 10^{-5}. The maximum iteration was 1000. The decay factor for the first momentum was set to 0.9. The decay factor for the infinity norm was set to 0.999.

10 Segmentation

10.1 Segmentation of reactive astrocytes

For the segmentation of reactive astrocytes, a generic U-Net architecture [196] implemented in PyTorch was used. The architecture consists of a 3x3 convolution and a convolution with stride 2x2 + Batch normalization + ReLU activation for the encoder and two 3x3 convolutions + Batch normalization + ReLU activation as well as upsampling by nearest-neighbor interpolation for the decoder per resolution stage. The number of features per resolution stage k is given by $64 \cdot 2^k$ for $k = 0, ..., 4$. The 64-channel output layer was then convolved with a 1x1 kernel to produce the reactive astrocyte segmentation map. The training data includes input-target pairs. The input is given by 101 cropped images of 256 x 256 pixels taken from the GFAP-stained histological data. This dataset consists of 2569 cells. The data acquisition was performed by our self-developed Napari tool **napari-nd-cropper**.

napari-nd-cropper enables users to easily define regions of interest within their multi-dimensional image data, as already described in section 7.1 already. By interactively selecting specific regions of interest, users can focus on extracting the relevant parts of very large data for the training process, covering the feature diversity to balance the training data and reduce sample bias.

The target dataset is given by the ground truth segmentation of the astrocytes in the 101 cropped images generated by three domain experts using Napari. The final target image corresponds to a binary image, where the value 0 represents the background and the value 1 represents the astrocyte cell.

Four exemplary input-target pairs are visualized in Figure 10.1.

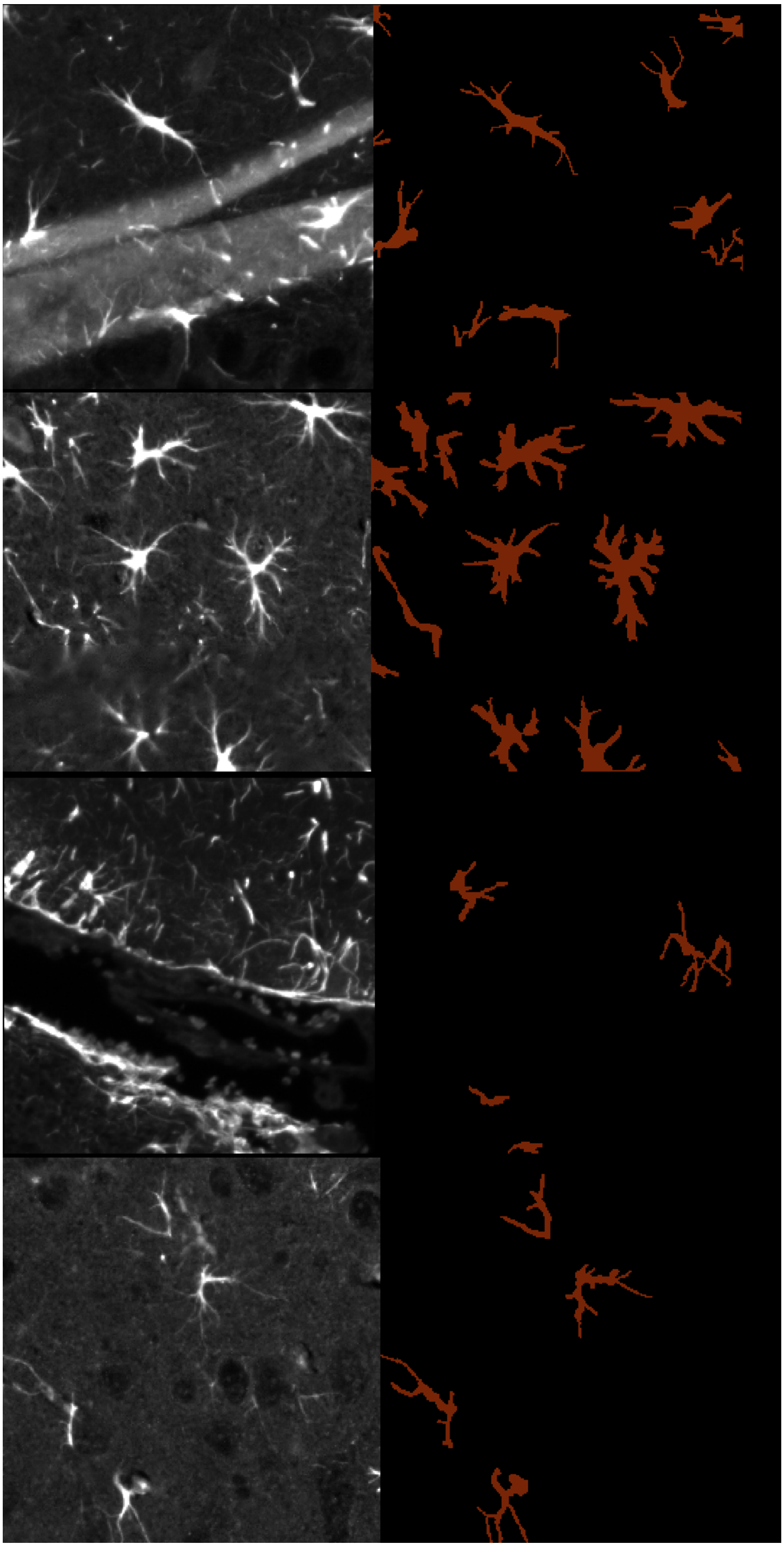

Fig. 10.1: Four samples of input-target pairs to train and validate the segmentation of reactive astrocytes. The left column corresponds to the input. The right column corresponds to the target.

To avoid overfitting, the data were additionally augmented according to the nnU-Net-architecture [89] with augmentations provided by the batchgenerator package [17]. The data loader is shown in Algorithm 13.

For our task, the main challenge is to capture the complex cellular morphology of reactive astrocytes. To address this a custom loss was implemented consisting of a Dice loss and a centerlineDice [214] was implemented as a regularization term to preserve the complex topology. The implementation follows [214]. This measure is calculated from the intersection of the segmentation masks and their morphological skeletons.

The loss is given by

$$L_{\text{Astrocyte\_Skeletonization}} = -\frac{1}{N}\sum_{i=1}^{N}\frac{\sum_{p=1}^{P} t_{p,i} f(w)_{p,i,c=2}}{\sum_{p=1}^{P} t_{p,i} + f(w)_{p,i,c=2}} - \frac{T_S \cdot T_P}{T_S + T_P} \tag{10.1}$$

with the topology sensitivity T_S and topology precision T_P

$$T_S = -\frac{\sum_{i=1}^{N}\sum_{p=1}^{P} s_{t_{p,i}} f(w)_{p,i,c=2}}{\sum_{i=1}^{N}\sum_{p=1}^{P} s_{t_{p,i}}} \tag{10.2}$$

$$T_P = -\frac{\sum_{i=1}^{N}\sum_{p=1}^{P} s_{f(w)_{p,i,c=2}} t_{p,i}}{\sum_{i=1}^{N}\sum_{p=1}^{P} s_{f(w)_{p,i,c=2}}}, \tag{10.3}$$

where $s_{t_{p,i}}$ and $s_{f(w)_{p,i,c=2}}$ correspond to the soft-skeleton of the ground truth segmentation map $t_{p,i}$ for each pixel and batch as well as the probability outcome of the last layer $f(w)_{p,i,c=2}$ defined for each pixel, batch and the foreground class, which is given by the softmax activation function according to

$$f(w)_{p,i,c=2} = \frac{e^{w_{p,i,c=2}}}{\sum_{j=1}^{C=c} e^{w_{p,i,j}}} \tag{10.4}$$

with the input weight $w_{p,i,c}$ for each pixel, batch and class (background + astrocyte= 2). C denotes the total number of classes. P denotes the total number of pixels of the target and the output segmentation, respectively. N corresponds to the mini-batch size. $c = 2$ corresponds to the foreground representing the astrocyte cells.

The soft-skeletonization was performed according to the implementation in [214], which approximates the skeletonization process by applying multiple times, k, 2 x minpooling to erode and 1 x maxpooling to dilate. Then the original image is subtracted from the resulting image and the absolute value is taken for each pixel. Finally, the results for each iteration are added up. $k = 5$ iterations were performed.

The optimization was performed by the Stochastic gradient descent optimizer proposed by PyTorch. The learning rate was given by 10^{-3}. 1000 epochs defined by 400 iterations with a batch size of 4 were trained. In addition, a 5-fold cross-validation was conducted. This means that the dataset was split into 5 folds, using the other 4 folds for training the model and the remaining fold for validating the model with the Dice Score. Repeat this for each of the 5 folds, using a different fold for validation each time. Finally, the mean Dice Score is calculated to provide an estimate of the

model's performance.
This Dice Score $D_{\text{UNET\_Skel}}$ was compared to the Dice Score $D_{\text{UNET\_Cross}}$ resulting from the training with a loss function, which was changed to the sum of the Dice Score and the cross entropy given by

$$L_{\text{Astrocyte\_Cross}} = -\frac{2}{N}\sum_{i=1}^{N}\frac{\sum_{p=1}^{P} t_{p,i} f(w)_{p,i,c=2}}{\sum_{p=1}^{P} t_{p,i} + f(w)_{p,i,c=2}} - \frac{\sum_{i=1}^{N}\sum_{p=1}^{P} t_{p,i} \ln f(w)_{p,i,c=2}}{NP}, \tag{10.5}$$

where P denotes the total number of pixels of the target and the output segmentation, respectively. N corresponds to the mini-batch size. $c = 2$ corresponds to the foreground representing the astrocyte cells. $t_{p,i}$ defined for each pixel and batch denotes the ground truth segmentation map. $f(w)_{p,i,c=2}$ defined for each pixel, batch, and foreground class represents the probability outcome of the last layer, which is given by a softmax activation function as defined in 10.4.
Additionally, the Dice Score $D_{\text{UNET\_Skel}}$ and the Dice Score $D_{\text{UNET\_Cross}}$ resulting from the training with the loss 10.1 and 10.5 were compared to the mean Dice Score D_{RF} resulting from a trained random forest via Ilastik [19]. The features were selected automatically using the wrapper method implemented in Ilastik. The training and validation procedure was performed by a 5-cross validation in the same way as was performed for U-Net training. Moreover, the resulting mean Dice Scores of $D_{\text{UNET\_Skel}}$, $D_{\text{UNET\_Cross}}$, and D_{RF} were compared to the Dice Score resulting from the Otsu thresholding method D_{Otsu} provided by scikit-image. All values greater than the threshold were labeled as reactive astrocytes with label 1 and less than the background with label 0. Finally, all four Dice Scores were compared to the calculated mean Dice Score D_{var} capturing the inter-rater variability among our domain experts. After all, the impact of the preprocessing as described in Section 7.2 was investigated by applying the U-Net model to the data without the preprocessing steps. In addition, the Jaccard index, J, for the detection of astrocytes was measured for each approach. The Jaccard index J is defined as

$$J = \frac{TP}{TP + FN + FP} \tag{10.6}$$

TP corresponds to the number of astrocytes correctly identified as astrocytes according to the ground truth dataset.
FN is the number of undetected astrocytes where an astrocyte exists at that location in the ground truth dataset.
FP corresponds to the number of detected astrocytes where no astrocyte exists at that location in the ground truth dataset.

Algorithm 13 Data loader: Segmentation of reactive astrocytes

```
Input: Training data
Output: (Input_Patch, Target_Patch)
$x_{\text{Astrocyte\_Images}}$, $x_{\text{Astrocyte\_Segmentations}}$ ← Choose a mini-batch at random
for ($x_{\text{Image}}, x_{\text{Seg}}$) in $x_{\text{Astrocyte\_Images}}$, $x_{\text{Astrocyte\_Segmentations}}$ do
    $x_{\text{Image}}$, $x_{\text{Seg}}$ ← SpatialTransform((256, 256),
      patch_center_dist_from_border=None,
      do_elastic_deform=True, alpha=U(0, 200), sigma=U(9, 13),
      do_rotation=True, angle_x=U($-\pi, \pi$), do_scale=True, scale=U(0.85, 1.25),
      border_mode_data="constant", random_crop=False,
      p_el_per_sample=0.2, p_scale_per_sample=0.2,
      p_rot_per_sample=0.2,)($x_{\text{Image}}, x_{\text{Seg}}$)
    $x_{\text{Image}}$, $x_{\text{Seg}}$ ← MirrorTransform(axes=(0,1),
    p_per_sample=0.3)($x_{\text{Image}}, x_{\text{Seg}}$)
    $x_{\text{Seg\_skeletonization}}$ ← Skeletonization($x_{\text{Seg}}$) {according to scikit-image implemntation}
    $x_{\text{Image}}$ ← GaussianNoiseTransform(noise_variance=U(0,0.1),
      p_per_sample=0.1)($x_{\text{Image}}$)
    $x_{\text{Img}}$ ← GaussianBlurTransform(sigma=U(0.5,1),
      p_per_sample=0.2)($x_{\text{Image}}$)
    $x_{\text{Image}}$ ← BrightnessMultiplicativeTransform(multiplier_range=U(0.75, 1.25),
      p_per_sample=0.15)($x_{\text{Image}}$)
    $x_{\text{Image}}$ ← ContrastAugmentationTransform(p_per_sample=0.15)($x_{\text{Image}}$)
    $x_{\text{Image}}$ ← SimulateLowResolutionTransform(zoom_range=U(0.5, 1),
      order_downsample=0, order_upsample=3, p_per_sample=0.25)($x_{\text{Image}}$)
    $x_{\text{Image}}$ ← GammaTransform(gamma_range=U(0.7, 1.5), invert_image=True,
    retrain_stats=True, p_per_sample=0.1)($x_{\text{Image}}$)
    $x_{\text{Image}}$ ← GammaTransform(gamma_range=U(0.7, 1.5), invert_image=False,
    retrain_stats=True, p_per_sample=0.3)($x_{\text{Image}}$)
    Input_Patch += $x_{\text{Image}}$
    Target_Patch += $x_{\text{Seg}}$+ $x_{\text{Seg\_skeletonization}}$
end for
return (Input_Patch, Target_Patch)
```

U(x_1, x_2) coresponds to the uniform distribution on the interval $[x_1, x_2] \subset$

Analysis

11

11.1 Analysis of number density of reactive astrocytes

This analysis method compares the non-irradiated hemisphere (of control mice and irradiated mice) to the irradiated hemisphere, by dividing each hemisphere into cubes of equal edge length of 0.5mm, taking into account the normal biological tissue variability through the hemispheres. For each cube in the non-irradiated hemisphere, the corresponding cube in the irradiated hemisphere is selected, and the cell number density is calculated separately for the non-irradiated and irradiated cubes. The cubes of the non-irradiated hemisphere are then divided by the corresponding cubes of the irradiated hemisphere, and the result is subtracted by one to set the upper limit at one. To obtain an output in relative units between 0 and 1, such as the doses, any value less than 0 was replaced by NaN (Not a Number). The cubes with NaN are then ignored in the analysis. Mathematically it is described by

$$n_{\mathrm{RA}} = \begin{cases} 1 - N_{\mathrm{NI}}/N_{\mathrm{I}}, & \text{if } N_{\mathrm{NI}}/N_{\mathrm{I}} \leq 1 \\ \mathrm{NaN}, & \text{otherwise} \end{cases}, \tag{11.1}$$

where N_{NI} corresponds to the number of astrocyte cells in the non-irradiated selected cube. N_{I} denotes the number of astrocyte cells in the tissue-equivalent irradiated cube. Following these steps, a set of multiple information of the irradiated cubes is now available: the normalized cell number density corresponding to the reactive astrocyte, the localization, the doses and the LET, which allows to investigate the effects of radiation exposure on brain tissue and to identify possible spatial patterns of GFAP-stained reactive astrocytes.

11.2 Analysis of reactive astrocytes using correlation functions

For the analysis of the tissue-specific spatial response, the concept of the 2-point density correlation function is used. This concept is commonly used to describe galaxy clustering and structure formation in astronomy [16, 192]. Nevertheless, the approach is useful, generalizable, and easily adaptable to our demands. To find another reactive astrocyte at distance r, considering a reactive astrocyte in the same tissue, can be described by the 2-point density correlation function $\xi(r)$ obeying the following condition

$$\xi(r) \geq -1. \tag{11.2}$$

In general, the 2-point density correlation function $\xi(r)$ is assumed to be isotropic. This means that the only the distance between two cells is crucial and not the direction (angle) relative to each other.

To estimate the 2-point density correlation function $\xi(r)$, the number of pairs within volumes around astrocytes in the considered irradiated tissue are counted and compared to the number in the corresponding non-irradiated tissue. The 2-point density correlation function $\xi(r)$ can be estimated by

$$\xi(r) = \frac{1}{N}\sum_{i=1}^{N}\frac{N_i(r)}{nV_i(r)} - 1, \tag{11.3}$$

where N corresponds to the total number of astrocytes in the irradiated tissue and n represents the mean number density in the corresponding non-irradiated tissue. $N_i(r)$ denotes the number of astrocytes lying in a shell of thickness δr from the ith astrocyte. $V_i(r)$ denotes the equivalent volume of the shell.
Thus, the power spectrum is defined as

$$P(k) = \frac{n}{(2\pi)^{3/2}}\int \xi(r)e^{\mathrm{i}kr}dr \tag{11.4}$$

Samples with the same dose and LET were compared in three different tissues: Hippocampus, midbrain, and thalamus. In addition, samples with an increasing dose and a low LET, as well as samples with a low dose and an increasing LET, were examined.

11.3 Analysis of the morphology of reactive astrocytes

As a first step, the elastic metric [225] was used to investigate the morphological changes of reactive astrocytes due to proton irradiation. This metric is suitable to capture the cell heterogeneity of cancer cells via local deformations given by stretching and bending [122]. Furthermore, the elastic metric can provide information on whether the morphology changes are dominated by shape or size changes, since it is invariant to reparameterization, scaling, rotation, and translation [225]. This approach was adapted to our astrocytic cells. The elastic metric $g_c^{\alpha,\beta}$ is given by

$$g_c^{\alpha,\beta} = \alpha\int_0^1 \langle D_s h, n\rangle\langle D_s k, n\rangle + \beta\int_0^1 \langle D_s h, v\rangle\langle D_s k, v\rangle \tag{11.5}$$

with the differential operator D_s respect to the arc length s defined by

$$D_s = \frac{1}{\|c'(s)\|}\frac{d}{ds} \quad \text{with } c'(t) \neq 0 \quad \forall \quad t \in [0,1], \tag{11.6}$$

where c denotes the curve which is parameterized to the unit interval. The arc length element ds is related to dt via

$$ds = e^{\phi(t)}dt, \tag{11.7}$$

where ϕ corresponds to the local stretching/compression along the curve c.
h and k describe two curve deformations in the tangent space and the constants α, $\beta \in \mathbb{R}$. The vector n represents the normal unit vector to the curve c. The vector v

represents the tangent unit vector to the curve c. The term corresponding to *alpha* describes the bending of the curve c. The term corresponding to β describes the stretching of the curve c. In this thesis , $\alpha = 1$ and $\beta = 0.25$. A geodesic distance between two curves c_0 and c_1 over a regular path p is then given by

$$d^{\alpha,\beta}(c_0, c_1) = \inf_{p:[0,1]\mapsto\mathbb{R}^2 \quad | \quad p(0)=c_0 \text{ and } p(1)=c_1} l^{\alpha,\beta}[p] \tag{11.8}$$

with the length l

$$l^{\alpha,\beta}[p] = \int_0^1 \sqrt{g^{\alpha,\beta}_{p(t)}(p'(t), p'(t))}\, dt \tag{11.9}$$

Furthermore, the Fréchet mean $\bar{c}$ was defined over all non-irradiated N astrocyte shapes/ curves (c_0,...,c_N),

$$\bar{c} = \operatorname*{argmin}_{c} \sum_{i=1}^{N} (d^{\alpha,\beta}(c_0, c_i))^2. \tag{11.10}$$

For the computation of the elastic metric, the geodesic distance and the Fréchet mean, the implementation of the Python package geomstats [150] was used. Finally, the shape of the cells as a function of tissue, dose deposition and LET can be considered. In a second step, the resizing of astrocyte processes was investigated as a function of brain region, dose, and LET. For this purpose, the skeleton of each astrocyte was determined to compute the length of each process. The total length of all astrocyte processes is then given by the sum over the length of each process. The necessary calculations were performed using the given skeleton algorithm provided by scikit-image.

Part IV

Results

Monte-Carlo beam transport simulations 89

Preprocessing 93

Quantification of dose delivery accuracy in 3D 99

Registration 107

Segmentation 115

Analysis 119

Monte-Carlo beam transport simulations

12

12.1 Monte-Carlo simulation of dose and LET

This section shows the simulated dose and LET distributions which have been computed in accordance with the section 6.1. Additionally, the impact of other particles on the LET was investigated and the mean statistical error of the dose $\bar{\rho}_{\mathrm{Dose}}$ and LET distribution $\bar{\rho}_{\mathrm{LET}}$ was determined for ten runs of each mouse. The results are presented in this section. Figure 12.3 shows an exemplary 3D view of the dose and LET distribution. In the figure 12.2, the corresponding depth dose and the corresponding LET are shown. The computation time is about 2 minutes on 64 threads for 10^8 protons.

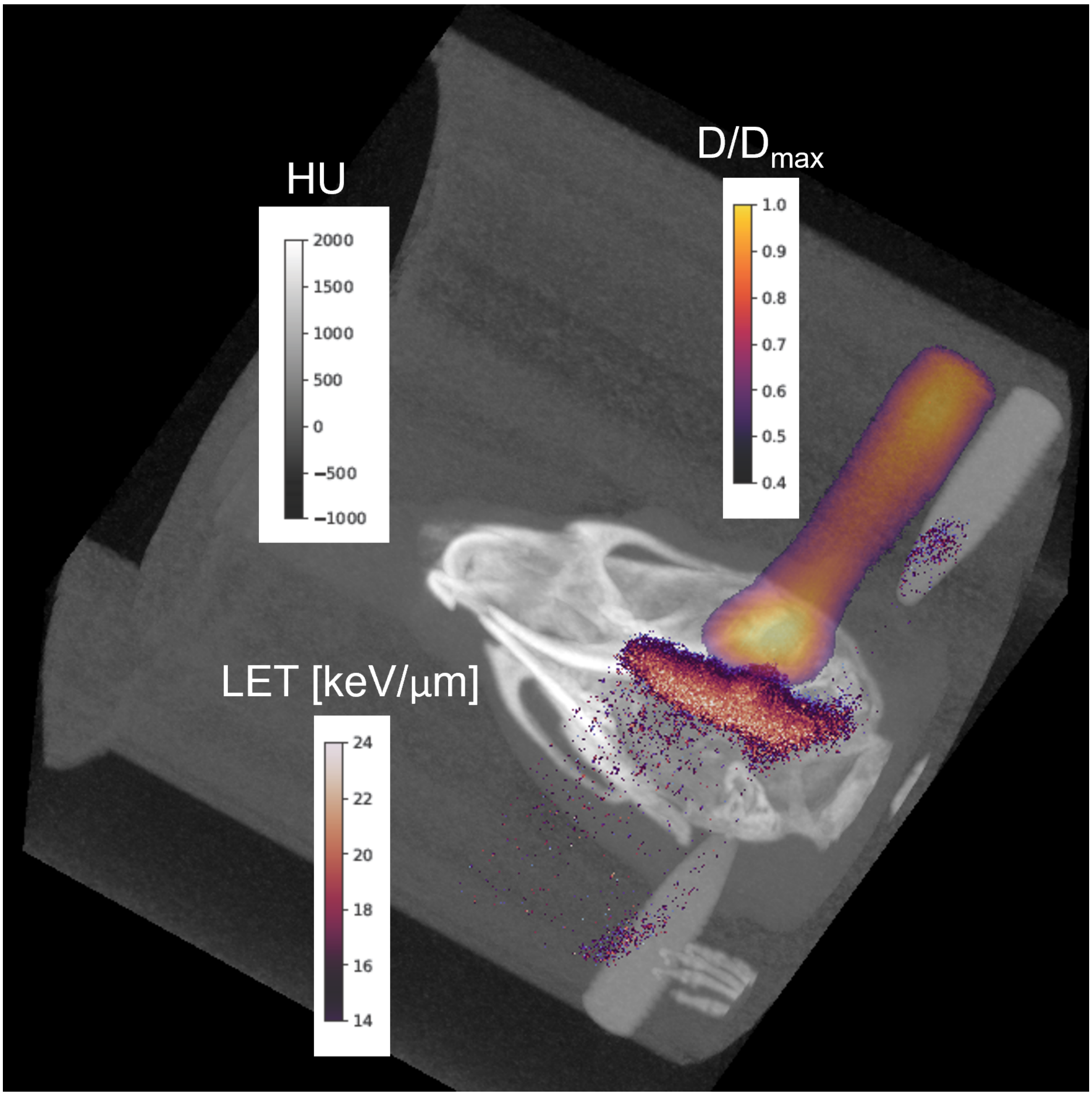

Fig. 12.1: An exemplary 3D dose distribution (colormap: inferno) normalized to the maximal Dose D_{max} and LET distribution (colormap: twilight) in keV/μm overlayed on CBCT image in Hounsfield units HU of a mouse with the earpins embedded in the mouse bed (colormap: gray).

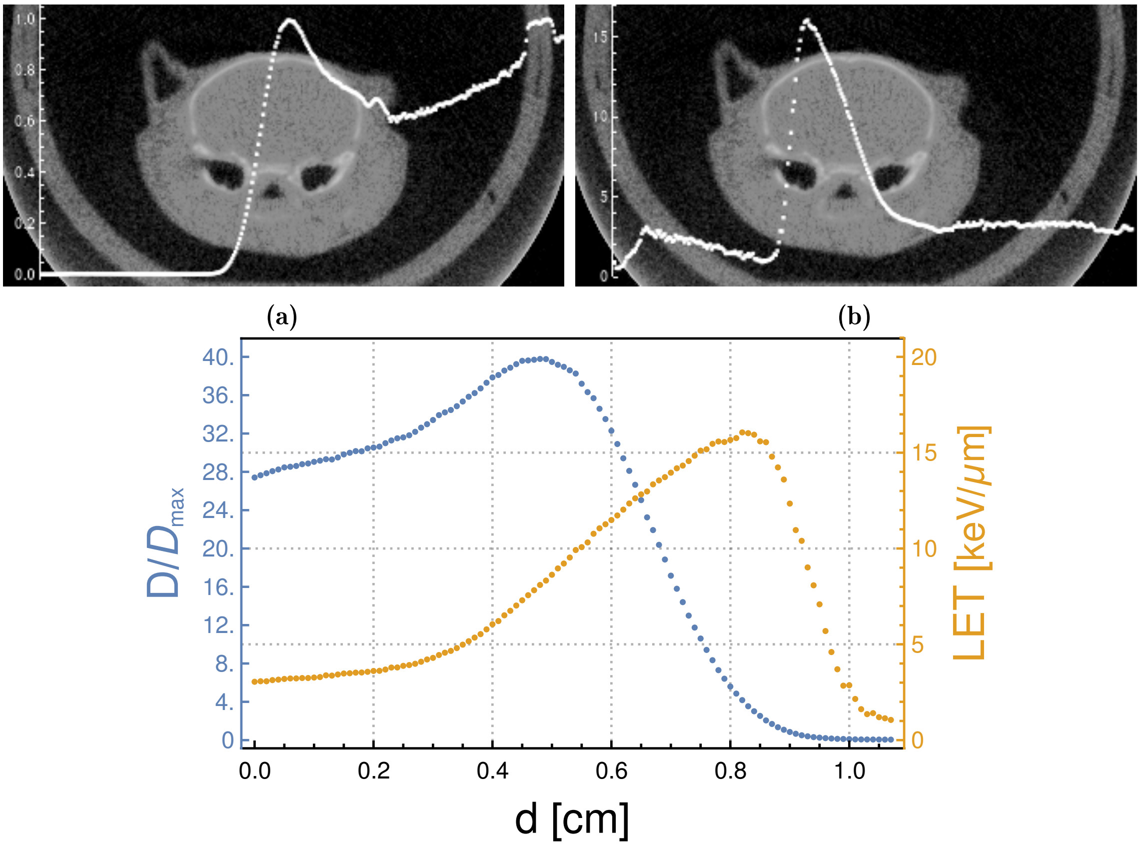

(a) (b)

(c)

Fig. 12.2: An exemplary depth dose distribution 12.2a normalized to the maximal Dose $D_{\max}$ and LET distribution 12.2b in keV/μm overlayed on the corresponding CBCT slice. The subfigure 12.2c shows the dose (subfigure 12.2a) and the LET (subfigure 12.2b) distribution together as function of the depth d of the mouse brain.

The mean statistical errors for the mouse brain and mouse bed defined by intensity values > 0 are presented in table 12.1.

Mouse	$\bar{\rho}_{\text{Dose}}$ [Gy]	$\bar{\rho}_{\text{LET}}$ [keV/μm]
B6: 45 Gy	0.02	0.14
B6: 65 Gy	0.02	0.13
B6: 85 Gy	0.04	0.14
C3H: 40 Gy	0.02	0.17
C3H: 60 Gy	0.03	0.18
C3H: 80 Gy	0.05	0.17

Tab. 12.1: The mean statistical error of the dose $\bar{\rho}_{\text{Dose}}$ and the LET distribution $\bar{\rho}_{\text{LET}}$ for 100 runs of each mouse.

The mean dose error over all mice is given by 0.03 Gy. The error of the dose is on

the order of 0.1% of the applied dose. The mean LET error amounts to 0.16 keV/μm. The error of the LET is on the order of 1%.
The figure 12.3 shows the difference ΔLET depending on the brain depth of the LET of protons and associated secondary electrons with the LET resulting from all particles including neutrons, heavier particles and alpha particles.

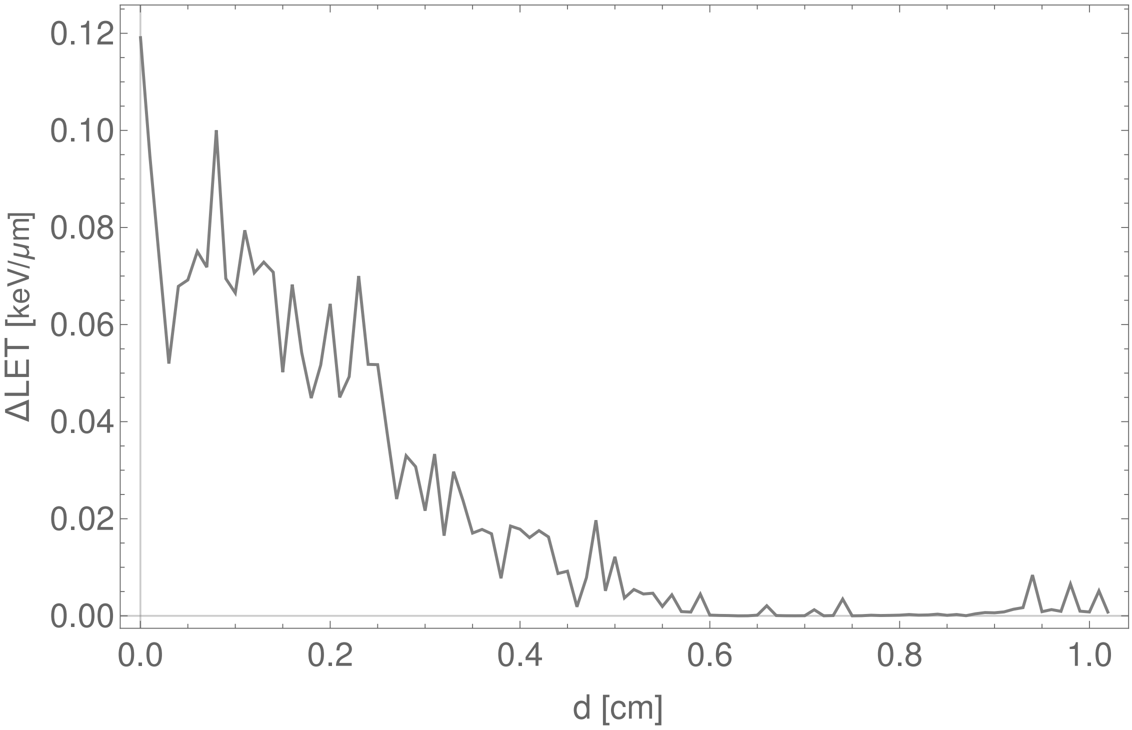

Fig. 12.3: The difference ΔLET as a function of brain depth d of the LET of protons and associated secondary electrons with the LET of all particles, including neutrons and including neutrons as well as heavier particles and alpha particles.

As observed, the LET for all particles at the brain entrance is larger than the LET of protons and associated secondary electrons. The maximum enhancement amounts to 0.12 keV/μm. However, this is of the same order as the mean statistical error of the LET. Nevertheless, the total LET of all particles is used in this work, because the enhancement is not random, but depends on the brain depth and is higher at the brain entrance due to heavier particles than protons.

13 Preprocessing

13.1 Preprocessing of the CBCT and X-ray images for 3D position reconstruction

In this section, the results are shown after applying the preprocessing steps described in Section 7.1 to remove the mouse bed, legs, shoulders, and earpins from the CBCT image. Figure 13.1 shows an exemplary raw CBCT image, the resulting segmentation mask of the mouse bed, legs, shoulders, and earpins as well as the final CBCT image after removal of the mouse bed and earpins using the segmentation map.

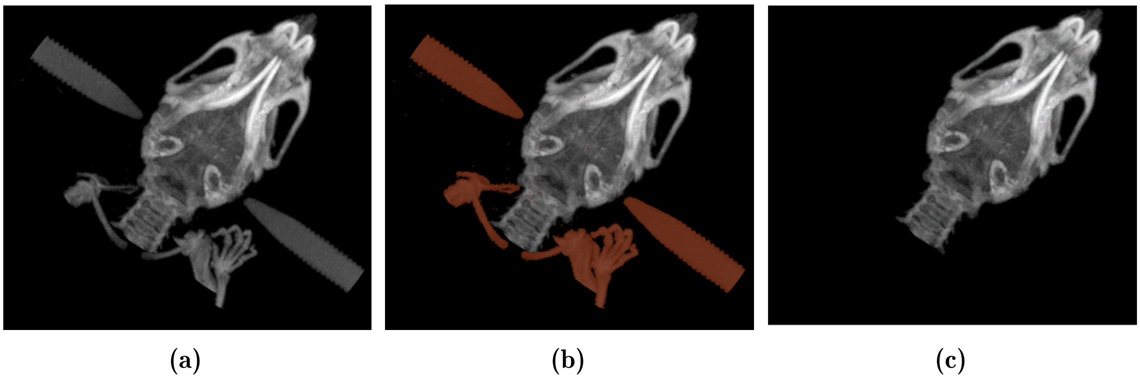
(a) (b) (c)

Fig. 13.1: An exemplary result in 3D view for applying the preprocessing steps for the CBCT images according to algorithm 8. The subfigure 13.1a shows an exemplary raw CBCT image. The subfigure 13.1b shows the resulting segmentation mask mouse bed, legs, shoulders, and earpins overlayed on the raw CBCT image. The subfigure 13.1c shows the final CBCT image after the removal of the mouse bed, legs, shoulders, and earpins using the segmentation mask.

In addition, the results of the preprocessing applied to the X-ray images used to quantify dose delivery accuracy are presented. In Figure 13.2, an exemplary resulting adjusted cumulative histogram of X-ray image matching the cumulative histograms of mean projection of the CBCT image after applying the preprocessing is shown. The cumulative histograms of the unprocessed X-ray image and the target 2D slice of the CBCT image are displayed for comparison. Only the foreground, defined by intensities greater than 0, is considered.

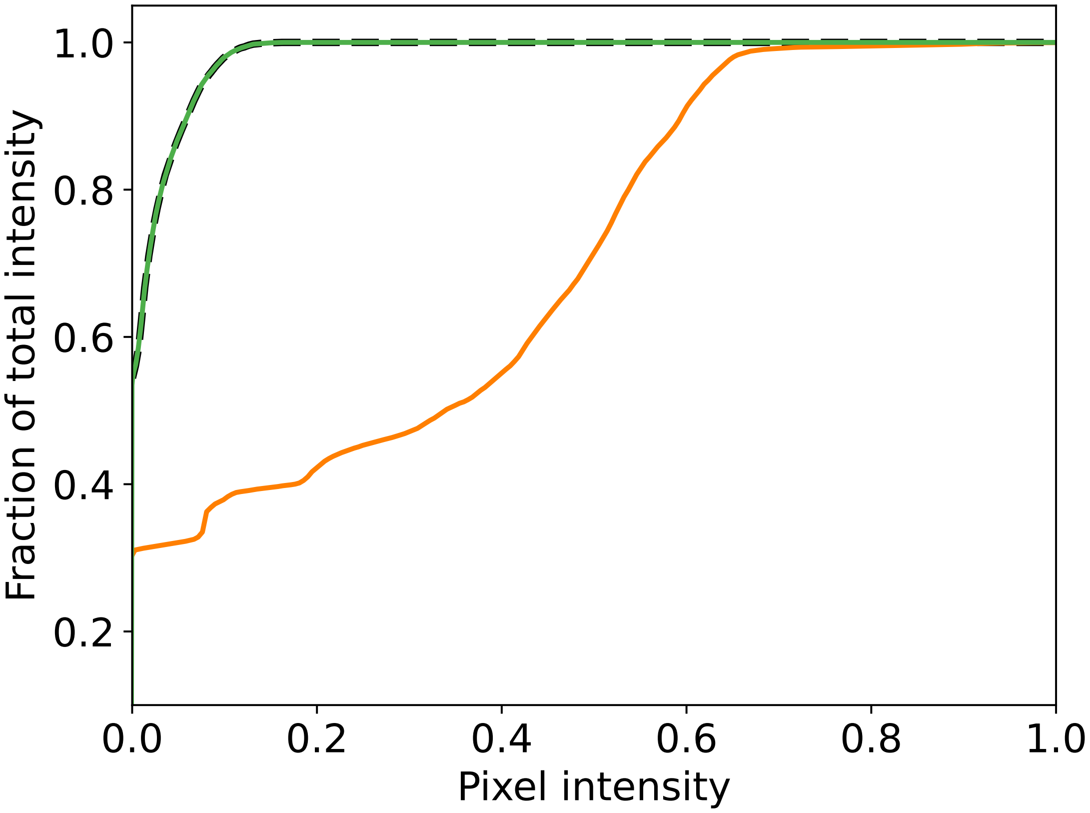

Fig. 13.2: An exemplary cumulative histogram of the non-preprocessed X-ray image (orange line), the preprocessed X-ray image (green line) as well as the target 2D slice given by the mean projection of the CBCT (dashed black line).

Figure 13.3 shows the corresponding images to the histograms.

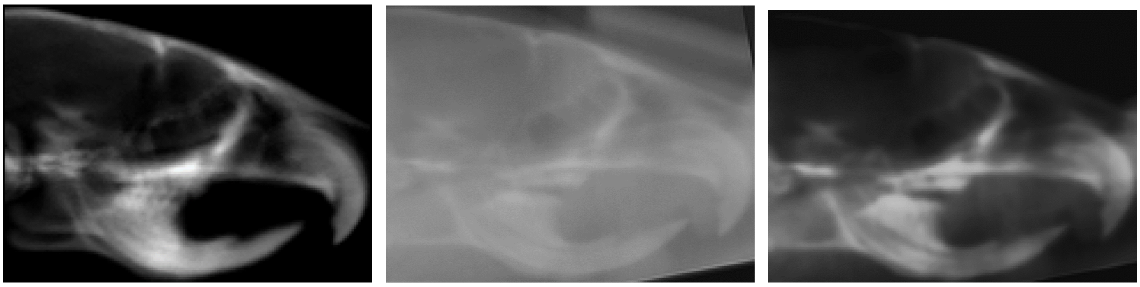

(a) (b) (c)

Fig. 13.3: An exemplary result for applying the preprocessing steps for the X-ray images according to algorithm 9. The subfigure 13.3a shows the CBCT as the reference image. The subfigure 13.3b shows the non-preprocessed X-ray image. The subfigure 13.3c shows the final preprocessed X-ray image.

For each mouse, the peak signal-to-noise ratio (PSNR) of the raw X-ray image and the preprocessed X-ray image are compared. The 2D mean projection of the respective CBCT is used as the reference. The PSNR is defined in decibels [dB] as

$$\mathrm{PSNR} = -\log_{10}(\mathrm{MSE}(R, P))\ [\mathrm{dB}] \tag{13.1}$$

with the mean square error of the reference image R and preprocessed image P,

$$\mathrm{MSE} = \frac{1}{I \cdot J} \sum_{i}^{I-1} \sum_{j}^{J-1} (R(i,j) - P(i,j))^2, \tag{13.2}$$

with the row and column index of images i, j. I and J denote the weight and height of the images. Note that the images was cropped to the same size for comparison. The computation was performed by the corresponding implementation provided by scikit-image. Table 13.1 shows the PSNR for the raw X-ray images and the 2D mean projection of the respective CBCT image ($\mathrm{PSNR}_{\mathrm{CBCT\_X\text{-}ray\_Raw}}$) as well as the preprocessed X-ray images and the 2D mean projection of the respective CBCT image ($\mathrm{PSNR}_{\mathrm{CBCT\_X\text{-}ray\_Preprocessed}}$) for each mouse.

Mouse	$\mathrm{PSNR}_{\mathrm{CBCT\_X\text{-}ray\_Raw}}$ [dB]	$\mathrm{PSNR}_{\mathrm{CBCT\_X\text{-}ray\_Preprocessed}}$ [dB]
B6: 0 Gy	8	33
B6: 45 Gy	7	34
B6: 65 Gy	9	33
B6: 85 Gy	8	32
C3H: 0 Gy	8	36
C3H: 40 Gy	8	36
C3H: 60 Gy	8	36
C3H: 80 Gy	8	36

Tab. 13.1: The PSNR for the raw X-ray images and the 2D mean projection of the respective CBCT images ($\mathrm{PSNR}_{\mathrm{CBCT\_X\text{-}ray\_Raw}}$) as well as the preprocessed X-ray images and the 2D mean projection of the respective CBCT images ($\mathrm{PSNR}_{\mathrm{CBCT\_X\text{-}ray\_Preprocessed}}$) for each mouse.

As can be seen, the PSNR of the X-ray image is increased for each mouse. This indicates that the developed preprocessing for X-ray images increases the image quality of the X-ray images to a level similar to that of the CBCT images. Eventually, this makes it easier to register them, as was conducted in Section 9.2, because the optimizer used has less local minima to deal with.

13.2 Preprocessing of the histological images

In this section, the results of the performed histological preprocessing, which was described in section 7.2, are presented. To quantify the effect, the homogeneity $\mathbb{H}$ was measured. The homogeneity $\mathbb{H}$ is defined as follows

$$\mathbb{H} = \frac{1}{T} \sum_{t=1}^{T} \frac{\sigma_{\mathbb{H},t}}{\mu_{\mathbb{H},t}}. \tag{13.3}$$

The mean $\mu_{\mathbb{H},t}$ corresponds to the mean intensity of a tile. The standard deviation $\sigma_{\mathbb{H},t}$ corresponds to the standard deviation of the intensity of a tile. T denotes the maximal number of tiles. In figure 13.4 an exemplary result before and after the execution of the preprocessing is shown.

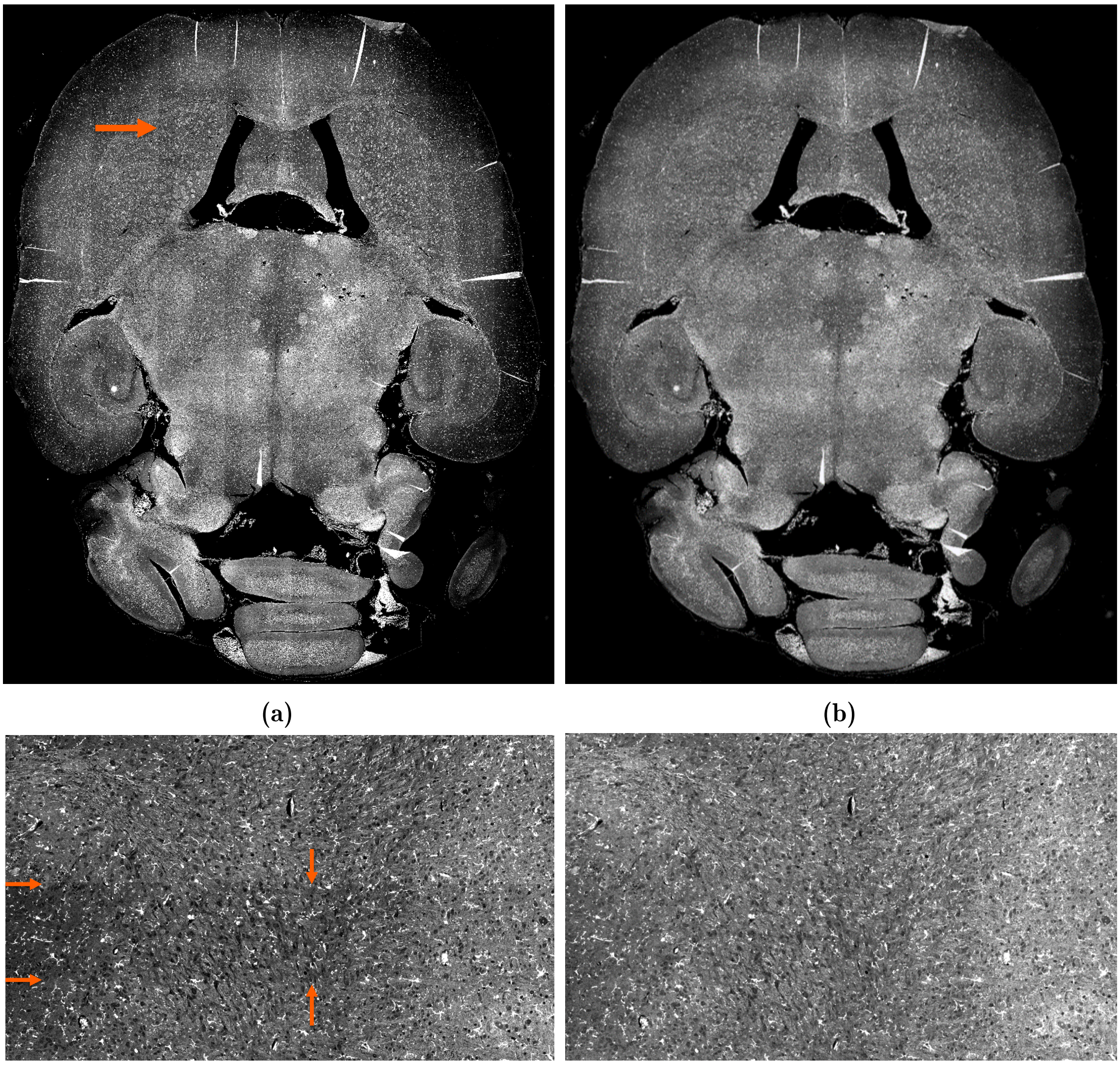

(a) (b)

(c) (d)

Fig. 13.4: Exemplary results to show the effect of the preprocessing to remove vignetting. Subfigure 13.4a shows an exemplary non-preprocessed slice of GFAP-stained reactive astrocytes. Subfigure 13.4b shows the outcome after applying the preprocessing to remove vignetting. Subfigure 13.4c shows an exemplary non-preprocessed tile of GFAP-stained reactive astrocytes. Subfigure 13.4d shows the preprocessed tile after applying the preprocessing to remove vignetting. The orange arrows indicates the darker areas producing the grid pattern.

Table 13.2 shows the mean homogeneity values for each non-preprocessed mouse $\mathbb{H}_{\mathrm{Raw}}$ as well as the mean homogeneity $\mathbb{H}_{\mathrm{Pre}}$ after applying the preprocessing for each mouse. The standard error $\Delta\mathbb{H}$ of the mean is on the order of 10^{-4}.

Mouse	$\mathbb{H}_{\text{Raw}}$	$\mathbb{H}_{\text{Pre}}$
B6: 0 Gy	0.41	0.39
B6: 45 Gy	0.34	0.32
B6: 65 Gy	0.36	0.35
B6: 85 Gy	0.50	0.48
C3H: 0 Gy	0.34	0.33
C3H: 40 Gy	0.42	0.40
C3H: 60 Gy	0.39	0.37
C3H: 80 Gy	0.41	0.39

Tab. 13.2: The mean homogeneity for each non-preprocessed $\mathbb{H}_{\text{Raw}}$ and the equivalent preprocessed $\mathbb{H}_{\text{Pre}}$ mouse following the preprocessing steps in Section 7.2.

As can be seen, the application of the described preprocessing is sufficient to remove vignetting and thus leads to an improved homogeneity (see Table 13.2).

14

Quantification of dose delivery accuracy in 3D

In this section, the results of the quantification of the dose delivery accuracy verification are presented in accordance with the methods described in Section 8.

14.1 Step A1: Repositioning Accuracy

The setup error analysis revealed normally distributed statistical misalignments of the mouse skull with standard deviations σ_a of 0.64 mm, 0.58 mm, 0.45 mm in x- y- and z- direction and 1.51°, 3.69° and 5.32° for the Euler angles pitch (rotation about z-axis), yaw (rotation about y-axis) and roll (rotation about x-axis), respectively (Figure 14.1 and Table 14.1).

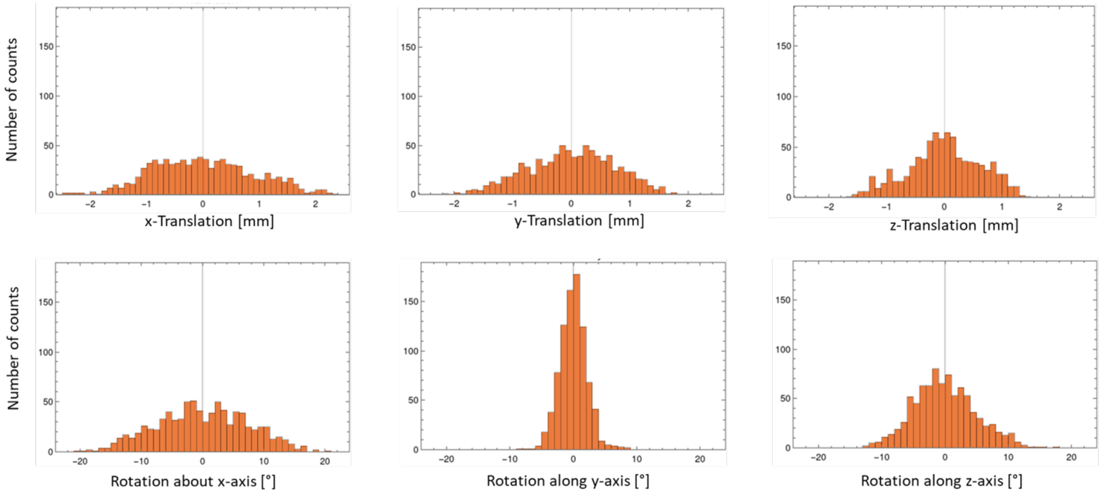

Fig. 14.1: Misalignment distributions for each positioning degree of freedom for pairwise rigidly registered CBCT images.

Rotation degree of freedom	Mean μ_a [°]	Standard deviation σ_a [°]
Rotation about x-axis	0.97	5.32
Rotation about y-axis	0.10	1.51
Rotation about z-axis	−1.73	3.69

(a)

Translation degree of freedom	Mean μ_a [mm]	Standard deviation σ_a [mm]
Translation in x-direction	0.10	0.65
Translation in y-direction	0.37	0.58
Translation in z-direction	0.07	0.45

(b)

Tab. 14.1: Repositioning accuracy of each positioning degree of freedom measured by the mean μ_a and standard deviation σ_a of the corresponding misalignment distribution in Figure 14.1.

14.2 Step A2: Uncertainties of A-priori dose

Table 14.2 and Figure 14.2 show the results of the a-priori dose error characterized by the shifts of the Bragg peak in all degrees of freedom. The misalignments in roll (rotation about x-axis) can lead to a relevant range shift of $-0.7/+0.4$ mm at the falling distal edge and to an overestimation/underestimation of the dose for transversal dose profiles. On the other hand, the small misalignments in yaw (rotation about y-axis) and pitch (rotation about z-axis) compared to the roll do not result in a dose delivery error below the image resolution. The translation in y-direction results in a relevant transversal dose shift and a range shift of $-0.1/+0.1$ mm. The misalignments in the x-direction lead to a significant transversal shift of the dose distribution. For the largest observable misalignment along the beamline (z-direction), no relevant range shift is observed. Ultimately, only the misalignments in roll and the lateral translational degrees of freedom have a relevant impact on the accuracy of dose delivery for our experimental study.

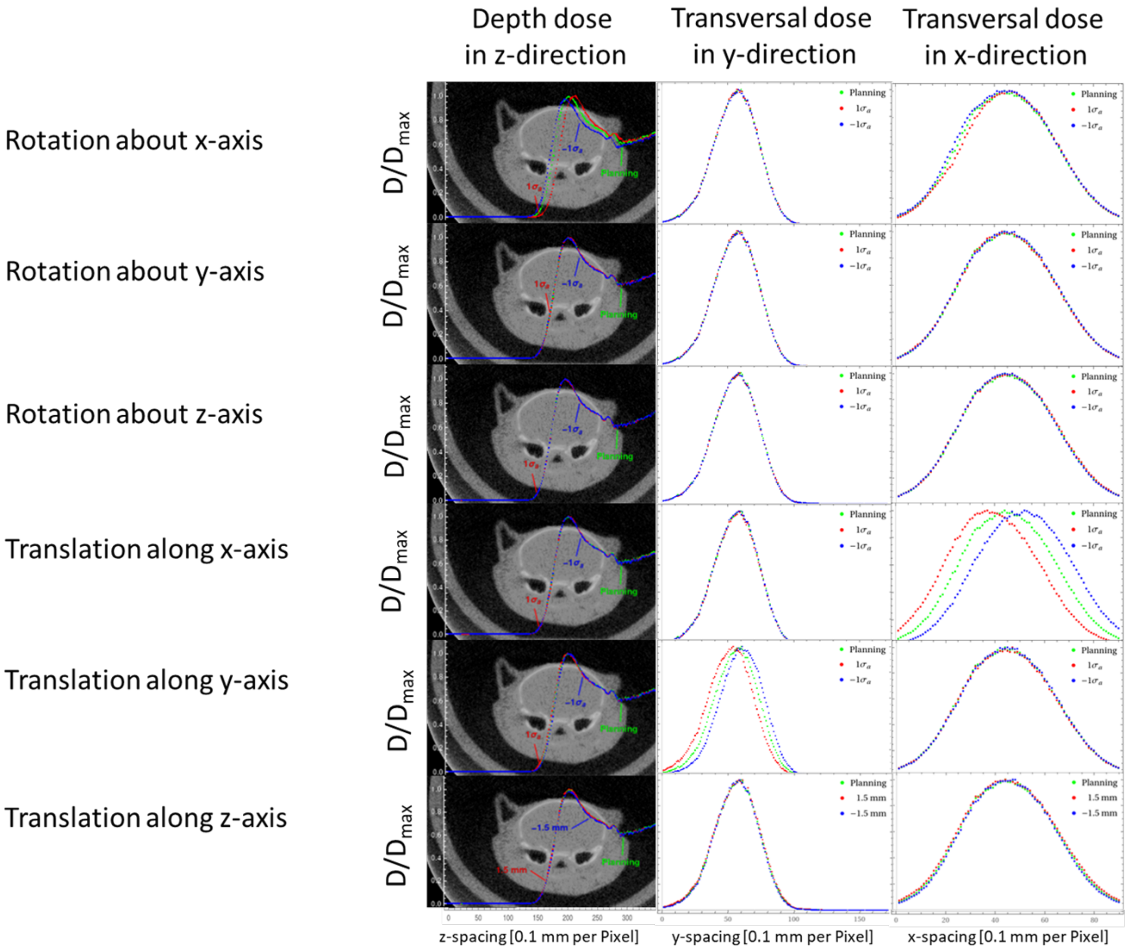

Fig. 14.2: Dosimetric impact of misalignment before 3D position reconstruction by 2D-3D image matching. Overlay of a mouse skull CBCT slice with depth-dose curves, plot of transversal dose curves along y-axis and x-axis for zero misalignment (green) and misalignment plus/minus (red/blue) of one standard deviation for each degree of freedom.

Degree of freedom	Distal range shift [mm]	Proximal range shift [mm]
Rotation about x-axis	0.40	0.70
Rotation about y-axis	0.02	0.04
Rotation about z-axis	0.00	0.01
Translation in x-direction	0.02	0.03
Translation in y-direction	0.11	0.11
Translation in z-direction	0.03	0.01

Tab. 14.2: A-priori dose error: The distal range shift is characterized by a shift of the Bragg peak according to $-\sigma_a$ in Figure 14.2. The proximal range shift is characterized by a shift of the Bragg peak according to σ_a in Figure 14.2.

14.3 Step B1: 3D Position Reconstruction

The computation time for the misalignment correction is given by a maximum of 15 s on the GPU (Nvidia Quadro RTX 6000). Complete treatment planning including pre-processing, misalignment correction, and simulation can be performed in less than 5 minutes. To make this accessible to users, the GUI "TP-Small-Animal" was developed based on Napari. An exemplary optimization process is shown in Figure 14.3.

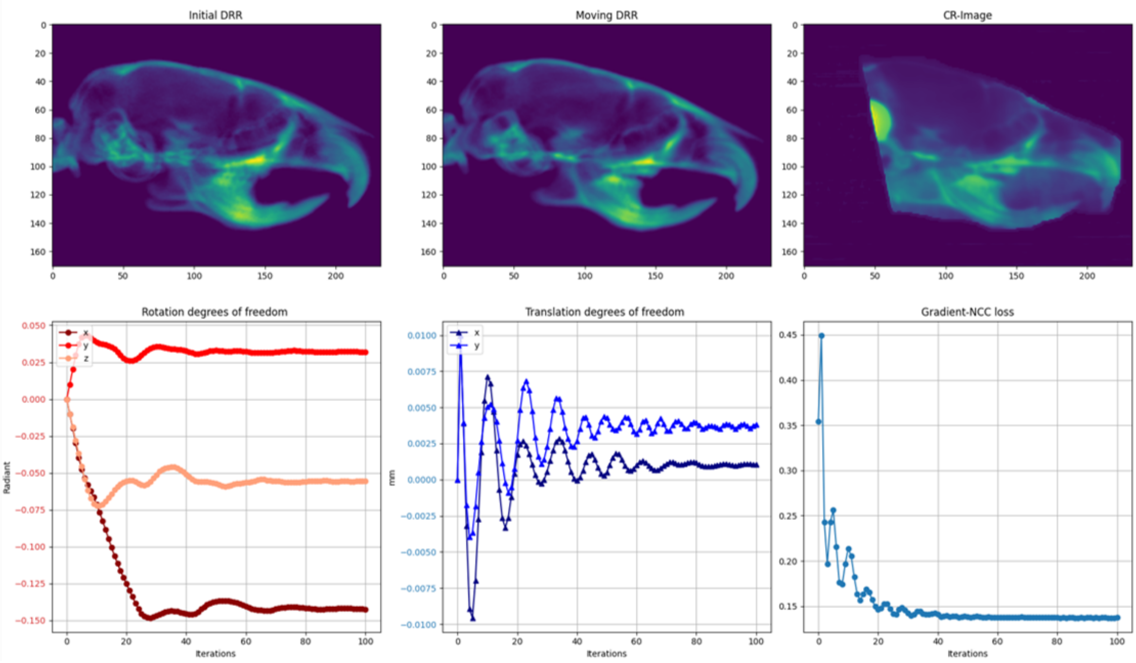

Fig. 14.3: Overview of an exemplary 3D position reconstruction by 2D-3D image matching. The top row shows an initial DRR generated by the CBCT (left), the final DRR generated by the CBCT (middle) matching the target X-ray image (right). The bottom row shows the evolution of the rotation (left) and translation (middle) parameters as well as the Gradient-NCC similarity (right).

14.4 Step B2: Evaluation of Position Uncertainty

Via 3D position reconstruction by 2D-3D image matching, the absolute mean misalignment μ_e could be reduced to ±1° for all rotations and to ±0.1 mm for all translations, except for the in z-direction, which was not corrected (Figure 14.4 and Table 14.3)

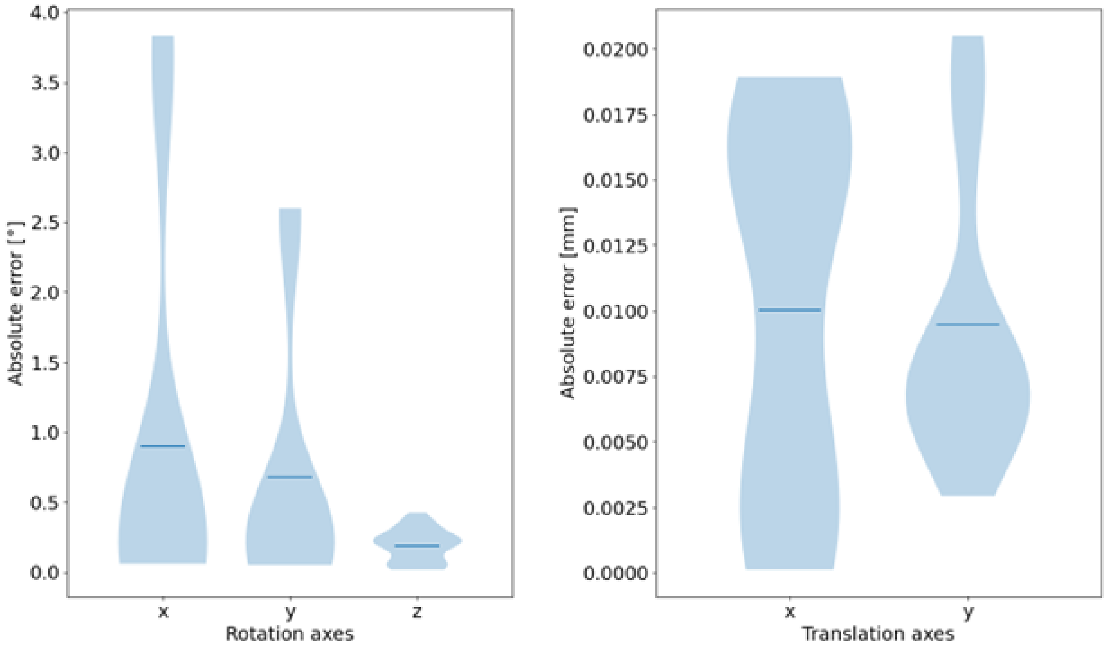

Fig. 14.4: Misalignment distribution for each translation and rotation parameter after 3D position reconstruction by 2D-3D image matching. The blue line denotes the mean error μ_e.

Rotation degree of freedom	Mean μ_e [°]	Standard mean error σ_e [°]
Rotation about x-axis	0.90	0.10
Rotation about y-axis	0.68	0.07
Rotation about z-axis	0.19	0.01

(a)

Translation degree of freedom	Mean μ_e [mm]	Standard mean error σ_e [mm]
Translation in x-direction	0.01	0.00
Translation in y-direction	0.01	0.01
Translation in z-direction	NC	NC

Note: NC = No correction was applied

(b)

Tab. 14.3: Absolute mean residual error after 3D position reconstruction by 2D-3D image matching corresponding to the misalignment distribution in Figure 14.4.

14.5 Step B3: Uncertainty of A-posteriori dose

After the 3D position reconstruction by 2D-3D image matching, the misalignment in roll and the lateral translational degrees of freedom lead to range shifts that are no longer observable (Figure 14.5 and Table 14.4).

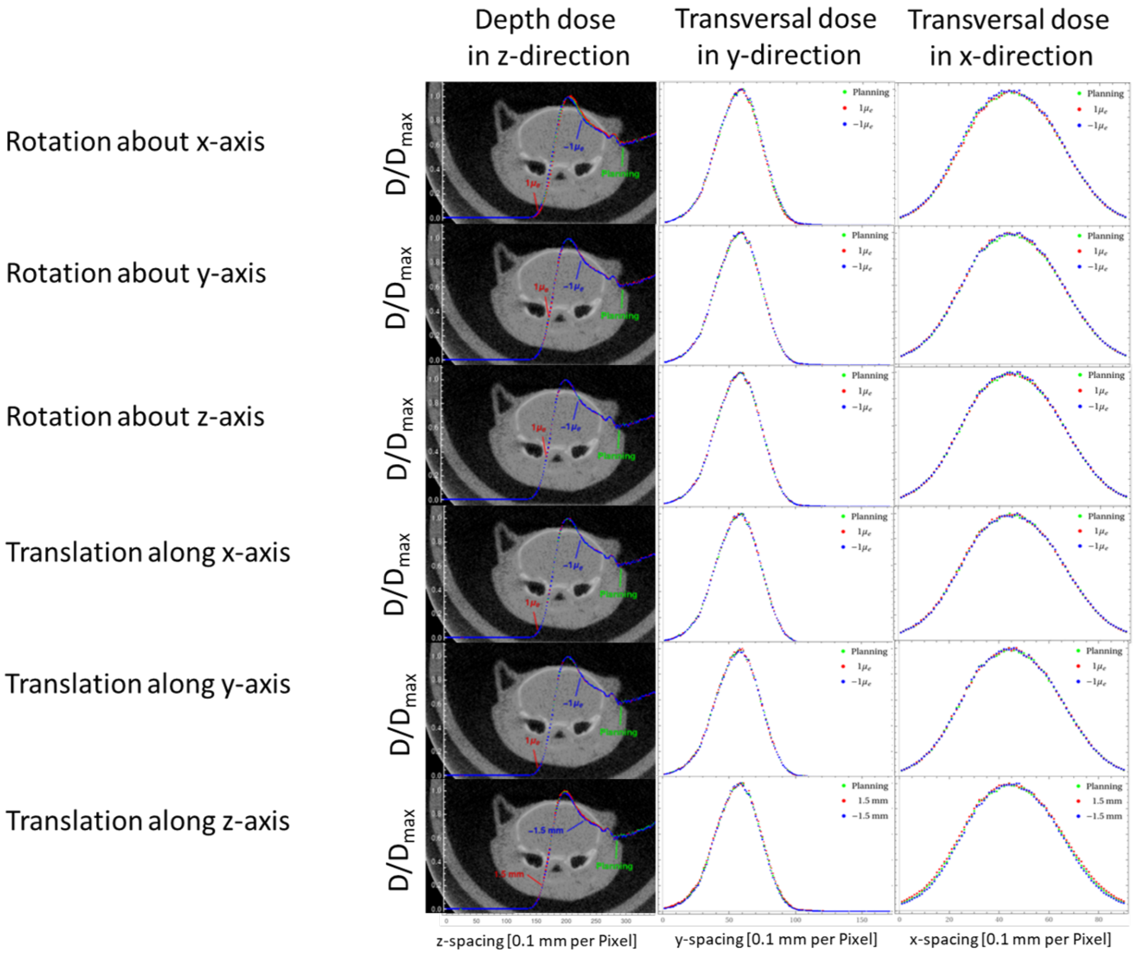

Fig. 14.5: Dosimetric impact of misalignment after 3D position reconstruction by 2D-3D image matching. Overlay of a mouse skull CBCT slice with depth-dose curves, plot of transversal dose curves along y-axis and x-axis for zero misalignment (green) and misalignment plus/minus (red/blue) of one standard deviation for each degree of freedom.

Degree of freedom	Distal range shift [mm]	Proximal range shift [mm]
Rotation about x-axis	0.09	0.12
Rotation about y-axis	0.02	0.01
Rotation about z-axis	0.00	0.00
Translation in x-direction	0.00	0.01
Translation in y-direction	0.00	0.00
Translation in z-direction	NC	NC

Note: NC = No correction was applied

Tab. 14.4: A-posteriori dose error: The distal range shift is characterized by a shift of the Bragg peak according to $-\mu_e$ in Figure 14.5. The proximal range shift is characterized by a shift of the Bragg peak according to μ_e in Figure 14.5.

Registration

15

15.1 CBCT-Atlas registration

In this section, the residual registration error $d_{\mathrm{MRRE\_CBCT\_MRI}}$ for each mouse is presented for the registration of the CBCT image to the MRI template that was previously registered to the combined DAPI-Nissl template generated by [229], as described in Section 9.2. The mean registration error quoted in [229] was 100 μm. In addition, some exemplary registration results are shown. Initially, the MRI template was registered to the combined DAPI-Nissl template. An exemplary 2D view of the resulting registration is shown in Figure 15.1.

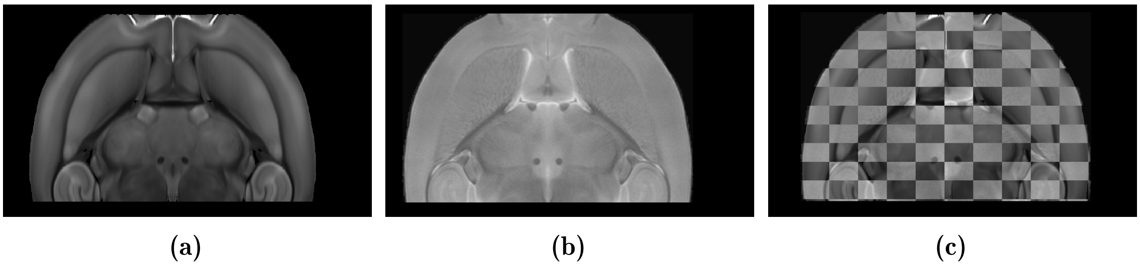

(a) (b) (c)

Fig. 15.1: An exemplary 2D view of a final MRI-Nissl-DAPI template registration. The subfigure 15.1a shows the target image corresponding to the combined DAPI-Nissl template. The subfigure 15.1b shows the final moving image corresponding to the MRI template. The subfigure 15.1c displays the corresponding checkerboard view of both.

The residual registration $d_{\mathrm{MRRE\_MRI\_DAPI\text{-}Nissl}}$, resulting from setting landmarks, amounts to 12μm. The results of the registration of the CBCT image to the MRI template for an exemplary mouse can be visually inspected in Figure 15.2.

Fig. 15.2: An exemplary 2D view overlay of the CBCT image registered to the MRI template.

The residual registration error $d_{\mathrm{MRRE\_CBCT\_MRI}}$ for each mouse was determined by setting landmarks according to the equation 9.17. Table 15.1 displays the error for each mouse.

Mouse	$d_{\mathrm{MRRE\_CBCT\_MRI}}$ [μm]
B6: 0 Gy	12
B6: 45 Gy	10
B6: 65 Gy	13
B6: 85 Gy	14
C3H: 0 Gy	57
C3H: 40 Gy	32
C3H: 60 Gy	82
C3H: 80 Gy	80

Tab. 15.1: The residual landmark-based registration error $d_{\mathrm{MRRE\_DAPI\_MRI}}$ for each mouse according to equation 9.17

All residual registration errors are less than 0.1 mm, which is less than the resolution of the dose and LET distributions.

15.2 Histology-Atlas registration

In this section, the residual registration error $d_{\mathrm{MRRE\_Histology\_Atlas}}$ for each mouse is presented for the registration of the histological images to the MRI-Nissl-DAPI template as described in Section . In addition, some exemplary results of restoration and registration are shown. Prior to registration, additional preprocessing was required to match the intensity distributions of the histological slices to the MRI-Nissl-DAPI template. For this preprocessing, the mean PSNR as defined in Section 13.1 according to the equation 13.1 for all GFAP-stained images shows an increase from 12 dB to 17 dB after applying the algorithm 12.
The residual registration errors $d_{\mathrm{MRRE\_Histology\_Atlas}}$ after applying the registration workflow as described in Section 15.2 according to the equation 9.17 are summarized in Table 15.2.

Mouse	$d_{\mathrm{MRRE\_Histology\_Atlas}}$ [μm]
B6: 0 Gy	92
B6: 45 Gy	89
B6: 65 Gy	98
B6: 85 Gy	137
C3H: 0 Gy	122
C3H: 40 Gy	154
C3H: 60 Gy	142
C3H: 80 Gy	127

Tab. 15.2: The residual landmark-based registration error $d_{\mathrm{MRRE\_Histology\_Atlas}}$ for each mouse according to equation 9.17.

An exemplary 2D view of a final fully reconstructed Histology-Atlas registration is shown in Figure 15.3.

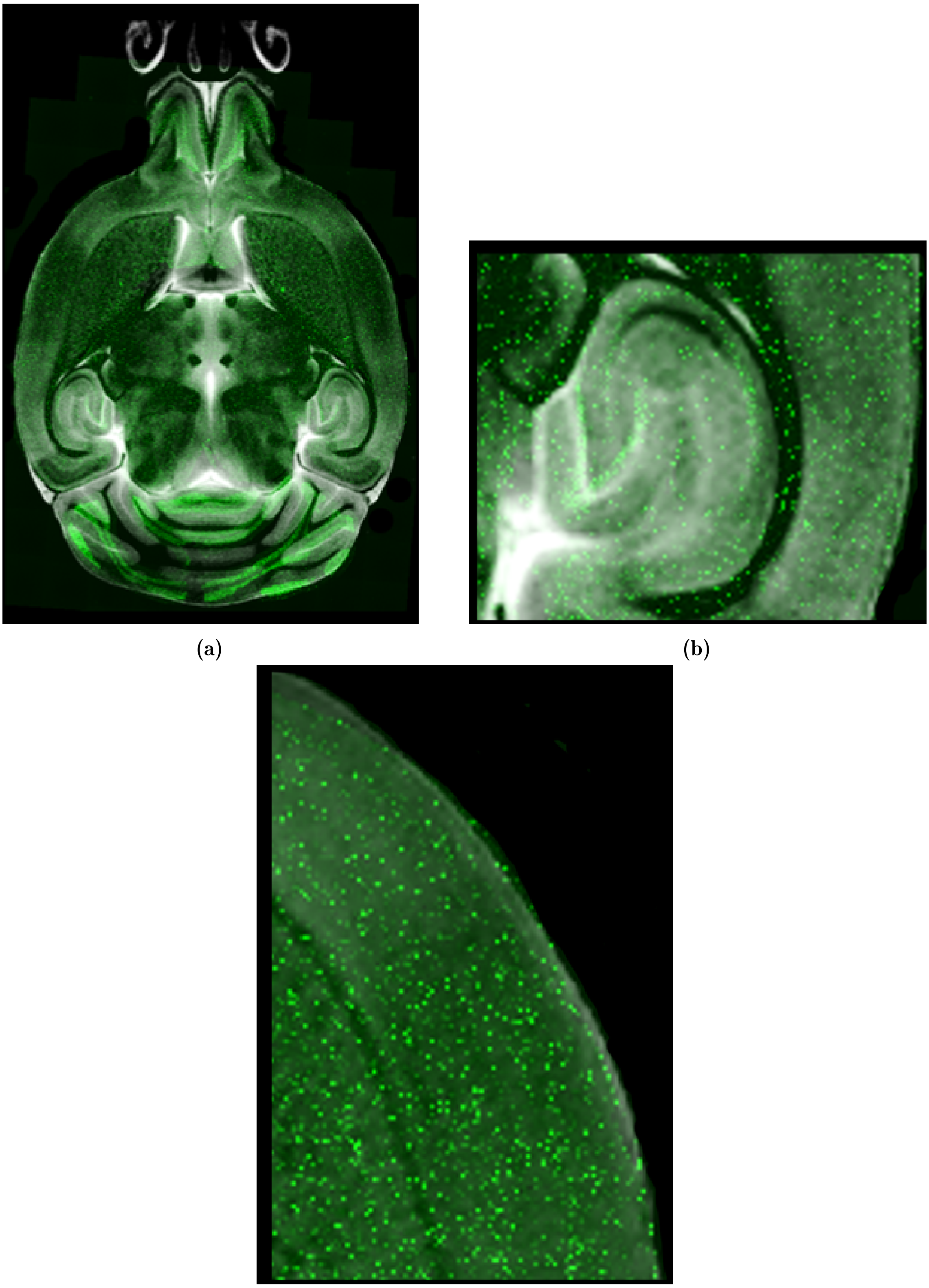

(a)

(b)

(c)

Fig. 15.3: An exemplary 2D view of a final full reconstructed Histology-Atlas registration. The subfigure 15.3a shows the brain slice as a whole. The subfigure 15.3b shows the zoom view of the right hippocampus. The subfigure 15.3c displays the zoom view of the right brain edge. Green denotes the DAPI-stained slices. White denotes the MRI-Nissl-DAPI template.

An exemplary restoration process of a DAPI slice using the **Partial-Aligner** is demonstrated in Figure 15.4.

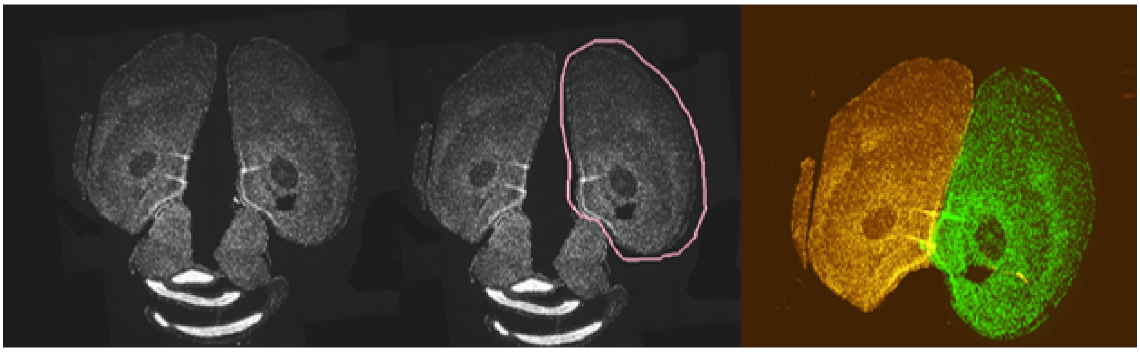

Fig. 15.4: An exemplary restoration process of a DAPI slice using the **Partial-Aligner**. The rose bordered right brain hemisphere defines the region of interest for the **Partial-Aligner**. Orange corresponds to the left hemisphere, which is fixed. Green corresponds to the right hemisphere, which was moved.

In Figure 15.5, an exemplary 2D view of a final Histology-Atlas registration is shown after applying the **Partial-Aligner** to restore the DAPI slice.

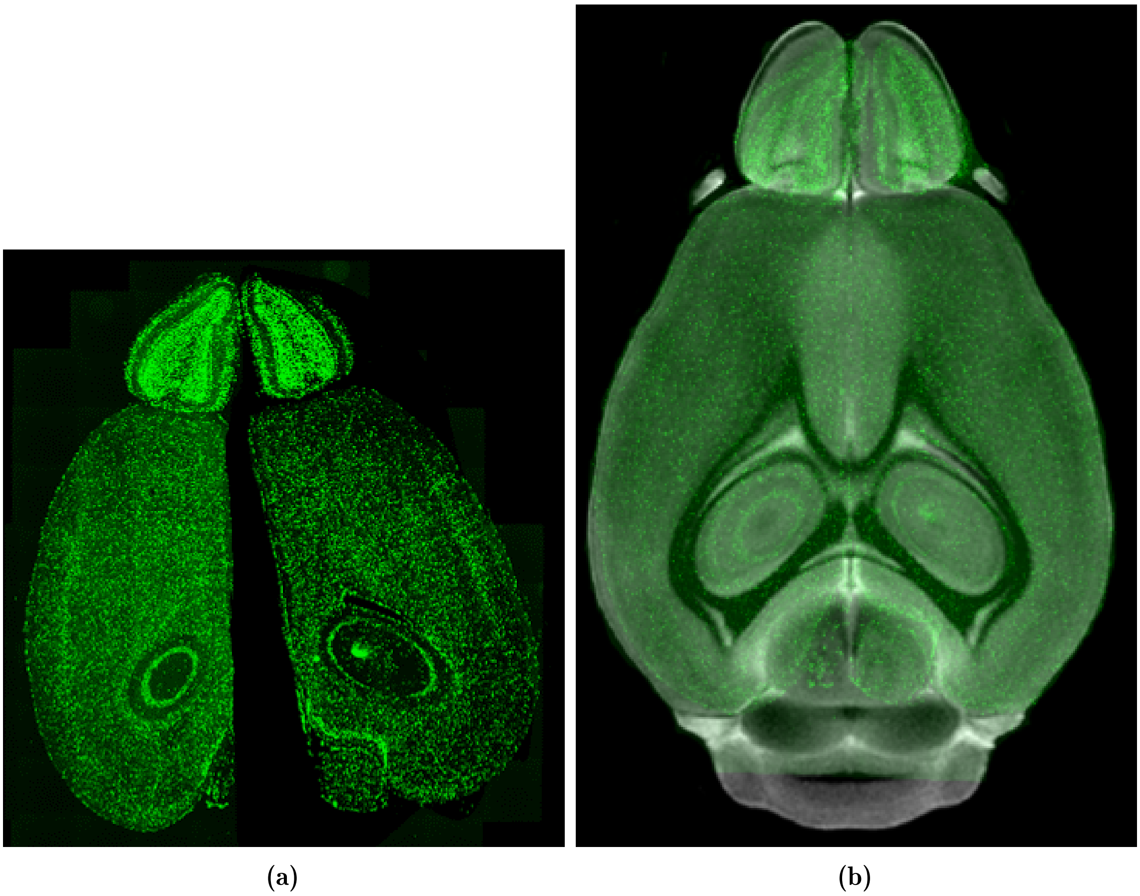
(a)
(b)

Fig. 15.5: An exemplary 2D view of a final Histology-Atlas registration is shown after applying the **Partial-Aligner** to restore DAPI slice. The subfigure 15.5a shows the no-restored brain slice. The subfigure 15.5b shows the restored one registered to the MRI-Nissl-DAPI atlas. Green denotes the DAPI-stained slice. White denotes the MRI-Nissl-DAPI template.

An exemplary 3D view of the final registration of a mouse is displayed in Figure 15.6.

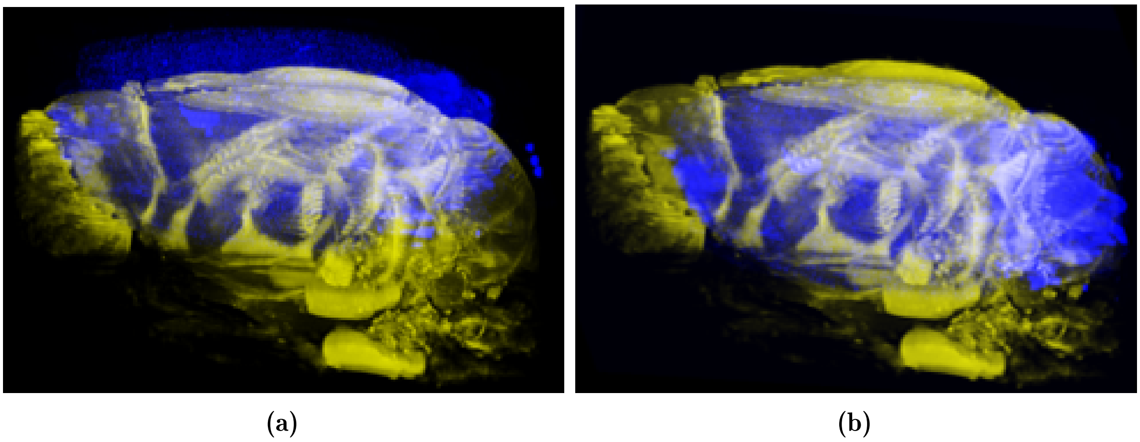
(a)

(b)

Fig. 15.6: An exemplary 3D view of a final Histology-Atlas registration. The subfigure 15.5a shows the unregistered histology (DAPI) and the MRI-Nissl-DAPI template. The subfigure 15.5b shows the registered DAPI slices to the MRI-Nissl-DAPI template. Blue denotes the DAPI-stained slices. Yellow denotes the MRI-Nissl-DAPI template.

The error estimation using landmarks indicates that all mice are registered with an accuracy on the order of 0.1 mm, corresponding to the resolution of the dose and LET distributions.
The total mean registration is 190 μm taking into account the mean registration errors for the registration of the CBCT images and MRI-Nissl-DAPI template determined in Section 15.1 and the residual range shift dose delivery error determined in Section 14.5. This corresponds to a maximum dose uncertainty of $\pm$2.5 Gy and a maximum LET uncertainty of $\pm$2 keV/μm (see Figure 12.2c) according to the resulting shift of the falling edge. In comparison to the statistical uncertainty of the Monte Carlo simulation in section 12.1, this is the dominant uncertainty. In comparison to the statistical uncertainty of the Monte Carlo simulation in section 12.1, this is the dominant uncertainty.

Segmentation

16

16.1 Segmentation of reactive astrocytes

In this section, the results of the segmentation of the reactive astrocytes by training our U-Net model according to the section 10.1 is shown. In addition, it is pointed out how the choice of the loss function and the preprocessing according to Section 7.2 affects the segmentation performance. Furthermore, the outcomes trained with the U-Net architecture are compared with the results obtained by applying a random forest provided by Ilastik or the Otsu's thresholding.

Table 16.1 displays the Dice scores, which measure the overlap between the prediction and the ground truth mask, and the Jaccard index, which measures the ability to identify astrocytes, for each segmentation approach.

Segmentation approaches	Dice score D	Jaccard index J
U-Net (Preprocessed data and loss 10.1)	0.86	0.72
U-Net (Non-preprocessed data and loss 10.1)	0.82	0.70
U-Net (Preprocessed data and loss 10.5)	0.79	0.73
Ilastik (Random Forest)	0.58	0.28
Otsu's method	0.51	0.38

Tab. 16.1: The Dice score measuring the overlap of prediction and ground truth mask and the Jaccard index measuring the ability to identify astrocytes for each segmentation approach.

In Figure 16.1, a sample of the segmented astrocytes resulting from the trained U-Net model with the loss 10.1 and the preprocessed data according to the section 7.2 is shown.

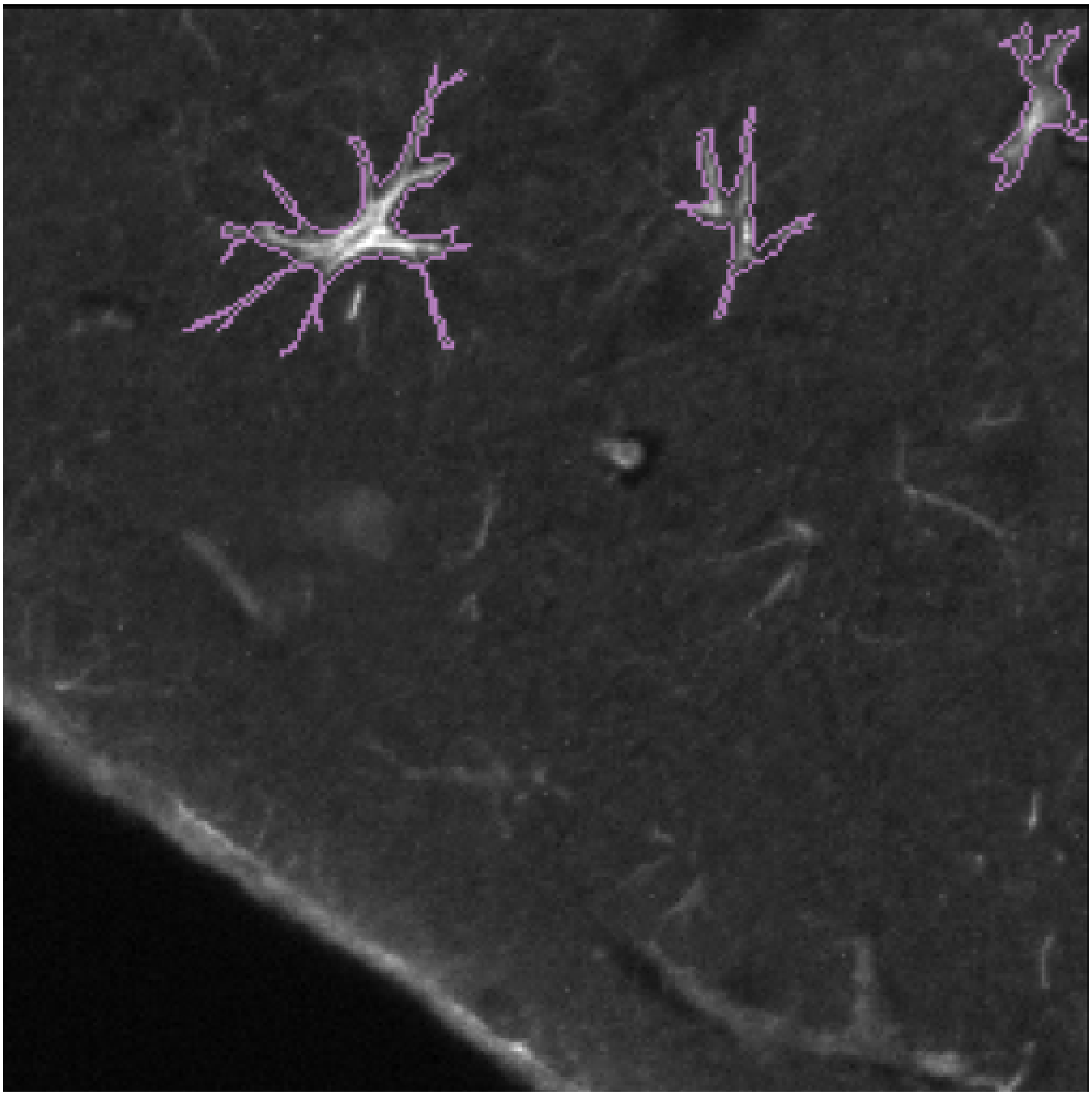

Fig. 16.1: A sample of the segmented astrocytes resulting from the trained U-Net architecture with the loss 10.1 and the preprocessed data according to the section 7.2. The segmented astrocytes are illustrated by by its segmented contour colored by violet.

An overview of the different outcomes concerning the training of the U-Net architecture with loss 10.1 or 10.5, as well as the application of a random forest and the application of Otsu's thresholding, is displayed in Figure 16.2.

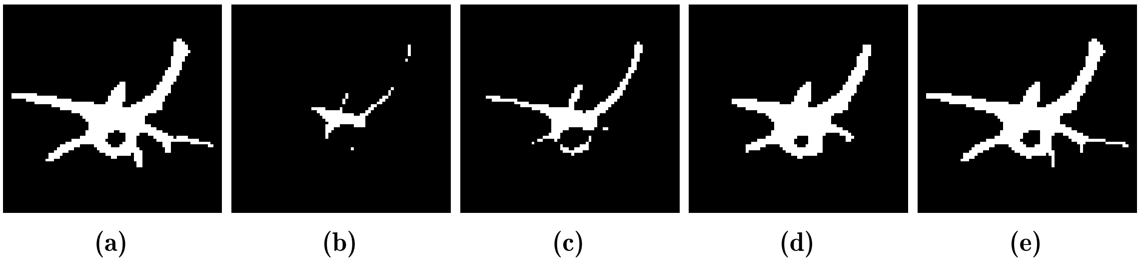
(a) (b) (c) (d) (e)

Fig. 16.2: An overview of the different outcomes concerning the U-Net architecture with loss 10.1 (subfigure 16.2e) and 10.5 (subfigure 16.2d), as well as the application of random forest (subfigure 16.2c) and the application of Otsu's thresholding (subfigure16.2b). The subfigure 16.2a shows the ground truth annotated reactive astrocyte cell.

As can be seen, the choice of loss is important for the preservation of the processes of astrocytes. The choice of loss 10.1 best preserves the morphology of the astrocytes. In addition, it is shown that our histological preprocessing steps to reduce illumination error according to the section 7.2 affect the segmentation result, leading to an increase in the Dice Score of 0.04. Furthermore, all trained U-Net models outperform older machine learning approaches such as random forest as well as traditional methods such as Otsu's thresholding in terms of accurate morphology segmentation and detection of reactive astrocytes. The inter-rater variability of the segmentation among our domain experts, measured by the Dice score D_{var}, is given by 0.92.

17 Analysis

17.1 Analysis of number density of reactive astrocytes

In this section, the number density of astrocytes, defined in cubes according to Section 11.1, is considered as a function of different brain regions, dose and LET. First, the number density defined in 11.1 was viewed axially to examine changes as a function of depth and the resulting curve was compared to the depth dose curve. In addition, the number density depth profile was compared to the product of LET and dose as a predictor of RBE [8].

Figures 17.2 and 17.1 show how the depth profile of the number density of astrocytes defined in 11.1 changes with doses of 40 Gy, 45 Gy, 60 Gy, 65 Gy, 80 Gy, and 85 Gy and the corresponding dose · LET profile for each of the six mice.

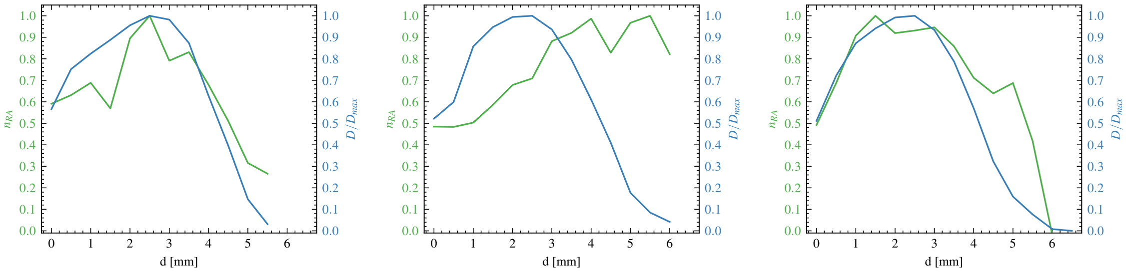

(a) B6 irradiated with 45 Gy **(b)** B6 irradiated with 65 Gy **(c)** B6 irradiated with 85 Gy

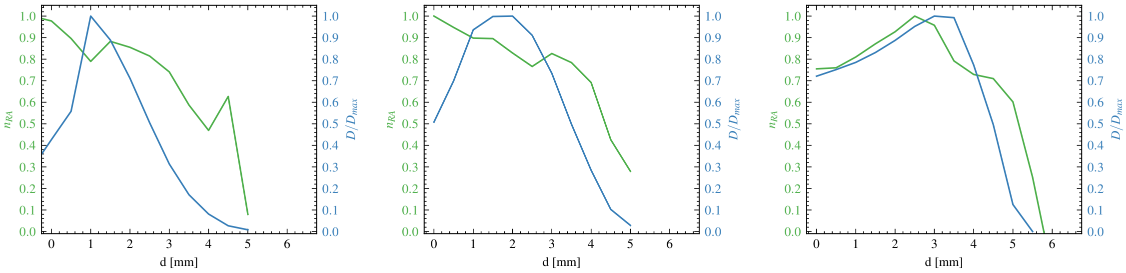

(d) C3H irradiated with 40 Gy **(e)** C3H irradiated with 60 Gy **(f)** C3H irradiated with 80 Gy

Fig. 17.1: The depth profiles for the number density n_{RA} of astrocytes defined by cubes of 0.5 mm and the dose in dependence of the brain depth d. Blue denotes the dose. Green corresponds to the number density.

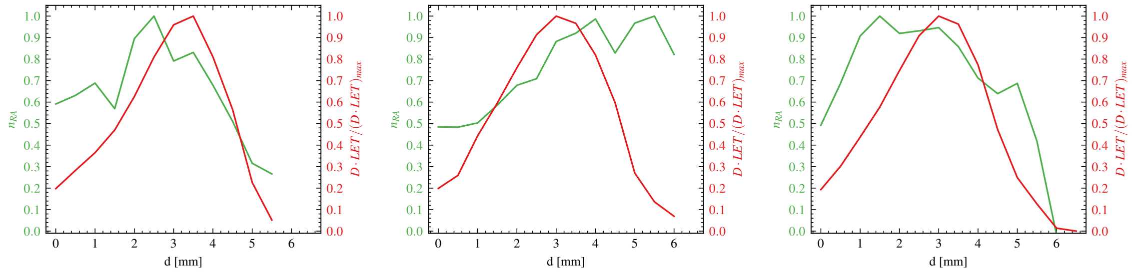

(a) B6 irradiated with 45 Gy **(b)** B6 irradiated with 65 Gy **(c)** B6 irradiated with 85 Gy

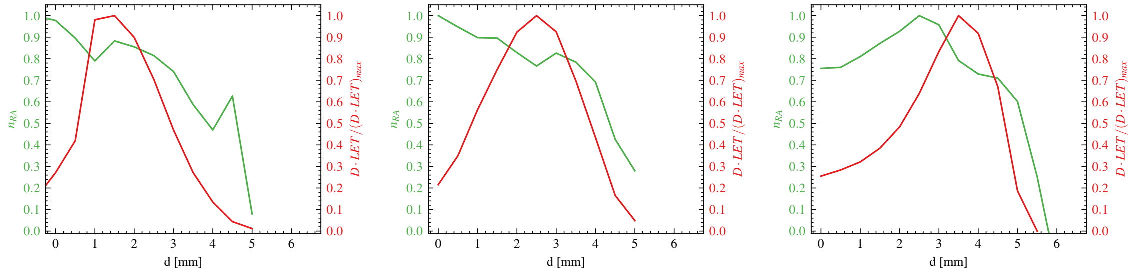

(d) C3H irradiated with 40 Gy **(e)** C3H irradiated with 60 Gy **(f)** C3H irradiated with 80 Gy

Fig. 17.2: The depth profiles for the number density n_{RA} of astrocytes defined by cubes of 0.5 mm and the dose times LET in dependence of the brain depth d. Red denotes the dose times LET profile. Green corresponds to the number density.

The same steps were applied to study the transversal profile (see Figure 17.3). However, the LET is nearly constant transversely. Therefore, no dose times LET transversal profile is shown.

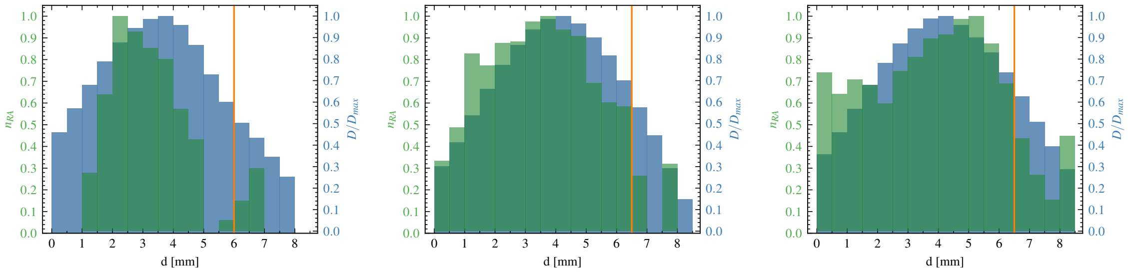

(a) B6 irradiated with 45 Gy **(b)** B6 irradiated with 65 Gy **(c)** B6 irradiated with 85 Gy

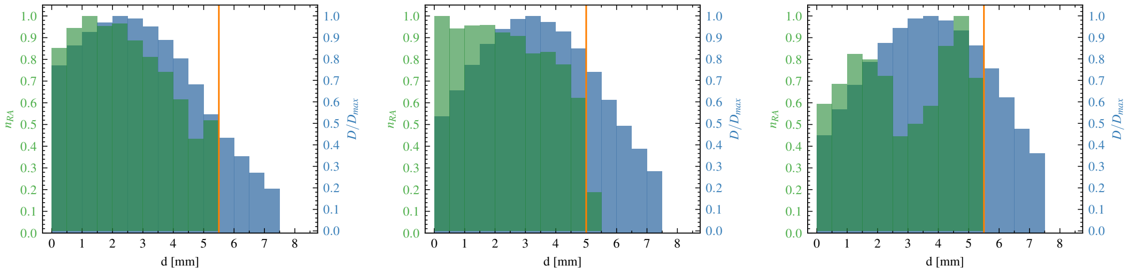

(d) C3H irradiated with 40 Gy **(e)** C3H irradiated with 60 Gy **(f)** C3H irradiated with 80 Gy

Fig. 17.3: The transversal profiles for the number density n_{RA} of astrocytes defined by cubes of 0.5 mm and the dose in dependence of the distance d from the outer edge of the ventricle in the transversal perspective. Blue denotes the dose. Green corresponds to the number density. The orange vertical line highlights the transition from the thalamus to the midbrain.

Considering the number density behavior of each cube as a function of the dose and dose times LET in Figure 17.4, a trend can be observed that the number density correlates with dose and dose times LET.

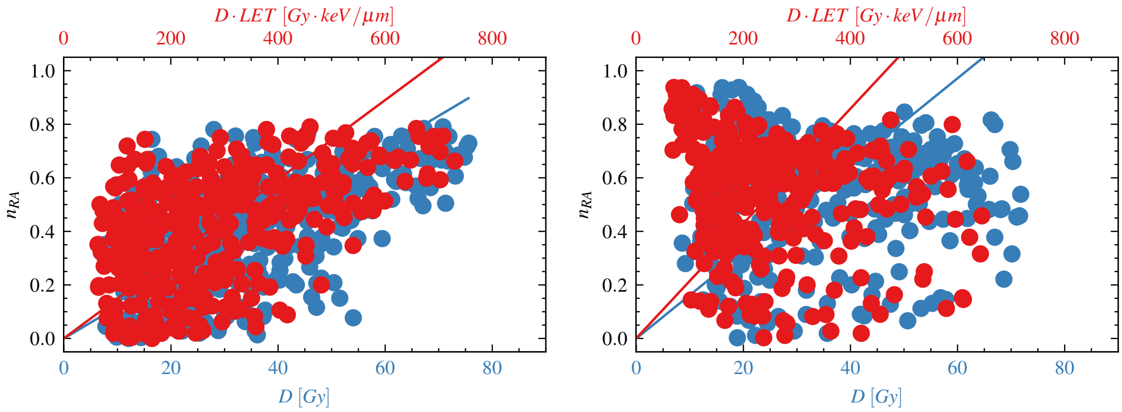

(a) B6 mice **(b)** C3H mice

Fig. 17.4: Scatter plot of number density n_{RA} of each cube in dependence of the Dose as well as Dose · LET

It also reveals that dose times LET may be a better predictor than dose alone. The slopes of the Dose times LET fits are given by $1.088^{+0.087}_{-0.084}$ [1/Gy · keV/μm] for B6 and $1.389^{+0.104}_{-0.102}$ [1/Gy · keV/μm] for C3H, which are larger than the slopes for the dose fits given by $0.903^{+0.073}_{-0.069}$ [1/Gy] for B6 and $1.166^{+0.090}_{-0.086}$ [1/Gy] for C3H. This indicates that the response of astrocytes is more pronounced in C3H than in B6. However, the differences between the two slopes are not significant concerning the 5% significance level. The reported errors are the percentiles matching the standard error of a Gaussian-distributed sample.

Looking at the depth and transverse profiles, the number density shows a complex characteristic: the number density does not follow the pattern of dose and dose times LET. In the depth view, it can be observed that the number density exceeds the dose, but also the dose times LET profile. In addition, increased number density can be observed at the entrance of the brain (see depth profiles in Figure 17.1) as well as near the ventricles (see transversal profile in Figure 17.3) in some C3H mice. The shift of the response to the ventricles can be quantified by the expected value of the transversal profiles.

Table 17.1 shows the mean values of the transversal dose profiles and the number densities of reactive astrocytes n_{RA}. Additionally, Table 17.1 displays the p-values under the null hypothesis that the dose distribution and n_{RA} have the same mean. The Welch t-test [264] was used for this.

Type of mouse irradiated with	$\mu_{\text{Dose}}[mm]$	μ_{RA} [mm]	p_{value}
B6: 45 Gy	3.144	3.029	$5.1 \cdot 10^{-11}$
B6: 65 Gy	3.618	3.361	$3.2 \cdot 10^{-20}$
B6: 85 Gy	3.585	3.433	$2.6 \cdot 10^{-10}$
C3H: 40 Gy	2.621	2.434	$8.9 \cdot 10^{-22}$
C3H: 60 Gy	2.681	2.339	$7.9 \cdot 10^{-75}$
C3H: 80 Gy	3.023	2.836	$4.8 \cdot 10^{-14}$

Tab. 17.1: The means of the transversal dose profiles and the number density profiles displayed in figure 17.3 as well as the p-value for the Welch t-test with the null hypothesis that dose distribution and n_{RA} have the same mean.

As can be seen from Table 17.1, the null hypothesis can be rejected for all considered mean values of dose and n_{RA} concerning a significance level of 5%. Furthermore, an underdensity of astrocytes can be observed in the transversal profiles (see Figure 17.3) at some point despite of the doses of cubes higher than 6 $\text{mm}^{+0.5\text{mm}}_{-0.5\text{mm}}$ for B6 and 5.5 $\text{mm}^{+0.5\text{mm}}_{-0.5\text{mm}}$. This transition point seems to correspond to the brain region transition from the midbrain to the thalamus, as can be easily visually inspected (see Figure 17.5).

In the next section, the results of the number density investigation in the hippocampus, thalamus, and midbrain are shown using 2-point density correlation functions, which were proposed to unravel the complex astrocyte occurrence pattern, to pursue the issue of tissue-specific astrocyte response in full 3D and not only based on the projected 1D depth and transversal perspective.

(a) Midbrain **(b)** Transition **(c)** Thalamus

Fig. 17.5: An exemplary image tiles of the distribution of reactive astrocytes, which were exposed to equal dose (67 Gy) and LET (7 keV/μm) in the midbrain, at the transition from the midbrain to the thalamus and in the thalamus. Subfigure 17.5a shows the distribution of reactive astrocytes in the midbrain. Subfigure 17.5b displays the distribution of reactive astrocytes at the transition between the midbrain and the thalamus, where the transition is characterized by the red line. Subfigure 17.5c corresponds to the distribution of reactive astrocytes in the thalamus.

17.2 Analysis of reactive astrocytes using correlation functions

As described previously, the distribution of astrocytes in the mouse brain after proton irradiation shows a complex pattern. To bring light into the darkness, 2-point density correlation functions ξ are defined for the hippocampus, thalamus, and midbrain according to Section 11.2. This factor indicates how the astrocytes are clustered in the sample. In other words, it reflects the probability of finding another astrocyte δP in a small element of volume δV at a distance r given by the formula

$$\delta P = (1 + \xi(r))\delta V. \tag{17.1}$$

For each tissue type, the low-dose region (0-30 Gy) and the high-dose region (>60 Gy) were considered, where astrocytes were exposed to the same LET ±2 keV/μm less than 10 keV/μm. The thresholds for the low-dose and high-dose regions were chosen so that the probability of complications in normal tissue is zero and close to one, respectively. The LET threshold was defined according to the International Commission on Radiological Protection (ICRP 60 [207]), which states that the RBE does not depend on LET less than 10 keV/μm. Figure 17.6 shows the results for the thalamus in the low-dose region and high-dose region exposing low LET. Results for the hippocampus and midbrain are shown in Figure 17.7 and Figure 17.8, respectively.

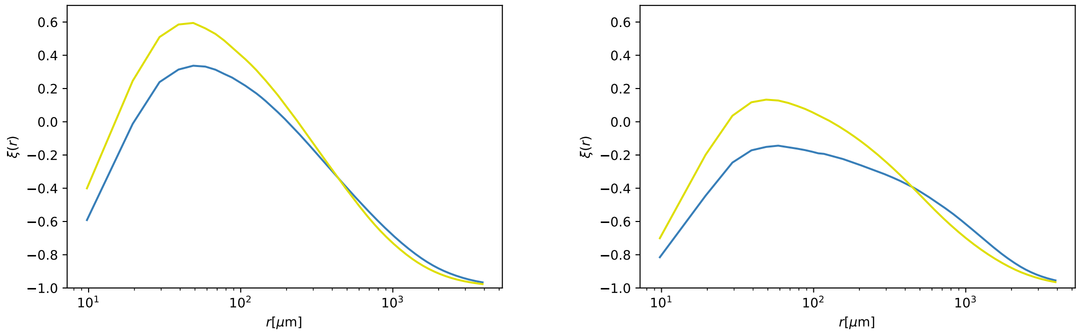

(a) B6 mice **(b)** C3H mice

Fig. 17.6: The 2−point density correlation functions ξ as a function of distance r for reactive astrocytes in the thalamus exposed to low doses less than 30 Gy (marked in blue) and high doses greater than 60 Gy (marked in yellow) with LET less than 10 keV/μm.

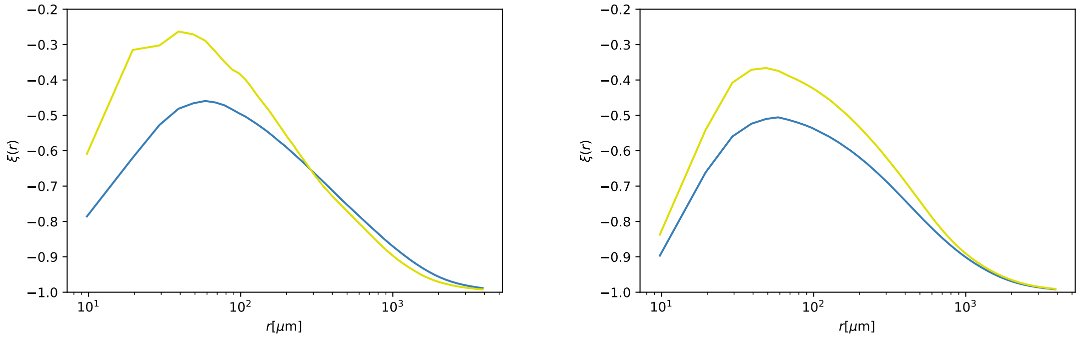

(a) B6 mice **(b)** C3H mice

Fig. 17.7: The 2−point density correlation functions ξ as a function of distance r for reactive astrocytes in the hippocampus exposed to low doses less than 30 Gy (marked in blue) and high doses greater than 60 Gy (marked in yellow) with LET less than 10 keV/μm.

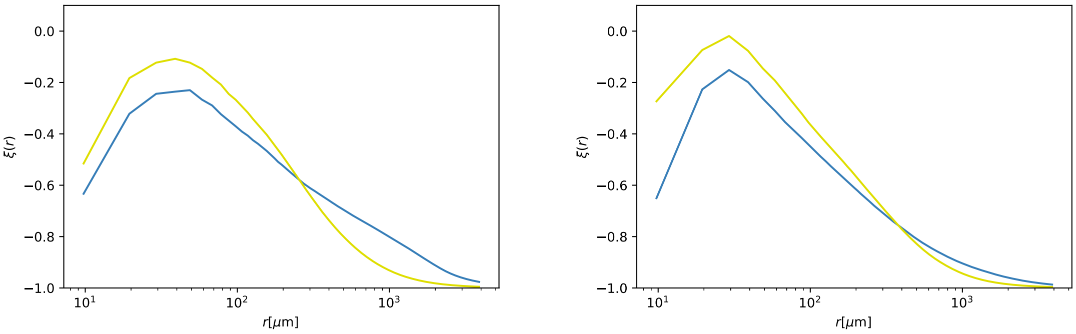

(a) B6 mice **(b)** C3H mice

Fig. 17.8: The 2−point density correlation functions ξ as a function of distance r for reactive astrocytes in the midbrain exposed to low doses less than 30 Gy (marked by blue) and high doses greater than 60 Gy (marked by yellow) with LET less than 10 keV/μm.

The figures reveal a clustering process with higher doses independent of the considered brain region determined by the maximum of $\xi(r)$, ξ_{max}. The maximum density correlation increase ξ_{max} for each brain region is summarized in Table 17.2.

Brain regions	$\xi_{\text{max, low doses}}$	$\xi_{\text{max, high doses}}$	$\xi_{\text{max, high doses}} - \xi_{\text{max, low doses}}$
B6: Hippocampus	-0.46	-0.26	0.20
C3H: Hippocampus	-0.51	-0.37	0.14
B6: Midbrain	-0.23	-0.11	0.12
C3H: Midbrain	-0.15	-0.02	0.13
B6: Thalamus	0.34	0.60	0.26
C3H: Thalamus	-0.14	0.13	0.27

Tab. 17.2: Values of the maximum density correlation ξ_{max} and its increase with higher doses for the brain regions hippocampus, thalamus and midbrain.

For the thalamus, astrocytes were considered to be exposed to LET less than 10 keV/μm before the Bragg peak and greater than 10 keV/μm after the Bragg peak at the same doses with an accuracy of ±2.5 Gy in the low-dose region (0-30 Gy). Figure 17.9 shows the corresponding 2-point density correlation function.

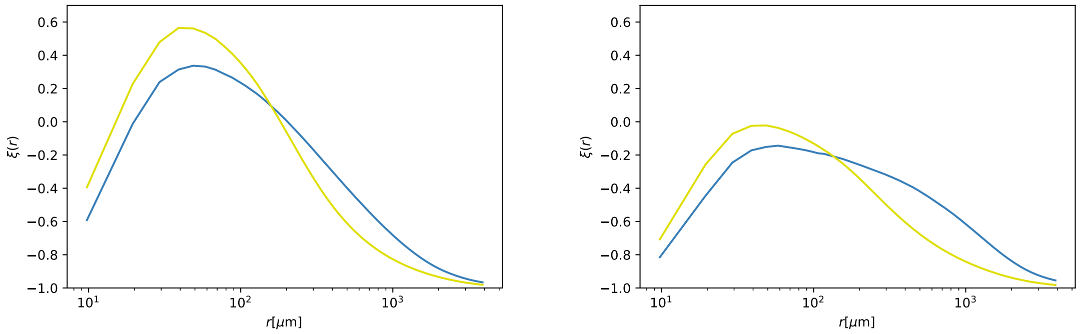

(a) B6 mice **(b)** C3H mice

Fig. 17.9: The 2−point correlation functions ξ as a function of distance r for reactive astrocytes in the thalamus exposed to LET less than 10 keV/μm (marked in blue) and LET greater than 10 keV/μm (marked in yellow) with doses less than 30 Gy.

The Figure also reveals a clustering process for LET larger than 10 keV/μm. However, the effect is not as pronounced as the effect of increased dose. The increase in maximum density correlation is 0.23 for B6 and 0.12 for C3H compared to 0.26 for B6 and 0.27 for C3H for high-dose regions.

To test whether the 2-point density correlation profiles ξ for different doses, LET, and brain regions did not originate from the same distribution, the Kolmogorov-Smirnow test [82] was performed. This test is a statistical test of the equality of two distributions (null hypothesis). Table 17.3 displays the corresponding p-values.

Type of ξ	p_{value}
ξ for low and high doses in the hippocampus of B6	$6.0 \cdot 10^{-29}$
ξ for low and high doses in the hippocampus of C3H	$4.8 \cdot 10^{-5}$
ξ for low and high doses in the midbrain of B6	$6.5 \cdot 10^{-35}$
ξ for low and high doses in the midbrain of C3H	$8.5 \cdot 10^{-19}$
ξ for low and high doses in the thalamus of B6	$6.1 \cdot 10^{-21}$
ξ for low and high doses in the thalamus of C3H	$1.5 \cdot 10^{-33}$
ξ for low and high LET in the thalamus of B6	$3.2 \cdot 10^{-69}$
ξ for low and high LET in the thalamus of C3H	$6.6 \cdot 10^{-119}$

Tab. 17.3: The p-value for the Kolmogorov-Smirnow test to test the equality of the 2-point density correlation profiles ξ for different doses, LET, and brain regions.

As can be seen, the null hypothesis can be rejected for each 2-point density correlation profile ξ for all considered doses, LET, and brain regions concerning the 5% significance level.

In Figure 17.10, samples of the same dose ±2.5 Gy and LET ±1 keV/μm are compared for the brain regions hippocampus, thalamus, and midbrain.

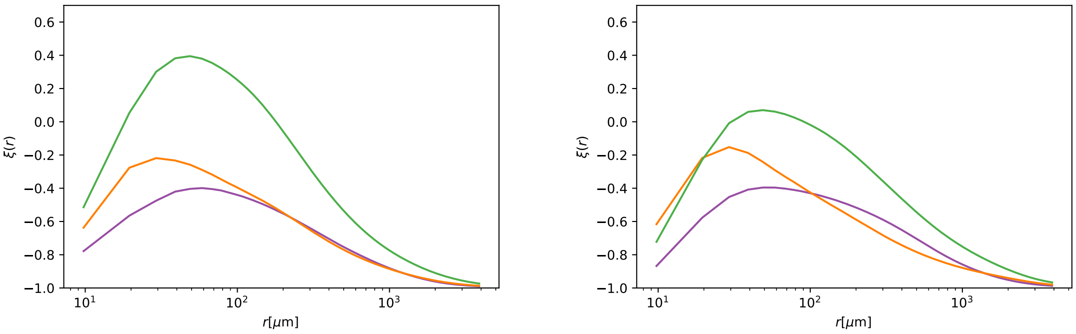

(a) B6 mice

(b) C3H mice

Fig. 17.10: The 2−point density correlation functions ξ as a function of the distance r for reactive astrocytes in the hippocampus (purple), midbrain (red), and thalamus (green), exposed to the same dose and LET.

As can be seen, the 2-point density correlation function ξ is much higher for the thalamus compared to the midbrain and hippocampus. It also shows that the hippocampal response is higher than the midbrain response. The respective maxima of $\xi(r)$, ξ_{max} and their increment are shown in Table 17.4. Table 17.5 shows the corresponding p-values for the null hypothesis that the 2-point density correlation functions follows the same distribution as tested by the Kolmogorov-Smirnow test.

Brain areas (type 1, type 2)	$\xi_{\text{max, type}_1}$	$\xi_{\text{max, type}_2}$	$\xi_{\text{max, type}_1} - \xi_{\text{max, type}_2}$
B6: (Thalamus, Hippocampus)	0.39	-0.40	0.79
C3H: (Thalamus, Hippocampus)	0.07	-0.40	0.47
B6: (Thalamus, Midbrain)	0.39	-0.22	0.61
C3H: (Thalamus, Midbrain)	0.07	-0.15	0.22
B6: (Midbrain, Hippocampus)	-0.22	-0.40	0.18
C3H: (Midbrain, Hippocampus)	-0.15	-0.40	0.25

Tab. 17.4: The values of the maximum density correlation ξ_{max} and their increment with higher doses for the brain regions hippocampus, thalamus, and midbrain.

Brain areas (type 1, type 2)	p_{value}
B6: (Thalamus, Hippocampus)	$9.6 \cdot 10^{-3}$
C3H: (Thalamus, Hippocampus)	$1.9 \cdot 10^{-12}$
B6: (Thalamus, Midbrain)	$8.9 \cdot 10^{-6}$
C3H: (Thalamus, Midbrain)	$1.3 \cdot 10^{-8}$
B6: (Midbrain, Hippocampus)	$6.1 \cdot 10^{-10}$
C3H: (Midbrain, Hippocampus)	$6.8 \cdot 10^{-23}$

Tab. 17.5: The p-value for the Kolmogorov-Smirnow test to test the equality of two 2-point density correlation profiles ξ.

According to Table 17.5, the null hypothesis can be rejected concerning a significance level of 5%.

Furthermore, a comparison of the maximum density correlation value ξ_{max} shows a more complex picture than the analysis in Section 17.1. For the thalamus, the B6 response is stronger than the C3H response, but vice versa for the midbrain. In addition, it can be seen that the probabilities for all brain regions except the thalamus show an underdensity compared to the corresponding Poisson sampling according to the number density of astrocytes of non-irradiated brain regions.

17.3 Analysis of the morphology of reactive astrocytes

This section presents the results of the morphology analysis described in the section 11.3. First, the results of the shape analysis using the elastic metric are presented and then the results of the investigation of the resizing of astrocyte processes are shown. Figure 17.11 shows an example of the geodesic distance between two shapes defined by the equation 11.8.

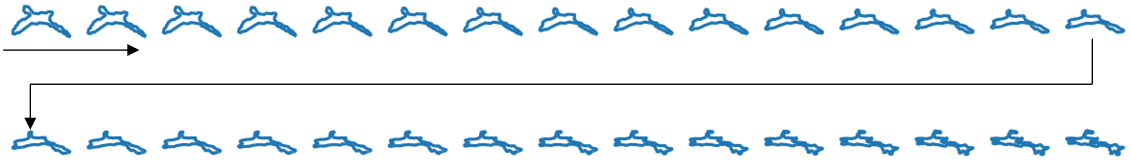

Fig. 17.11: An example of the geodesic distance between the shape of two reactive astrocytes displayed from left to right.

In the same way as in the previous section, the brain regions were distinguished anatomically, dose-dependently and LET-dependently. The Figures 17.12, 17.13, and 17.14 show the corresponding shape distributions measured by the so-called Square Root Velocity metric, given by $\alpha = 1$ and $\beta = 0.25$ in the equation 11.5, which determines the distance between the velocities of the two shapes.

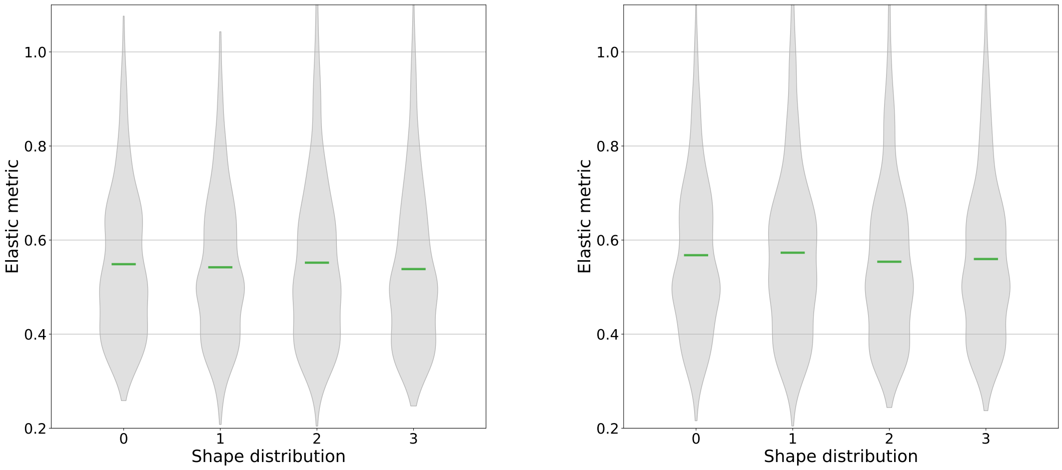

(a) B6 mice

(b) C3H mice

Fig. 17.12: The shape distributions of reactive astrocytes in the thalamus for the two mouse strains B6 (17.12a) and C3H (17.12b) dependent on the dose and LET measured by equation 11.5. The shape distribution labeled by 0 corresponds to the astrocytes in the thalamus, which were not irradiated. The shape distributions (1 and 2) denote the shape distribution of astrocytes exposed to low doses less than 30 Gy (1) and high doses greater than 60 Gy (2) with LET less than 10 keV/μm. Shape distribution 3 corresponds to astrocytes exposed to LET greater than 10 keV/μm with doses less than 30 Gy. The green line marks the mean of the respective shape distribution.

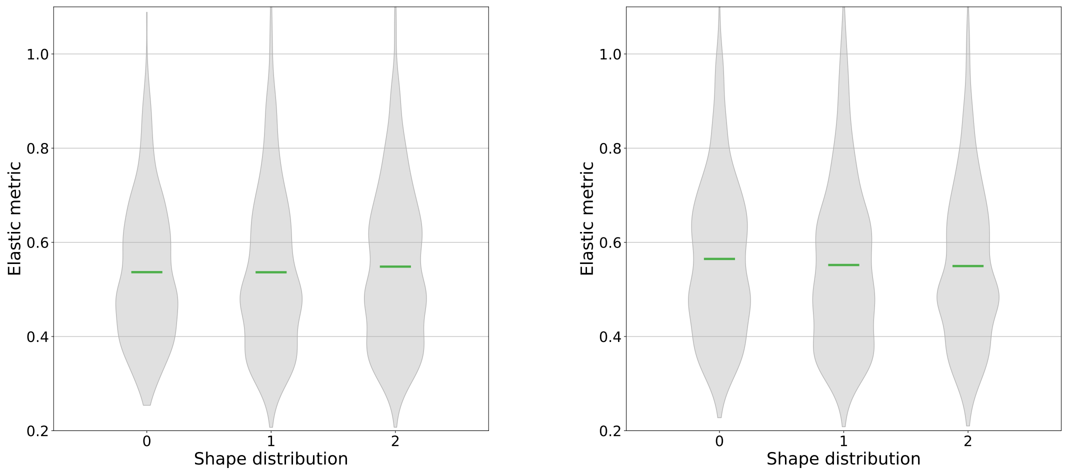

(a) B6 mice

(b) C3H mice

Fig. 17.13: The shape distributions of reactive astrocytes in the midbrain for the two mouse strains B6 (17.13a) and C3H (17.13b) dependent on the dose and LET measured by equation 11.5. The shape distribution labeled by 0 corresponds to the astrocytes in the midbrain, which were not irradiated. The shape distributions (1 and 2) denote the shape distribution of astrocytes exposed to low doses less than 30 Gy (1) and high doses greater than 60 Gy (2) with LET less than 10 keV/μm. The green line marks the mean of the respective shape distribution.

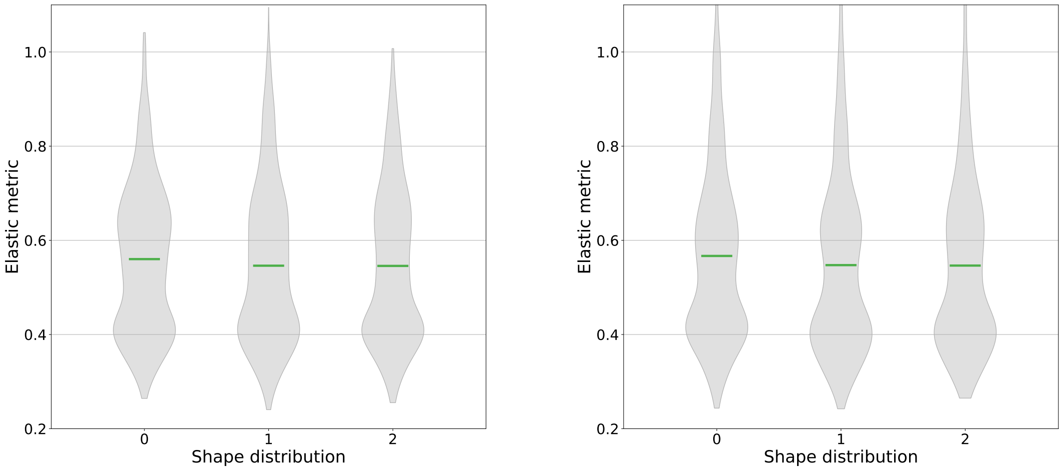

(a) B6 mice **(b)** C3H mice

Fig. 17.14: The shape distributions of reactive astrocytes in the hippocampus for the two mouse strains B6 (17.14a) and C3H (17.14b) dependent on the dose and LET measured by equation 11.5. The shape distribution labeled by 0 corresponds to the astrocytes in the hippocampus, which were not irradiated. The shape distributions (1 and 2) denote the shape distribution of astrocytes exposed to low doses less than 30 Gy (1) and high doses greater than 60 Gy (2) with LET less than 10 keV/μm. The green line marks the mean of the respective shape distribution.

As can be seen, all shape distributions follow a multimodal (bimodal) distribution. In addition, no significant differences between the brain regions themselves as well as between the irradiated and non-irradiated regions can be observed for the two mouse strains B6 and C3H (Welch t-test with a significance level of 5%). However, the form of the shape distribution differs between brain regions slightly. The only significant difference can be observed between the astrocytes of the two mouse strains B6 and C3H in the midbrain (p-value: $8 \cdot 10^{-5}$).
As can be seen in Figures 17.12, 17.13 and 17.14, there are generally no significant shape variations. However, when the size of the processes of astrocytes is considered (see Figures 17.15, 17.16, 17.17 and Table 17.6) , a significant increase in size in response to dose or LET is observed.

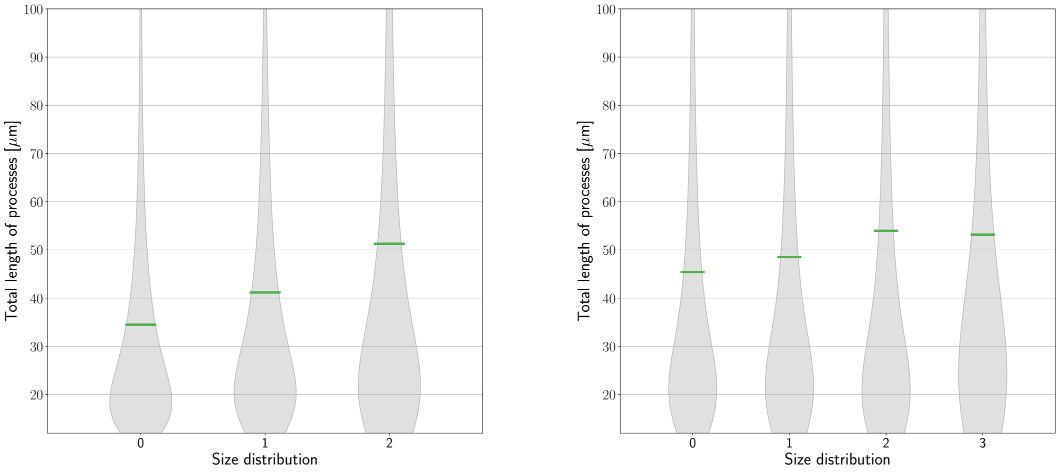

(a) B6 mice **(b)** C3H mice

Fig. 17.15: The size distributions of reactive astrocytes in the thalamus for the two mouse strains B6 (17.15a) and C3H (17.15b) dependent on the dose and LET measured by equation 11.5. The size distribution labeled by 0 corresponds to the astrocytes in the thalamus, which were not irradiated. The size distributions (1 and 2) denote the size distribution of astrocytes exposed to low doses less than 30 Gy (1) and high doses greater than 60 Gy (2) with LET less than 10 keV/μm. Size distribution 3 corresponds to astrocytes exposed to LET greater than 10 keV/μm with doses less than 30 Gy. The green line marks the mean of the respective size distribution.

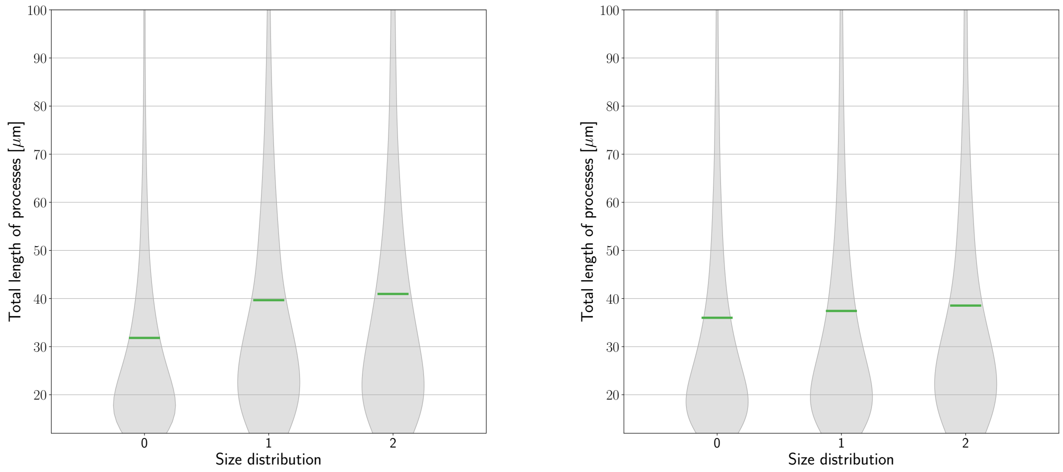

(a) B6 mice

(b) C3H mice

Fig. 17.16: The size distributions of reactive astrocytes in the midbrain for the two mouse strains B6 (17.16a) and C3H (17.16b) dependent on the dose and LET measured by equation 11.5. The size distribution labeled by 0 corresponds to the astrocytes in the midbrain, which were not irradiated. The size distributions (1 and 2) denote the size distribution of astrocytes exposed to low doses less than 30 Gy (1) and high doses greater than 60 Gy (2) with LET less than 10 keV/μm. The green line marks the mean of the respective size distribution.

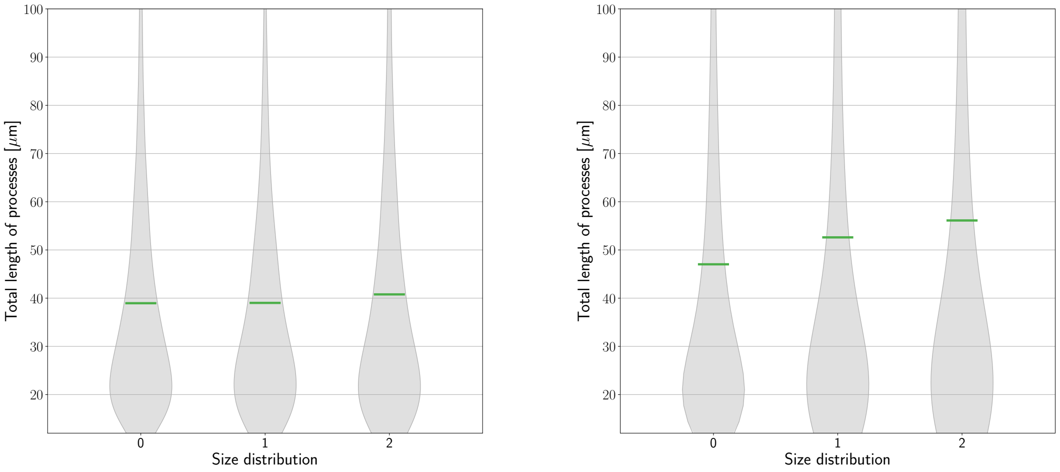

(a) B6 mice

(b) C3H mice

Fig. 17.17: The size distributions of reactive astrocytes in the hippocampus for the two mouse strains B6 (17.17a) and C3H (17.17b) dependent on the dose and LET measured by equation 11.5. The size distribution labeled by 0 corresponds to the astrocytes in the hippocampus, which were not irradiated. The size distributions (1 and 2) denote the size distribution of astrocytes exposed to low doses less than 30 Gy (1) and high doses greater than 60 Gy (2) with LET less than 10 keV/μm. The green line marks the mean of the respective size distribution.

Size Distribution	μ_{size} [μm]	sem_{size} [μm]	p_{value}
B6, Thalamus: 0	34.50	0.19	$2.3 \cdot 10^{-19}$
B6, Thalamus: 1	41.17	0.34	$1.8 \cdot 10^{-64}$
B6, Thalamus: 2	51.31	0.65	$3.1 \cdot 10^{-133}$
B6, Thalamus: 3	45.97	0.34	$1.6 \cdot 10^{-188}$
C3H, Thalamus: 0	45.41	0.27	$7.8 \cdot 10^{-148}$
C3H, Thalamus: 1	48.51	0.51	$6.6 \cdot 10^{-8}$
C3H, Thalamus: 2	53.99	0.42	$4.8 \cdot 10^{-65}$
C3H, Thalamus: 3	51.19	1.26	$8.9 \cdot 10^{-10}$
B6, Midbrain: 0	31.81	0.23	$1.8 \cdot 10^{-103}$
B6, Midbrain: 1	39.66	0.70	$5.0 \cdot 10^{-26}$
B6, Midbrain: 2	40.95	0.72	$7.8 \cdot 10^{-33}$
C3H, Midbrain: 0	36.00	0.24	$1.8 \cdot 10^{-183}$
C3H, Midbrain: 1	37.42	0.33	$4.8 \cdot 10^{-4}$
C3H, Midbrain: 2	38.54	0.75	$1.4 \cdot 10^{-3}$
B6, Hippocampus: 0	38.95	0.24	$2.9 \cdot 10^{-48}$
B6, Hippocampus: 1	39.02	0.38	$8.9 \cdot 10^{-1}$
B6, Hippocampus: 2	40.78	0.39	$6.8 \cdot 10^{-5}$
C3H, Hippocampus: 0	47.02	0.29	$5.0 \cdot 10^{-5}$
C3H, Hippocampus: 1	52.61	0.78	$2.4 \cdot 10^{-11}$
C3H, Hippocampus: 2	56.11	1.02	$1.3 \cdot 10^{-17}$

Tab. 17.6: The mean μ_{size} and the standard error of the mean sem of the size distributions of the reactive astrocytes in the thalamus, midbrain, and hippocampus shown in the Figures 17.15, 17.16, and 17.17. The p_{value} quantify the null hypothesis by the Welch t-test that the mean of the respective considered size distribution of the astrocytes in the irradiated brain region is equal to the mean of the corresponding size distribution of astrocytes in the corresponding non-irradiated brain region. The stated p_{value} for the astrocytes in the non-irradiated thalami refer to the test with the astrocytes in the non-irradiated midbrains. The stated p_{value} for the astrocytes in the non-irradiated midbrains refer to the test with the astrocytes in the non-irradiated hippocampi. The stated p_{value} for the astrocytes in the non-irradiated hippocampi refer to the test with the astrocytes in the non-irradiated thalami.

This dose- or LET-dependent increase in size is significant for all brain regions considered, except for astrocytes in the hippocampus of B6 mice in the low-dose region (0-30 Gy) exposed to LET less than 10 keV/μm. The Welch t-test with a significance level of 5% was performed again to test whether the two samples possess the same mean (see table 17.6). Furthermore, it is observed that astrocytes in the hippocampus (B6: 39 μm, C3H: 47 μm) have the largest mean size of astrocyte processes compared to the thalamus (B6: 35 μm, C3H: 45 μm) and the midbrain (B6: 32 μm, C3H: 36 μm). In addition, the reactive astrocytes of the B6 mouse strain are smaller than those of the C3H mouse strain in all brain regions (Welch t-test, Thalamus: $p_{\text{value}} = 1.5 \cdot 10^{-237}$, midbrain: $p_{\text{value}} = 5.9 \cdot 10^{-36}$, and hippocampus: $p_{\text{value}} = 1.1 \cdot 10^{-101}$).

Part V

& Discussion & Conclusion

Disccusion and Conclusion

18

18.1 Discussion: Monte-Carlo Simulation

For our mouse model it is succeeded to implement a fast and accurate MC simulation in TOPAS MC based on the generation of a phase space file as well as the automatic transformation of the experimental coordinates and the TOPAS coordinate system on top of the raw Monte Carlo simulation of the experimental setup parameters and the dosimetry provided by [31]. Our implementation achieved a computation time of 10^8 of seconds. This short computation time will allow us to perform real-time treatment planning virtually concurrently with upcoming small animal proton irradiations in the future.

The comparison of the raw proton LET with secondary electrons and the LET of all particles reveals that the LET of all particles is higher at the brain entrance due to heavier particles than protons (maximal enhancement: 0.12 keV/μm). However, this is of the same order as the mean statistical error of the LET, 0.16 keV/μm.

In general, the higher relative error of the LET computations ($\sim$ 1 % compared to the maximum) compared to the Dose calculations ($\sim$ 0.1 % compared to the maximum) is caused by spikes in the LET distribution. These spikes are the result of a high-LET cutoff value chosen to score particles with higher LET. This means that particles are produced with a mean path length larger than the voxel size, which leads to these spikes in the LET distributions [73, 76]. To reduce the variance the high-LET cutoff value should be set to lower values resulting in taking into account fewer high-LET particles or a secondary particle production threshold can be set [73]. However, the choice of these values is somewhat arbitrary and requires further investigations. Therefore, a very high LET cutoff was chosen. In general, our result shows a good balance between variance reduction and scoring of high-LET particles. However, our statistical dose uncertainty in dose is below the clinically acceptable statistical uncertainty of 1-2% [65, 68]. Nevertheless, a comparison with Fluka is underway.

18.2 Discussion: Dose delivery quantification

The most accurate approach to animal irradiation studies is 3D image guidance, which is an attempt to reproduce the dose planning results, i.e. the dose is planned first and then delivered as closely to the plan as possible. This was termed as a-priori dose calculation. This type of experiment usually investigates a physiological endpoint, e.g. failure of some organ function [148, 236, 252]. However, at many preclinical proton facilities or experimental beamlines and for experiments with the proton Bragg peak, the preconditions for 3D image guidance are frequently lacking. The experimental setup considered here differs in the definition of the endpoint. The purpose of this experiment is to quantify histological observables in a 3D volume within a single organ with the goal of measuring RBE. Thus, it was postulated that the opposite approach, i.e. irradiate first and then compute the delivered dose, might not be inferior to 3D image guidance. This was termed as a-posteriori dose calculation. The objective of this part was to quantify the contribution of residual setup errors to the dose localization uncertainty of our experiment. Even though the methods were developed for a specific experiment that could only rely on 2D imaging for setup correction, the three key elements of the procedure can be applied in a general setting.

Regardless of the on-beam imaging modality, residual setup errors are difficult to quantify. Hence, a bootstrap was developed and employed that exploits the anatomical similarity of mice of the same strain to generate the otherwise practically inaccessible distributions of setup errors in 6 degrees of freedom (DoF) (Step 1). Subsequently, the impact of these DoFs on the dose localization uncertainty was quantified to identify those DoFs that do not matter for this experimental setup, Thus, both random and systematic errors in these DoFs can be safely neglected (Step 2). For the remaining DoF, dose localization errors were quantified for setup and dosimetric uncertainties, which essentially act as setup errors (Step 3). For this purpose, a 3D-2D matching algorithm was designed. In general, this allows an estimate of the localization uncertainty due to imaging, setup, and irradiation. For our experiment, this uncertainty amounts to 0.1 mm.

Compared to 3D image guidance by CBCT [45, 145, 270], where mouse brains were irradiated with photons, an uncertainty of 0.2 mm was reported. Despite the superior image guidance capability, the uncertainty of our approach is of the same order of magnitude. In [280], CBCT-guided photon irradiation of the entire bone marrow of mice was performed with an accuracy of 1.5 mm. It is likely that our approach will achieve at least a similar accuracy for this type of irradiation due to the rigid structure of bone. In addition, such 3D multimodal systems have shown some advantages, but typical imaging doses are around 0.3 Gy or even higher for micro-CT, which must be taken into account especially for studies of irradiation of normal tissue irradiation [253]. An uncertainty of 0.3 mm was determined for flash proton irradiation of the mouse lung using a 2D image-guided setup over multiple kV X-ray images [175]. Since the rigid structure of the skull provides significant advantages for image registration and positioning without any fine-tuning, it can be assumed that our approach will generate a significantly larger error for this application. However, our approach can be easily extended to process multiple X-ray images to capture the motion of organs such as the lungs, achieving an uncertainty of the same order or better. In [200], proton irradiation of the spinal cord of rats was performed by covering each position of the spinal cord in the spread-out Bragg peak. In [154] induced tumors in the left shoulder of mice were irradiated with protons. For this type of proton irradiation, where the goal is to deliver a homogeneous dose to the entire target, position uncertainty is irrelevant because the problem of the location of the high-LET region does not arise. So a safety margin was simply set to 2mm and 2.5mm respectively. Compared to 2D X-ray image-guided proton irradiation of the rat spinal cord [134], which reported an uncertainty of 0.12 mm, our approach is in the same order of magnitude despite the fact of better positioning of the animals. In addition, our approach achieved the recommended position accuracy of 0.2 mm for small animal experiments in the review [255].

However, the 2D-3D matching algorithm is limited in terms of CT reconstruction kernels and artifacts. Thus, it is important to avoid CT artifacts and reduce the effects of CT reconstruction, which was done by adjusting the X-ray image so that its cumulative histogram matched that of the CBCT image. Further proton range uncertainties may arise from an offset of the alignment of imaging and beam coordinate system, as well as dosimetric uncertainties. The former can result in lateral shifts, which have been shown to be a relevant source of dose positioning uncertainty. This highlights the importance of quality assurance in aligning the isocenters of imaging and irradiation. The latter adds a range uncertainty of ±0.13 mm, as was quantified for our experimental beamline in [31].

In conclusion, the specific results are difficult to generalize, but the developed methods can be generalized. Nevertheless, our approach proves to be adequate for the experiment investigating in vivo RBE and achieves similar quality as alternative 3D methods using CBCT.

18.3 Discussion: Registration

Our approach involves a multi-step registration procedure based on local-affine transformations to assign a dose and a LET value to individual cells. The registration approach encompasses image registration of multimodal images in the form of 3D CBCT images associated with 3D dose and LET distribution to 2D histological fluorescence slices. In general, 3D-2D registration is very challenging because it can easily become ill-posed, especially for deformable registration models [103, 247]. The task is aggravated by the fact that histological fluorescence sections are relatively susceptible to distortions and artifacts related to fixation, mounting, floatation, etc., such as air bubbles, due to the complex preparation and workflow required for fluorescence microscopy [240]. In addition, the information content of fluorescent histological sections is limited to a specific signal provided by the antibody, such as cell nuclei (DAPI) or glial fibrillary acidic protein (GFAP), and does not provide a signal related to specific anatomic soft tissues. Furthermore, CBCT images have comparatively low soft tissue information.

To address this, our approach enables the adjustment and the manual monitoring with a self-developed GUI based on Napari using local-affine transformations. Furthermore, a MRI-Nissl-DAPI template was introduced to divide the registration tasks into two separate tasks: a 3D-3D relatively easy rigid registration of CBCT image and MRI-Nissl-DAPI template as well as a local-affine 3D-2D registration of MRI-Nissl-DAPI template and histology with enhanced available information content. Our registration accuracy of 161μm is comparable to similar approaches using deformable registration models (163μm [174]) or, at first glance, seems to be inferior (56μm [272]). In the following, our results are described in more detail to compare the approaches and to discuss several potential improvements.

Both approaches ([174] and [272]) are based on Nissl stained histology images, which is a classic stain with no fluorescent properties [113]. It was used as the target of the registration procedure. In our approach, this imaging modality is used as an intermediate stage provided by the Allen mouse brain atlas [260] to improve soft tissue information. However, both imaging modalities visualize the same pattern of nuclei [209], but DAPI imaging shows larger ventricles compared to e.g. Nissl staining [229], further increasing the registration uncertainty.

The approach in [272] was evaluated only on simulated slices generated by the Nissl-stained Allen mouse brain atlas [260], without real distortions and artifacts resulting from the experimental preparation and staining procedure. Therefore, it is difficult to compare the results of [272] with our results.

In [174], all three cardinal planes of Nissl-stained histology are used with the goal of creating a MRI-histology atlas. This provides additional useful 3D information and improves registration accuracy, and is well suited for histology template generation, but has no application for the required registration as in our case, where the biological response of a mouse can only be stored in one plane. However, this approach also involves a multi-step registration approach and was evaluated on real data compared to [272]. In contrast to our available MRI and CBCT dataset with a resolution of 100 μm, CT and MR images with higher resolutions (CT: 18.16 μm, MRI: 62.5 μm, isotropic [3]) were used in [174]. Better resolution of MR images and CBCT images may lead to improved registration accuracy. Nevertheless, this also depends on whether there is a significant improvement in the resolution of the equivalent structures in the histology and CBCT/MR images. Nonetheless, this is questionable due to the limited information in the histology. In summary, it turns out that our approach achieves comparable results with only one available plane. However, our approach is semi-automatic, allowing manual feedback loops to compensate for registration uncertainties due to outliers.

In order to further improve the accuracy of the registration, there are generally two ways to proceed.

The first way would be during the experimental cutting process. One option would be to use micro-CT imaging [153] or optical tomography [92, 117, 164] to monitor the cutting process, revealing cutting angles and slice locations. A disadvantage of optical tomography is the longer acquisition time (minutes [164]) compared to CT (seconds [153]). Moreover, it can be used a laser microtome reducing mechanical and thermal side effects [132]. However, a laser microtome is very cost-intensive compared to traditional microtomes due to the required high-power femtosecond laser, which isn't worth it for a few data due to the required high-power laser.

Other options exist on the software side after image acquisition. One approach might be to use more advanced registration models, such as the deformable registration models in [174]. However, deformable registration is rather ambiguous due to the limited anatomical soft tissue information. In other words, due to the high dimensionality of the parameter space, the deformation transformation tends to overfit, producing results without any internal anatomical structure equivalence. Furthermore, deformable transformations are also difficult to explain for physically computed data such as dose and LET distribution, which are not invariant with respect to spatial transformation. Our local-affine transformation approach is limited to affine transformations on a predefined scale corresponding to the internal anatomical structure of the mouse brain, but provides an intermediate interpretable solution for large-scale deformations. In the future, as more data becomes available, Deep learning can be used to automatically detect and select internal anatomical structures of the mouse brain, such as the ventricles.

Another option might be to use a Deep learning model for some steps of the multi-step registration process. For example, the correct cutting angles and slice location can be determined using a Deep learning model. However, it requires a lot of ground truth data, which unfortunately was not available in our case. In [35], this was developed for coronal slices of multiple histological stains. They achieve a median accuracy of 140 μm for predicting the slice location and the two cutting angles according to the Allen mouse brain Nissl atlas ([52, 118, 163, 232, 260]). However, the out-of-the-box application of Deep learning registration approaches to a small amount of self-acquired data is often not so easy to realize, as in this case the modality of the images or the cutting plane is different, and the model is often not generalizable. Adapting or developing a fully automated Deep learning registration approach is usually very time and resource consuming and requires a large data set. Our approach provides an alternative that allows manual correction and monitoring of the entire registration process using our self-developed Napari plugins.

In summary, a mean registration uncertainty of 190 μm was achieved in the order of the resolution of CBCT associated with the dose and LET distribution, including the position uncertainty described in section 14. A higher value of the matching uncertainty, greater than 300 μm, makes it more and more difficult to investigate radiation-induced responses [63], especially at the cellular level. In conclusion, our approach enables the accurate investigation of RBE effects and the modeling of RBE in vivo in 3D at the single cell level..

18.4 Discussion: Segmentation

Our proposed Deep learning model, based on the U-Net architecture, is capable of accurately identifying and segmenting GFAP-stained astrocytes while preserving their topology. It has been observed that our Deep learning model outperforms other machine learning approaches such as Random Forest or non-machine learning approaches such as Thresholding. This is not a new observation. In general, Deep learning models outperform Random Forests and Thresholding methods for computer vision tasks [128, 139, 257] because they provide the ability to automatically learn relevant contextual features from image data through multiple layers, such as convolutional layers at different scales, compared to older approaches that require a lot of manual feature engineering. However, it has been observed that feature engineering in the form of data preprocessing can be beneficial. The model performance of models trained with image artifacts such as the vignetting in our data, as described in section 7.2, is generally lower (preprocessed Dice score: 0.86 vs. non-preprocessed

Dice score: 0.82) because such artifacts have to be additionally learned over multiple layers and the optimization process is influenced by non-relevant features of the data [60, 128, 159]. An additional challenge in general is that required operations such as the median operation do not possess well-defined gradients mathematically [173]. In addition, the influence of the non-relevant features may cause the optimizer to deal with more local minima, increasing the risk of getting stuck in one. Overall, this makes optimization more difficult. Thus, it is a common approach to eliminate these before training, without adding additional learnable parameters during training.

It can also be seen that the performance of the model depends on the choice of a sufficient loss. This is not unexpected and is also shown in related work for other segmentation and classification tasks [54, 85, 91]. In general, the choice of loss depends on the specific task and desired output. Our goal was to preserve the complex, string-star-shaped topology of astrocyte cells as closely as possible. In [214] a loss function was proposed to preserve topology in general, which was demonstrated by applying this loss to the segmentation of roads, retinal vessels, and neurons. Our adapted loss of [214] to segment and identify astrocytes shows a significant segmentation improvement compared to using cross entropy instead. This segmentation improvement, as measured by the Dice score, is 0.07. In contrast to the improvement of about 0.03 in [214] for segmenting neurons, this is a decent improvement. However, the segmentation improvements measured by the Dice score are difficult to compare because the performance of a Deep learning model generally depends on a number of parameters, such as patch size, batch size, training data size, image resolution, preprocessing including data augmentation, and optimizer settings, which differ here. Nevertheless, a general improvement can be observed by using the proposed topology-aware loss function based on the morphological skeletons (see equation 10.1). However, the ability to identify astrocytes remains quite the same when using the proposed topology-aware loss function (the improvement for the identification of astrocytes measured by the Jaccard index: 0.01). This is not surprising since the loss function 10.1 is designed to preserve the topology, but the design does not additionally boost the detection ability to identify astrocytes.

Compared to other Deep learning based approaches for segmentation and detection of GFAP-stained astrocytes [23, 102], our approach offers an alternative approach involving simultaneous segmentation and detection of astrocytes on the whole histological slice to preserve morphology. For example, the proposed U-Net-based model in [102] only performs segmentation of individual astrocytes, which were detected by non-learnable directional filtering as a preprocessing step. Nonetheless, our results are comparable to [102] and achieve even better model performance independent of our choice of loss and preprocessing. The model in [102] achieves a Dice score of 0.76 (our model: 0.79-0.86) for the segmentation of astrocytes and a Jaccard index of 0.67 (our model: 0.70-0.73) for the detection of astrocytes. However, a clear evaluation is not possible here either, since the data used in [102] are not publicly available. Nonetheless, both approaches outperform Random Forest by Ilastik and Otsu's thresholding. This once again confirms the enormous potential of Deep learning approaches compared to previous methods for the segmentation and detection of

astrocytes.
Astrocytes can also be labeled by calcium [279]. The proposed model in [23] is based on the U-Net and Inception-Resnet-v2 modules [234]. They used one model for detection and a separate model for segmentation of astrocytes, which are optimized together. The approach proposed in [23] disjoints an astrocyte into two classes, the somata and processes, instead of one class for an astrocyte in our work. This means that the model is trained on annotated data and designed to predict pixels divided into a total of three classes: somata, processes, and background. The used loss was also the sum of the cross entropy and the Dice score according to the equation 10.5. The model in [23] achieves a similar Dice score of 0.84 for the segmentation of somata and a Jaccard index of 0.74 (our model: 0.70-0.73) for the detection of astrocytes. However, the Dice-Score for the segmentation of processes of astrocytes corresponds to 0.60. This confirmed that the choice of the loss is essential to address the preservation of the topology of astrocytes, especially the processes of astrocytes. Furthermore, this proposed approach also emphasizes that Deep learning approaches generally outperform threshold-based approaches. As already mentioned before, the segmentation improvements measured by the Dice score are difficult to compare again, since both approaches share only a few common features, such as the used loss function.
Overall, further improvement in segmentation and identification of astrocytes is complicated to achieve. The complex morphology of astrocytes leads to an inter-rater variability when performing the annotation (Dice score in our case: $D_{\text{var}} = 0.92$). In general, this can be considered as the limit of the maximum achievable accuracy. A slightly lower inter-rater variability was found on the annotated data of the equal resolution for the soma segmentation of astrocytes in [23]($D_{\text{var}} = 0.89$). This may be a result of the additional task of the annotators to distinguish between the soma and the processes of the astrocytes. Other objects, such as DAPI-stained nuclei, can be segmented with Dice scores of 0.95 and higher due to their straightforward topology [138].
In conclusion, our topology-aware approach is suitable for identifying and segmenting our GFAP-stained astrocytes, and tends to preserve topology with higher accuracy than state-of-the-art Deep learning models, older machine learning techniques, or traditional methods, providing the opportunity to analyze effects such as astrogliosis.

18.5 Discussion: Analysis

Our analysis consists of two parts: the analysis of number density and the analysis of cell morphology as a function of brain region, dose and LET.
The analysis of the number density of reactive astrocytes reveals that there is hidden information concerning LET and RBE effects beyond the pure definition of the scalar number densities in predefined regions such as cubes. The average reduction of the interaction of astrocytes to a simple scalar quantity, such as the number density defined on cubes is not sufficient to disclose effects such as the astrogliosis in its entirety. The choice of a predefined volume size biases the outcomes and adds an

additional subjectively chosen parameter to the analysis. The parameter can be selected according to specified criteria such as in our case that the volume size must be larger than the registration error and must have sufficient statistics.

Nonetheless, small-scale effects caused by dose and LET are averaged out on the predefined scale. In general, it is difficult to capture effects at small scales with this type of number density analysis. It is also prone to introducing noise.

However, to capture large-scale effects such as higher number density of astrocytes in certain brain regions, the analysis by defining number density in cubes of predefined size is sufficient. Compared to the midbrain, astrogliosis was more pronounced in the thalamus. In other words, the thalamus is more radiosensitive concerning the astrogliosis. In other words, the thalamus is more radiosensitive in terms of astrogliosis. In addition, higher astrogliosis was observed near the periventricular region. In general, the observation of brain region-specific RBE effects is not new. Eulitz, et al [59] and Bahn, et al [8]. show increased periventricular sensitivity to radiation-induced brain injuries in proton-treated patients with glioma.

To investigate small-scale effects, the concept of two-point density correlation functions was used as described in Section 17.2. For this purpose, brain regions with either increasing dose or increasing LET were considered. This type of analysis provides access to these small-scale effects associated with dose and LET in addition to the large-scale effects as no additional parameter on the cell level is necessary and no effect of smoothing occurs.

In our work, only the two-point autocorrelation of the location of a cell type was considered. However, this correlation analysis not only allows to study the effects of one cell type on different scales, but also provides an approach to investigate the interaction and correlation of different cell types (density cross-correlations) as well as higher order (three-point density autocorrelation). Furthermore, the analysis is not limited to location and can easily be extended to other quantities such as shape or cell-typical temporal changes. For deeper insights, our adapted estimator 11.3 can be replaced by more advanced estimators [49] to model the control cells as a non-poisson distribution. However, this results in even longer computation times. Another limitation is the assumption of isotropy, which is a reasonable hypothesis for cell depth in the interior of the tissue, but problematic for cells at the boundaries of brain regions. However, the number of cells at the borders is much smaller than the number of cells far from the border. In this work, only a first estimation was performed to show that the calculation of correlation functions is a promising approach that opens a new physical path in the biological description of CNS cells and radiation-induced cell response.

Our analysis using a 2-point density correlation function shows that astrogliosis is dose-dependent with different strengths in brain regions. Thalamus is most clustered (B6: 0.60, C3H: 0.13) compared to midbrain (B6: -0.11, C3H: -0.02) and hippocampus (B6: -0.26, C3H: -0.37) at high doses greater than 60 Gy. In summary, the respective brain regions show different responses at the same dose and LET (Thalamus: 0.39 for B6 and 0.07 for C3H, Midbrain: -0.22 for B6 and -0.15 for C3H, Hippocampus: -0.40 for B6 and -0.40 for C3H). The analysis with cubes was already an indication of this. In general, the variation of the number density of different brain regions was also found in [87]. The radiation-induced astrogliosis associated with increasing doses was also observed in [88, 269] as an early effect in mice and rats with up to a dose of 20 Gy and as a late effect for doses up to 45 Gy in mice [41] after X-ray irradiation as measured by the GFAP fluorescence intensity. However, no dose-dependent early response was found in vitro after X-ray irradiation up to a dose of 8 Gy [194]. Nevertheless, the observation of late radiation-induced astrogliosis after proton irradiation in vivo months ago, which is dose-dependent for high-LET radiation such as protons, is novel. Overall, this indicates that there may also be substantial differences in response between in vivo and in vitro experiments, limiting the translational power of in vitro experiments.

In addition, it was observed that the effect of astrogliosis is enhanced with increasing LET, resulting in a higher proton RBE. The observation of increasing RBE with higher LET for protons and carbon has also been made in vivo for the endpoint radiation-induced myelopathy [200] as well as in vitro [142]. To our knowledge, this is the first observation of increased RBE associated with increased LET on normal brain region responses like astrogliosis. In addition, studying the effects of RBE in normal brain tissue, for example, in terms of astrogliosis, or modeling RBE at the single cell level in vivo in 3D is possible with our analysis pipeline compared to the traditional way of predicting RBE for cancer [266].

Furthermore, it can be observed that the maximum of the 2-point correlation function is located at about 50 μm independent of the dose, LET, or brain region. In other words, astrogliosis also causes maximum accumulation of astrocytes at a fixed scale, but they are not completely clumped together. This can be understood physically as an interaction similar to the dynamics caused by gravity and pressure, with an attractive force that supports clustering and a repulsive force that prevents and counteracts complete clustering. The result is that there is no overlap of astrocytes, which is also visually observable in our data. The non-overlapping behavior of reactive astrocytes was also described in [44, 221]. This behavior is also known as astrocyte tiling. one hypothesis is that astrocyte tiling is caused by the contact inhibition of astrocytes [51]. This means that the process of segregation is generated by physical cell-cell interactions that cause movement in the opposite direction. Nevertheless, quantitative descriptions as in our work have not yet been established, confirming the observation. However, the underlying mechanisms are still not understood until today [12]. Another way to explain this could be that cells such as astrocytes should be understood not only as individually acting cells, but also as cells acting as a physical functional unit with a higher-level organization in the central nervous system, possessing information beyond the individual cells [244], as proposed in [4]. Another indication is that this shown non-overlapping property of astrocytes can break as observed for epilepsy [221]. However, this was not observed for the radiation-induced astrogliosis in our data. In general, the observed complex response of astrocytes indicates that the picture of individually acting cells should be rethought. Furthermore, it was observed that the response in B6 is stronger than the response in C3H for the thalamus and hippocampus, but vice versa for the midbrain.

A clear general relation can not be deduced.

To quantify how astrogliosis changes the morphology of astrocytes, bending and stretching of the shape was measured with the so-called square velocity metric. This metric allows to compare two shapes independent of the size and reparametrization [74]. In addition, the total length of each astrocyte was measured to examine changes in size. The analysis was separated into shape and size analysis to investigate which dominates the morphology changes. The shape analysis shows that there are no significant differences in astrocytes among brain regions as well as between irradiated brain regions and non-irradiated brain regions in general. The only significant difference concerning the mean is observed between the astrocytes of the two mouse strains B6 and C3H in the midbrain. One reason for this observation may be that the sample size in the midbrain is relatively small, as shown by the number density analysis, which gives more weight to the shape outlier. One reason for the lack of significant shape changes induced by radiation may be that the astrocytic morphology of mice is substantially less complex than in humans [87] making differences more difficult to measure. Nevertheless, the form of the shape distribution differs slightly between brain regions. All in all, it seems that the shape is generally unaffected by radiation. In contrast to the shape analysis, the size analysis based on the measurement of the total length of the processes shows significant differences as a function of brain region, dose, and LET. In general, an increased size of processes of an astrocyte enables the astrocyte to communicate, operate, and react on a larger scale using neurotransmitters [44]. Increasing astrocyte size, as measured by the total length of processes, was observed with higher doses in all considered brain regions examined. Dose-dependent morphological changes were also reported by He, et al. [81] and Hwang, et al. [88] for X-ray irradiation of the mice and rats with a single dose of 50 Gy and 15 Gy, respectively. However, no quantitative approach has been developed to investigate radiation-induced morphological changes until now. In particular, the response to high-LET particle radiation has not been studied.

Furthermore, a LET-dependent increase in size was observed, confirming an increased RBE in addition to the observed increase in astrocyte density (LET enhancement of B6 mice: 11.53 μm, LET enhancement of C3H mice: 5.68 μm). In general, astrocytes in the hippocampus (B6: 39 μm, C3H: 47 μm) have the largest mean size of processes compared to the thalamus (B6: 35 μm, C3H: 45 μm) and the midbrain (B6: 32 μm, C3H: 36 μm). As shown the astrocytes of the B6 mouse strain are smaller than the astrocytes of the C3H mouse strain in total. This is somewhat surprising because it was found a higher response in terms of higher density of astrocytes in B6 compared to C3H conversely. However, this can be understood again if the astrocytes are considered as a functional unit that strives to maintain the segregation of astrocytes known as astrocyte tiling.

In summary, morphological changes between different brain regions were also described qualitatively in [7, 178, 251]. Nevertheless, quantitative approaches to discriminate between shape and size, as in our work to investigate whether morphological changes are caused by shape or size changes, have not yet been established. This approach shows that radiation-induced morphological changes are mainly dom-

inated by an increase in the length of astrocyte processes and not by bending or stretching. In summary, our approach provides a robust estimator of morphology changes for cells with processes such as astrocytes. This provides additional ansatz to investigate changes in the morphology of cells such as astrocytes in general.
Overall, a complex response of astrocytes of the CNS depending on brain region, dose and LET was found, revealing a non-trivial RBE. Our results demonstrate that cells of the central nervous system, such as astrocytes, behave more like a dynamic, self-organizing, functional physical system than a mere collection of individually acting cells. Furthermore, our results provide additional motivation for the establishment of MR-guided particle radiotherapy due to the brain-specific radiosensitivity observed for emerging astrogliosis. However, more data are needed to confirm our observations and to gain new insights into radiation-induced responses in general.
In conclusion, our proposed analysis is able to reveal cellular changes associated with the enhancement of astrogliosis as shown, but the analysis can easily be used for further investigations to correlate physiological effects with underlying cellular processes in the future beyond radiotherapy.

18.6 Conclusion

The aim of this work was to better understand the altered cellular processes and potential RBE effects at the cellular level of normal brain tissue after proton irradiation, which may lead to radiation injury such as necrosis. For this purpose, an end-to-end pipeline was developed to examine the dose and LET response to proton irradiation at the single cell level in vivo. With this proposed end-to-end pipeline, it is possible to analyze cell responses of normal tissues in vivo with a high accuracy allowing the investigation of clinically relevant RBE effects for proton irradiation.
The pipeline consists of five modules in total to investigate correlations of number density and morphology of cells with received dose and LET:
Monte Carlo simulation, dose delivery quantification, registration, segmentation, and analysis.
Applying the pipeline to a mouse model mimicking the proton irradiation of the human brain reveals that astrogliosis caused by proton irradiation is a complex response depending on the brain region, dose, and LET, indicating non-trivial RBE for proton irradiation.

Part VI

Appendix

List of Acronyms 153

Publications 155

Bibliography 157

List of Figures 185

List of Tables 188

19

List of Acronyms

2D	Two-dimensional
3D	Three-dimensional
CT	Computed tomography
CBCT	Cone-beam computed tomography
DRR	Digitally reconstructed radiograph
PSNR	Peak signal-to-noise ratio
MSE	Mean square error
DAPI	4′,6-Diamidin-2-phenylindol
GFAP	Glial fibrillary acidic protein
DNA	Deoxyribonucleic acid
DSB	Double-strand breaks
TCP	Tumor complication probability
NTCP	Normal tissue complication probability
CNS	Central nervous system
DoF	Degree of freedom
MR	Magnetic resonance
MRI	Magnetic resonance imaging
RF	Radiofrequency
NMR	Nuclear magnetic resonance
MC	Monte Carlo
CNN	Convolutional neural network
GPU	Graphics processing unit
CPU	Central processing unit
ReLU	Rectified Linear Unit
DICOM	Digital Imaging and Communications in Medicine
NIfTI	Neuroimaging Informatics Technology Initiative

ROI	Region of interest
GUI	Graphical user interface
LET	Linear energy transfer
RBE	Relative biological effectiveness
PMMA	Polymethylmethacrylat
PC	Polycarbonat
HLUT	Hounsfield look-up table
NCC	Normalized Correlation Coefficient
MI	Mutual Information
SGD	Stochastic Gradient descent method
ICRP	International Commission on Radiological Protection

Publications

20

20.1 Peer-Reviewed articles

- **Boucsein M**, Koch R, Suckert T, Nexiphi S, Beyreuther E, Alber M, Lühr A, Dietrich A, Bahn E. Quantifica-tion of dose delivery accuracy for small animal proton brain irradiation. submitted to Physics and Imaging in Radiation Oncology. 2023.
- Koch RA, **Boucsein M**, Brons S, Alber M, Bahn E. A time-resolved clonogenic assay for improved cell survival and RBE measurements. Clin Transl Radiat Oncol. 2023 Sep;42:100662.
- Soltwedel J, Suckert T, Beyreuther E, Schneider M, **Boucsein M**, Bodenstein E, Nexhipi S, Stolz-Kieslich L, Krause M, von Neubeck C, Haase R, Lühr A, Dietrich A. Slice2Volume: Fusion of multimodal medical imag-ing and light microscopy data of irradiation-injured brain tissue in 3D. Radiother Oncol. 2023 Feb 28;182:109591. doi: 10.1016/j.radonc.2023.109591.

20.2 Oral presentation at conferences

- **Particle Therapy Co-Operative Group (PTGOG 60, Miami)**:
  "A multimodal 3D image registration toolkit to investigate proton radiation-induced brain injury"
- **European Society Radiation Oncology (ESTRO 2020, Madrid)**:
  "CT-less 3D image guidance for high-precision small animal particle irradiation"
- **29. Symposium für Experimentelle Strahlentherapie und Klinische Strahlenbiologie**:
  "A framework for CT-less 3D image guidance for high precision small animal particle irradiation"

Bibliography

[1] N. J. Abbott, L. Rönnbäck, and E. Hansson. “Astrocyte–endothelial interactions at the blood–brain barrier”. In: *Nature Reviews Neuroscience* 7.1, Jan. 2006. Number: 1 Publisher: Nature Publishing Group, pages 41–53. ISSN: 1471-0048. DOI: 10.1038/nrn1824.

[2] C. C. Aggarwal. *Neural Networks and Deep Learning: A Textbook*. Cham: Springer International Publishing, 2018. ISBN: 978-3-319-94462-3 978-3-319-94463-0. DOI: 10.1007/978-3-319-94463-0.

[3] M. Aggarwal, J. Zhang, M. I. Miller, R. L. Sidman, and S. Mori. “Magnetic Resonance Imaging and Micro-Computed Tomography Combined Atlas of Developing and Adult Mouse Brains for Stereotaxic Surgery”. In: *Neuroscience* 162.4, Sept. 15, 2009, pages 1339–1350. ISSN: 0306-4522. DOI: 10.1016/j.neuroscience.2009.05.070.

[4] M. Alber and C. Belka. “A normal tissue dose response model of dynamic repair processes”. In: *Physics in Medicine & Biology* 51.1, Dec. 2005, page 153. ISSN: 0031-9155. DOI: 10.1088/0031-9155/51/1/012.

[5] F. S. Ali, O. Arevalo, S. Zorofchian, A. Patrizz, R. Riascos, N. Tandon, A. Blanco, L. Y. Ballester, and Y. Esquenazi. “Cerebral Radiation Necrosis: Incidence, Pathogenesis, Diagnostic Challenges, and Future Opportunities”. In: *Current Oncology Reports* 21.8, June 19, 2019, page 66. ISSN: 1534-6269. DOI: 10.1007/s11912-019-0818-y.

[6] M. A. Anderson, J. E. Burda, Y. Ren, Y. Ao, T. M. O’Shea, R. Kawaguchi, G. Coppola, B. S. Khakh, T. J. Deming, and M. V. Sofroniew. “Astrocyte scar formation aids CNS axon regeneration”. In: *Nature* 532.7598, Apr. 14, 2016, pages 195–200. ISSN: 0028-0836. DOI: 10.1038/nature17623.

[7] R. M. Bachoo, R. S. Kim, K. L. Ligon, E. A. Maher, C. Brennan, N. Billings, S. Chan, C. Li, D. H. Rowitch, W. H. Wong, and R. A. DePinho. “Molecular diversity of astrocytes with implications for neurological disorders”. In: *Proceedings of the National Academy of Sciences of the United States of America* 101.22, June 1, 2004, pages 8384–8389. ISSN: 0027-8424. DOI: 10.1073/pnas.0402140101.

[8] E. Bahn, J. Bauer, S. Harrabi, K. Herfarth, J. Debus, and M. Alber. “Late Contrast Enhancing Brain Lesions in Proton-Treated Patients With Low-Grade Glioma: Clinical Evidence for Increased Periventricular Sensitivity and Variable RBE”. In: *International Journal of Radiation Oncology, Biology, Physics* 107.3, July 1, 2020, pages 571–578. ISSN: 1879-355X. DOI: 10.1016/j.ijrobp.2020.03.013.

[9] G. Balakrishnan, A. Zhao, M. R. Sabuncu, J. Guttag, and A. V. Dalca. “VoxelMorph: A Learning Framework for Deformable Medical Image Registration”. In: *IEEE Transactions on Medical Imaging* 38.8, Aug. 2019. Conference Name: IEEE Transactions on Medical Imaging, pages 1788–1800. ISSN: 1558-254X. DOI: 10.1109/TMI.2019.2897538.

[10] S. Balentova and M. Adamkov. “Molecular, Cellular and Functional Effects of Radiation-Induced Brain Injury: A Review”. In: *International Journal of Molecular Sciences* 16.11, Nov. 2015. Publisher: Multidisciplinary Digital Publishing Institute (MDPI), page 27796. DOI: `10.3390/ijms161126068`.

[11] C. N. Banwell and E. M. McCash. *Fundamentals of Molecular Spectroscopy.* Google-Books-ID: CJwgnwEACAAJ. McGraw-Hill, 1994. 332 pages. ISBN: 978-0-07-707976-5.

[12] H. M. Barber, M. F. Ali, and S. Kucenas. “Glial Patchwork: Oligodendrocyte Progenitor Cells and Astrocytes Blanket the Central Nervous System”. In: *Frontiers in Cellular Neuroscience* 15, Jan. 5, 2022, page 803057. ISSN: 1662-5102. DOI: `10.3389/fncel.2021.803057`.

[13] W. H. Barkas. *Nuclear research emulsions: W.H. Barkas.* OCLC: 52028679. New York: Academic Press, 1963. 2 pages.

[14] B. A. Barres. “The mystery and magic of glia: a perspective on their roles in health and disease”. In: *Neuron* 60.3, Nov. 6, 2008, pages 430–440. ISSN: 1097-4199. DOI: `10.1016/j.neuron.2008.10.013`.

[15] H. H. Barschall, M. B. Chadwick, D. T. L. Jones, J. P. Meulders, H. Schuhmacher, and P. G. Young. “Report 63”. In: *Journal of the ICRU* os32.2, Mar. 2000. Conference Name: Journal of the ICRU, NP–NP. ISSN: 1742-3422. DOI: `10.1093/jicru/os32.2.Report63`.

[16] M. Bartelmann. *Das kosmologische Standardmodell: Grundlagen, Beobachtungen und Grenzen.* 1. Aufl. 2019 edition. Berlin Heidelberg: Springer Spektrum, Oct. 1, 2019. 288 pages. ISBN: 978-3-662-59626-5.

[17] “batchgenerators - a python framework for data augmentation”. In: DOI: `10.5281/zenodo.3632567`.

[18] J. Beatty. “The Radon Transform and the Mathematics of Medical Imaging”. In: *Honors Theses*, Jan. 1, 2012.

[19] S. Berg, D. Kutra, T. Kroeger, C. N. Straehle, B. X. Kausler, C. Haubold, M. Schiegg, J. Ales, T. Beier, M. Rudy, K. Eren, J. I. Cervantes, B. Xu, F. Beuttenmueller, A. Wolny, C. Zhang, U. Koethe, F. A. Hamprecht, and A. Kreshuk. “ilastik: interactive machine learning for (bio)image analysis”. In: *Nature Methods* 16.12, Dec. 2019. Number: 12 Publisher: Nature Publishing Group, pages 1226–1232. ISSN: 1548-7105. DOI: `10.1038/s41592-019-0582-9`.

[20] A. Bielajew. “Fundamentals of the Monte Carlo method for neutral and charged particle transport”. In: Oct. 17, 2001.

[21] C. M. Bishop. *Pattern Recognition and Machine Learning.* 1st ed. 2006. Corr. 2nd printing 2011 edition. New York: Springer, Jan. 1, 2007. 798 pages. ISBN: 978-0-387-31073-2.

[22] N. Bohr. “LX. On the decrease of velocity of swiftly moving electrified particles in passing through matter”. In: *The London, Edinburgh, and Dublin Philosophical Magazine and Journal of Science* 30.178, Oct. 1, 1915, pages 581–612. ISSN: 1941-5982. DOI: `10.1080/14786441008635432`.

[23] J. Bonato, S. Curreli, S. Romanzi, S. Panzeri, and T. Fellin. “ASTRA: a deep learning algorithm for fast semantic segmentation of large-scale astrocytic networks”. In: *bioRxiv: The Preprint Server for Biology*, May 3, 2023, page 2023.05.03.539211. DOI: `10.1101/2023.05.03.539211`.

[24] F. Bookstein. “Principal warps: thin-plate splines and the decomposition of deformations”. In: *IEEE Transactions on Pattern Analysis and Machine Intelligence* 11.6, June 1989. Conference Name: IEEE Transactions on Pattern Analysis and Machine Intelligence, pages 567–585. ISSN: 1939-3539. DOI: `10.1109/34.24792`.

[25] S. Bradbury and B. Bracegirdle. *Introduction to Light Microscopy*. Google-Books-ID: NmdY9AjTyt8C. Bios Scientific Publishers, 1998. 138 pages. ISBN: 978-1-85996-121-6.

[26] S. Brahmachari, Y. K. Fung, and K. Pahan. “Induction of Glial Fibrillary Acidic Protein Expression in Astrocytes by Nitric Oxide”. In: *The Journal of Neuroscience* 26.18, May 3, 2006, pages 4930–4939. ISSN: 0270-6474. DOI: `10.1523/JNEUROSCI.5480-05.2006`.

[27] L. Breiman. “Random Forests”. In: *Machine Learning* 45.1, Oct. 1, 2001, pages 5–32. ISSN: 1573-0565. DOI: `10.1023/A:1010933404324`.

[28] T. Briand and A. Davy. “Optimization of Image B-spline Interpolation for GPU Architectures”. In: *Image Processing On Line* 9, Aug. 2, 2019, pages 183–204. ISSN: 2105-1232. DOI: `10.5201/ipol.2019.257`.

[29] J. K. Bronk, A. Amer, S. Khose, D. Flint, A. Adair, P. Yepes, D. Grosshans, J. Johnson, and C. Chung. “Brain Radiation Necrosis Outside the Target Volume After Proton Radiation Therapy: Analyses of Multiparametric Imaging and Proton Biologic Effectiveness”. In: *Advances in Radiation Oncology* 7.6, Aug. 6, 2022, page 101044. ISSN: 2452-1094. DOI: `10.1016/j.adro.2022.101044`.

[30] R. W. Brown, Y.-C. N. Cheng, E. M. Haacke, M. R. Thompson, and R. Venkatesan. *Magnetic Resonance Imaging: Physical Principles and Sequence Design*. 2. edition. Hoboken, New Jersey: Wiley-Blackwell, June 20, 2014. 976 pages. ISBN: 978-0-471-72085-0.

[31] A. Brueggemann. *Verbesserung der Dosimetrie für die Kleintierbestrahlung mit Protonen*. 2019.

[32] T. G. Bush, N. Puvanachandra, C. H. Horner, A. Polito, T. Ostenfeld, C. N. Svendsen, L. Mucke, M. H. Johnson, and M. V. Sofroniew. “Leukocyte infiltration, neuronal degeneration, and neurite outgrowth after ablation of scar-forming, reactive astrocytes in adult transgenic mice”. In: *Neuron* 23.2, June 1999, pages 297–308. ISSN: 0896-6273. DOI: `10.1016/s0896-6273(00)80781-3`.

[33] T. M. Buzug. “Computed Tomography”. In: *Springer Handbook of Medical Technology*. Springer Berlin Heidelberg, 2011, pages 311–342. DOI: `10.1007/978-3-540-74658-4_16`.

[34] R. Cabezas, M. Ávila, J. Gonzalez, R. S. El-Bachá, E. Báez, L. M. García-Segura, J. C. Jurado Coronel, F. Capani, G. P. Cardona-Gomez, and G. E. Barreto. “Astrocytic modulation of blood brain barrier: perspectives on Parkinson’s disease”. In: *Frontiers in Cellular Neuroscience* 8, Aug. 4, 2014, page 211. ISSN: 1662-5102. DOI: `10.3389/fncel.2014.00211`.

[35] H. Carey, M. Pegios, L. Martin, C. Saleeba, A. J. Turner, N. A. Everett, I. E. Bjerke, M. A. Puchades, J. G. Bjaalie, and S. McMullan. “DeepSlice: rapid fully automatic registration of mouse brain imaging to a volumetric atlas”. In: *Nature Communications* 14.1, Sept. 21, 2023. Number: 1 Publisher: Nature Publishing Group, page 5884. ISSN: 2041-1723. DOI: `10.1038/s41467-023-41645-4`.

[36] G. Casella, C. P. Robert, and M. T. Wells. “Generalized Accept-Reject sampling schemes”. In: *A Festschrift for Herman Rubin*. Volume 45. Institute of Mathematical Statistics, Jan. 1, 2004, pages 342–348. DOI: `10.1214/lnms/1196285403`.

[37] D. S. Chang, F. D. Lasley, I. J. Das, M. S. Mendonca, and J. R. Dynlacht. *Basic Radiotherapy Physics and Biology*. Cham: Springer International Publishing, 2021. ISBN: 978-3-030-61898-8 978-3-030-61899-5. DOI: `10.1007/978-3-030-61899-5`.

[38] S. T. Chao, M. S. Ahluwalia, G. H. Barnett, G. H. J. Stevens, E. S. Murphy, A. L. Stockham, K. Shiue, and J. H. Suh. “Challenges with the diagnosis and treatment of cerebral radiation necrosis”. In: *International Journal of Radiation Oncology, Biology, Physics* 87.3, Nov. 1, 2013, pages 449–457. ISSN: 1879-355X. DOI: `10.1016/j.ijrobp.2013.05.015`.

[39] Z. Chen, Z. Yuan, S. Yang, Y. Zhu, M. Xue, J. Zhang, and L. Leng. “Brain Energy Metabolism: Astrocytes in Neurodegenerative Diseases”. In: *CNS Neuroscience & Therapeutics* 29.1, Oct. 3, 2022, pages 24–36. ISSN: 1755-5930. DOI: `10.1111/cns.13982`.

[40] J. D. Cherry, J. A. Olschowka, and M. K. O’Banion. “Neuroinflammation and M2 microglia: the good, the bad, and the inflamed”. In: *Journal of Neuroinflammation* 11.1, June 3, 2014, page 98. ISSN: 1742-2094. DOI: `10.1186/1742-2094-11-98`.

[41] C. S. Chiang, W. H. McBride, and H. R. Withers. “Radiation-induced astrocytic and microglial responses in mouse brain”. In: *Radiotherapy and Oncology* 29.1, Oct. 1, 1993, pages 60–68. ISSN: 0167-8140. DOI: 10.1016/0167-8140(93)90174-7.

[42] R. A. Chiareli, G. A. Carvalho, B. L. Marques, L. S. Mota, O. C. Oliveira-Lima, R. M. Gomes, A. Birbrair, R. S. Gomez, F. Simão, F. Klempin, M. Leist, and M. C. X. Pinto. “The Role of Astrocytes in the Neurorepair Process”. In: *Frontiers in Cell and Developmental Biology* 9, 2021. ISSN: 2296-634X.

[43] S. S. Choi, H. J. Lee, I. Lim, J.-i. Satoh, and S. U. Kim. “Human Astrocytes: Secretome Profiles of Cytokines and Chemokines”. In: *PLoS ONE* 9.4, Apr. 1, 2014, e92325. ISSN: 1932-6203. DOI: 10.1371/journal.pone.0092325.

[44] W.-S. Chung, N. J. Allen, and C. Eroglu. “Astrocytes Control Synapse Formation, Function, and Elimination”. In: *Cold Spring Harbor Perspectives in Biology* 7.9, Sept. 2015, a020370. ISSN: 1943-0264. DOI: 10.1101/cshperspect.a020370.

[45] R. Clarkson, P. E. Lindsay, S. Ansell, G. Wilson, S. Jelveh, R. P. Hill, and D. A. Jaffray. “Characterization of image quality and image-guidance performance of a preclinical microirradiator”. In: *Medical Physics* 38.2, Feb. 2011, pages 845–856. ISSN: 0094-2405. DOI: 10.1118/1.3533947.

[46] P. Colautti, G. Magrin, H. Palmans, M. A. Cortés-Giraldo, and V. Conte. “Characterizing Radiation Effectiveness in Ion-Beam Therapy Part II: Microdosimetric Detectors”. In: *Frontiers in Physics* 8, 2020. ISSN: 2296-424X.

[47] T. M. Cover and J. A. Thomas. *Elements of Information Theory*. Google-Books-ID: VWq5GG6ycxMC. John Wiley & Sons, Nov. 28, 2012. 771 pages. ISBN: 978-1-118-58577-1.

[48] *czifile: Read Carl Zeiss(r) Image (CZI) files*. Version 2019.7.2.

[49] M. Davis, A. Meiksin, M. A. Strauss, L. N. da Costa, and A. Yahil. “On the Universality of the Two-Point Galaxy Correlation Function”. In: *The Astrophysical Journal* 333, Oct. 1, 1988. ADS Bibcode: 1988ApJ...333L...9D, page L9. ISSN: 0004-637X. DOI: 10.1086/185275.

[50] L. R. Dice. “Measures of the Amount of Ecologic Association Between Species”. In: *Ecology* 26.3, 1945, pages 297–302. ISSN: 1939-9170. DOI: 10.2307/1932409.

[51] C. Distler, Z. Dreher, and J. Stone. “Contact spacing among astrocytes in the central nervous system: an hypothesis of their structural role”. In: *Glia* 4.5, 1991, pages 484–494. ISSN: 0894-1491. DOI: 10.1002/glia.440040508.

[52] H. W. Dong. *The Allen reference atlas: A digital color brain atlas of the C57Bl/6J male mouse*. The Allen reference atlas: A digital color brain atlas of the C57Bl/6J male mouse. Pages: ix, 366. Hoboken, NJ, US: John Wiley & Sons Inc, 2008. ix, 366. ISBN: 978-0-470-05408-6.

[53] A. E. Dorr, J. P. Lerch, S. Spring, N. Kabani, and R. M. Henkelman. “High resolution three-dimensional brain atlas using an average magnetic resonance image of 40 adult C57Bl/6J mice”. In: *NeuroImage* 42.1, Aug. 1, 2008, pages 60–69. ISSN: 1095-9572. DOI: 10.1016/j.neuroimage.2008.03.037.

[54] S. Dräger and J. Dunkelau. *Evaluating the Impact of Loss Function Variation in Deep Learning for Classification.* Oct. 28, 2022. DOI: 10.48550/arXiv.2210.16003. arXiv: 2210.16003[cs].

[55] M. Dyba and S. W. Hell. “Focal Spots of Size $\ensuremath{\lambda}/23$ Open Up Far-Field Florescence Microscopy at 33 nm Axial Resolution”. In: *Physical Review Letters* 88.16, Apr. 4, 2002. Publisher: American Physical Society, page 163901. DOI: 10.1103/PhysRevLett.88.163901.

[56] W. Dörr. “Radiobiology of tissue reactions”. In: *Annals of the ICRP* 44.1, June 2015, pages 58–68. ISSN: 1872-969X. DOI: 10.1177/0146645314560686.

[57] M. Eddleston and L. Mucke. “Molecular profile of reactive astrocytes- Implications for their role in neurologic disease”. In: *Neuroscience* 54.1, May 1993, pages 15–36. ISSN: 0306-4522. DOI: 10.1016/0306-4522(93)90380-X.

[58] A. D. Elliott. “Confocal Microscopy: Principles and Modern Practices”. In: *Current protocols in cytometry* 92.1, Mar. 2020, e68. ISSN: 1934-9297. DOI: 10.1002/cpcy.68.

[59] J. Eulitz, E. G. C. Troost, F. Raschke, E. Schulz, B. Lutz, A. Dutz, S. Löck, P. Wohlfahrt, W. Enghardt, C. Karpowitz, M. Krause, and A. Lühr. “Predicting late magnetic resonance image changes in glioma patients after proton therapy”. In: *Acta Oncologica (Stockholm, Sweden)* 58.10, Oct. 2019, pages 1536–1539. ISSN: 1651-226X. DOI: 10.1080/0284186X.2019.1631477.

[60] C. Fan, M. Chen, X. Wang, J. Wang, and B. Huang. “A Review on Data Preprocessing Techniques Toward Efficient and Reliable Knowledge Discovery From Building Operational Data”. In: *Frontiers in Energy Research* 9, 2021. ISSN: 2296-598X.

[61] C. Farina, F. Aloisi, and E. Meinl. “Astrocytes are active players in cerebral innate immunity”. In: *Trends in Immunology* 28.3, Mar. 2007, pages 138–145. ISSN: 1471-4906. DOI: 10.1016/j.it.2007.01.005.

[62] J. W. Fawcett and R. A. Asher. “The glial scar and central nervous system repair”. In: *Brain Research Bulletin* 49.6, Aug. 1, 1999, pages 377–391. ISSN: 0361-9230. DOI: 10.1016/S0361-9230(99)00072-6.

[63] T. V. Feddersen, P. Rowshanfarzad, T. N. Abel, and M. A. Ebert. “Commissioning and performance characteristics of a pre-clinical image-guided radiotherapy system”. In: *Australasian Physical & Engineering Sciences in Medicine* 42.2, June 1, 2019, pages 541–551. ISSN: 1879-5447. DOI: 10.1007/s13246-019-00755-4.

[64] L. A. Feldkamp, L. C. Davis, and J. W. Kress. “Practical cone-beam algorithm”. In: *JOSA A* 1.6, June 1, 1984. Publisher: Optica Publishing Group, pages 612–619. ISSN: 1520-8532. DOI: `10.1364/JOSAA.1.000612`.

[65] F. Fracchiolla, E. Engwall, M. Janson, F. Tamm, S. Lorentini, F. Fellin, M. Bertolini, C. Algranati, R. Righetto, P. Farace, M. Amichetti, and M. Schwarz. “Clinical validation of a GPU-based Monte Carlo dose engine of a commercial treatment planning system for pencil beam scanning proton therapy”. In: *Physica Medica* 88, Aug. 1, 2021, pages 226–234. ISSN: 1120-1797. DOI: `10.1016/j.ejmp.2021.07.012`.

[66] Y. Fu, N. M. Brown, S. U. Saeed, A. Casamitjana, Z. M. c. Baum, R. Delaunay, Q. Yang, A. Grimwood, Z. Min, S. B. Blumberg, J. E. Iglesias, D. C. Barratt, E. Bonmati, D. C. Alexander, M. J. Clarkson, T. Vercauteren, and Y. Hu. “DeepReg: a deep learning toolkit for medical image registration”. In: *Journal of Open Source Software* 5.55, Nov. 4, 2020, page 2705. ISSN: 2475-9066. DOI: `10.21105/joss.02705`.

[67] *GAFchromic^{TM} (2019): Gafchromic^{TM}, Dosimetry Media, Type EBT-3*. URL: `https://www.citedrive.com/overleaf`.

[68] J. Gajewski, M. Garbacz, C.-W. Chang, K. Czerska, M. Durante, N. Krah, K. Krzempek, R. Kopeć, L. Lin, N. Mojżeszek, V. Patera, M. Pawlik-Niedzwiecka, I. Rinaldi, M. Rydygier, E. Pluta, E. Scifoni, A. Skrzypek, F. Tommasino, A. Schiavi, and A. Rucinski. “Commissioning of GPU–Accelerated Monte Carlo Code FRED for Clinical Applications in Proton Therapy”. In: *Frontiers in Physics* 8, 2021. ISSN: 2296-424X.

[69] S. Giordanengo and H. Palmans. “Dose detectors, sensors, and their applications”. In: *Medical Physics* 45.11, Nov. 2018, e1051–e1072. ISSN: 2473-4209. DOI: `10.1002/mp.13089`.

[70] A. Gopinath, A. Collins, H. Khoshbouei, and W. J. Streit. “Microglia and Other Myeloid Cells in Central Nervous System Health and Disease”. In: *The Journal of Pharmacology and Experimental Therapeutics* 375.1, Oct. 2020, pages 154–160. ISSN: 0022-3565. DOI: `10.1124/jpet.120.265058`.

[71] G. R. J. Gordon, S. J. Mulligan, and B. A. MacVicar. “Astrocyte control of the cerebrovasculature”. In: *Glia* 55.12, 2007, pages 1214–1221. ISSN: 1098-1136. DOI: `10.1002/glia.20543`.

[72] A. A. Goshtasby. *Image Registration: Principles, Tools and Methods*. Google-Books-ID: n7CgKedNatMC. Springer Science & Business Media, Jan. 13, 2012. 454 pages. ISBN: 978-1-4471-2457-3.

[73] D. A. Granville and G. O. Sawakuchi. “Comparison of linear energy transfer scoring techniques in Monte Carlo simulations of proton beams”. In: *Physics in Medicine & Biology* 60.14, July 2015. Publisher: IOP Publishing, N283. ISSN: 0031-9155. DOI: `10.1088/0031-9155/60/14/N283`.

[74] M. Grasmair. *A square root velocity framework for curves of bounded variation.* Mar. 13, 2022. DOI: `10.48550/arXiv.2203.06633`. arXiv: `2203.06633[cs, math]`.

[75] W. Gu, S. Bai, and L. Kong. “A review on 2D instance segmentation based on deep neural networks”. In: *Image and Vision Computing* 120, Apr. 1, 2022, page 104401. ISSN: 0262-8856. DOI: `10.1016/j.imavis.2022.104401`.

[76] F. Guan, C. Peeler, L. Bronk, C. Geng, R. Taleei, S. Randeniya, S. Ge, D. Mirkovic, D. Grosshans, R. Mohan, and U. Titt. “Analysis of the track- and dose-averaged LET and LET spectra in proton therapy using the geant4 Monte Carlo code”. In: *Medical Physics* 42.11, Nov. 2015, pages 6234–6247. ISSN: 0094-2405. DOI: `10.1118/1.4932217`.

[77] Y. Guo, Y. Liu, A. Oerlemans, S. Lao, S. Wu, and M. S. Lew. “Deep learning for visual understanding: A review”. In: *Neurocomputing.* Recent Developments on Deep Big Vision 187, Apr. 26, 2016, pages 27–48. ISSN: 0925-2312. DOI: `10.1016/j.neucom.2015.09.116`.

[78] E. J. Hall and A. J. Giaccia. *Radiobiology for the radiologist.* 7th ed. Philadelphia, Pa. Londo: Wolters Kluwer Lippincott Williams & Wilkins, 2012. 546 pages. ISBN: 978-1-60831-193-4.

[79] M. E. Hamby and M. V. Sofroniew. “Reactive astrocytes as therapeutic targets for CNS disorders”. In: *Neurotherapeutics* 7.4, Oct. 2010, pages 494–506. ISSN: 1933-7213. DOI: `10.1016/j.nurt.2010.07.003`.

[80] C. R. Harris, K. J. Millman, S. J. van der Walt, R. Gommers, P. Virtanen, D. Cournapeau, E. Wieser, J. Taylor, S. Berg, N. J. Smith, R. Kern, M. Picus, S. Hoyer, M. H. van Kerkwijk, M. Brett, A. Haldane, J. F. del Río, M. Wiebe, P. Peterson, P. Gérard-Marchant, K. Sheppard, T. Reddy, W. Weckesser, H. Abbasi, C. Gohlke, and T. E. Oliphant. “Array programming with NumPy”. In: *Nature* 585.7825, Sept. 2020. Number: 7825 Publisher: Nature Publishing Group, pages 357–362. ISSN: 1476-4687. DOI: `10.1038/s41586-020-2649-2`.

[81] B. He, X. Wang, Y. He, H. Li, Y. Yang, Z. Shi, Q. Liu, M. Wu, H. Sun, J. Xie, Z. Zhang, P. Yu, J. Jiang, J. Cheng, J. Yang, Y. Li, W.-J. Lin, Y. Tang, and X. Wang. “Gamma ray-induced glial activation and neuronal loss occur before the delayed onset of brain necrosis”. In: *The FASEB Journal* 34.10, 2020, pages 13361–13375. ISSN: 1530-6860. DOI: `10.1096/fj.202000365RR`.

[82] J. Hedderich and L. Sachs. *Angewandte Statistik.* Berlin, Heidelberg: Springer, 2016. ISBN: 978-3-662-45690-3 978-3-662-45691-0. DOI: `10.1007/978-3-662-45691-0`.

[83] S. W. Hell. “Microscopy and its focal switch”. In: *Nature Methods* 6.1, Jan. 2009, pages 24–32. ISSN: 1548-7105. DOI: `10.1038/nmeth.1291`.

[84] M. Hemati-Gourabi, T. Cao, M. K. Romprey, and M. Chen. “Capacity of astrocytes to promote axon growth in the injured mammalian central nervous system”. In: *Frontiers in Neuroscience* 16, 2022. ISSN: 1662-453X.

[85] D. Herrera, G. Ochoa-Ruiz, M. Gonzalez-Mendoza, and C. Mata. *Impact of loss function in Deep Learning methods for accurate retinal vessel segmentation.* June 1, 2022. DOI: `10.48550/arXiv.2206.00536`. arXiv: `2206.00536[cs, eess]`.

[86] T. Herrmann, M. Baumann, and W. Dörr. *Klinische Strahlenbiologie.* Jena Stuttgart: Urban & Fischer Verlag, Jan. 1, 2006. ISBN: 978-3-437-31140-6.

[87] M. Holt. "Astrocyte heterogeneity and interactions with local neural circuits". In: *Essays in Biochemistry* 67.1, Mar. 2023, pages 93–106. ISSN: 0071-1365. DOI: `10.1042/EBC20220136`.

[88] S.-Y. Hwang, J.-S. Jung, T.-H. Kim, S.-J. Lim, E.-S. Oh, J.-Y. Kim, K.-A. Ji, E.-H. Joe, K.-H. Cho, and I.-O. Han. "Ionizing radiation induces astrocyte gliosis through microglia activation". In: *Neurobiology of Disease* 21.3, Mar. 1, 2006, pages 457–467. ISSN: 0969-9961. DOI: `10.1016/j.nbd.2005.08.006`.

[89] F. Isensee, P. F. Jaeger, S. A. A. Kohl, J. Petersen, and K. H. Maier-Hein. "nnU-Net: a self-configuring method for deep learning-based biomedical image segmentation". In: *Nature Methods* 18.2, Feb. 2021. Number: 2 Publisher: Nature Publishing Group, pages 203–211. ISSN: 1548-7105. DOI: `10.1038/s41592-020-01008-z`.

[90] M. Jaderberg, K. Simonyan, A. Zisserman, and K. Kavukcuoglu. *Spatial Transformer Networks.* Feb. 4, 2016. DOI: `10.48550/arXiv.1506.02025`. arXiv: `1506.02025[cs]`.

[91] S. Jadon. "A survey of loss functions for semantic segmentation". In: *2020 IEEE Conference on Computational Intelligence in Bioinformatics and Computational Biology (CIBCB)*, Oct. 27, 2020. Conference Name: 2020 IEEE Conference on Computational Intelligence in Bioinformatics and Computational Biology (CIBCB) ISBN: 9781728194684 Place: Via del Mar, Chile Publisher: IEEE, pages 1–7. DOI: `10.1109/CIBCB48159.2020.9277638`.

[92] T. Jiang, H. Gong, and J. Yuan. "Whole-brain Optical Imaging: A Powerful Tool for Precise Brain Mapping at the Mesoscopic Level". In: *Neuroscience Bulletin*, Sept. 16, 2023. ISSN: 1995-8218. DOI: `10.1007/s12264-023-01112-y`.

[93] X. Jiang, A. Hadid, Y. Pang, E. Granger, and X. Feng, editors. *Deep Learning in Object Detection and Recognition.* Singapore: Springer, 2019. ISBN: 978-981-10-5151-7 978-981-10-5152-4. DOI: `10.1007/978-981-10-5152-4`.

[94] X. Jiang and H. Gao. *Neurotoxicity of Nanomaterials and Nanomedicine.* Academic Press, Oct. 3, 2016. 368 pages. ISBN: 978-0-12-804620-3.

[95] H. J. Johnson, M. M. McCormick, and L. Ibanez. *The ITK Software Guide Book 1: Introduction and Development Guidelines.* ITK 4.7 Edition. New York, NY: Kitware, Incorporated, Jan. 16, 2015. 248 pages. ISBN: 978-1-930934-27-6.

[96] H. J. Johnson, M. M. McCormick, and L. Ibanez. *The ITK Software Guide Book 2: Design and Functionality*. ITK 4.7 edition. New York, NY: Kitware, Incorporated, Jan. 16, 2015. 520 pages. ISBN: 978-1-930934-28-3.

[97] K. A. Johnson and G. M. Hagen. “Artifact-free whole-slide imaging with structured illumination microscopy and Bayesian image reconstruction”. In: *GigaScience* 9.4, Apr. 1, 2020, giaa035. ISSN: 2047-217X. DOI: `10.1093/gigascience/giaa035`.

[98] N. de Jonge and D. B. Peckys. “Live Cell Electron Microscopy Is Probably Impossible”. In: *ACS Nano* 10.10, Oct. 25, 2016. Publisher: American Chemical Society, pages 9061–9063. ISSN: 1936-0851. DOI: `10.1021/acsnano.6b02809`.

[99] M. A. Kahn, J. A. Ellison, G. J. Speight, and J. de Vellis. “CNTF regulation of astrogliosis and the activation of microglia in the developing rat central nervous system”. In: *Brain Research* 685.1, July 10, 1995, pages 55–67. ISSN: 0006-8993. DOI: `10.1016/0006-8993(95)00411-I`.

[100] T. Kamiryo, N. F. Kassell, Q. A. Thai, M. B. S. Lopes, K. S. Lee, and L. Steiner. “Histological changes in the normal rat brain after gamma irradiation”. In: *Acta Neurochirurgica* 138.4, Apr. 1, 1996, pages 451–459. ISSN: 0942-0940. DOI: `10.1007/BF01420308`.

[101] H. Kawano, J. Kimura-Kuroda, Y. Komuta, N. Yoshioka, H. P. Li, K. Kawamura, Y. Li, and G. Raisman. “Role of the lesion scar in the response to damage and repair of the central nervous system”. In: *Cell and Tissue Research* 349.1, July 1, 2012, pages 169–180. ISSN: 1432-0878. DOI: `10.1007/s00441-012-1336-5`.

[102] C. B. Kayasandik, W. Ru, and D. Labate. “A multistep deep learning framework for the automated detection and segmentation of astrocytes in fluorescent images of brain tissue”. In: *Scientific Reports* 10.1, Mar. 20, 2020. Number: 1 Publisher: Nature Publishing Group, page 5137. ISSN: 2045-2322. DOI: `10.1038/s41598-020-61953-9`.

[103] M. D. Ketcha, T De Silva, A Uneri, M. W. Jacobson, J Goerres, G Kleinszig, S Vogt, J.-P. Wolinsky, and J. H. Siewerdsen. “Multi-Stage 3D-2D Registration for Correction of Anatomical Deformation in Image-Guided Spine Surgery”. In: *Physics in medicine and biology* 62.11, June 7, 2017, pages 4604–4622. ISSN: 0031-9155. DOI: `10.1088/1361-6560/aa6b3e`.

[104] S. U. Kim and J. de Vellis. “Microglia in health and disease”. In: *Journal of Neuroscience Research* 81.3, Aug. 1, 2005, pages 302–313. ISSN: 0360-4012. DOI: `10.1002/jnr.20562`.

[105] Y. Kim, J. Park, and Y. K. Choi. “The Role of Astrocytes in the Central Nervous System Focused on BK Channel and Heme Oxygenase Metabolites: A Review”. In: *Antioxidants* 8.5, May 5, 2019, page 121. ISSN: 2076-3921. DOI: `10.3390/antiox8050121`.

[106] D. P. Kingma and J. Ba. *Adam: A Method for Stochastic Optimization.* Jan. 29, 2017. DOI: 10.48550/arXiv.1412.6980. arXiv: 1412.6980[cs].

[107] S. Klein, M. Staring, K. Murphy, M. A. Viergever, and J. P. W. Pluim. “elastix: a toolbox for intensity-based medical image registration”. In: *IEEE transactions on medical imaging* 29.1, Jan. 2010, pages 196–205. ISSN: 1558-254X. DOI: 10.1109/TMI.2009.2035616.

[108] G. D. Knott. *Interpolating Cubic Splines.* Boston, MA: Birkhäuser, 2000. ISBN: 978-1-4612-7092-8 978-1-4612-1320-8. DOI: 10.1007/978-1-4612-1320-8.

[109] R. A. Koch, M. Boucsein, S. Brons, M. Alber, and E. Bahn. “A time-resolved clonogenic assay for improved cell survival and RBE measurements”. In: *Clinical and Translational Radiation Oncology* 42, Sept. 2023, page 100662. ISSN: 2405-6308. DOI: 10.1016/j.ctro.2023.100662.

[110] J. Kreer. “A question of terminology”. In: *IRE Transactions on Information Theory* 3.3, Sept. 1957. Conference Name: IRE Transactions on Information Theory, pages 208–208. ISSN: 2168-2712. DOI: 10.1109/TIT.1957.1057418.

[111] H. Krieger. *Grundlagen der Strahlungsphysik und des Strahlenschutzes.* Berlin, Heidelberg: Springer, 2023. ISBN: 978-3-662-67609-7 978-3-662-67610-3. DOI: 10.1007/978-3-662-67610-3.

[112] A. Kumar, I. C. Fontana, and A. Nordberg. “Reactive astrogliosis: A friend or foe in the pathogenesis of Alzheimer’s disease”. In: *Journal of Neurochemistry* 164.3, 2023, pages 309–324. ISSN: 1471-4159. DOI: 10.1111/jnc.15565.

[113] A. Kádár, G. Wittmann, Z. Liposits, and C. Fekete. “Improved method for combination of immunocytochemistry and Nissl staining”. In: *Journal of Neuroscience Methods* 184.1, Oct. 30, 2009, pages 115–118. ISSN: 0165-0270. DOI: 10.1016/j.jneumeth.2009.07.010.

[114] D. Labate and C. Kayasandik. “Advances in quantitative analysis of astrocytes using machine learning”. In: *Neural Regeneration Research* 18.2, June 2, 2022, pages 313–314. ISSN: 1673-5374. DOI: 10.4103/1673-5374.346474.

[115] J. R. Lakowicz. *Principles of Fluorescence Spectroscopy.* Springer Science & Business Media, Dec. 5, 2007. 961 pages. ISBN: 978-0-387-46312-4.

[116] J. M. Lawrence, K. Schardien, B. Wigdahl, and M. R. Nonnemacher. “Roles of neuropathology-associated reactive astrocytes: a systematic review”. In: *Acta Neuropathologica Communications* 11.1, Mar. 13, 2023, page 42. ISSN: 2051-5960. DOI: 10.1186/s40478-023-01526-9.

[117] J. Lefebvre, A. Castonguay, P. Pouliot, M. Descoteaux, and F. Lesage. “Whole mouse brain imaging using optical coherence tomography: reconstruction, normalization, segmentation, and comparison with diffusion MRI”. In: *Neurophotonics* 4.4, Oct. 2017, page 041501. ISSN: 2329-423X. DOI: 10.1117/1.NPh.4.4.041501.

[118] E. S. Lein et al. “Genome-wide atlas of gene expression in the adult mouse brain”. In: *Nature* 445.7124, Jan. 2007. Number: 7124 Publisher: Nature Publishing Group, pages 168–176. ISSN: 1476-4687. DOI: `10.1038/nature05453`.

[119] L. Lemieux, R. Jagoe, D. R. Fish, N. D. Kitchen, and D. G. Thomas. “A patient-to-computed-tomography image registration method based on digitally reconstructed radiographs”. In: *Medical Physics* 21.11, Nov. 1994, pages 1749–1760. ISSN: 0094-2405. DOI: `10.1118/1.597276`.

[120] W. R. Leo. *Techniques for Nuclear and Particle Physics Experiments: A How-to Approach*. Google-Books-ID: W7vHQgAACAAJ. Springer, 1994. 400 pages. ISBN: 978-0-387-57280-2.

[121] K. Li, J. Li, J. Zheng, and S. Qin. “Reactive Astrocytes in Neurodegenerative Diseases”. In: *Aging and disease* 10.3, June 1, 2019. Number: 3, pages 664–675. ISSN: 2152-5250. DOI: `10.14336/AD.2018.0720`.

[122] W. Li, A. Prasad, N. Miolane, and K. D. Duc. *Using a Riemannian elastic metric for statistical analysis of tumor cell shape heterogeneity*. Pages: 2023.06.11.544518 Section: New Results. June 12, 2023. DOI: `10.1101/2023.06.11.544518`.

[123] S. A. Liddelow and B. A. Barres. “Reactive Astrocytes: Production, Function, and Therapeutic Potential”. In: *Immunity* 46.6, June 20, 2017, pages 957–967. ISSN: 1097-4180. DOI: `10.1016/j.immuni.2017.06.006`.

[124] S. G. Lipson, H. Lipson, and D. S. Tannhauser. *Optical Physics*. Google-Books-ID: g0PwDAEACAAJ. Cambridge University Press, July 27, 1995. 520 pages. ISBN: 978-0-521-43631-1.

[125] G. Litjens, T. Kooi, B. E. Bejnordi, A. A. A. Setio, F. Ciompi, M. Ghafoorian, J. A. W. M. van der Laak, B. van Ginneken, and C. I. Sánchez. “A survey on deep learning in medical image analysis”. In: *Medical Image Analysis* 42, Dec. 1, 2017, pages 60–88. ISSN: 1361-8415. DOI: `10.1016/j.media.2017.07.005`.

[126] X. Liu, J. Ying, X. Wang, Q. Zheng, T. Zhao, S. Yoon, W. Yu, D. Yang, Y. Fang, and F. Hua. “Astrocytes in Neural Circuits: Key Factors in Synaptic Regulation and Potential Targets for Neurodevelopmental Disorders”. In: *Frontiers in Molecular Neuroscience* 14, 2021. ISSN: 1662-5099.

[127] J. S. Loeffler and M. Durante. “Charged particle therapy—optimization, challenges and future directions”. In: *Nature Reviews Clinical Oncology* 10.7, July 2013. Number: 7 Publisher: Nature Publishing Group, pages 411–424. ISSN: 1759-4782. DOI: `10.1038/nrclinonc.2013.79`.

[128] M. A. Lones. *How to avoid machine learning pitfalls: a guide for academic researchers*. Feb. 9, 2023. DOI: `10.48550/arXiv.2108.02497`. arXiv: `2108.02497[cs]`.

[129] J. Long, E. Shelhamer, and T. Darrell. *Fully Convolutional Networks for Semantic Segmentation*. Mar. 8, 2015. DOI: `10.48550/arXiv.1411.4038`. arXiv: `1411.4038[cs]`.

[130] A. Lopez Juarez, D. He, and Q. Richard Lu. “Oligodendrocyte progenitor programming and reprogramming: Toward myelin regeneration”. In: *Brain Research*. NG2-glia: the fourth glial cell type? 1638, May 1, 2016, pages 209–220. ISSN: 0006-8993. DOI: 10.1016/j.brainres.2015.10.051.

[131] D. A. Low, W. B. Harms, S. Mutic, and J. A. Purdy. “A technique for the quantitative evaluation of dose distributions”. In: *Medical Physics* 25.5, May 1998, pages 656–661. ISSN: 0094-2405. DOI: 10.1118/1.598248.

[132] H. Lubatschowski. “Laser Microtomy”. In: *Optik & Photonik* 2.2, 2007, pages 49–51. ISSN: 2191-1975. DOI: 10.1002/opph.201190252.

[133] S.-M. Lucas, N. J. Rothwell, and R. M. Gibson. “The role of inflammation in CNS injury and disease”. In: *British Journal of Pharmacology* 147, Suppl 1 Jan. 2006, S232–S240. ISSN: 0007-1188. DOI: 10.1038/sj.bjp.0706400.

[134] P. van Luijk, H. P. Bijl, R. P. Coppes, A. J. van der Kogel, A. W. Konings, J. A. Pikkemaat, and J. M. Schippers. “Techniques for precision irradiation of the lateral half of the rat cervical spinal cord using 150 MeV protons [corrected]”. In: *Physics in Medicine and Biology* 46.11, Nov. 2001, pages 2857–2871. ISSN: 0031-9155. DOI: 10.1088/0031-9155/46/11/307.

[135] G. Lutz. *Semiconductor Radiation Detectors: Device Physics*. 1st ed. 1999. 2nd printing 2007 edition. Berlin: Springer Berlin Heidelberg, Oct. 10, 2008. 368 pages. ISBN: 978-3-540-71678-5.

[136] A. Lühr, C. von Neubeck, M. Krause, and E. G. C. Troost. “Relative biological effectiveness in proton beam therapy – Current knowledge and future challenges”. In: *Clinical and Translational Radiation Oncology* 9, Feb. 1, 2018, pages 35–41. ISSN: 2405-6308. DOI: 10.1016/j.ctro.2018.01.006.

[137] C.-M. Ma, J. S. Li, S. B. Jiang, T. Pawlicki, W. Xiong, L. H. Qin, and J. Yang. “Effect of statistical uncertainties on Monte Carlo treatment planning”. In: *Physics in Medicine & Biology* 50.5, Feb. 2005, page 891. ISSN: 0031-9155. DOI: 10.1088/0031-9155/50/5/013.

[138] A. Mahbod, G. Schaefer, C. Löw, G. Dorffner, R. Ecker, and I. Ellinger. “Investigating the Impact of the Bit Depth of Fluorescence-Stained Images on the Performance of Deep Learning-Based Nuclei Instance Segmentation”. In: *Diagnostics (Basel, Switzerland)* 11.6, May 27, 2021, page 967. ISSN: 2075-4418. DOI: 10.3390/diagnostics11060967.

[139] N. O. Mahony, S. Campbell, A. Carvalho, S. Harapanahalli, G. Velasco-Hernandez, L. Krpalkova, D. Riordan, and J. Walsh. *Deep Learning vs. Traditional Computer Vision*. Volume 943. 2020. DOI: 10.1007/978-3-030-17795-9. arXiv: 1910.13796[cs].

[140] A. Mairani, S. Mein, E. Blakely, J. Debus, M. Durante, A. Ferrari, H. Fuchs, D. Georg, D. R. Grosshans, F. Guan, T. Haberer, S. Harrabi, F. Horst, T. Inaniwa, C. P. Karger, R. Mohan, H. Paganetti, K. Parodi, P. Sala, C. Schuy, T. Tessonnier, U. Titt, and U. Weber. "Roadmap: helium ion therapy". In: *Physics in Medicine & Biology* 67.15, Aug. 2022. Publisher: IOP Publishing, 15TR02. ISSN: 0031-9155. DOI: 10.1088/1361-6560/ac65d3.

[141] A. Margiotta. "Role of SNAREs and Rabs in Myelin Regulation". In: *International Journal of Molecular Sciences* 24.11, June 5, 2023, page 9772. ISSN: 1422-0067. DOI: 10.3390/ijms24119772.

[142] T. I. Marshall, P. Chaudhary, A. Michaelidesová, J. Vachelová, M. Davídková, V. Vondráček, G. Schettino, and K. M. Prise. "Investigating the Implications of a Variable RBE on Proton Dose Fractionation Across a Clinical Pencil Beam Scanned Spread-Out Bragg Peak". In: *International Journal of Radiation Oncology, Biology, Physics* 95.1, May 1, 2016, pages 70–77. ISSN: 0360-3016. DOI: 10.1016/j.ijrobp.2016.02.029.

[143] D Mason. "SU-E-T-33: Pydicom: An Open Source DICOM Library". In: *Medical Physics* 38.6, 2011, pages 3493–3493. ISSN: 2473-4209. DOI: 10.1118/1.3611983.

[144] W. T. Mason. *Fluorescent and Luminescent Probes for Biological Activity: A Practical Guide to Technology for Quantitative Real-time Analysis.* Google-Books-ID: k0CJewkhhL8C. Academic Press, 1993. 474 pages. ISBN: 978-0-12-477829-0.

[145] M. Matinfar, E. Ford, I. Iordachita, J. Wong, and P. Kazanzides. "Image-guided small animal radiation research platform: calibration of treatment beam alignment". In: *Physics in Medicine and Biology* 54.4, Feb. 21, 2009, pages 891–905. ISSN: 0031-9155. DOI: 10.1088/0031-9155/54/4/005.

[146] Y. Matsumoto, N. Fukumitsu, H. Ishikawa, K. Nakai, and H. Sakurai. "A Critical Review of Radiation Therapy: From Particle Beam Therapy (Proton, Carbon, and BNCT) to Beyond". In: *Journal of Personalized Medicine* 11.8, Aug. 23, 2021, page 825. ISSN: 2075-4426. DOI: 10.3390/jpm11080825.

[147] M. McCormick, X. Liu, L. Ibanez, J. Jomier, and C. Marion. "ITK: enabling reproducible research and open science". In: *Frontiers in Neuroinformatics* 8, 2014. ISSN: 1662-5196.

[148] J. Meyer, J. Eley, T. E. Schmid, S. E. Combs, R. Dendale, and Y. Prezado. "Spatially fractionated proton minibeams". In: *The British Journal of Radiology* 92.1095, Mar. 2019, page 20180466. ISSN: 0007-1285. DOI: 10.1259/bjr.20180466.

[149] A. Micke, D. F. Lewis, and X. Yu. "Multichannel film dosimetry with nonuniformity correction: Multichannel film dosimetry with nonuniformity correction". In: *Medical Physics* 38.5, May 2, 2011, pages 2523–2534. ISSN: 00942405. DOI: 10.1118/1.3576105.

[150] N. Miolane, A. L. Brigant, J. Mathe, B. Hou, N. Guigui, Y. Thanwerdas, S. Heyder, O. Peltre, N. Koep, H. Zaatiti, H. Hajri, Y. Cabanes, T. Gerald, P. Chauchat, C. Shewmake, B. Kainz, C. Donnat, S. Holmes, and X. Pennec. *Geomstats: A Python Package for Riemannian Geometry in Machine Learning.* Apr. 7, 2020. DOI: `10.48550/arXiv.2004.04667`. arXiv: `2004.04667[cs]`.

[151] R. Mohan and D. Grosshans. "Proton therapy – Present and future". In: *Advanced Drug Delivery Reviews.* Radiotherapy for cancer: present and future 109, Jan. 15, 2017, pages 26–44. ISSN: 0169-409X. DOI: `10.1016/j.addr.2016.11.006`.

[152] O. A. Montesinos López, A. Montesinos López, and J. Crossa. "Fundamentals of Artificial Neural Networks and Deep Learning". In: *Multivariate Statistical Machine Learning Methods for Genomic Prediction.* Edited by O. A. Montesinos López, A. Montesinos López, and J. Crossa. Cham: Springer International Publishing, 2022, pages 379–425. ISBN: 978-3-030-89010-0. DOI: `10.1007/978-3-030-89010-0_10`.

[153] J. Mrzílková, M. Patzelt, P. Gallina, Z. Wurst, M. Šeremeta, J. Dudák, F. Krejčí, J. Žemlička, V. Musil, J. Karch, J. Rosina, and P. Zach. "Imaging of Mouse Brain Fixated in Ethanol in Micro-CT". In: *BioMed Research International* 2019, July 14, 2019, page 2054262. ISSN: 2314-6133. DOI: `10.1155/2019/2054262`.

[154] C. Müller, M. De Prado Leal, M. D. Dominietto, C. A. Umbricht, S. Safai, R. L. Perrin, M. Egloff, P. Bernhardt, N. P. van der Meulen, D. C. Weber, R. Schibli, and A. J. Lomax. "Combination of Proton Therapy and Radionuclide Therapy in Mice: Preclinical Pilot Study at the Paul Scherrer Institute". In: *Pharmaceutics* 11.9, Sept. 2, 2019, page 450. ISSN: 1999-4923. DOI: `10.3390/pharmaceutics11090450`.

[155] J. Müller, M. Schürer, C. Neubert, F. Tillner, E. Beyreuther, T. Suckert, N. Peters, C. v. Neubeck, A. Lühr, M. Krause, R. Bütof, and A. Dietrich. "Multimodality bedding platform for combined imaging and irradiation of mice". In: *Biomedical Physics & Engineering Express* 6.3, Apr. 2020. Publisher: IOP Publishing, page 037003. ISSN: 2057-1976. DOI: `10.1088/2057-1976/ab79f1`.

[156] "napari: a multi-dimensional image viewer for Python". In: DOI: `10.5281/zenodo.8115575`.

[157] "napari/magicgui: v0.6.0". In: DOI: `10.5281/zenodo.7254817`.

[158] K.-A. Nave and H. B. Werner. "Myelination of the nervous system: mechanisms and functions". In: *Annual Review of Cell and Developmental Biology* 30, 2014, pages 503–533. ISSN: 1530-8995. DOI: `10.1146/annurev-cellbio-100913-013101`.

[159] N. M. Nawi, W. H. Atomi, and M. Z. Rehman. “The Effect of Data Preprocessing on Optimized Training of Artificial Neural Networks”. In: *Procedia Technology*. 4th International Conference on Electrical Engineering and Informatics, ICEEI 2013 11, Jan. 1, 2013, pages 32–39. ISSN: 2212-0173. DOI: `10.1016/j.protcy.2013.12.159`.

[160] M. Nedergaard, B. Ransom, and S. A. Goldman. “New roles for astrocytes: redefining the functional architecture of the brain”. In: *Trends in Neurosciences* 26.10, Oct. 2003, pages 523–530. ISSN: 0166-2236. DOI: `10.1016/j.tins.2003.08.008`.

[161] Y. Nesterov. “A method for solving the convex programming problem with convergence rate O(1/k^2)”. In: *Proceedings of the USSR Academy of Sciences*, 1983.

[162] W. D. Newhauser and R. Zhang. “The physics of proton therapy”. In: *Physics in Medicine & Biology* 60.8, Mar. 2015. Publisher: IOP Publishing, R155. ISSN: 0031-9155. DOI: `10.1088/0031-9155/60/8/R155`.

[163] L. Ng, S. Pathak, C. Kuan, C. Lau, H.-W. Dong, A. Sodt, C. Dang, B. Avants, P. Yushkevich, J. Gee, D. Haynor, E. Lein, A. Jones, and M. Hawrylycz. “Neuroinformatics for genome-wide 3D gene expression mapping in the mouse brain”. In: *IEEE/ACM transactions on computational biology and bioinformatics* 4.3, 2007, pages 382–393. ISSN: 1545-5963. DOI: `10.1109/tcbb.2007.1035`.

[164] D. Nguyen, P. J. Marchand, A. L. Planchette, J. Nilsson, M. Sison, J. Extermann, A. Lopez, M. Sylwestrzak, J. Sordet-Dessimoz, A. Schmidt-Christensen, D. Holmberg, D. Van De Ville, and T. Lasser. “Optical projection tomography for rapid whole mouse brain imaging”. In: *Biomedical Optics Express* 8.12, Nov. 15, 2017, pages 5637–5650. ISSN: 2156-7085. DOI: `10.1364/BOE.8.005637`.

[165] K. Nojima, T. Nakadai, Y. Khono, and S. Nagaoka. *Effects of heavy particle irradiation on central nervous system*. NIRS-M–173 INIS Reference Number: 36045798. Japan, 2004, pages 62–64.

[166] Y. Ota, A. T. Zanetti, and R. M. Hallock. “The Role of Astrocytes in the Regulation of Synaptic Plasticity and Memory Formation”. In: *Neural Plasticity* 2013, 2013, page 185463. ISSN: 2090-5904. DOI: `10.1155/2013/185463`.

[167] N. Otsu. “A Threshold Selection Method from Gray-Level Histograms”. In: *IEEE Transactions on Systems, Man, and Cybernetics* 9.1, Jan. 1979. Conference Name: IEEE Transactions on Systems, Man, and Cybernetics, pages 62–66. ISSN: 2168-2909. DOI: `10.1109/TSMC.1979.4310076`.

[168] H. Paganetti. “Relative biological effectiveness (RBE) values for proton beam therapy. Variations as a function of biological endpoint, dose, and linear energy transfer”. In: *Physics in Medicine and Biology* 59.22, Nov. 21, 2014, R419–472. ISSN: 1361-6560. DOI: `10.1088/0031-9155/59/22/R419`.

[169] H. Paganetti, E. Blakely, A. Carabe-Fernandez, D. J. Carlson, I. J. Das, L. Dong, D. Grosshans, K. D. Held, R. Mohan, V. Moiseenko, A. Niemierko, R. D. Stewart, and H. Willers. "Report of the AAPM TG-256 on the relative biological effectiveness of proton beams in radiation therapy". In: *Medical Physics* 46.3, Mar. 2019, e53–e78. ISSN: 2473-4209. DOI: 10.1002/mp.13390.

[170] H. Paganetti and P. van Luijk. "Biological considerations when comparing proton therapy with photon therapy". In: *Seminars in Radiation Oncology* 23.2, Apr. 2013, pages 77–87. ISSN: 1532-9461. DOI: 10.1016/j.semradonc.2012.11.002.

[171] H. Paganetti, A. Niemierko, M. Ancukiewicz, L. E. Gerweck, M. Goitein, J. S. Loeffler, and H. D. Suit. "Relative biological effectiveness (RBE) values for proton beam therapy". In: *International Journal of Radiation Oncology, Biology, Physics* 53.2, June 1, 2002, pages 407–421. ISSN: 0360-3016. DOI: 10.1016/s0360-3016(02)02754-2.

[172] S. H. Park and J. O. Kang. "Basics of particle therapy I: physics". In: *Radiation Oncology Journal* 29.3, Sept. 2011, pages 135–146. ISSN: 2234-1900. DOI: 10.3857/roj.2011.29.3.135.

[173] A. Paszke, S. Gross, F. Massa, A. Lerer, J. Bradbury, G. Chanan, T. Killeen, Z. Lin, N. Gimelshein, L. Antiga, A. Desmaison, A. Köpf, E. Yang, Z. DeVito, M. Raison, A. Tejani, S. Chilamkurthy, B. Steiner, L. Fang, J. Bai, and S. Chintala. *PyTorch: An Imperative Style, High-Performance Deep Learning Library*. Dec. 3, 2019. DOI: 10.48550/arXiv.1912.01703. arXiv: 1912.01703[cs,stat].

[174] J. Patel. "THE MOUSE BRAIN: A 3D ATLAS REGISTERING MRI, CT, AND HISTOLOGICAL SECTIONS IN THE THREE CARDINAL PLANES". PhD thesis. Johns Hopkins University, Aug. 20, 2018.

[175] A. Patriarca, C. Fouillade, M. Auger, F. Martin, F. Pouzoulet, C. Nauraye, S. Heinrich, V. Favaudon, S. Meyroneinc, R. Dendale, A. Mazal, P. Poortmans, P. Verrelle, and L. De Marzi. "Experimental Set-up for FLASH Proton Irradiation of Small Animals Using a Clinical System". In: *International Journal of Radiation Oncology, Biology, Physics* 102.3, Nov. 1, 2018, pages 619–626. ISSN: 1879-355X. DOI: 10.1016/j.ijrobp.2018.06.403.

[176] J. Pawley. *Handbook of Biological Confocal Microscopy*. Google-Books-ID: 8encBwAAQBAJ. Springer Science & Business Media, Apr. 17, 2013. 639 pages. ISBN: 978-1-4757-5348-6.

[177] G. Paxinos and K. B. J. Franklin. *Paxinos and Franklin's the Mouse Brain in Stereotaxic Coordinates*. Google-Books-ID: 8RJZLwEACAAJ. Elsevier Science, Oct. 25, 2012. 360 pages. ISBN: 978-0-12-391057-8.

[178] M. Pekny and M. Pekna. "Astrocyte reactivity and reactive astrogliosis: costs and benefits". In: *Physiological Reviews* 94.4, Oct. 2014, pages 1077–1098. ISSN: 1522-1210. DOI: 10.1152/physrev.00041.2013.

[179] L. Pellerin and P. Magistretti. “Pellerin L & Magistretti PJ.Glutamate uptake into astrocytes stimulates aerobic glycolysis: A mechanism coupling neuronal activity to glucose utilization. Proc Natl Acad Sci USA 91: 10625-10629”. In: *Proceedings of the National Academy of Sciences of the United States of America* 91, Nov. 1, 1994, pages 10625–9. DOI: 10.1073/pnas.91.22.10625.

[180] J. Perl, J. Shin, J. Schumann, B. Faddegon, and H. Paganetti. “TOPAS: an innovative proton Monte Carlo platform for research and clinical applications”. In: *Medical Physics* 39.11, Nov. 2012, pages 6818–6837. ISSN: 0094-2405. DOI: 10.1118/1.4758060.

[181] F. F. Permatasari, J. Eulitz, C. Richter, P. Wohlfahrt, and A. Lühr. “Material assignment for proton range prediction in Monte Carlo patient simulations using stopping-power datasets”. In: *Physics in Medicine and Biology* 65.18, Sept. 11, 2020, page 185004. ISSN: 1361-6560. DOI: 10.1088/1361-6560/ab9702.

[182] F. Pezoa, J. L. Reutter, F. Suarez, M. Ugarte, and D. Vrgoč. “Foundations of JSON schema”. In: *Proceedings of the 25th International Conference on World Wide Web*. International World Wide Web Conferences Steering Committee. 2016, pages 263–273.

[183] F. Pezoa, J. L. Reutter, F. Suarez, M. Ugarte, and D. Vrgoč. “Foundations of JSON Schema”. In: *Proceedings of the 25th International Conference on World Wide Web*. WWW ’16. Republic and Canton of Geneva, CHE: International World Wide Web Conferences Steering Committee, Apr. 11, 2016, pages 263–273. ISBN: 978-1-4503-4143-1. DOI: 10.1145/2872427.2883029.

[184] M. Pluta. *Advanced Light Microscopy: Principles and basic properties*. Google-Books-ID: j2XwAAAAMAAJ. Elsevier, 1988. 496 pages. ISBN: 978-0-444-98939-0.

[185] *Proton Therapy Physics*. Boca Raton: CRC Press, Apr. 19, 2016. 704 pages. ISBN: 978-0-367-80355-1. DOI: 10.1201/9780367803551.

[186] M. Puderbaugh and P. D. Emmady. “Neuroplasticity”. In: *StatPearls*. Treasure Island (FL): StatPearls Publishing, 2023.

[187] J. Puyal, V. Ginet, and P. G. H. Clarke. “Multiple interacting cell death mechanisms in the mediation of excitotoxicity and ischemic brain damage: A challenge for neuroprotection”. In: *Progress in Neurobiology* 105, June 1, 2013, pages 24–48. ISSN: 0301-0082. DOI: 10.1016/j.pneurobio.2013.03.002.

[188] PyQT. “PyQt Reference Guide”. In: 2012.

[189] L. R. Qiu, D. J. Fernandes, K. U. Szulc-Lerch, J. Dazai, B. J. Nieman, D. H. Turnbull, J. A. Foster, M. R. Palmert, and J. P. Lerch. “Mouse MRI shows brain areas relatively larger in males emerge before those larger in females”. In: *Nature Communications* 9.1, July 5, 2018. Number: 1 Publisher: Nature Publishing Group, page 2615. ISSN: 2041-1723. DOI: 10.1038/s41467-018-04921-2.

[190] N. Ren, J. Liang, X. Qu, J. Li, B. Lu, and J. Tian. “GPU-based Monte Carlo simulation for light propagation in complex heterogeneous tissues”. In: *Optics Express* 18.7, Mar. 29, 2010. Publisher: Optica Publishing Group, pages 6811–6823. ISSN: 1094-4087. DOI: 10.1364/OE.18.006811.

[191] K. Richards, C. Watson, R. F. Buckley, N. D. Kurniawan, Z. Yang, M. D. Keller, R. Beare, P. F. Bartlett, G. F. Egan, G. J. Galloway, G. Paxinos, S. Petrou, and D. C. Reutens. “Segmentation of the mouse hippocampal formation in magnetic resonance images”. In: *NeuroImage* 58.3, Oct. 1, 2011, pages 732–740. ISSN: 1095-9572. DOI: 10.1016/j.neuroimage.2011.06.025.

[192] A. R. Rivolo. “The Two-Point Galaxy Correlation Function of the Local Supercluster”. In: *The Astrophysical Journal* 301, Feb. 1, 1986. ADS Bibcode: 1986ApJ...301...70R, page 70. ISSN: 0004-637X. DOI: 10.1086/163873.

[193] R. B. Rock, G. Gekker, S. Hu, W. S. Sheng, M. Cheeran, J. R. Lokensgard, and P. K. Peterson. “Role of Microglia in Central Nervous System Infections”. In: *Clinical Microbiology Reviews* 17.4, Oct. 2004, pages 942–964. ISSN: 0893-8512. DOI: 10.1128/CMR.17.4.942-964.2004.

[194] M. D. Roggan, J. Kronenberg, E. Wollert, S. Hoffmann, H. Nisar, B. Konda, S. Diegeler, C. Liemersdorf, and C. E. Hellweg. “Unraveling astrocyte behavior in the space brain: Radiation response of primary astrocytes”. In: *Frontiers in Public Health* 11, 2023, page 1063250. ISSN: 2296-2565. DOI: 10.3389/fpubh.2023.1063250.

[195] R. Rojas. *Neural Networks*. Berlin, Heidelberg: Springer, 1996. ISBN: 978-3-540-60505-8 978-3-642-61068-4. DOI: 10.1007/978-3-642-61068-4.

[196] O. Ronneberger, P. Fischer, and T. Brox. “U-Net: Convolutional Networks for Biomedical Image Segmentation”. In: *Medical Image Computing and Computer-Assisted Intervention – MICCAI 2015*. Edited by N. Navab, J. Hornegger, W. M. Wells, and A. F. Frangi. Lecture Notes in Computer Science. Cham: Springer International Publishing, 2015, pages 234–241. ISBN: 978-3-319-24574-4. DOI: 10.1007/978-3-319-24574-4_28.

[197] F. W. D. Rost. *Fluorescence Microscopy*. Cambridge University Press, 1992. 486 pages. ISBN: 978-0-521-41088-5.

[198] D. Ruijters and P. Thevenaz. “GPU Prefilter for Accurate Cubic B-spline Interpolation”. In: *The Computer Journal* 55.1, Jan. 1, 2012, pages 15–20. ISSN: 0010-4620, 1460-2067. DOI: 10.1093/comjnl/bxq086.

[199] D. E. Rumelhart, G. E. Hinton, and R. J. Williams. “Learning representations by back-propagating errors”. In: *Nature* 323.6088, Oct. 1986. Number: 6088 Publisher: Nature Publishing Group, pages 533–536. ISSN: 1476-4687. DOI: 10.1038/323533a0.

[200] M. Saager, P. Peschke, S. Brons, J. Debus, and C. P. Karger. “Determination of the proton RBE in the rat spinal cord: Is there an increase towards the end of the spread-out Bragg peak?” In: *Radiotherapy and Oncology: Journal of the European Society for Therapeutic Radiology and Oncology* 128.1, July 2018, pages 115–120. ISSN: 1879-0887. DOI: `10.1016/j.radonc.2018.03.002`.

[201] S. Sakata. “[Volume effect models in radiation therapy]”. In: *Gan No Rinsho. Japan Journal of Cancer Clinics* 33.13, Oct. 1987, pages 1532–1541. ISSN: 0021-4949.

[202] A. Sale, N. Berardi, and L. Maffei. “Environment and Brain Plasticity: Towards an Endogenous Pharmacotherapy”. In: *Physiological Reviews* 94.1, Jan. 2014. Publisher: American Physiological Society, pages 189–234. ISSN: 0031-9333. DOI: `10.1152/physrev.00036.2012`.

[203] R. Sauer. *Strahlentherapie und Onkologie*. 4th edition. München: Urban & Fischer Verlag/Elsevier GmbH, July 1, 2003. 644 pages. ISBN: 978-3-437-47500-9.

[204] C.-L. Schengrund and R. K. Yu, editors. *Glycobiology of the Nervous System*. Volume 29. Advances in Neurobiology. Cham: Springer International Publishing, 2023. ISBN: 978-3-031-12389-4 978-3-031-12390-0. DOI: `10.1007/978-3-031-12390-0`.

[205] W. Schlegel, C. P. Karger, and O. Jäkel, editors. *Medizinische Physik: Grundlagen – Bildgebung – Therapie – Technik*. Berlin, Heidelberg: Springer, 2018. ISBN: 978-3-662-54800-4 978-3-662-54801-1. DOI: `10.1007/978-3-662-54801-1`.

[206] W. Schneider, T. Bortfeld, and W. Schlegel. “Correlation between CT numbers and tissue parameters needed for Monte Carlo simulations of clinical dose distributions”. In: *Physics in Medicine and Biology* 45.2, Feb. 2000, pages 459–478. ISSN: 0031-9155. DOI: `10.1088/0031-9155/45/2/314`.

[207] J. A. Scott. “ICRP Publication 60. 1990 Recommendations of the International Commission on Radiological Protection: New York, Pergamon Press, 1991, 201 pp, $142.50”. In: *Journal of Nuclear Medicine* 33.5, May 1, 1992. Publisher: Society of Nuclear Medicine Section: Departments, pages 821–821. ISSN: 0161-5505, 2159-662X.

[208] J. Seco and F. Verhaegen. *Monte Carlo Techniques in Radiation Therapy: Applications to Dosimetry, Imaging, Preclinical Radiotherapy*. Google-Books-ID: K69qzgEACAAJ. CRC Press, Oct. 2021. 274 pages. ISBN: 978-1-00-321248-5.

[209] A. M. H. Seelke, J. C. Dooley, and L. A. Krubitzer. “Differential changes in the cellular composition of the developing marsupial brain”. In: *The Journal of comparative neurology* 521.11, Aug. 1, 2013, pages 2602–2620. ISSN: 0021-9967. DOI: `10.1002/cne.23301`.

[210] M. Sezgin and B. Sankur. “Survey over image thresholding techniques and quantitative performance evaluation”. In: *Journal of Electronic Imaging* 13.1, Jan. 2004. Publisher: SPIE, pages 146–165. ISSN: 1017-9909, 1560-229X. DOI: 10.1117/1.1631315.

[211] D. P. Shamonin, E. E. Bron, B. P. F. Lelieveldt, M. Smits, S. Klein, M. Staring, and Alzheimer’s Disease Neuroimaging Initiative. “Fast parallel image registration on CPU and GPU for diagnostic classification of Alzheimer’s disease”. In: *Frontiers in Neuroinformatics* 7, 2013, page 50. ISSN: 1662-5196. DOI: 10.3389/fninf.2013.00050.

[212] D. S. Sharma. “Proton Therapy Physics (Second Edition)”. In: *Journal of Medical Physics* 45.3, 2020, pages 195–196. ISSN: 0971-6203. DOI: 10.4103/jmp.JMP_86_20.

[213] D. Shen, G. Wu, and H.-I. Suk. “Deep Learning in Medical Image Analysis”. In: *Annual review of biomedical engineering* 19, June 21, 2017, pages 221–248. ISSN: 1523-9829. DOI: 10.1146/annurev-bioeng-071516-044442.

[214] S. Shit, J. C. Paetzold, A. Sekuboyina, I. Ezhov, A. Unger, A. Zhylka, J. P. W. Pluim, U. Bauer, and B. H. Menze. “clDice - a Novel Topology-Preserving Loss Function for Tubular Structure Segmentation”. In: *2021 IEEE/CVF Conference on Computer Vision and Pattern Recognition (CVPR)*, June 2021. Conference Name: 2021 IEEE/CVF Conference on Computer Vision and Pattern Recognition (CVPR) ISBN: 9781665445092 Place: Nashville, TN, USA Publisher: IEEE, pages 16555–16564. DOI: 10.1109/CVPR46437.2021.01629.

[215] J. Silver and J. H. Miller. “Regeneration beyond the glial scar”. In: *Nature Reviews Neuroscience* 5.2, Feb. 2004. Number: 2 Publisher: Nature Publishing Group, pages 146–156. ISSN: 1471-0048. DOI: 10.1038/nrn1326.

[216] K. Simonyan and A. Zisserman. *Very Deep Convolutional Networks for Large-Scale Image Recognition.* Apr. 10, 2015. DOI: 10.48550/arXiv.1409.1556. arXiv: 1409.1556[cs].

[217] M. V. Sofroniew. “Reactive Astrocytes in Neural Repair and Protection”. In: *The Neuroscientist* 11.5, Oct. 1, 2005. Publisher: SAGE Publications Inc STM, pages 400–407. ISSN: 1073-8584. DOI: 10.1177/1073858405278321.

[218] M. V. Sofroniew. “Molecular dissection of reactive astrogliosis and glial scar formation”. In: *Trends in Neurosciences* 32.12, Dec. 2009, pages 638–647. ISSN: 1878-108X. DOI: 10.1016/j.tins.2009.08.002.

[219] M. V. Sofroniew. “Astrogliosis”. In: *Cold Spring Harbor Perspectives in Biology* 7.2, Feb. 2015, a020420. ISSN: 1943-0264. DOI: 10.1101/cshperspect.a020420.

[220] M. V. Sofroniew. “Astrocyte Reactivity: Subtypes, States, and Functions in CNS Innate Immunity”. In: *Trends in Immunology* 41.9, Sept. 2020, pages 758–770. ISSN: 1471-4981. DOI: 10.1016/j.it.2020.07.004.

[221] M. V. Sofroniew and H. V. Vinters. “Astrocytes: biology and pathology”. In: *Acta Neuropathologica* 119.1, 2010, pages 7–35. ISSN: 0001-6322. DOI: 10.1007/s00401-009-0619-8.

[222] J. Soltwedel, T. Suckert, E. Beyreuther, M. Schneider, M. Boucsein, E. Bodenstein, S. Nexhipi, L. Stolz-Kieslich, M. Krause, C. von Neubeck, R. Haase, A. Lühr, and A. Dietrich. “Slice2Volume: Fusion of multimodal medical imaging and light microscopy data of irradiation-injured brain tissue in 3D”. In: *Radiotherapy and Oncology: Journal of the European Society for Therapeutic Radiology and Oncology* 182, May 2023, page 109591. ISSN: 1879-0887. DOI: 10.1016/j.radonc.2023.109591.

[223] F. Spanos and S. A. Liddelow. “An Overview of Astrocyte Responses in Genetically Induced Alzheimer’s Disease Mouse Models”. In: *Cells* 9.11, Nov. 2020. Number: 11 Publisher: Multidisciplinary Digital Publishing Institute, page 2415. ISSN: 2073-4409. DOI: 10.3390/cells9112415.

[224] S. Sra, S. Nowozin, and S. J. Wright. *Optimization for Machine Learning*. Google-Books-ID: JPQx7s2L1A8C. MIT Press, 2012. 509 pages. ISBN: 978-0-262-01646-9.

[225] A. Srivastava, E. Klassen, S. H. Joshi, and I. H. Jermyn. “Shape Analysis of Elastic Curves in Euclidean Spaces”. In: *IEEE transactions on pattern analysis and machine intelligence* 33.7, July 2011, pages 1415–1428. ISSN: 1939-3539. DOI: 10.1109/TPAMI.2010.184.

[226] R. Srivastava, S. Kumar, and B. Kumar. “7 - Classification model of machine learning for medical data analysis”. In: *Statistical Modeling in Machine Learning*. Edited by T. Goswami and G. R. Sinha. Academic Press, Jan. 1, 2023, pages 111–132. ISBN: 978-0-323-91776-6. DOI: 10.1016/B978-0-323-91776-6.00017-8.

[227] P. E. Steadman, J. Ellegood, K. U. Szulc, D. H. Turnbull, A. L. Joyner, R. M. Henkelman, and J. P. Lerch. “Genetic effects on cerebellar structure across mouse models of autism using a magnetic resonance imaging atlas”. In: *Autism Research: Official Journal of the International Society for Autism Research* 7.1, Feb. 2014, pages 124–137. ISSN: 1939-3806. DOI: 10.1002/aur.1344.

[228] C. C. Stichel and H. W. Müller. “The CNS lesion scar: new vistas on an old regeneration barrier”. In: *Cell and Tissue Research* 294.1, Sept. 1, 1998, pages 1–9. ISSN: 1432-0878. DOI: 10.1007/s004410051151.

[229] F. F. Stæger, K. N. Mortensen, M. S. N. Nielsen, B. Sigurdsson, L. K. Kaufmann, H. Hirase, and M. Nedergaard. “A three-dimensional, population-based average of the C57BL/6 mouse brain from DAPI-stained coronal slices”. In: *Scientific Data* 7.1, July 13, 2020. Number: 1 Publisher: Nature Publishing Group, page 235. ISSN: 2052-4463. DOI: 10.1038/s41597-020-0570-z.

[230] T. Suckert, E. Beyreuther, J. Müller, B. Azadegan, M. Meinhardt, F. Raschke, E. Bodenstein, C. von Neubeck, A. Lühr, M. Krause, and A. Dietrich. “Late Side Effects in Normal Mouse Brain Tissue After Proton Irradiation”. In: *Frontiers in Oncology* 10, 2021. ISSN: 2234-943X.

[231] T. Suckert, J. Müller, E. Beyreuther, B. Azadegan, A. Brüggemann, R. Bütof, A. Dietrich, M. Gotz, R. Haase, M. Schürer, F. Tillner, C. von Neubeck, M. Krause, and A. Lühr. “High-precision image-guided proton irradiation of mouse brain sub-volumes”. In: *Radiotherapy and Oncology: Journal of the European Society for Therapeutic Radiology and Oncology* 146, May 2020, pages 205–212. ISSN: 1879-0887. DOI: `10.1016/j.radonc.2020.02.023`.

[232] S. M. Sunkin, L. Ng, C. Lau, T. Dolbeare, T. L. Gilbert, C. L. Thompson, M. Hawrylycz, and C. Dang. “Allen Brain Atlas: an integrated spatio-temporal portal for exploring the central nervous system”. In: *Nucleic Acids Research* 41, Database issue Jan. 2013, pages D996–D1008. ISSN: 1362-4962. DOI: `10.1093/nar/gks1042`.

[233] I. Sutskever. “Training recurrent neural networks”. AAINS22066 ISBN-13: 9780499220660. PhD thesis. CAN: University of Toronto, 2013. 149 pages.

[234] C. Szegedy, S. Ioffe, V. Vanhoucke, and A. Alemi. *Inception-v4, Inception-ResNet and the Impact of Residual Connections on Learning*. Aug. 23, 2016. DOI: `10.48550/arXiv.1602.07261`. arXiv: `1602.07261[cs]`.

[235] B. S. Sørensen, J. Pawelke, J. Bauer, N. G. Burnet, A. Dasu, M. Høyer, C. P. Karger, M. Krause, M. Schwarz, T. S. A. Underwood, D. Wagenaar, G. A. Whitfield, and A. Lühr. “Does the uncertainty in relative biological effectiveness affect patient treatment in proton therapy?” In: *Radiotherapy and Oncology* 163, Oct. 1, 2021, pages 177–184. ISSN: 0167-8140. DOI: `10.1016/j.radonc.2021.08.016`.

[236] B. S. Sørensen. “Commentary: RBE in proton therapy – where is the experimental in vivo data?” In: *Acta Oncologica* 58.10, Oct. 3, 2019, pages 1337–1339. ISSN: 0284-186X. DOI: `10.1080/0284186X.2019.1669819`.

[237] B. S. Sørensen, N. Bassler, S. Nielsen, M. R. Horsman, L. Grzanka, H. Spejlborg, J. Swakoń, P. Olko, and J. Overgaard. “Relative biological effectiveness (RBE) and distal edge effects of proton radiation on early damage in vivo”. In: *Acta Oncologica (Stockholm, Sweden)* 56.11, Nov. 2017, pages 1387–1391. ISSN: 1651-226X. DOI: `10.1080/0284186X.2017.1351621`.

[238] T. Sørensen. *A Method of Establishing Groups of Equal Amplitude in Plant Sociology Based on Similarity of Species Content and Its Application to Analyses of the Vegetation on Danish Commons*. Google-Books-ID: rpS8GAAACAAJ. Munksgaard in Komm., 1948. 34 pages.

[239] J. Tang, M. Bair, and G. Descalzi. “Reactive Astrocytes: Critical Players in the Development of Chronic Pain”. In: *Frontiers in Psychiatry* 12, May 28, 2021, page 682056. ISSN: 1664-0640. DOI: `10.3389/fpsyt.2021.682056`.

[240] S. A. Taqi, S. A. Sami, L. B. Sami, and S. A. Zaki. “A review of artifacts in histopathology”. In: *Journal of Oral and Maxillofacial Pathology : JOMFP* 22.2, 2018, page 279. ISSN: 0973-029X. DOI: `10.4103/jomfp.JOMFP_125_15`.

[241] T. Tessonnier, S. Ecker, J. Besuglow, J. Naumann, S. Mein, F. K. Longarino, M. Ellerbrock, B. Ackermann, M. Winter, S. Brons, A. Qubala, T. Haberer, J. Debus, O. Jäkel, and A. Mairani. “Commissioning of Helium Ion Therapy and the First Patient Treatment With Active Beam Delivery”. In: *International Journal of Radiation Oncology, Biology, Physics* 116.4, July 15, 2023. Publisher: Elsevier, pages 935–948. ISSN: 0360-3016. DOI: `10.1016/j.ijrobp.2023.01.015`.

[242] F. Tillner, P. Thute, S. Löck, A. Dietrich, A. Fursov, R. Haase, M. Lukas, B. Rimarzig, M. Sobiella, M. Krause, M. Baumann, R. Bütof, and W. Enghardt. “Precise image-guided irradiation of small animals: a flexible non-profit platform”. In: *Physics in Medicine & Biology* 61.8, Mar. 2016. Publisher: IOP Publishing, page 3084. ISSN: 0031-9155. DOI: `10.1088/0031-9155/61/8/3084`.

[243] F. Tommasino and M. Durante. “Proton radiobiology”. In: *Cancers* 7.1, Feb. 12, 2015, pages 353–381. ISSN: 2072-6694. DOI: `10.3390/cancers7010353`.

[244] A. Trewavas. “A Brief History of Systems Biology: “Every object that biology studies is a system of systems.” Francois Jacob (1974).” In: *The Plant Cell* 18.10, Oct. 2006. Publisher: Oxford University Press, page 2420. DOI: `10.1105/tpc.106.042267`.

[245] H. K. Tuy. “An Inversion Formula for Cone-Beam Reconstruction”. In: *SIAM Journal on Applied Mathematics* 43.3, June 1983. Publisher: Society for Industrial and Applied Mathematics, pages 546–552. ISSN: 0036-1399. DOI: `10.1137/0143035`.

[246] J. F. P. Ullmann, C. Watson, A. L. Janke, N. D. Kurniawan, and D. C. Reutens. “A segmentation protocol and MRI atlas of the C57BL/6J mouse neocortex”. In: *NeuroImage* 78, Sept. 2013, pages 196–203. ISSN: 1095-9572. DOI: `10.1016/j.neuroimage.2013.04.008`.

[247] M. Unberath, C. Gao, Y. Hu, M. Judish, R. H. Taylor, M. Armand, and R. Grupp. “The Impact of Machine Learning on 2D/3D Registration for Image-Guided Interventions: A Systematic Review and Perspective”. In: *Frontiers in Robotics and AI* 8, 2021. ISSN: 2296-9144.

[248] M. Unser. “Splines: a perfect fit for signal and image processing”. In: *IEEE Signal Processing Magazine* 16.6, Nov. 1999. Conference Name: IEEE Signal Processing Magazine, pages 22–38. ISSN: 1558-0792. DOI: `10.1109/79.799930`.

[249] M. Unser, A. Aldroubi, and M. Eden. “B-spline signal processing. I. Theory”. In: *IEEE Transactions on Signal Processing* 41.2, Feb. 1993. Conference Name: IEEE Transactions on Signal Processing, pages 821–833. ISSN: 1941-0476. DOI: `10.1109/78.193220`.

[250] M. Unser, A. Aldroubi, and M. Eden. “B-Spline Signal-Processing .2. Efficient Design and Applications”. In: *Signal Processing, IEEE Transactions on* 41, Mar. 1, 1993, pages 834–848. DOI: 10.1109/78.193221.

[251] F. Vasile, E. Dossi, and N. Rouach. “Human astrocytes: structure and functions in the healthy brain”. In: *Brain Structure & Function* 222.5, July 2017, pages 2017–2029. ISSN: 1863-2661. DOI: 10.1007/s00429-017-1383-5.

[252] F. Verhaegen, K. T. Butterworth, A. J. Chalmers, R. P. Coppes, D. d. Ruysscher, S. Dobiasch, J. D. Fenwick, P. V. Granton, S. H. J. Heijmans, M. A. Hill, C. Koumenis, K. Lauber, B. Marples, K. Parodi, L. C. G. G. Persoon, N. Staut, A. Subiel, R. D. W. Vaes, S. v. Hoof, I. L. Verginadis, J. J. Wilkens, K. J. Williams, G. D. Wilson, and L. J. Dubois. “Roadmap for precision preclinical x-ray radiation studies”. In: *Physics in Medicine & Biology* 68.6, Mar. 2023. Publisher: IOP Publishing, 06RM01. ISSN: 0031-9155. DOI: 10.1088/1361-6560/acaf45.

[253] F. Verhaegen, L. Dubois, S. Gianolini, M. A. Hill, C. P. Karger, K. Lauber, K. M. Prise, D. Sarrut, D. Thorwarth, C. Vanhove, B. Vojnovic, R. Weersink, J. J. Wilkens, and D. Georg. “ESTRO ACROP: Technology for precision small animal radiotherapy research: Optimal use and challenges”. In: *Radiotherapy and Oncology: Journal of the European Society for Therapeutic Radiology and Oncology* 126.3, Mar. 2018, pages 471–478. ISSN: 1879-0887. DOI: 10.1016/j.radonc.2017.11.016.

[254] F. Verhaegen, P. Granton, and E. Tryggestad. “Small animal radiotherapy research platforms”. In: *Physics in Medicine and Biology* 56.12, June 21, 2011, R55–83. ISSN: 1361-6560. DOI: 10.1088/0031-9155/56/12/R01.

[255] F. Verhaegen, S. van Hoof, P. V. Granton, and D. Trani. “A review of treatment planning for precision image-guided photon beam pre-clinical animal radiation studies”. In: *Zeitschrift Fur Medizinische Physik* 24.4, Dec. 2014, pages 323–334. ISSN: 1876-4436. DOI: 10.1016/j.zemedi.2014.02.004.

[256] P. Virtanen, R. Gommers, T. E. Oliphant, M. Haberland, T. Reddy, D. Cournapeau, E. Burovski, P. Peterson, W. Weckesser, J. Bright, S. J. van der Walt, M. Brett, J. Wilson, K. J. Millman, N. Mayorov, A. R. J. Nelson, E. Jones, R. Kern, E. Larson, C. J. Carey, Polat, Y. Feng, E. W. Moore, J. VanderPlas, D. Laxalde, J. Perktold, R. Cimrman, I. Henriksen, E. A. Quintero, C. R. Harris, A. M. Archibald, A. H. Ribeiro, F. Pedregosa, and P. van Mulbregt. “SciPy 1.0: fundamental algorithms for scientific computing in Python”. In: *Nature Methods* 17.3, Mar. 2020. Number: 3 Publisher: Nature Publishing Group, pages 261–272. ISSN: 1548-7105. DOI: 10.1038/s41592-019-0686-2.

[257] A. Voulodimos, N. Doulamis, A. Doulamis, and E. Protopapadakis. “Deep Learning for Computer Vision: A Brief Review”. In: *Computational Intelligence and Neuroscience* 2018, 2018, page 7068349. ISSN: 1687-5273. DOI: 10.1155/2018/7068349.

[258] T. Vöth. “3D Reconstruction of Interventional Material from Very Few X-Ray Projections for Interventional Image Guidance”. PhD thesis. Heidelberg University, 2023. DOI: 10.11588/heidok.00033627.

[259] S. v. d. Walt, J. L. Schönberger, J. Nunez-Iglesias, F. Boulogne, J. D. Warner, N. Yager, E. Gouillart, and T. Yu. “scikit-image: image processing in Python”. In: *PeerJ* 2, June 19, 2014. Publisher: PeerJ Inc., e453. ISSN: 2167-8359. DOI: 10.7717/peerj.453.

[260] Q. Wang, S.-L. Ding, Y. Li, J. Royall, D. Feng, P. Lesnar, N. Graddis, M. Naeemi, B. Facer, A. Ho, T. Dolbeare, B. Blanchard, N. Dee, W. Wakeman, K. E. Hirokawa, A. Szafer, S. M. Sunkin, S. W. Oh, A. Bernard, J. W. Phillips, M. Hawrylycz, C. Koch, H. Zeng, J. A. Harris, and L. Ng. “The Allen Mouse Brain Common Coordinate Framework: A 3D Reference Atlas”. In: *Cell* 181.4, May 14, 2020, 936–953.e20. ISSN: 0092-8674. DOI: 10.1016/j.cell.2020.04.007.

[261] M. Wannenmacher, F. Wenz, and J. Debus, editors. *Strahlentherapie*. Berlin, Heidelberg: Springer, 2013. ISBN: 978-3-540-88304-3 978-3-540-88305-0. DOI: 10.1007/978-3-540-88305-0.

[262] I. M. Watt. *The Principles and Practice of Electron Microscopy*. 2nd edition. Cambridge: Cambridge University Press, 1997. ISBN: 978-0-521-43591-8. DOI: 10.1017/CBO9781139170529.

[263] D. C. Wei and E. H. Morrison. *Histology, Astrocytes*. Treasure Island (FL): StatPearls Publishing, 2023.

[264] B. L. WELCH. “THE GENERALIZATION OF ‘STUDENT’S’ PROBLEM WHEN SEVERAL DIFFERENT POPULATION VARLANCES ARE INVOLVED”. In: *Biometrika* 34.1, Jan. 1, 1947, pages 28–35. ISSN: 0006-3444. DOI: 10.1093/biomet/34.1-2.28.

[265] H.-P. Wieser, E. Cisternas, N. Wahl, S. Ulrich, A. Stadler, H. Mescher, L.-R. Müller, T. Klinge, H. Gabrys, L. Burigo, A. Mairani, S. Ecker, B. Ackermann, M. Ellerbrock, K. Parodi, O. Jäkel, and M. Bangert. “Development of the open-source dose calculation and optimization toolkit matRad”. In: *Medical Physics* 44.6, 2017, pages 2556–2568. ISSN: 2473-4209. DOI: 10.1002/mp.12251.

[266] H. Willers, A. Allen, D. Grosshans, S. J. McMahon, C. von Neubeck, C. Wiese, and B. Vikram. “Toward A variable RBE for proton beam therapy”. In: *Radiotherapy and Oncology: Journal of the European Society for Therapeutic Radiology and Oncology* 128.1, July 2018, pages 68–75. ISSN: 1879-0887. DOI: 10.1016/j.radonc.2018.05.019.

[267] J. P. Williams, S. L. Brown, G. E. Georges, M. Hauer-Jensen, R. P. Hill, A. K. Huser, D. G. Kirsch, T. J. MacVittie, K. A. Mason, M. M. Medhora, J. E. Moulder, P. Okunieff, M. F. Otterson, M. E. Robbins, J. B. Smathers, and W. H. McBride. “Animal Models for Medical Countermeasures to Radiation Exposure”. In: *Radiation research* 173.4, Apr. 2010, pages 557–578. ISSN: 0033-7587. DOI: 10.1667/RR1880.1.

[268] K. I. Willig, S. O. Rizzoli, V. Westphal, R. Jahn, and S. W. Hell. “STED microscopy reveals that synaptotagmin remains clustered after synaptic vesicle exocytosis”. In: *Nature* 440.7086, Apr. 2006. Number: 7086 Publisher: Nature Publishing Group, pages 935–939. ISSN: 1476-4687. DOI: 10.1038/nature04592.

[269] C. M. Wilson, M. W. Gaber, O. M. Sabek, J. A. Zawaski, and T. E. Merchant. “Radiation-Induced Astrogliosis and Blood-Brain Barrier Damage Can Be Abrogated Using Anti-TNF Treatment”. In: *International Journal of Radiation Oncology, Biology, Physics* 74.3, July 1, 2009. Publisher: Elsevier, pages 934–941. ISSN: 0360-3016. DOI: 10.1016/j.ijrobp.2009.02.035.

[270] J. Wong, E. Armour, P. Kazanzides, I. Iordachita, E. Tryggestad, H. Deng, M. Matinfar, C. Kennedy, Z. Liu, T. Chan, O. Gray, F. Verhaegen, T. McNutt, E. Ford, and T. L. DeWeese. “A high resolution small animal radiation research platform (SARRP) with x-ray tomographic guidance capabilities”. In: *International journal of radiation oncology, biology, physics* 71.5, Aug. 1, 2008, pages 1591–1599. ISSN: 0360-3016. DOI: 10.1016/j.ijrobp.2008.04.025.

[271] B. G. Wouters, G. K. Y. Lam, U. Oelfke, K. Gardey, R. E. Durand, and L. D. Skarsgard. “Measurements of Relative Biological Effectiveness of the 70 MeV Proton Beam at TRIUMF Using Chinese Hamster V79 Cells and the High-Precision Cell Sorter Assay”. In: *Radiation Research* 146.2, 1996. Publisher: Radiation Research Society, pages 159–170. ISSN: 0033-7587. DOI: 10.2307/3579588.

[272] J. Xiong, J. Ren, L. Luo, and M. Horowitz. “Mapping Histological Slice Sequences to the Allen Mouse Brain Atlas Without 3D Reconstruction”. In: *Frontiers in Neuroinformatics* 12, 2018. ISSN: 1662-5196.

[273] T. Yang, Y. Dai, G. Chen, and S. Cui. “Dissecting the Dual Role of the Glial Scar and Scar-Forming Astrocytes in Spinal Cord Injury”. In: *Frontiers in Cellular Neuroscience* 14, 2020. ISSN: 1662-5102.

[274] T. S. Yoo, M. J. Ackerman, W. E. Lorensen, W. Schroeder, V. Chalana, S. Aylward, D. Metaxas, and R. Whitaker. “Engineering and algorithm design for an image processing Api: a technical report on ITK–the Insight Toolkit”. In: *Studies in Health Technology and Informatics* 85, 2002, pages 586–592. ISSN: 0926-9630.

[275] O. Zachariadis, A. Teatini, N. Satpute, J. Gómez-Luna, O. Mutlu, O. J. Elle, and J. Olivares. “Accelerating B-spline interpolation on GPUs: Application to medical image registration”. In: *Computer Methods and Programs in Biomedicine* 193, Sept. 1, 2020, page 105431. ISSN: 0169-2607. DOI: 10.1016/j.cmpb.2020.105431.

[276] M. Zaider and H. H. Rossi. “On the Question of RBE Reversal at High Doses”. In: *Radiation Research* 130.1, 1992. Publisher: Radiation Research Society, pages 117–120. ISSN: 0033-7587. DOI: 10.2307/3578488.

[277] R. Zhang, Y. Wu, F. Xie, Y. Zhong, Y. Wang, M. Xu, J. Feng, J. Charish, P. P. Monnier, and X. Qin. “RGMa mediates reactive astrogliosis and glial scar formation through TGF1/Smad2/3 signaling after stroke”. In: *Cell Death & Differentiation* 25.8, Aug. 2018. Number: 8 Publisher: Nature Publishing Group, pages 1503–1516. ISSN: 1476-5403. DOI: 10.1038/s41418-018-0058-y.

[278] X. Zhang, Y. Li, X. Li, X. Rong, Y. Tang, and Y. Peng. “Neuroprotective effect of Dl-3-n-butylphthalide on patients with radiation-induced brain injury: a clinical retrospective cohort study”. In: *The International Journal of Neuroscience* 127.12, Dec. 2017, pages 1059–1064. ISSN: 1563-5279. DOI: 10.1080/00207454.2017.1310727.

[279] Z. Zhang, Z. Ma, W. Zou, H. Guo, M. Liu, Y. Ma, and L. Zhang. “The Appropriate Marker for Astrocytes: Comparing the Distribution and Expression of Three Astrocytic Markers in Different Mouse Cerebral Regions”. In: *BioMed Research International* 2019, June 24, 2019, page 9605265. ISSN: 2314-6133. DOI: 10.1155/2019/9605265.

[280] D. Zuro, S. S. Madabushi, J. Brooks, B. T. Chen, J. Goud, A. Salhotra, J. Y. Song, L. E. Parra, A. Pierini, J. F. Sanchez, A. Stein, M. A. Malki, M. Kortylewski, J. Y. C. Wong, P. Alaei, J. Froelich, G. Storme, and S. K. Hui. “First Multimodal, Three-Dimensional, Image-Guided Total Marrow Irradiation Model for Preclinical Bone Marrow Transplantation Studies”. In: *International Journal of Radiation Oncology, Biology, Physics* 111.3, Nov. 1, 2021, pages 671–683. ISSN: 1879-355X. DOI: 10.1016/j.ijrobp.2021.06.001.

List of Figures

5.1 Overview of the workflow for the preclinical experiment to investigate radiation-induced response after the proton irradiation of normal brain tissue. 33
5.2 An exemplary CBCT slice and an exemplary X-ray image of a mouse. . 34
5.3 Experimental preclinical beamline. 35
5.4 An exemplary MRI follow-up (T1-weighted) of a mouse irradiated with 65 Gy showing contrast enhancing brain lesions. 36
5.5 An exemplary GFAP-stained histological slice overlayed on the corresponding DAPI-stained slice of a C3H mouse irradiated with 60 Gy. 37

7.1 The Graphical User Interface of the Napari plugin **napari-nd-cropper**. . 48
7.2 The Graphical User Interface of the Napari plugin **napari-elementary-numpy-operations**. 49
7.3 An example of vignetting grid pattern in our fluorescence microscopy image data. 51

8.1 Overview of the presented steps for a-priori dose and a-posteriori dose calculation consisting of quantification of the repositioning/residual uncertainty and the resulting dose localization uncertainty. 54
8.2 The Graphical User Interface of the Napari plugin **Treatment Planning System (TPS)**. 58

9.1 An exemplary JSON Data format input file for the CBCT-Atlas registration. 64
9.2 An exemplary 2D view of the MRI template and a CBCT image with the set of seeded landmarks. 65
9.3 An exemplary 2D view of the DAPI-Nissl combined template and the MRI template with the set of seeded landmarks. 66
9.4 An exemplary 2D view of a DAPI-stained slice and the MRI-Nissl-DAPI template with the set of seeded landmarks. 67
9.5 The Graphical User Interface of the Napari plugin **Partial-Aligner**. 72
9.6 The established interaction box to Napari. 73
9.7 An exemplary JSON Data format input file for the Histology-Atlas 3D-2D registration. 75
9.8 The Graphical User Interface of the Napari plugin **napari-3D-Slicer**. . . . 76

10.1 Four samples of input-target pairs to train and validate the segmentation of reactive astrocytes. 78

12.1 An exemplary 3D dose distribution normalized to the maximal Dose and LET distribution overlayed on CBCT image. 90

12.2 An exemplary depth dose distribution normalized to the maximal Dose and LET distribution overlayed on the corresponding CBCT slice. 91

12.3 The difference ΔLET as a function of brain depth d of the LET of protons and associated secondary electrons with the LET of all particles, including neutrons and including neutrons as well as heavier particles and alpha particles. 92

13.1 An exemplary result in 3D view for applying the preprocessing steps for the CBCT images according to algorithm 8. 93

13.2 An exemplary cumulative histogram of the non-preprocessed X-ray image, the preprocessed X-ray image as well as the target 2D slice given by the mean projection of the CBCT. 94

13.3 An exemplary result for applying the preprocessing steps for the X-ray images according to algorithm 9. 94

13.4 Exemplary results of the preprocessing to remove vignetting. 97

14.1 Misalignment distributions for each positioning degree of freedom for pairwise rigidly registered CBCT images. 99

14.2 Dosimetric impact of misalignment before 3D position reconstruction. 101

14.3 Overview of an exemplary 3D position reconstruction by 2D-3D image matching. 102

14.4 Misalignment distribution for each translation and rotation parameter after 3D position reconstruction. 103

14.5 Dosimetric impact of misalignment after 3D position reconstruction. . 104

15.1 An exemplary 2D view of a final MRI-Nissl-DAPI template registration. 107

15.2 An exemplary 2D view overlay of the CBCT image registered to the MRI template. 108

15.3 An exemplary 2D view of a final Histology-Atlas registration. 110

15.4 An exemplary restoration process of a DAPI slice using the napari plugin **Partial-Aligner**. 111

15.5 An exemplary 2D view of a final Histology-Atlas registration is shown after applying the **Partial-Aligner** to restore DAPI slice. 112

15.6 An exemplary 3D view of a final Histology-Atlas registration. 113

16.1 A sample of the segmented astrocytes resulting from the trained U-Net architecture. 116

16.2 An overview of the different outcomes of segmentation approaches. . 117

17.1 The depth profiles for the number density of astrocytes and dose. . . . 119

17.2 The depth profiles for the number density of astrocytes and dose · LET. 120

17.3 The transversal profiles for the number density of astrocytes. 121

17.4 Scatter plot of number density n_{RA} of each cube in dependence of the Dose as well as Dose · LET. 121

17.5 An exemplary image tiles of the distribution of reactive astrocytes, which were exposed to equal dose (67 Gy) and LET (7 keV/μm) in the midbrain. . . 123

17.6 The $2-$point density correlation functions ξ for reactive astrocytes in the thalamus dependent on dose. 124

17.7 The $2-$point density correlation functions ξ for reactive astrocytes in the hippocampus dependent on dose. 124

17.8 The $2-$point density correlation functions ξ for reactive astrocytes in the midbrain dependent on dose. 125

17.9 The $2-$point correlation functions ξ for reactive astrocytes in the thalamus dependent on LET. 126

17.10 The $2-$point density correlation functions ξ for reactive astrocytes in the hippocampus, midbrain, and thalamus, exposed to the same dose and LET. 127

17.11 Geodesic distance between the shape of two astrocytes. 128

17.12 The shape distributions of reactive astrocytes in the thalamus for the two mouse strains. 129

17.13 The shape distributions of reactive astrocytes in the midbrain for two mouse strains. 130

17.14 The shape distributions of reactive astrocytes in the hippocampus for two mouse strains. 131

17.15 The size distributions of reactive astrocytes in the thalamus for two mouse strains. 132

17.16 The size distributions of reactive astrocytes in the midbrain for two mouse strains. 133

17.17 The size distributions of reactive astrocytes in the hippocampus for two mouse strains. 134

List of Tables

2.1 The contributions to the absorbed dose from Coulomb interactions for different proton energies. 10

12.1 The mean statistical error of the dose $\bar{\rho}_{\text{Dose}}$ and the LET distribution $\bar{\rho}_{\text{LET}}$ for 100 runs of each mouse. 91

13.1 The PSNR for the raw X-ray images and the 2D mean projection of the respective CBCT images as well as the preprocessed X-ray images and the 2D mean projection of the respective CBCT images for each mouse. 95

13.2 The mean homogeneity for each non-preprocessed $\mathbb{H}_{\text{Raw}}$ and the equivalent preprocessed $\mathbb{H}_{\text{Pre}}$ mouse following the preprocessing steps in Section 7.2. . 98

14.1 Repositioning accuracy of each positioning degree of freedom. 100

14.2 A-priori dose error. 101

14.3 Absolute mean residual error after 3D position reconstruction. 103

14.4 A-posteriori dose error. 105

15.1 The residual landmark-based registration error $d_{\text{MRRE\_CBCT\_MRI}}$. 109

15.2 The residual landmark-based registration error $d_{\text{MRRE\_Histology\_Atlas}}$. . . . 109

16.1 The Dice Score measuring the overlap of prediction and ground truth mask and the Jaccard index measuring the ability to identify astrocytes for each segmentation approach. 115

17.1 The means of the transversal dose profiles and number density profiles as well as the corresponding p-value. 122

17.2 Values of the maximum density correlation ξ_{max} and its increase with higher doses for the brain regions hippocampus, thalamus and midbrain. 125

17.3 The p-value for the Kolmogorov-Smirnow test to test the equality of the 2-point density correlation profiles ξ for different doses, LET, and brain regions. 126

17.4 The values of the maximum density correlation ξ_{max} and their increment with higher doses for the brain regions hippocampus, thalamus, and midbrain. . . 127

17.5 The p-value for the Kolmogorov-Smirnow test to test the equality of two 2-point density correlation profiles ξ. 128

17.6 The mean μ_{size} and the standard error of the mean sem of the size distributions of the reactive astrocytes in the thalamus. 135

Acknowledgements

Now it's time to say: Thank you!

First of all, I would like to thank my first supervisor Prof. Dr. Dr. Debus and my group leader Prof. Dr. Markus Alber. Thanks Prof. Dr. Dr. Debus for being a member of this group and for your excellent supervision! Thank you for the intense discussions and insights into various fields of physics and medicine. Thank you Markus. You've always been there to listen, to discuss, and to have a sympathetic ear for me. You've answered questions with a clarity that always offers new insights and perspectives. I have learned so much from you.

I would also like to thank Prof. Dr. Hausmann as my second reviewer for taking the time to review my thesis.

Furthermore, I would also like to thank my colleagues Dr. Julia Bauer, Dr. Emanuel Bahn, Dr. Annika Simon and Robin Koch. Especially Robin, as a colleague and friend, for sticking together, motivating etc. in difficult Corona times.

I would also like to thank my collaborators Prof. Dr. Armin Lühr, Dr. Elke Beyreuther, Dr. Antje Dietrich, Dr. Theresa Suckert, Dr. Johannes Soltwedel and Sindi Nexihipi for their biological input and data acquisition.

In addition, I would also like to thank other close friends, my coffee group consisting of Killian Dietrich and Yannis Arck, for distracting me in between and helping me to switch off mentally.

Finally, a big thank you goes out to my family, my wife and daughter, for whom there has been little time lately.

Especially to my wife, who has always taken everything in her stride...and has always had my back. My wonderful wife, who empathized with me and showed understanding when I was absent again, especially intellectually, and always stood by me. I hope to be able to return some of this in the future! And my daughter, who is simply the best and brings a smile no matter what. I love you.

And where would I be now if it wasn't for my parents, who paved the way for my studies, were always ready to help in any way, always my tower of strength, support me and always believed in me.

Thank you all so much. If I forgot anyone, I'm sorry... Thank you for your support.

Declaration

I hereby assure, that I composed this work by myself and did not use any other than the listed resources.

Heidelberg, January 17, 2024

M. Boucsein

Marc Boucsein